ORGANIC ELECTRONIC MATERIALS FOR NANOSCALE SYSTEMS: FROM LUMINESCENT BOTTLEBRUSH COPOLYMERS TO ULTRASTABLE FLUOROPHORES

by

Ethan R. Sauvé

B.Sc., The University of Western Ontario, 2016

A THESIS SUBMITTED IN PARTIAL FULFILLMENT OF

THE REQUIREMENTS FOR THE DEGREE OF

DOCTOR OF PHILOSPHY

in

THE FACULTY OF GRADUATE AND POSTDOCTORAL STUDIES

(CHEMISTRY)

THE UNIVERSITY OF BRITISH COLUMBIA

(Vancouver)

April 2021

The following individuals certify that they have read, and recommend to the Faculty of Graduate and Postdoctoral Studies for acceptance, the dissertation entitled:

Organic Electronic Materials for Nanoscale Systems: From Luminescent Bottlebrush Copolymers to Ultrastable Fluorophores

submitted by Ethan R. Sauvé in partial fulfillment of the requirements for

the degree of Doctor of Philosophy

in Chemistry

Examining Committee:

Zachary M. Hudson, Assistant Professor, Chemistry, University of British Columbia
Supervisor

Mark Thachuk, Associate Professor, Chemistry, University of British Columbia
Supervisory Committee Member

Peyman Servati, Professor, Electrical and Computer Engineering, University of British Columbia
University Examiner

Michael D. Fryzuk, Professor, Chemistry, University of British Columbia
University Examiner

Luis M. Campos, Associate Professor, Chemistry, Columbia University
External Examiner

Additional Supervisory Committee Members:

Jennifer A. Love, Professor, Chemistry, University of Calgary
Supervisory Committee Member

Derek P. Gates, Professor, Chemistry, University of British Columbia
Supervisory Committee Member

Abstract

Synthesis of multicomponent nanoscale structures with precisely addressable function is critical to discover new phenomena and new applications in nanotechnology. Though self-assembly offers a route such materials, these methods often require building blocks with particular structural motifs, limiting the scope of nanomaterials that can be prepared. Work described in the thesis uses a bottom-up approach based on covalent chemistry to synthesize a series of bottlebrush copolymers (BBCPs) – polymeric side chains attached covalently to a linear backbone – from organic semiconductors. Methods are also presented for the efficient synthesis of planar thermally activated delayed fluorescence (TADF) materials and stable organic fluorophores, incorporating them into nanoscale systems for biological imaging. A series of acrylic monomers was synthesized based on p-type organic semiconductor motifs found commonly in organic electronic devices. These monomers were polymerized by Cu(0)-reversible deactivation radical polymerization (RDRP), the kinetics of which are described in detail. By combining Cu(0)-RDRP and ring opening metathesis polymerization, narrowly dispersed multiblock bottlebrush fibers were prepared from monotelechelic dye-functionalized acrylate polymers with polymerizable norbornene end-functions (macromonomers). This strategy was used to construct nanofibers with the structure of phosphorescent organic light emitting diodes (OLEDs) on single macromolecules, such that the photophysical properties of each component of an OLED could be independently observed. Red, green, and blue (RGB) luminescent macromonomers were prepared using Cu(0)-RDRP, which were used to prepare multiblock organic nanofibers structurally analogous to nanoscale RGB pixels and multilayer white OLEDs. Changes in energy transfer efficiency and interchromophore distance were quantified using a Förster resonance energy transfer model.

Additionally, donor-acceptor dyes were prepared using a novel acceptor based on *N*-phenylbenzimidazole constrained in a coplanar fashion with a methylene tether (IMAC). Emitters were designed with a twisted conformation between donor and acceptor resulting in effective spatial separation of the highest occupied molecular orbital and lowest unoccupied molecular orbital and small singlet-triplet energy gaps to give TADF. In fluorescent IMAC derivatives, locking these chromophores into planar configurations was demonstrated to improve their cross-section for two-photon excited fluorescence and reduce the rate of photobleaching. Proof-of concept studies incorporating these dyes into water-soluble polymer dots suitable for biological imaging was also demonstrated.

Lay Summary

Organic light emitting diodes (OLEDs) are an emerging technology that have the potential to significantly reduce the energy consumption of artificial lighting. They consist of a series of stratified thin films of emissive organic semiconducting compound that are situated between two electrodes. The work described in this thesis focuses on preparing organic semiconductors with novel optical properties and morphologies. The preparation of polymer nanowires, termed 'bottlebrush' polymers, from organic semiconducting materials is described. Emphasis is placed on how the bottlebrush architecture can be used to control optical and electronic interactions in these materials, giving unique photonic properties with potential for application in electronic devices such as OLEDs and in encryption/encoding. Novel luminescent dyes were also prepared that exhibit a special type of fluorescence, termed 'thermally activated delayed fluorescence'. Due to this, these materials should find application in OLEDs with improved efficiency. Highly planarized versions of these dyes were prepared and found to have improved lifetimes when irradiated with light. Proof-of-concept studies incorporating these dyes into water-soluble nanoparticles suitable for biological imaging were also demonstrated.

Preface

In all chapters I am the principal author of the work reported in this thesis, under the supervision of Prof. Zachary M. Hudson. I performed all the experiments, interpreted the results and drafted the manuscript with additional contributions and collaborations noted below.

Excerpts of **Chapter 1** have previously been published: E. R. Sauvé, C. M. Tonge and Z. M. Hudson, Organization of Chromophores into Multiblock Bottlebrush Nanofibers Allows for Regulation of Energy Transfer Processes, *Chem. Mater.*, **2020**, *32*, 2208–2219. Writing was equally split between myself and C. M. Tonge.

Chapter 2 has previously been published: E. R. Sauvé, C. M. Tonge, N. R. Paisley, S. Cheng and Z. M. Hudson, Cu(0)-RDRP of acrylates based on p-type organic semiconductors, *Polym. Chem.*, **2018**, *9*, 1397–1403. C. M. Tonge assisted with synthesis of monomers. S. Cheng performed the synthesis of **5d**. N. R. Paisley performed the chain extension of PMA_{10k}.

Chapter 3 has previously been published: C. M. Tonge, E. R. Sauvé, S. Cheng, T. A. Howard and Z. M. Hudson, Multiblock Bottlebrush Nanofibers from Organic Electronic Materials, *J. Am. Chem. Soc.*, **2018**, *140*, 11599–11603. Experimental work and writing were shared equally between myself and C. M. Tonge with assistance from S. Cheng and T. A. Howard.

Chapter 4 has previously been published: E. R. Sauvé, C. M. Tonge and Z. M. Hudson, Aggregation-Induced Energy Transfer in Color-Tunable Multiblock Bottlebrush Nanofibers, *J. Am. Chem. Soc.*, **2019**, *141*, 16422–16431. C. M. Tonge prepared the monomer **tBuODA**.

Chapter 5 has previously been published: E. R. Sauvé, J. Paeng, S. Yamaguchi and Z. M. Hudson, Donor–Acceptor Materials Exhibiting Thermally Activated Delayed Fluorescence Using a Planarized *N*-Phenylbenzimidazole Acceptor, *J. Org. Chem.*, **2020**, *85*, 108–117. J. Paeng

assisted with the synthesis and preliminary photophysical characterization of **PTZ-IMAC**, **PXZ-IMAC**, **ACR-IMAC**, and **CZ-IMAC**, and the project was jointly supervised by S. Yamaguchi and Z. M. Hudson. B. O. Patrick performed the X-ray crystallography.

Chapter 6 has previously been published: E. R. Sauvé, C. M. Tonge and Z. M. Hudson, Deep-blue fluorophores with imidazoacridine acceptors: enhancing photostability and two-photon fluorescence using structural constraint, *J. Mater. Chem. C.*, **2021**, Advance Article, DOI: 10.1039/D0TC05241H. C. M. Tonge prepared **6.4** and performed the 2PEF and photostability measurements.

Table of Contents

List of Tables

List of Figures

List of Symbols

E	energy
$E_{1/2}^{ox}$	oxidation potential
E_g	optical energy gap
eq.	equivalents
GM	Goeppert-Mayer (10^{-50} cm^4 s photon^{-1})
k_p	propagation rate
M_n	number average molecular weight
T_g	glass transition temperature
ΔE_{ST}	singlet-triplet energy gap
ε	molar absorptivity
λ	wavelength
μ_{OFET}	charge mobility
τ	lifetime
Φ_F	fluorescence quantum yield

List of Abbreviations

2PEF	two-photon excited fluorescence
A	acceptor
A(R)GET-ATRP	activator (re)generated by electron transfer ATRP
ACR	9,9-dimethylacridan
AFM	atomic force microscopy
AIE	aggregation-induced emission
ATRP	atom transfer radical polymerization
BBCP	bottlebrush copolymer
CBB	soft colloidal building block
CIE	Commission Internationale de l'Éclairage
CT	charge transfer
CuAAC	copper-catalyzed azide-alkyne cycloaddition
CV	cyclic voltammogram
CZ	carbazole
Đ	dispersity
D	donor
DF	delayed fluorescence
DLS	dynamic light scattering
DMAc	*N*,*N*-dimethylacetamide
DMF	dimethylformamide
DMSO	dimethylsulfoxide

DP_n	degree of polymerization
DPEPO	bis[2-(diphenylphosphino)phenyl] ether oxide
DSC	differential scanning calorimetry
EBiB	ethyl α-bromoisobutyrate
EI	electron impact
EML	emissive layer
ESIPT	excited-state intramolecular proton transfer
ET	energy transfer
ETL	electron-transport layer
FRET	Förster resonance energy transfer
f_w	fraction of water
FWHM	full-width at half maxima
GPC	gel permeation chromatography
HMAT	hexamethylazatriangulene
HOMO	highest occupied molecular orbital
HOPG	highly oriented pyrolytic graphite
HRMS	high resolution mass spectrometry
HTL	hole-transport layer
IC	internal conversion
ICAR-ATRP	initiators for continuous activator regeneration ATRP
IMAC	6,6-dimethyl-6H-imidazo[4,5,1-de]acridine
IQE	internal quantum efficiency
ISC	intersystem crossing

ISET	inner sphere electron transfer
LSP	living supramolecular polymerization
LUMO	lowest unoccupied molecular orbital
MA	methyl acrylate
Me	methyl
Me_6TREN	tris[2-(dimethylamino)ethyl]amine
MMs	macromonomers
MRI	magnetic resonance imaging
MWDs	molecular weight distributions
n-type	electron-transporting
NHC	nitrogen-heterocyclic carbene
NMP	*N*-methyl-2-pyrrolidone
NMR	nuclear magnetic resonance
NTA	nanoparticle tracking analysis
OLED	organic light emitting diode
OSET	outer-sphere electron transfer
OTFT	organic thin film transistor
p-type	hole-transporting
P3AS	poly(3-alkylselenophene)
P3HT	poly(3-hexylthiophene)
PBI	*N*-phenylbenzimidazole
PDI	polydispersity
Pdots	polymer dots

PF	prompt fluorescence
PL	photoluminescence
PLA	polylactic acid
PLQY	photoluminescent quantum yield
PS	polystyrene
PSMA	poly(styrene-co-maleic anhydride)
PTZ	phenothiazine
PVK	polyvinylcarbazole
PXZ	phenoxazine
RAFT	reversible addition−fragmentation polymerization
RDRP	reversible deactivation radical polymerization
RI	refractive index
RISC	reverse intersystem crossing
ROMP	ring opening metathesis polymerization
S_1	lowest singlet
SARA-ATRP	supplemental activator and reducing agent atom transfer radical polymerization
SEC	size exclusion chromatography
SET-LRP	single electron transfer living radical polymerization
STED	stimulated emission depletion
T_1	lowest triplet
TADF	thermally activated delayed fluorescence
tBu	*tert*-butyl
TD-DFT	time-dependent density functional theory

TEMPO	2,2,6,6-tetramethylpiperidinyloxyl
TGA	thermogravimetric analysis
THF	tetrahydrofuran
TLC	thin-layer chromatography
TSCT	through space charge transfer
UV	ultraviolet
WOLED	white organic light emitting diode

Acknowledgements

First and foremost, I would like to offer my gratitude to my supervisor, Prof. Zachary Hudson for his guidance and support over the course of my PhD. I am truly grateful for all of his mentorship, encouragement, friendship and support. Always enthusiastic, Zac provided a collaborative workspace dedicated to helping me succeed. Additionally, Zac generously provided me with opportunities to conduct research abroad and present at international conferences, for which I am appreciative. I cannot stress enough how lucky I have been to complete my PhD in his group.

I would also like to thank past and present members of my research group for their support and valuable discussions throughout my PhD. In particular, I would like to thank Dr. Christopher Tonge with whom I collaborated with on numerous projects; running columns or doing base bath would have been far more boring without Kanye playing on full blast. Particular thanks also go out to Theresa Howard, Jay Paeng, Nathan Paisley, Susan Cheng, Kelly Wang, Don Mayder, Cheyenne Christopherson, Alex Polgar, Jade Poisson, Dr. Feng Shao and our honorary postdoc Dr. Corey Sanz.

I would like to thank Profs. Shigehiro Yamaguchi, Aiko Fukazawa, and Soichiro Ogi for hosting me in their laboratory at Nagoya University in Nagoya, Japan, and will always remember the hospitality and work ethic of my labmates there. In particular, I would like to thank Dr. Hiroaki Ogasawara, Dr. Masato Hirai, Mika Sakai, and Johannes Nebauer for making my time in Japan both memorable and productive.

I would like to thank the staff in the Chemistry Department for their assistance, including; the MS lab, the NMR lab, the mech shop staff, Brian Patrick and Anita Lam in the X-ray lab, Brian Ditchburn, Saied Kamal in LASIR, and chemical stores personnel especially George Kamel, Pat Olsthoorn, Alex Moya and Elan Vered for help with purchasing, shipping, and the friendly conversations.

I would like to thank my thesis readers, as well as my committee members Profs. Derek P. Gates, Jennifer A. Love and Mark Thachuk for providing me with constructive feedback over the years.

Thank you to my partner (Jennifer Yuan) for all the love and support she's given me over the years. I couldn't have done it without you. And to her family (Bo, Jing, and Harvey Yuan) for their kindness and encouragement during our time in graduate school.

I would like to especially thank my Aunt and Uncle (Deborah and Marc Sauvé) for their generosity and cheerfulness while I have been away at school. Additionally, I extend thanks to all of my friends and relatives who have supported me (as there would be far too many names to list).

Most importantly, I must thank my parents (Richard Sauvé and Tracey Masterson), my brother (Bradley Sauvé) and his partner (Glenna Martel). Their ongoing support throughout my years of education has been pivotal to my success. I am forever grateful for all they have given me.

Dedicated to My Parents, Rick and Tracey

Chapter 1: Introduction

1.1 Overview

Emerging methods for the fabrication of multifunctional nanostructures from soft matter have led to rapid innovation in nanoscience. Self-assembly techniques have been at the forefront of these efforts, giving low-entropy structures when molecular or polymeric building blocks are exposed to specific environmental conditions. This research has provided routes to polymer nanomaterials with diverse and ordered morphologies, including multicompartment platelets,[1–4] scarf-like nanoribbons,[5–7] and micelle superlattices.[8,9] The fabrication of multicompartment nanowires in particular has attracted significant attention, due to their unique applications in electronics,[10,11] data encoding,[12–14] and nanomedicine.[15–17] Most importantly, the study of these structures has uncovered entirely new phenomena, for example long-range exciton transport through self-assembled nanowires.[18] As new morphologies, properties and applications of polymer nanomaterials emerge, the need for robust methods for their fabrication will only continue to rise. Overall this thesis focuses on the incorporation of luminescent and charge-transport materials into soft-matter nanostructures, as well as development of novel organic luminescent materials.

1.2 Methods to Fabricate Soft-Matter Nanowires

Nature routinely generates complex materials with advanced functionality across a wide range of sizes with a high degree of precision.[19] Taking inspiration from this, scientists have greatly increased the diversity and structural complexity of nanomaterials which can be formed by tuning the topology of synthetic polymers. However, it remains difficult to form cylindrical nanostructures using common self-assembly protocols, despite it being entirely routine in Nature. Advanced methods such as crystallization driven self-assembly (CDSA), supramolecular

polymerization, polymerization induced self-assembly (PISA) and hierarchical solution self-assembly (HSSA) have been recently developed to prepare cylindrical nanomaterials with impressive complexity and function.

1.2.1 Crystallization Driven Self-Assembly

In 1998, Manners, Winnik and coworkers discovered amphiphilic copolymers composed of a soluble poly(dimethylsiloxane) block and a crystalline poly(ferrocenylsilane) (PFS) block could readily assemble into cylindrical nanostructures when placed in a selective solvent for the former.[20] In the years since, their group and others have found that crystallization of the core PFS block drives the self-assembly to form low-curvature structures such as cylinders and platelets. Additionally, it was found that the exposed ends of the cylindrical micelle remained active toward addition of free block copolymer chains. Using a seeded growth approach, analogous to living polymerization, micelles with exact length and very low dispersity could be obtained (Figure 1.1).[21] This process, termed "living" CDSA, has been extended to other semicrystalline polymer systems, including poly(L-lactide),[22] poly(ε-caprolactone),[23] and polyethylene.[24,25] Further, CDSA has been extended to semicrystalline π-conjugated materials such as poly(3-hexylthiophene),[26] oligo(p-phenylenevinylene),[27] and polyselenophene[28] with potential applications in organic electronics.

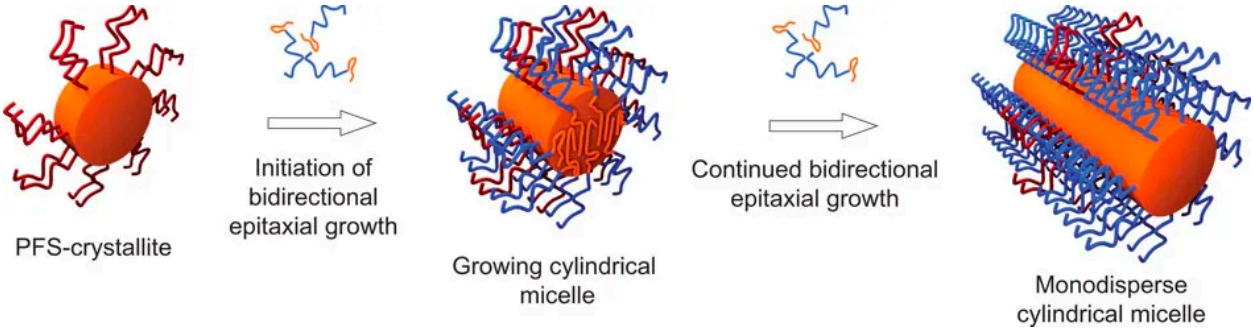

Figure 1.1. Schematic for bi-directional seeded growth of amphiphilic PFS-containing copolymers to form monodisperse cylindrical micelles. The polymers used in the study are shown in orange (PFS), red (poly(dimethylsiloxane)) and blue (polyisoprene). Reproduced from reference 21 with permission from Springer Nature © 2010.

Polymer-based nanowires prepared using CDSA are promising for use in organic electronics due to their anisotropic charge-transport properties. For example, Manners and coworkers prepared electroactive fibre-like micelles made of a crystalline regioregular poly(3-hexylthiophene) core and a solubilizing, amorphous regiosymmetric poly(3-hexylthiophene) or polystyrene corona.[29] They demonstrated that the individual fibres exhibit appreciable conductivity by using tunnelling atomic force microscopy. Further, by incorporating the fibres as the active layer in field-effect transistors they found charge carrier mobilities to be dependent on both the degree of polymerization of the core-forming block and the fibre length. Friend, Manners and coworkers also developed organic semiconducting nanofibers made of a crystalline poly(di-n-hexylfluorene) core with a central polyethylene glycol corona and terminal polythiophene coronas.[18] The well-ordered, crystalline nanofiber core allowed for exciton transfer from the core to the terminal polythiophene coronas to occur over a far greater length (>200 nm) than is typical for organic semiconductors.

1.2.2 Living Supramolecular Polymerization

Supramolecular polymerization has also been used to generate conductive nanofibers via well-controlled noncovalent interactions, giving fibers up to several hundred nanometers in length.[30,31] Living supramolecular polymerization (LSP) effectively works in the same manner as CDSA whereby a seed nucleus is added to a solution of kinetically trapped monomer units yielding narrowly disperse fibres of controllable length.[32] First developed for porphyrin-bisamides by Takeuchi and coworkers, the LSP protocol has been extended to a large range of other metasatable supramolecular assemblies. For example, Würthner and coworkers utilized LSP of a perylene bisimide dye to afford fluorescent nanowires[33] and Takeuchi and coworkers were able to regulate the LSP of an amide-functionalized azobenzene using light.[34]

Drawing analogy between supramolecular polymerization and covalent polymerization, researchers identified making well-defined supramolecular copolymers as an intriguing challenge.[35,36] Supramolecular block copolymers of Cu and Zn porphyrins has been reported, giving a B-A-B triblock-type structure.[37] Meijer, Palmans and coworkers reported the noncovalent synthesis of triarylamine triamide-based supramolecular copolymers which possess fluorescence and are potentially semiconductive.[38] In addition, the Würthner group expanded their work on LSP of perylene bisimide dyes. They found that perylene bisimides, functionalized in the bay position with Cl, OMe or SMe, could be copolymerized to form A-B-A and B-A-B supramolecular block copolymer patterns (Figure 1.2).[39] It should be noted however that in all copolymer examples the monomer structures have to be very similar, severely limiting the scope of materials that may be made.

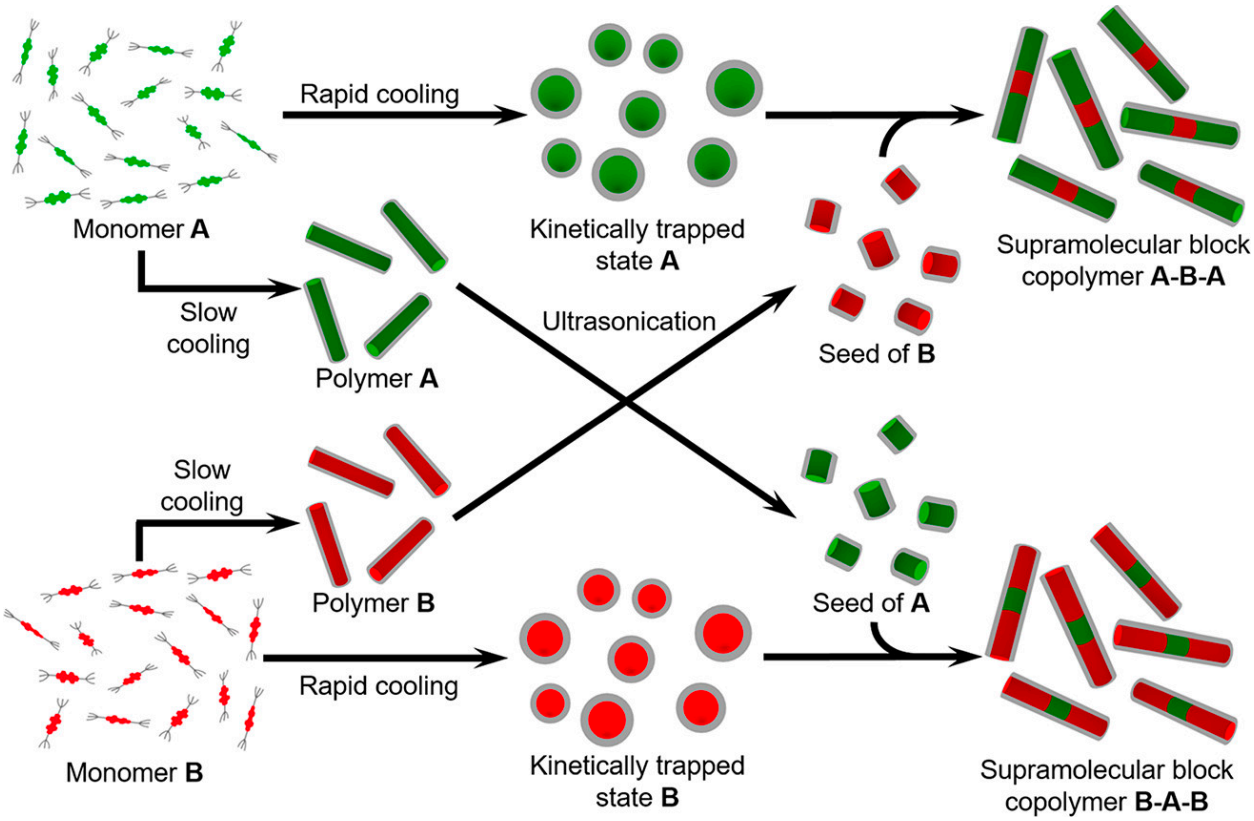

Figure 1.2. Schematic illustration of the two-component seeded living polymerization to obtain supramolecular triblock copolymers with A-B-A or B-A-B pattern under kinetic control. Reproduced from reference 39 with permission from the American Chemical Society © 2019.

1.2.3 Hierarchical Solution and Polymerization Induced Self-Assembly

Complex wormlike materials have also been prepared via hierarchical solution self-assembly (HSSA) and polymerization induced self-assembly (PISA), by restricting the conformational space of multiblock copolymers with differing solubilities.[8,40,41] Recently, Müller and co-workers established methodology wherein multicompartment micelles are used as soft colloidal building blocks (CBBs), which can be assembled to higher levels of hierarchy (Figure 1.3). In this way, they were able to access well-ordered, compartmentalized materials on the micron scale. To accomplish this, they guided the self-assembly of ABC triblock terpolymers in selective solvents

to form mono- and divalent CBBs. If kept separate, the CBBs underwent self-assembly into spherical or linear superstructures, while when two or more CBBs differing in size were combined, they underwent co-assembly into mixed superstructures.

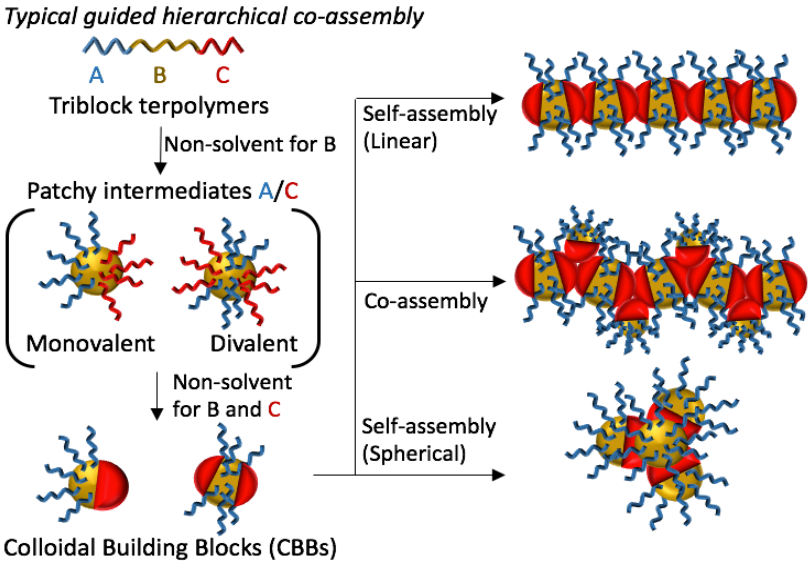

Figure 1.3. Dispersion of ABC triblock terpolymers in a non-solvent for B yields B-core particles with A/C corona patches.[8] During transfer into a non-solvent for A and B, these develop into monovalent and divalent units with sticky A patches (CBBs). The CBBs were further assembled into linear, spherical and mixed superstructures.

Polymerization-induced self-assembly represents an attractive alternative self-assembly method as it can be performed at high concentration (10-50% w/w) in one-pot.[42,43] Leveraging *in situ* self-assembly of amphiphilic block copolymers, the majority of reports on PISA involve either reversible deactivation radical polymerization (RDRP) or ring opening metathesis polymerization (ROMP) techniques.[44–47] PISA worms have found use as light-responsive drug delivery vehicles[48,49] and as ice-crystallization inhibitors for cryopreservation.[50] Similar to HSSA, the morphology obtained in PISA is primarily controlled by the relative volume fractions of the soluble corona and insoluble core-forming blocks.[51] Thus, while it is possible to obtain cylindrical

architectures, doing so often requires the laborious process of constructing complete morphology diagrams.

1.3 Bottlebrush Copolymers

As discussed previously, approaches to nanomaterials based on self-assembly often face several limitations. Most notably, reliance on noncovalent interactions between building blocks means that specific solvents, temperatures, or concentrations are required if the desired local energy minimum conformation is to be maintained. As a result, while self-assembled nanomaterials may be highly stable under specific conditions, changes in the environment can cause the structure to fragment, change shape, or redissolve. Since self-assembly generally relies on intermolecular interactions (typically <25 kJ/mol) they are much more sensitive to changes in environmental conditions[52–54] compared to covalently bound species (typical energy >150 kJ/mol). This metastability both limits the range of applications that a material can access and complicates the measurement of emergent properties they may exhibit. Motivated by these challenges, we sought to develop methods for the fabrication of multifunctional polymer nanofibers using covalent chemistry, giving robust structures while maintaining a high degree of control over the material's components and their arrangement along the nanofiber.

1.3.1 Strategies to Prepare Bottlebrush Copolymers

Bottlebrush copolymers (BBCPs) provide one such route to nanofibers without relying on noncovalent self-assembly. Formed from polymeric side chains attached to a linear backbone, BBCPs adopt extended conformations due to steric interactions between the densely packed side chains (Figure 1.4).[55–57] Several strategies exist for the preparation of BBCPs, commonly referred

to as “grafting-to”, “grafting-from”, and “grafting-through” methods (Figure 1.5).[58–62] Grafting-to synthesis involves the preparation of a polymer backbone with multiple reactive sites, to which polymer side chains are directly coupled. Grafting-from synthesis involves first preparing a “polyinitiator” backbone, then conducting a second, orthogonal polymerization to grow the side chains off this backbone at each initiator site. Finally, grafting-through methods involve the synthesis of linear side chains, or “macromonomers,” functionalized with a reactive handle amenable to a second, orthogonal polymerization. This second polymerization generates the bottlebrush backbone, maximizing grafting density and increasing the rigidity of the BBCP. These bottom-up, covalent approaches provide routes to nanofibers with complex function that can be isolated without compromising the structural order in the material.

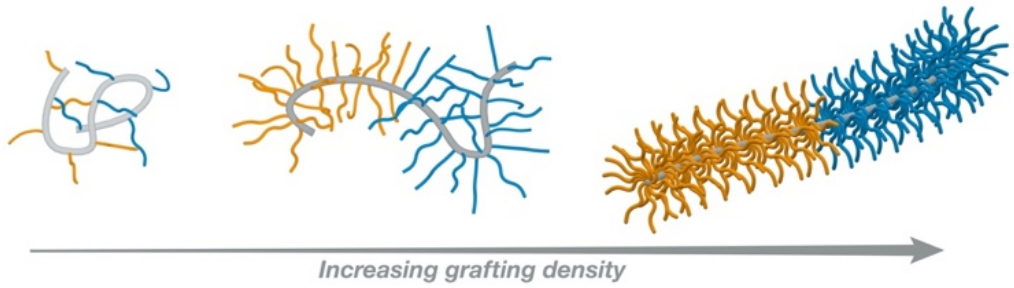

Figure 1.4. The conformation and physical properties of bottlebrush polymers are controlled by the steric repulsion of the densely grafted side chains.

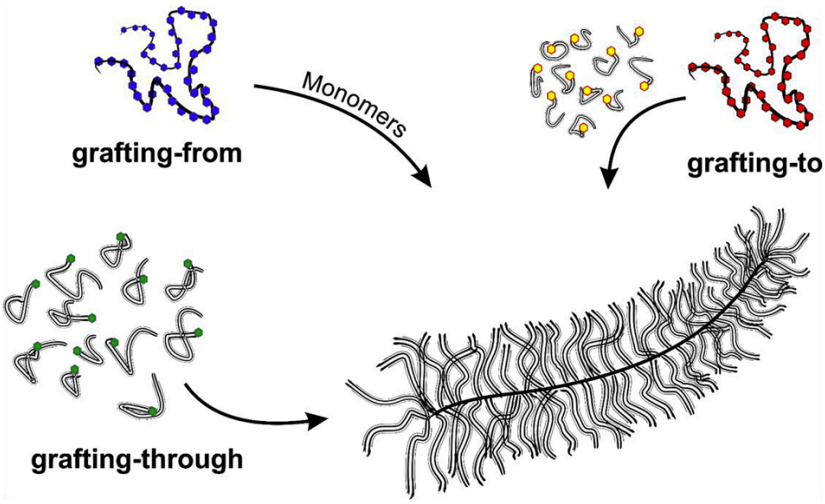

Figure 1.5. Schematic of the three grafting strategies most commonly used to prepare BBCPs. Reproduced from reference 62 with permission from Elsevier © 2016.

1.3.2 Applications of Bottlebrush Copolymers

Due to their unique morphology and limited chain entanglement, bottlebrush polymers have now been explored for a wide variety of applications.[63–66] Their large sizes and low-entropy conformations allow BBCPs to rapidly self-assemble into photonic crystals, with tunable domain sizes capable of selective reflection throughout the visible spectrum.[67–69] Grubbs and others have recently found that blending BBCPs with linear polymers,[70] brush polymers,[71] or nanoparticles[72] represents a facile methodology to rapidly tune the photonic band gap (Figure 1.6).

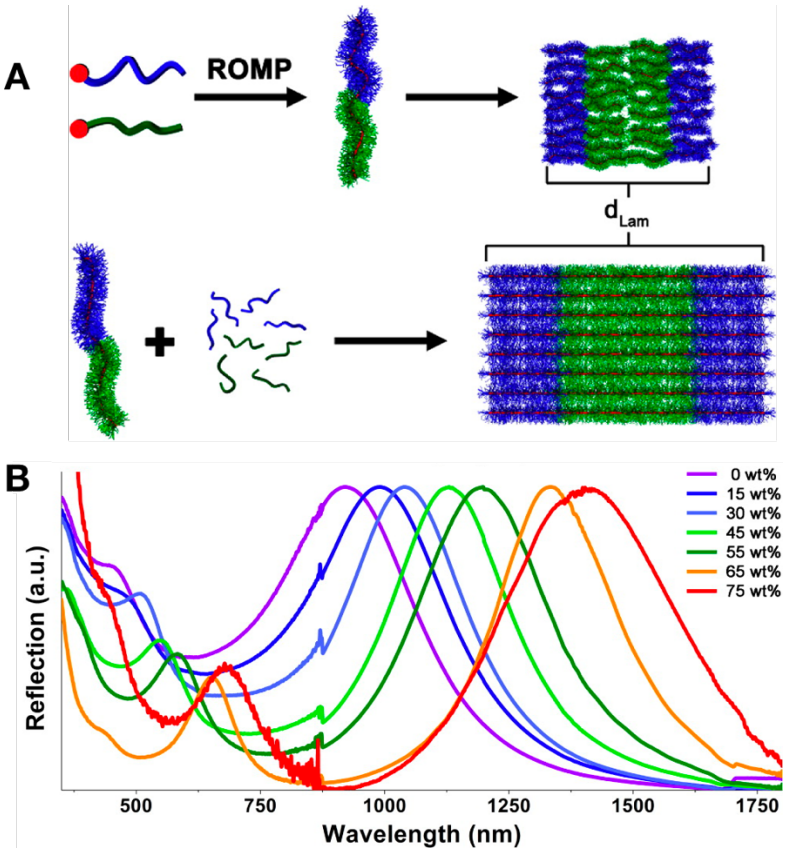

Figure 1.6. (A) BBCPs consisting of polystyrene (PS) and polylactic acid (PLA) blocks self-assemble into lamellar arrays with large periodicities. Adding small PS and PLA homopolymers swells these arrays, increasing their domain spacing. (B) UV-vis spectra of a BBCP with increasing homopolymer wt%. Reproduced from reference 70 with permission from the American Chemical Society © 2014.

BBCPs have also attracted interest for biological applications, as cylindrical nanostructures have been shown to exhibit longer residence times in the body than spheres of equivalent molecular weight.[73] Specifically, they have recently been developed as dual-responsive materials for Magnetic resonance imaging (MRI) and fluorescence imaging[74] as well as polymer carriers for drug delivery.[75,76] Grubbs and coworkers have also explored BBCPs as materials for polymer electrolyte membranes, using the bottlebrush morphology to separate conductive polymer domains from those required for mechanical support.[77] Finally, BBCPs are unique building blocks for

solution self-assembly in their own right, behaving as 'giant polymeric surfactants' to give micelles in selective solvents.[78–81]

1.3.3 Bottlebrush Polymers from Organic Electronic Materials

With well-known applications in organic solar cells and thin film transistors, polythiophenes are perhaps the most widely studied class of organic semiconducting polymer. Several groups have described the incorporation of polythiophenes into BBCPs in the past five years, using a combination of grafting-to and grafting-through strategies. For example, Brochon and Hadziioannou used both grafting-through and grafting-to methods to synthesize BBCPs with polyisoprene, poly(vinyl alcohol), or poly(butyl acrylate) backbones grafted with poly(3-hexylthiophene) (P3HT) side chains.[82] Shortly after, Thelakkat used nitroxide-mediated polymerization to synthesize an azide-functionalized polystyrene (PS) backbone, which was then functionalized to give PS-*g*-P3HT using a copper-catalyzed azide-alkyne cycloaddition (CuAAC).[83] These authors found a strong correlation between the charge carrier mobility of PS-*g*-P3HT bottlebrushes and their side-chain lengths, with mobility increasing by five orders of magnitude as M_n for the P3HT side chains increased from 1.4 to 15.9 kDa (Figure 1.7A). Tang[84] and Kilbey[85] have also studied polythiophene-based bottlebrushes formed from the ring-opening metathesis polymerization of norbornenes, utilizing these materials in dielectrics and self-assembled micelles, respectively. These works exemplify nonconjugated graft copolymers – bottlebrush polymers in which the backbone itself is not conjugated.

By contrast, BBCPs in which the backbones and side chains are both formed from conjugated polymers remain rare. In 2013, Higashihara and coworkers reported all-conjugated graft copolymers composed of P3HT side chains connected to either p-type or n-type conjugated

backbones (Figure 1.7B). These were achieved in a two-step method combining Stille coupling and Kumada catalyst-transfer polycondensation, and subsequently employed as the active layer in organic thin film transistors.[86] The following year, Luscombe and coworkers reported a graft-through synthesis for all-conjugated graft copolymers, using a Suzuki coupling polymerization to construct carbazole-diketopyrrolopyrrole backbones with appended P3HT side chains.[87] More recently, Seferos and coworkers reported the grafting of poly(3-alkylselenophene) (P3AS) side-chains to poly(3-alkylthiophene) (P3AT) backbones to give all-conjugated P3AS-*g*-P3AT polymers using CuAAC (Figure 1.7C).[88] This architecture was a particularly attractive target, as Seferos has previously shown that block copolymers of P3HT and P3AS can be used advantageously in organic solar cells.[89,90] This strategy was found to be most effective at low to moderate grafting densities, while high grafting densities proved a challenge even when short side chains were used. An additional important finding of this study was that the use of the organic-soluble catalyst $[Cu(CH_3CN)_4]PF_6^-$/tris-(benzyltriazolylmethyl)amine for the CuAAC reaction was successful in suppressing unwanted Glaser coupling of the alkyne side chains, greatly improving the efficiency of the grafting reaction.

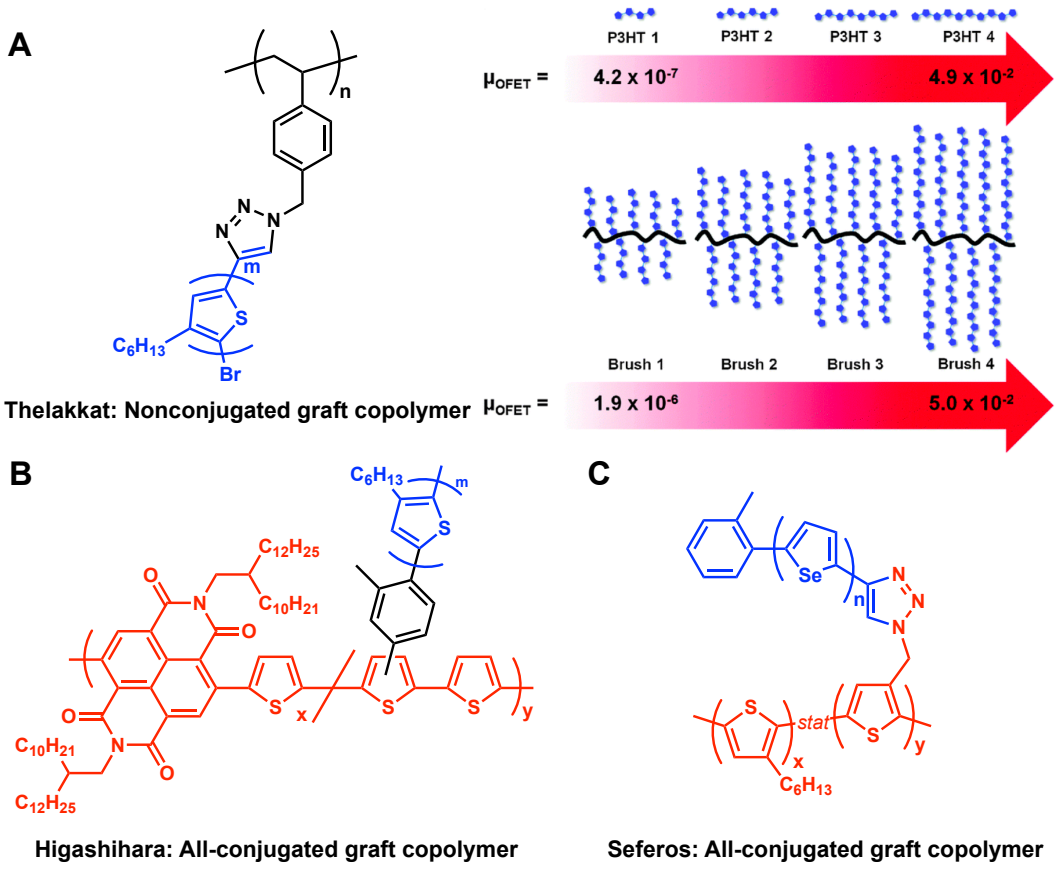

Figure 1.7. (A) Chemical structure of PS-*g*-P3HT (left) and a diagram highlighting the dependency of μ_{OFET} on the P3HT chain length (right). (B) Chemical structure of an all-conjugated graft copolymer composed of P3HT side chains connected to an n-type conjugated backbone. (C) Chemical structure of all-conjugated P3AS-*g*-P3AT polymers.

1.4 Polymerization Methods

Reversible deactivation radical polymerization (RDRP) techniques such as nitroxide-mediated polymerization,[91] atom transfer radical polymerization (ATRP),[92,93] and reversible addition−fragmentation polymerization (RAFT),[94] offer significant advantages in terms of architectural control when compared to conventional radical polymerization. As such, RDRP has been widely employed for the synthesis of structurally diverse families of polymers and various advanced materials.[95,96] While each of the three major RDRP techniques has certain advantages

and limitations, they all rely on the concept of dynamic equilibrium to furnish polymers with precise molecular weights, narrow molecular weight distributions (MWDs), and high end-group fidelity.[97] A major distinction between the three techniques is the mechanism by which they attain their dynamic equilibrium. All three mechanisms fundamentally rely upon a mediating species to balance the equilibrium between propagating macroradicals and dormant species, allowing monomer units to be added to the propagating chain incrementally. Nitroxide-mediated polymerization employs stable radical species as its mediator, while ATRP is usually mediated catalytically by transition metal complexes. In contrast, RAFT employs the use of a chain transfer agent which facilitates degenerate transfer between propagating radicals and a dormant species.

Copper-catalyzed ATRP is one of the most popular RDRP techniques researchers commonly employ.[98] Mechanistically, dormant species in the form of initiating alkyl halides/macromolecular species (P_n–X) react periodically with low oxidation state Cu(I) complexes (rate constant = k_{act}) forming the corresponding propagating radicals (P_n•) and higher oxidation state Cu(II) halide complexes (Scheme 1.1). In this way, the Cu(I) species acts as an activator of the polymer chain and the Cu(II) acts as a deactivator. In the analogous reverse reaction, the deactivator can react with the propagating radical to reform the dormant species and the activator (rate constant = k_{deact}). It should be noted that ATRP is considered to proceed through an energetically favored inner sphere electron transfer (ISET) mechanism, where the radical and the deactivating species are formed through the concerted homolytic atom transfer of the halogen radical from the dormant species to the activating species.

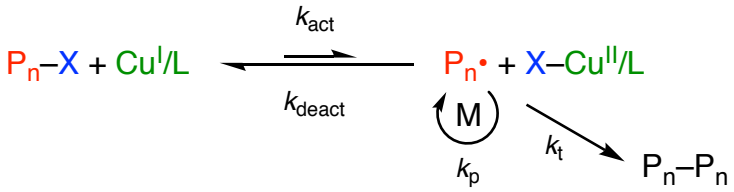

Scheme 1.1. Copper-catalyzed ATRP mechanism.

1.4.1 Cu(0)-mediated Reversible Deactivation Radical Polymerization

Traditional ATRP obeys the persistent radical effect:[99] propagating radicals that are irreversibly terminated through reaction with species other than the $Cu^{II}X/L$ (eg. disproportionation) result in a slight excess of deactivating species. In turn, PRE shifts the equilibrium toward the dormant species. The importance of this effect is that traditional ATRP has required relatively high catalyst concentrations (>1000 ppm) to preserve a high polymerization rate. Efforts to reduce catalyst loading below this limit has led to the development of more advanced ATRP techniques,[98] which use different methods to regenerate the Cu(I) complex. These include activator (re)generated by electron transfer ATRP (A(R)GET-ATRP),[100,101] initiators for continuous activator regeneration ATRP (ICAR-ATRP),[100] electrochemically mediated ATRP,[102] and photochemically mediated ATRP.[103,104] In addition to these methods, zerovalent metals have also been used, with the most common being Cu(0).

The mechanism of RDRP in the presence of Cu(0) is significantly complicated by the introduction of a third possible oxidation state for the Cu species. This has resulted in a passionate debate in literature between two proposed models (Scheme 1.2);[105–109] single electron transfer living radical polymerization (SET-LRP) and supplemental activator and reducing agent atom transfer radical polymerization (SARA-ATRP). The SET-LRP mechanism suggests that Cu(0) or "nascent" Cu(0) particles act as the major activator of alkyl halides and no major activation occurs

by Cu(I) complexes due to their rapid and instantaneous disproportionation. Meanwhile, the SARA-ATRP mechanism names Cu(I) species as the major activator, with Cu(0) acting as a supplemental activator and reducing agent of alkyl halides. Another key difference in their mechanisms is that the activation step in SET-LRP is suggested to occur *via* an outer-sphere electron transfer (OSET) mechanism through a radical anion intermediate, while in SARA-ATRP activation occurs through an ISET, in concordance with traditional ATRP.

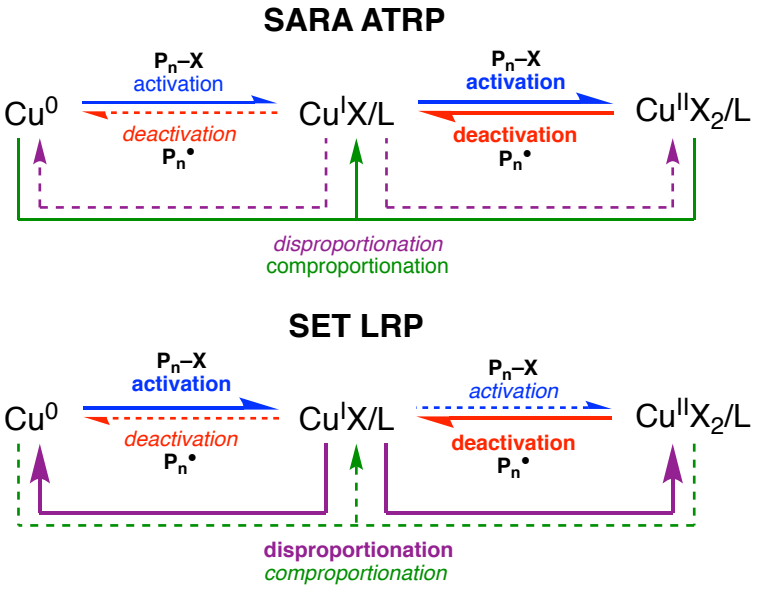

Scheme 1.2. SARA ATRP and SET-LRP mechanisms. Bold, filled, and dashed lines represent major, minor, and negligible contributors to the mechanism, respectively. Reproduced from reference 105 with permission from the Royal Society of Chemistry © 2014**.**

Regardless of the Cu(0)-RDRP mechanism, techniques using Cu(0) have now been widely explored for the polymerization of acrylates, methacrylates, styrenes, acrylamides and others.[108–115] This method offers a facile route to materials with low polydispersity and high end-group fidelity, typically retaining first-order polymerization kinetics at high monomer conversion. Furthermore, the technique is particularly advantageous in situations where a simple set-up is

required, harsh reaction conditions must be avoided, or high conversions are necessary. Cu(0)-RDRP thus presents an attractive tool for the polymerization of high-value monomers which are either costly to prepare or difficult to remove from the polymer product following the reaction.

1.4.2 Ring-opening Metathesis Polymerization

Ring-opening metathesis polymerization (ROMP) is a type of olefin metathesis chain-growth polymerization.[116] The main driving force of ROMP is the release of ring strain in cyclic olefins such as norbornenes. The ROMP method is a living polymerization in which the chain ends remain active to further polymerization once all the available monomer is consumed, providing a convenient route to block copolymers if a second monomer is added. Mechanistically ROMP involves three key steps: initiation, propagation, and termination (Figure 1.8). Initiation begins with coordination of a cyclic olefin to a metal alkylidene, followed by a [2+2] cycloaddition to produce a metallacyclobutane intermediate which then undergoes cycloreversion. During propagation the same analogous steps are repeated until either the monomer is completely consumed or the reaction is terminated. Termination is typically achieved by the addition of an alkene such as ethyl vinyl ether which removes the metal from the polymer chain end.

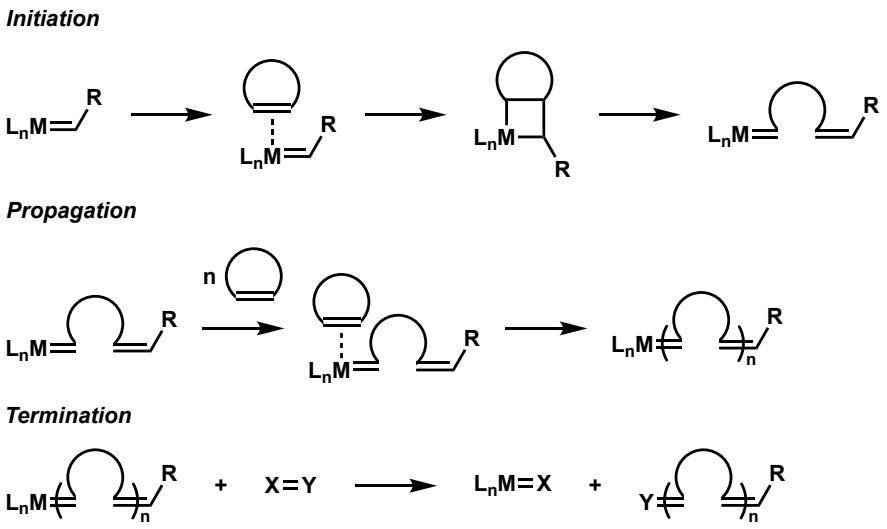

Figure 1.8. Mechanism of ROMP.

Catalyst **1.1**, known as Grubbs first-generation catalyst, is capable of catalyzing a wide scope of monomers and substrates for metathesis chemistry (Figure 1.9).[117,118] Improving on their design, Grubbs and coworkers introduced nitrogen-heterocyclic carbene (NHC) ligands in place of the weaker sigma-donating and more labile phosphines to give catalyst **1.2**.[119] This second-generation catalyst was far more stable and possessed higher activity in ROMP because the NHC ligand increased dissociation of the trans-phosphine ligand from the Ru to give the metathesis-active species. However, the slow initiation by **1.2** yields poor control over molecular weight and polydispersity (PDI) in resultant polymers. By incorporating the strongly ligating NHC and weakly coordinating brominated pyridines the Grubbs third-generation ruthenium catalyst (**1.3**) offers many advantages.[120–122] The fast initiation and high reactivity of this catalyst make it ideal for the polymerization of macromonomers, which are typically difficult to polymerize due to the demanding steric hindrance of side chains. Furthermore, the catalyst has shown great functional group tolerance, allowing for the polymerization of a wide range of monomers.

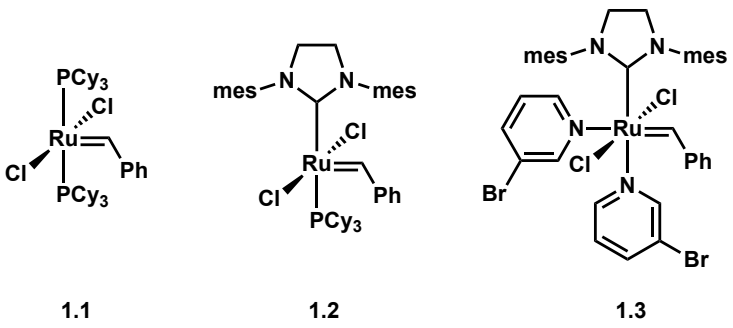

1.1 1.2 1.3

Figure 1.9. Chemical structures of Grubbs first, second and third-generation Ru metathesis catalysts.

1.5 Principles of Luminescence

A type of cold-body radiation, luminescence is the emission of light not resulting from heating. The principle driving force of this process is the release of energy in the form of an emitted photon. To understand luminescent processes further the different possible electronic states must be considered. Depending on the nature of the electronic excited state luminescence is divided into two categories – fluorescence and phosphorescence. In fluorescence the excited state is a singlet (denoted 'S'), meaning the excited electron and ground state electron maintain their antiparallel spins. As a result, relaxation to the ground state (S_0) is spin allowed and occurs rapidly (~10^8 s^{-1}). In the rare case of doublet emission ($D_1 \rightarrow D_0$) from an excited state radical species, this process would also be spin-allowed and thus termed fluorescence. In contrast, phosphorescence is the emission of a photon from a triplet excited state (denoted 'T'), meaning the excited electron and ground state electron have unpaired parallel spins. Relaxation in this case would violate the Pauli exclusion principle, requiring a spin-forbidden $T_1 \rightarrow S_0$ transition. Spin-forbidden transition can still occur in quantum mechanics, however they are kinetically unfavored with much slower emission rates (10^3 to 10^0 s^{-1} or less).

Jablonski diagrams are typically used to discuss the processes occurring from absorption and emission of light and a typical diagram is provided in Figure 1.10. The singlet ground, first, and second electronic states are depicted by S_0, S_1, and S_2, respectively. Absorption of light by a material is represented by the transition $S_0 \rightarrow S_1$ or from S_0 to a higher-energy excited state (S_2, S_3, etc.). At each electronic energy level, the molecule can exist in a number of vibrational energy levels, depicted by 0, 1, 2, etc. Non-radiative relaxation from $S_2 \rightarrow S_1$ or from a higher vibrational energy level to a lower vibrational energy level is known as internal conversion (IC) and normally occurs within 10^{-12} s or less. Intersystem crossing (ISC) is the process by which a molecule in the S_1 state is converted to the first triplet state T_1. As the $S_1 \rightarrow T_1$ transition is spin-forbidden the rate of ISC in purely organic molecules is generally low. Molecules containing heavy atoms such as bromine, iodine or transition metals benefit from spin-orbit coupling which enhances the rate of ISC.

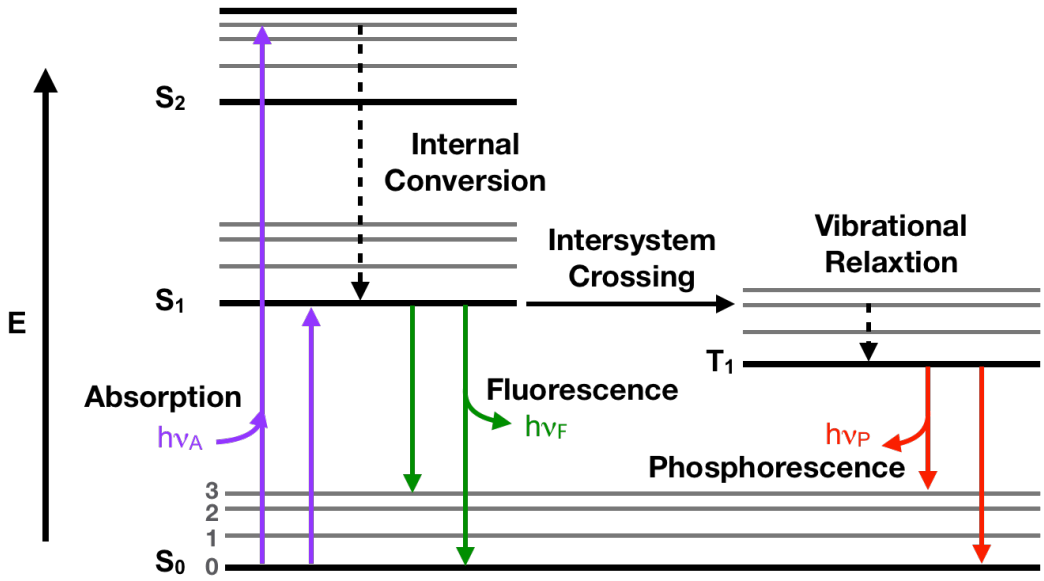

Figure 1.10. Jablonski diagram illustrating the typical processes involved in luminescence.

Many emissive molecules contain both an electron-donating and an electron-accepting group which allows formation of an internal charge transfer (CT) state. In such molecules, following excitation there is an increase in charge separation and significant redistribution of electron density. Emission from a CT transition is typically broad and featureless compared to $\pi \rightarrow \pi^*$ or $n \rightarrow \pi^*$ transitions. Additionally, the large transition dipole moment of CT transitions makes this class of emission highly sensitive to the polarity of the environment. Polar media effectively stabilize the excited CT state, lowering it in energy and reducing the S_0-S_1 gap. The result is a further broadened and red-shifted emission spectrum.

1.6 Thermally Activated Delayed Fluorescence

1.6.1 Organic Light Emitting Diodes

Organic light emitting diodes (OLEDs) are an emerging technology that have the potential to significantly reduce the energy consumption of artificial lighting.[1] They consist of a series of stratified thin films of emissive organic compounds that are situated between two electrodes. Their light weight, durability and excellent efficiencies compared to traditional fluorescent light sources make them excellent candidates for use in solid-state lighting applications. However, there are several weaknesses such as high power consumptions and short lifetimes of current OLED devices that have significantly hindered their broad implementation. One of the key parameters affecting an OLED's power consumption is described by its internal quantum efficiency (IQE) – defined as the ratio of photons generated to the number of electrons injected.

Luminescence in OLED devices originates from the recombination of electrically generated electron-hole pairs, called excitons, in the emissive layer. Since electrons and holes are produced with uncorrelated spins, singlet and triplet excitons are formed with 25% and 75%

probabilities, respectively. First-generation OLEDs utilized fluorescent emitters which resulted in a maximum IQE of about 25%.[123–125] To overcome this challenge second-generation OLEDs leveraged phosphorescent heavy metal complexes (typically Ir and Pt) to achieve IQEs of near 100%.[126]

More recently the implementation of thermally activated delayed fluorescence (TADF) has revolutionized organic light-emitting diode (OLED) technology, enabling the fabrication of OLEDs with 100% internal quantum efficiencies using purely organic emitters.[127–131] Capable of converting triplet excitons to singlets through reverse intersystem crossing (RISC), TADF compounds have attracted significant recent attention as robust, efficient and scalable emissive materials.[132–136] To achieve efficient RISC, TADF materials are typically designed to minimize the energy difference between the lowest triplet (T_1) and lowest singlet (S_1) excited states, termed ΔE_{ST}.

1.6.2 Principle of Thermally Activated Delayed Fluorescence

Prior to its application in OLED technology TADF was known as E-type delayed fluorescence, named for the molecule eosin. In E-type delayed fluorescence triplet excitons can be converted to singlet excitons via RISC, which is activated by thermal energy (Figure 1.11). TADF materials typically show two-component emission lifetimes as a result of the ISC/RISC process. The first component is generally very fast (comparable to fluorescence), originating from prompt emission from the singlet excited state. The second component arises from the ISC/RISC process and results in an extended lifetime (usually on the order of microseconds).

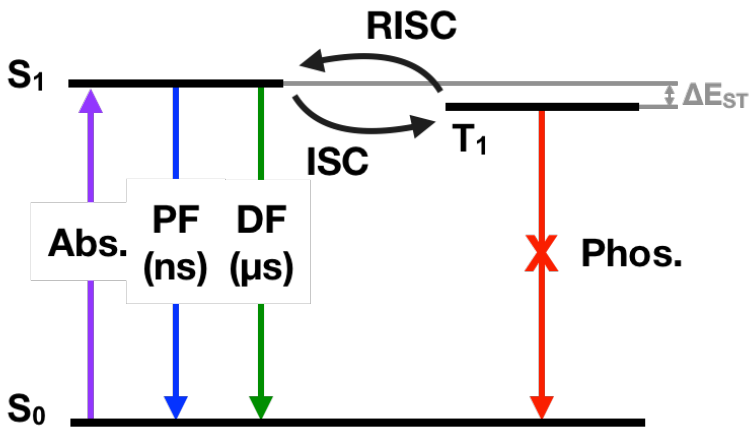

Figure 1.11. Jablonski diagram illustrating key processes involved in TADF, where PF is prompt fluorescence and DF is delayed fluorescence.

1.6.3 Design Strategy for Thermally Activated Delayed Fluorescence Materials

While T_1 states are substantially lower in energy than their S_1 counterparts in the vast majority of molecules, a small ΔE_{ST} can be achieved by minimizing the Pauli repulsion (or exchange energy) between ground and excited state electrons. In practical terms, this is commonly achieved by designing materials with minimal overlap between their HOMO and LUMO, such that the electrons of the frontier orbitals will occupy different regions of space when the material is excited. This is often obtained by the coupling of donor and acceptor units in a twisted conformation,[137,138] sometimes using steric bulk to ensure that the π systems of the donor and acceptor remain orthogonal, as exemplified by **4CzIPN** (Figure 1.12).[127] This type of conformation also results in emitters with large transition dipoles and significant charge-transfer character, including broad emission bands and large Stokes shifts.

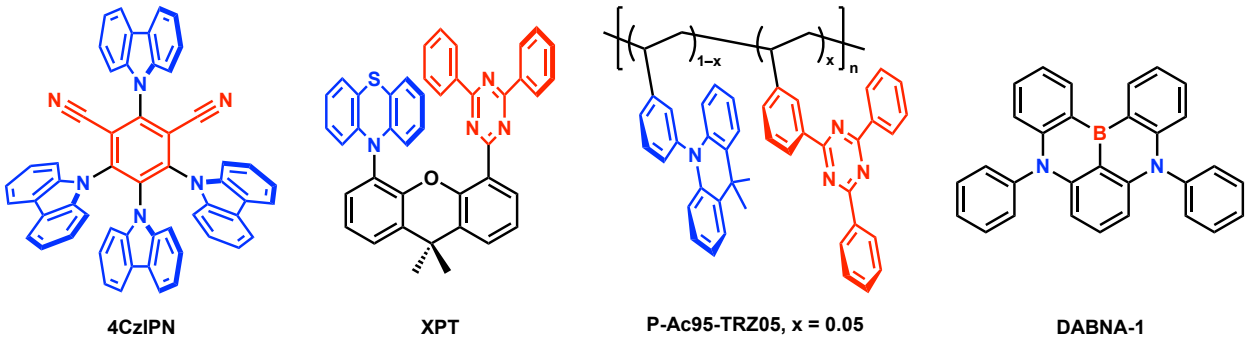

Figure 1.12. Select examples of molecules that exhibit TADF. Donor and acceptor moieties are coloured blue and red, respectively.

An alternative approach is a through-space interaction wherein the donor (D) and acceptor (A) are physically separated but are spatially close together. This design separates the HOMO and LUMO sufficiently to achieve small ΔE_{ST} with the advantage of higher radiative decay rates. Swager, Baldo and coworkers have utilized triptycene and xanthene as scaffolds to hold donor and acceptor fragments in close proximity, achieving high efficiency through space charge transfer (TSCT) TADF emitters such as **XPT** (Figure 1.12).[139,140] Lu and coworkers placed carbazole on the *ortho* position of a triarylborane achieving TADF in a similar fashion.[141] Blue TADF polymers with non-conjugated polyethylene backbones, as in **P-Ac95-TRZ05**, have also been recently reported by Wang and coworkers.[142,143]

Multiple resonance effects have recently been proposed as a way to promote efficient TADF with very narrow emission spectra and small Stokes shifts. Hatakeyama and coworkers leveraged the organoboron compound **DABNA-1**, possessing two nitrogen atoms, in a rigid polycyclic aromatic framework and related compounds to produce ultrapure blue TADF emitters in this fashion (Figure 1.12).[130,144,145] Following their discovery, theoretical and computational efforts were made to examine the origin for the reduced ΔE_{ST} in such molecules.[146] Zysman-

Colman and others have since doped other polyaromatic hydrocarbons such as heptacene with B and N to yield new multiresonant TADF compounds with exciting luminescent properties.[147]

1.7 Thesis Scope

The work described herein focuses on preparing organic semiconductors with novel optoelectronic properties and morphologies. Emphasis is placed on how the bottlebrush architecture can be used to control optoelectronic interactions in these materials, giving unique photonic properties. The work described will also address interesting problems of closely related fields, including the efficient synthesis of planar TADF materials and stable organic fluorophores.

Chapter 2 describes a series of acrylic monomers synthesized based on p-type organic semiconductor motifs found commonly in organic electronic devices. These monomers were polymerized by Cu(0)-RDRP, the kinetics of which are described in detail. The title polymers were obtained in high yield with low polydispersities and display first-order polymerization kinetics up to high (>90%) monomer conversion. The optical, electrochemical and thermal properties for each of these p-type materials are also described.

Chapter 3 describes methods for the preparation of fiber-like nanomaterials that mimic the multilayer structure of organic electronic devices on individual polymer chains. By combining Cu(0)-RDRP and ROMP, narrowly dispersed multiblock bottlebrush fibers were prepared from materials commonly used as the hole transport, electron transport, and host materials in organic electronics. This strategy was used to construct nanofibers with the structure of phosphorescent OLEDs on single macromolecules, such that the photophysical properties of each component of an OLED can be independently observed.

Chapter 4 expands on the work in chapter 3, describing the synthesis of a series of bottlebrush copolymers from red, green, and blue luminescent macromonomers, which were then used to prepare multiblock organic nanofibers structurally analogous to nanoscale RGB pixels. Changes in energy transfer efficiency and interchromophore distance were quantified using a Förster resonance energy transfer (FRET) model. Preliminary demonstration of these materials as polarity-sensitive inks for encryption and encoding were also demonstrated using a red/blue fluorescence switch upon exposure to solvent. Finally, the potential complexity of optoelectronic materials accessible with these methods was demonstrated by combining these building blocks with charge-transporting materials to give organic nanofibers with ordered structures mimicking that of multilayer white OLEDs.

Chapter 5 describes the design of an *N*-phenylbenzimidazole constrained in a coplanar fashion with a methylene tether (IMAC) that was used to prepare a series of emitters exhibiting thermally activated delayed fluorescence (TADF). The twisted conformation between donor and acceptor in these molecules resulted in effective spatial separation of the HOMO and LUMO and small singlet−triplet energy gaps. Crystallographic properties, electronic structures, thermal stabilities, photophysical properties, and energy levels were studied systematically.

Chapter 6 describes the synthesis of three donor-acceptor dyes based on benzimidazole acceptors and triphenylamine donors. These materials have deep blue emission, International Commission on Illumination (CIE) (x, y) < (0.17, 0.09), quantum yields above 95 % and narrow emission spectra. We demonstrate that restriction of rotational freedom in these compounds, particularly in the triarylamine donor, reduces the rate of photobleaching by up to a factor of 4. Locking these chromophores into planar configurations also improves their cross-section for two-

photon excited fluorescence. Proof-of concept studies incorporating these dyes into water-soluble polymer dots suitable for bio-imaging was also demonstrated.

Chapter 2: Cu(0)-RDRP of acrylates based on p-type organic semiconductors

2.1 Introduction

Reversible deactivation radical polymerization (RDRP) techniques using Cu(0) have opened new avenues for the synthesis of structurally diverse families of polymers.[108–115] Now widely explored for the polymerization of acrylates, methacrylates, styrenes, acrylamides and others, the technique offers a facile route to materials with low polydispersity and high end-group fidelity, typically retaining first-order polymerization kinetics at high monomer conversion. Alternatively referred to as SET-LRP or SARA-ATRP,[105–107] the technique is particularly advantageous in situations where a simple set-up is required, harsh reaction conditions must be avoided, or high conversions are necessary. Cu(0)-RDRP thus presents an attractive tool for the polymerization of high-value monomers which are either costly to prepare or difficult to remove from the polymer product following the reaction.

As such, this technique is very well-suited to the polymerization of many of the classes of π-conjugated organic semiconductors now widely used in plastic electronics. While organic semiconductors often require extensive conjugation through the polymer backbone, useful electronic properties can also be achieved with π-conjugated pendant side chains connected to a styrenic or (meth)acrylic all-carbon main chain.[148–151] Polymers bearing electron-rich triarylamine side chains, for example, have found widespread use as *p*-type materials in organic electronics, including organic light-emitting diodes (OLEDs),[150,152–155] solar cells,[156–160] and organic thin-film transistors.[161] These materials offer flexible, lightweight alternatives to inorganic semiconductors which can be easily processed over large areas at low cost. Previous work exploring the RDRP of triarylamines has examined their polymerization by free-radical polymerization, reversible addition/fragmentation chain transfer polymerization (RAFT),[162–166] traditional atom-transfer

radical polymerization (ATRP),[150,151] and light-mediated ATRP.[167] Due to the low cost, scalability, and reduced monomer waste offered by Cu(0)-RDRP, this technique is advantageous for the polymerization of such materials. Investigations to date on the Cu(0)-RDRP of optoelectronic materials has been limited, though a recent report by Gohy and coworkers demonstrated the utility of the technique in the synthesis of electroactive polymers based on 2,2,6,6-tetramethylpiperidinyloxyl (TEMPO) radicals.[168]

Here we describe optimized conditions for the Cu(0)-RDRP of a series of four new *p*-type organic semiconductor monomers, giving polymers with low polydispersity in high yield (Scheme 2.1). These polymerizations are simple to carry out and can be conducted at room temperature. Furthermore, the reactions display linear first-order kinetics up to high monomer conversion (≥93% in all cases), and can be run to near-complete conversion without significant broadening of the PDI. In this way, Cu(0)-RDRP is shown to be an effective method for the controlled polymerization of high-value semiconductor monomers requiring multiple steps to prepare, minimizing unused monomer waste from the reaction. In addition to kinetic data for each of these polymerizations, the optical, electrochemical, and thermal properties of this series of *p*-type polymeric materials are also discussed.

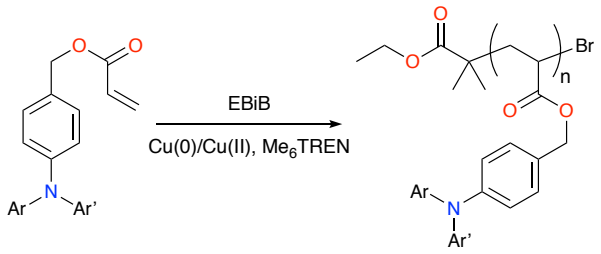

Scheme 2.1. General scheme for Cu(0)-mediated RDRP of *p*-type organic acrylates.

2.2 Monomer Synthesis

Four p-type monomers were synthesized based on triarylamine motifs used frequently as p-type semiconductors in organic electronic devices (Scheme 2.2). Triarylamine-based materials such as **2.5a-c** are the most common class of materials used in the hole-transporting layer of OLEDs[169,170] and perovskite solar cells,[160] and have also been used as the donor material in organic photovoltaic devices and organic thin film transistors (OTFTs).[161] Carbazoles such as **2.5d** are commonly used as both hole-transport and host materials in OLEDs,[170,171] and **2.5d** is also a structural homologue of polyvinylcarbazole (PVK), a material used in photocopiers as a photoconductive material.

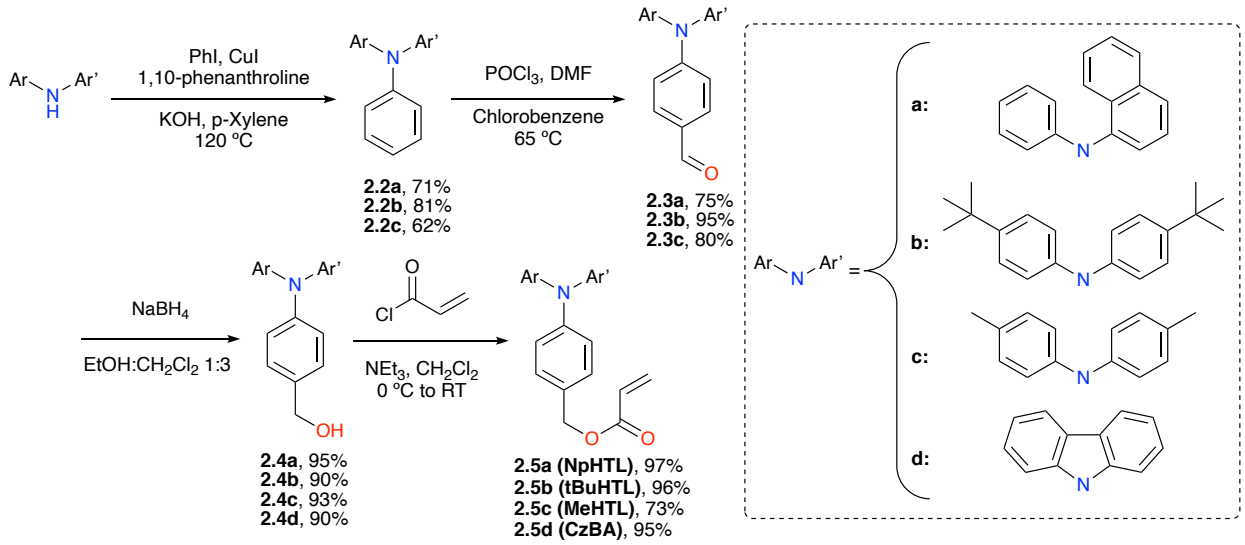

Scheme 2.2. Synthesis of acrylate monomers prepared based on commercial p-type organic semiconductors.

Compounds **2.5a-c** may be conveniently synthesized by *N*-arylation of commercially available diarylamines, using copper-catalyzed Goldberg reactions to give triarylamines **2.2a-c**. Subsequent Vilsmeier-Haack formylation using $POCl_3$ and dimethylformamide (DMF) selectively furnishes the monoformylated products **2.3a-c** in all cases, while 4-(9*H*-carbazol-9-yl)benzaldehyde **2.3d** was prepared by a previously reported nucleophilic aromatic substitution

protocol.[172,173] Reduction with $NaBH_4$ and reaction with acryloyl chloride gives monomers **2.5a-d** in reasonable overall yields, with syntheses that were readily scaled to yield >50 g of each product in our laboratory.

It is noteworthy that the *p*-alkyl substituents in **2.5b** and **2.5c** markedly improve the stability of these monomers relative to **2.5a**, which must be purified on silica quickly to avoid decomposition over time. In contrast, monomers **2.5b-d** are more robust and thus easier to purify; in addition, **5d** can be recrystallized readily from CH_2Cl_2/hexanes. To simplify naming in future chapters compounds **2.5a-d** have also been assigned names based on their structure and/or function in an OLED (Scheme 2.2).

2.3 Polymer Synthesis

Selecting an appropriate solvent for the Cu(0)-RDRP of **2.5a-d** proved challenging, as these highly hydrophobic monomers exhibited limited solubility in the highly polar solvents typically used to promote the disproportionation of Cu(I) to Cu(0) and Cu(II) in this reaction, such as DMF, dimethylsulfoxide (DMSO), or isopropanol. We determined that *N*-methyl-2-pyrrolidone (NMP) provided an adequate balance of solubility while still supporting catalyst activity[174–176] and proved to be an effective solvent for the polymerization of all four arylamine monomers.

To avoid the introduction of oxygen impurities, these reactions were carried out in a nitrogen-atmosphere glovebox and sampled throughout the reaction. Polymerizations were conducted with 0.5 cm of 18 gauge Cu(0) wire per 10 μmol of ethyl α-bromoisobutyrate (EBiB), pre-treated with HCl for 15 minutes to remove surface impurities, then washed with water and acetone, and dried *in vacuo*. Using [EBiB]/[$CuBr_2$]/[Me_6TREN] in 1:0.065:0.068 molar ratios, the

amount of monomer was chosen to give polymers with molecular weights of 10 kDa at full conversion (Table 2.1). These reactions gave polymers with narrow PDIs ranging from 1.12-1.28.

Table 2.1. Synthesis of donor-type polymers by Cu(0)-RDRP.

Entry[a]	k_p (10^{-5} s^{-1})	t (h)	$M_{n,\,SEC}$[b]	$M_{n,\,NMR}$[c]	$M_{n,\,theory}$	Đ	Conv. (%)[c]
2.5a$_{10k}$	1.14	70	10800	10100	9900	1.23	99
2.5b$_{10k}$	3.78	26	9500	9000	9400	1.13	94
2.5c$_{10k}$	8.56	26	9400	8600	9000	1.28	90
2.5d$_{10k}$	6.93	26	9800	10900	9700	1.12	97

[a]Reaction conditions: Monomer/EBiB/$CuBr_2$/Me_6TREN = M/1/0.065/0.068; NMP = 1.15 mL; 18 gauge Cu(0) wire = 1.15 cm (**2.5a**: M = 26, **2.5b**: M = 23, **2.5c**: M = 28, **2.5d**: M = 30). [b] Determined by gel permeation chromatography (GPC) in tetrahydrofuran (THF). [c] Determined by ^{1}H NMR in $CDCl_3$.

Upon completion of the polymerizations of **2.5a-d**, reactions were removed from the glovebox and quenched by the addition of water, then isolated by centrifugation. Further purification by preparatory size exclusion chromatography to remove residual monomer gave polymers **2.5a-d$_{10k}$**, which were then characterized by nuclear magnetic resonance (NMR), UV-visible and fluorescence spectroscopy, cyclic voltammetry, differential scanning calorimetry (DSC) and thermogravimetric analysis (TGA). These polymers can also be conveniently purified by reprecipitation in methanol (**2.5a-2.5c**) or hexanes (**2.5d**).

2.4 Photophysical and Electrochemical Properties

Polymers **2.5a-d$_{10k}$** all show strong absorption in the UV region, with absorption maxima ranging from 293 nm (**2.5d$_{10k}$**) to 303 nm (**2.5c$_{10k}$**). **2.5a$_{10k}$** and **2.5d$_{10k}$** are highly fluorescent, with quantum yields of 0.29 and 0.20 and emission in the blue (λ_{max} = 431 nm) and ultraviolet (λ_{max} =

347 nm) regions of the spectrum, respectively (Figure 2.1). Interestingly, **2.5b$_{10k}$** and **2.5c$_{10k}$** show highly red-shifted emission spectra, with maxima at 543 and 548 nm, respectively. Coupled with their exceedingly low quantum yields (Table 2.2), this behavior indicates the formation of excimers along the polymer backbone in CH_2Cl_2. Consistent with this hypothesis, structured emission bands at 345 and 367 nm can be seen in the emission spectra of **2.5b$_{10k}$** and **2.5c$_{10k}$**, more closely resembling the emission spectrum of **2.5d$_{10k}$** which shows no excimer behavior. **2.5a$_{10k}$**, possessing the lower-bandgap naphthyl substituent, behaves as a conventional blue emitter with π-π* character.

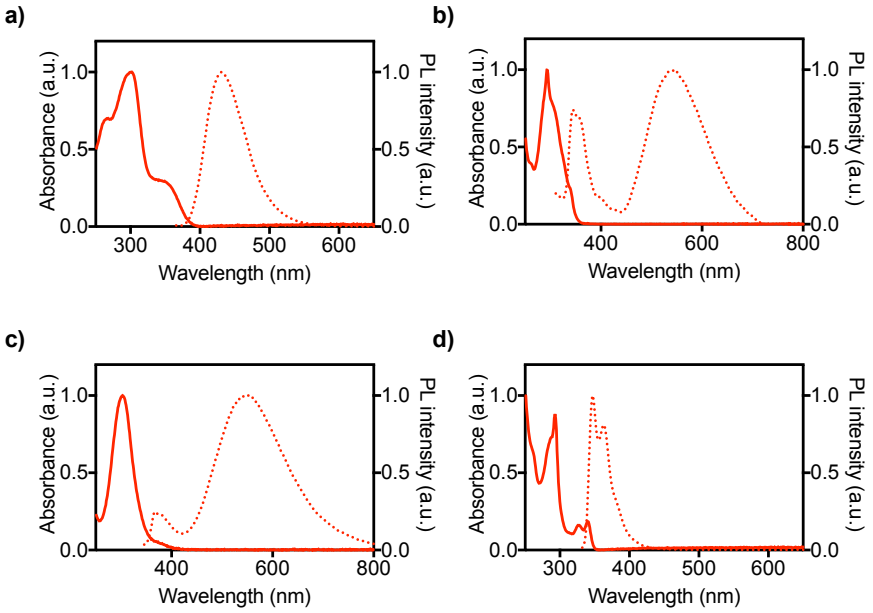

Figure 2.1. Normalized absorbance (solid) and photoluminescence (PL, dashed) spectra of polymers **2.5a$_{10k}$** (a), **2.5b$_{10k}$** (b), **2.5c$_{10k}$** (c), **2.5d$_{10k}$** (d).

Table 2.2. Photophysical properties of semiconducting monomers and their corresponding polymers.

Entry	$\lambda_{max,\ abs}$	$\lambda_{max,\ em}$	Φ_F	ε (10^4 M^{-1} cm^{-1})
2.5a	301	432	0.31	2.2
2.5b	304	528	0.09	2.8
2.5c	303	367	<0.01	3.1
2.5d	293	347	0.25	2.5
2.5a$_{10k}$	302	431	0.29	79
2.5b$_{10k}$	294	543	0.02	39
2.5c$_{10k}$	303	548	<0.01	53
2.5d$_{10k}$	293	347	0.20	39

In a promising sign for optoelectronic applications of these materials, all four polymers underwent highly reversible one-electron oxidation by cyclic voltammetry in CH_2Cl_2, using tetrabutylammonium hexafluorophosphate as electrolyte (Table 2.3). The most electron-rich of these materials, **2.5a$_{10k}$** underwent oxidation at 0.41V relative to $FeCp_2^{0/+}$, while **2.5d$_{10k}$** showed two reversible oxidation waves in the electrochemical window of CH_2Cl_2.

These trends in electrochemical behavior were further confirmed by density functional theory on individual monomers of **2.5a-d**, substituting the vinyl group found in these acrylates with a *sec*-butyl substituent to simulate the saturated carbon-carbon backbone in **2.5a-d$_{10k}$**. Calculations at the B3LYP/6-31+g(d) level of theory showed significant electron density on the nitrogen atom in the HOMO in all cases, with the lowest energy transitions in all materials showing π-π*character in the absence of excimer formation.

Table 2.3. Simulated and experimental electronic properties of polymers **2.5a-d$_{10k}$**.

Entry	$E_{1/2}^{ox}$[a]	HOMO (eV)		LUMO (eV)	
		Calc.	Exp.[b]	Calc.	Exp.[c]
2.5a$_{10k}$	0.412	–5.41	–5.21	–1.57	–1.10
2.5b$_{10k}$	0.419	–5.21	–5.21	–0.86	–0.99
2.5c$_{10k}$	0.417	–5.21	–5.22	–0.89	–1.13
2.5d$_{10k}$	0.535	–5.66	–5.34	–1.09	–1.11

[a] In CH_2Cl_2 relative to $FeCp^{0/+}$. [b] Calculated from $E_{1/2}^{ox}$ relative to the $FeCp^{0/+}$ HOMO level (4.80 eV). [c] Calculated from the HOMO level and the optical energy gap, E_g. E_g was determined from the low-energy UV-vis absorption band edge.

2.5 Thermal Properties

Finally, the thermal properties of **2.5a-d$_{10k}$** were evaluated by thermogravimetric analysis (TGA) and differential scanning calorimetry (DSC, Figure 2.2) to assess the stability of these materials for practical use in optoelectronics. Polymer **2.5a$_{10k}$** proved to be the least thermally stable by TGA, reaching a temperature of 200 °C, where relatively slow degradation occurred in two steps. The first step (200 − 490 °C) involved a mass loss of 34%, the second (490 − 800 °C) 35% to give an overall char yield of 31%. DSC studies of polymer **2.5a$_{10k}$** revealed a T_g of 109 °C. The most thermally stable polymer, **2.5b$_{10k}$**, was stable up to a temperature of 287 °C, where rapid degradation occurred in one step involving a mass loss of 92% to give a char yield of 8%. DSC studies on this polymer gave a T_g of 109 °C. TGA revealed that polymer **2.5c$_{10k}$** was thermally stable up to a temperature of 259 °C, where rapid degradation occurred in two steps. The first step (260 − 360 °C) involved a mass loss of 19%, the second (360 − 800 °C) 68% to give an overall char yield of 13%. DSC studies of polymer **2.5c$_{10k}$** revealed a T_g of 71 °C. TGA revealed that polymer **2.5d$_{10k}$** was thermally stable up to a temperature of 256 °C, where rapid degradation

occurred in two steps. The first step (255 − 500 °C) involved a mass loss of 35%, the second (500 − 800 °C) 25% to give an overall char yield of 40%. DSC studies of polymer **2.5d$_{10k}$** revealed a T_g of 76 °C.

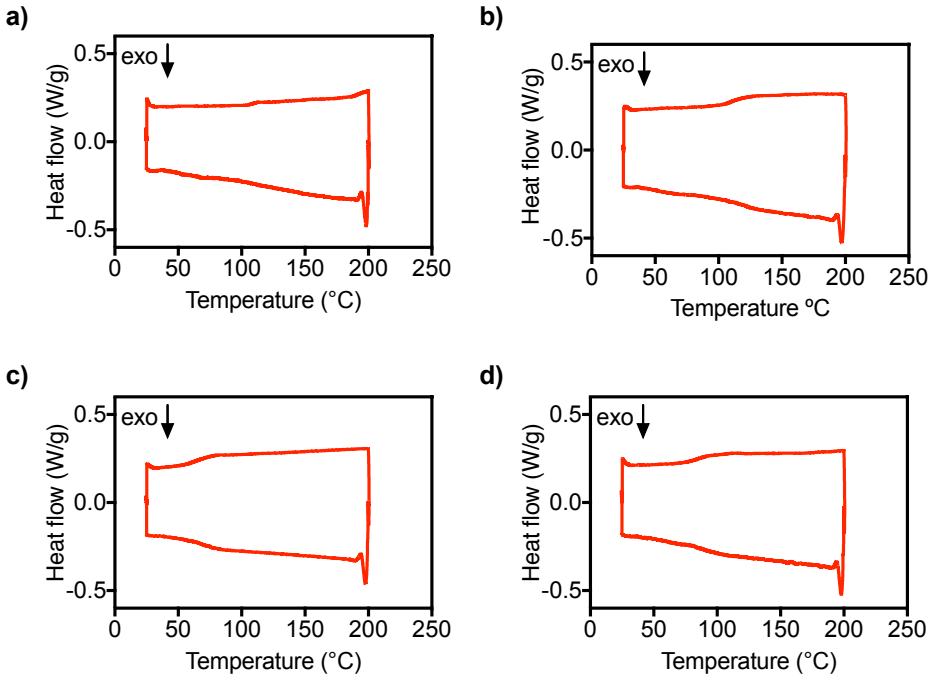

Figure 2.2. DSC traces of polymers **2.5a$_{10k}$**, **2.5b$_{10k}$**, **2.5c$_{10k}$**, **2.5d$_{10k}$**, run at a rate of 10 °C min^{-1} under a 50 mL min^{-1} flow of nitrogen. Three consecutive heating and cooling cycles were performed, the second (d) or third (a, b, c) is shown

2.6 Synthesis of High Molecular Weight Polymers

In NMP, all monomers show linear first-order behaviour up to ~85% conversion (Figure 2.3), with propagation rates k_p between 1.14 x 10^{-6} and 8.56 x 10^{-5} s^{-1}. Above this limit, linear behaviour in the semilogarithmic plots of ln([M$_0$]/[M]) are no longer observed, indicating that the concentration of the active species is not constant towards the end of the reaction (Figure 2.3). Similar behaviour has been observed previously for the Cu(0)-RDRP of methyl acrylate in MeCN using

Me_6TREN,[177,178] where it was noted that similar constraints on chain-end livingness were present above ~65% conversion. Interestingly, an induction period was reproducibly observed in the kinetic plot for the polymerization of monomer **2.5a** in NMP. This was not seen for control polymerizations performed simultaneously on **2.5b-c** using the same batch of copper wire, and as such we rule out the presence of a copper oxide layer in this reaction as the likely cause of this phenomenon. As the presence of trace impurities which can act as polymerization inhibitors are known to induce such induction periods by Cu(0)-RDRP,[179,180] combined with the observation that **2.5a** shows only modest stability we speculate that trace impurities from monomer decomposition are the cause, even when **2.5a** is purified on silica immediately prior to use. These issues are effectively alleviated by substitution of these electron-rich triarylamines with alkyl groups at the nucleophilic *para*-position in **2.5b** and **2.5c**. Monomer **2.5d**, in contrast, has a HOMO energy 300 mV lower in energy than **2.5a**, which may explain its added stability in the absence of alkylation.

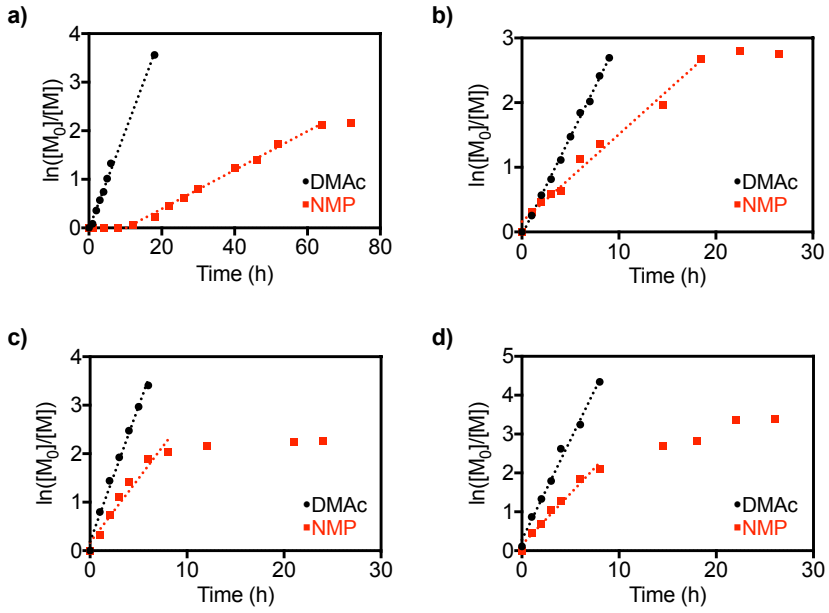

Figure 2.3. Kinetic study comparison of the synthesis by Cu(0)-RDRP of **2.5a**$_{10k}$ (a), **2.5b**$_{10k}$ (b), **2.5c**$_{10k}$ (c), **2.5d**$_{10k}$ (d) in NMP and DMAc: ln([M_0]/[M]) vs. time plot. At high conversion in NMP, the rate becomes non-linear with respect to [M].

When conducted in *N*,*N* dimethylacetamide (DMAc), however, the polymerizations of **2.5a-5d** were found to remain living throughout the polymerization, displaying linear first-order kinetics until maximum conversion (93-97%) was reached. This was accompanied by an increase in rate constant k_p for all materials (Figure 2.3, Table 2.4). Most importantly, the improved livingness of these four polymerizations in DMAc facilitated the preparation of higher molecular weight materials, which could be obtained only as ill-defined polymers with broad PDI in NMP (Figure 2.4).

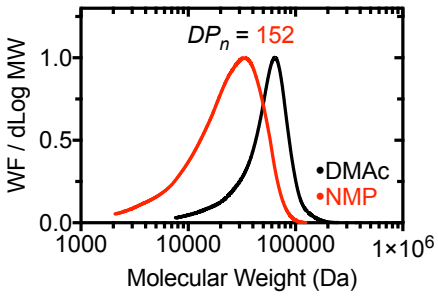

Figure 2.4. Example polymerizations of (**2.5d**) in NMP (red) and DMAc (black) with a target M_n of 50,000 Da at 52 h. Reaction conditions: **2.5d**/EBiB/$CuBr_2$/Me_6TREN = 152/1/0.065/0.068, DMAc or NMP = 1.15 mL; 18 gauge Cu(0) wire = 0.23 cm. Target degree of polymerization (DP_n) is indicated above the trace, while GPC data indicates an M_n of 15,700 and a PDI of 1.77.

Table 2.4 Synthesis of high molecular weight donor-type polymers by Cu(0)-RDRP

Entry	k_p (10^{-5} s^{-1})	t (h)	$M_{n,\,SEC}$[d]	$M_{n,\,theory}$	$Đ$	Conv. (%)[e]
2.5a$_{10k}$[a]	5.6	18	10100	9700	1.43	97
2.5b$_{10k}$[a]	8.42	9	10900	9300	1.14	93
2.5c$_{10k}$[a]	15.5	6	9900	9700	1.15	97
2.5d$_{10k}$[a]	14.7	8	10100	9600	1.11	96
2.5a$_{50k}$[b]	0.53	96	43200	42200	1.87	84
2.5b$_{50k}$[c]	1.14	24	29800	31400	1.44	63
2.5c$_{50k}$[b]	1.99	30	43300	43800	1.34	88
2.5d$_{50k}$[b]	1.22	48	43000	44400	1.34	89

Reaction conditions: Monomer/EBiB/$CuBr_2$/Me_6TREN = M/1/0.065/0.068. [a] DMAc = 1.15 mL; 18 gauge Cu(0) wire = 1.15 cm (**2.5a**: M = 26, **2.5b**: M = 23, **2.5c**: M = 28, **2.5d**: M = 30). [b] DMAc = 1.15 mL; 18 gauge Cu(0) wire = 0.23 cm (**2.5a**: M = 132, **2.5c**: M = 140, **2.5d**: M = 152). [c] DMAc = 4.6 mL; 18 gauge Cu(0) wire = 4.6 cm **2.5b**: M = 113. [d] Determined by GPC in THF. [c] Determined by ^{1}H NMR in $CDCl_3$.

Polymers with M_n = 50,000 were then targeted, with degrees of polymerization ranging from 113 to 152 (Figure 2.5). These polymers reached high conversion in case of **2.5a**, **2.5c** and

2.5d (84-89%), with some broadening in polydispersity from 1.11-1.43 in the case of the M_n = 10,000 polymers to 1.34-1.87 in their larger analogues. In the case of **2.5b**, however, the solubility of the polymer worsened as the molecular weight increased, consistent with the highly hydrophobic structure of this monomer. Nonetheless, conversion of 63% for a final molecular weight of 29,800 could be achieved if the amount of solvent and Cu(0) wire was increased (Table 2.4). These results indicate that the use of DMAc is preferable in the polymerization of these materials, resulting in faster polymerization rates, improved chain-end livingness, and permitting the synthesis of high molecular weight materials. Importantly, we note that the living polymerizations facilitated by DMAc can also be used in the preparation of block copolymers. Polymerization of methyl acrylate (MA) in DMAc for 8 h under identical conditions (MA/EBiB/$CuBr_2$/Me_6TREN = 100/1/0.065/0.068) gave a well-defined polymer with PDI = 1.03, which was then chain-extended upon addition of **2.5d** in DMAc with additional $CuBr_2$/Me_6TREN catalyst and Cu(0) wire (Figure 2.6). The resulting PMA_{10k}-*b*-**2.5d$_{10k}$** block copolymer showed a monomodal distribution and PDI = 1.11, indicating minimal termination before the addition of the functional block. This result indicates that Cu(0)-RDRP should facilitate the facile preparation of multiblock copolymers based on functional organic semiconductors, which could lead to materials with applications as redox-active gels, luminescent polymer dots (Pdots),[181] or lithographic resists.

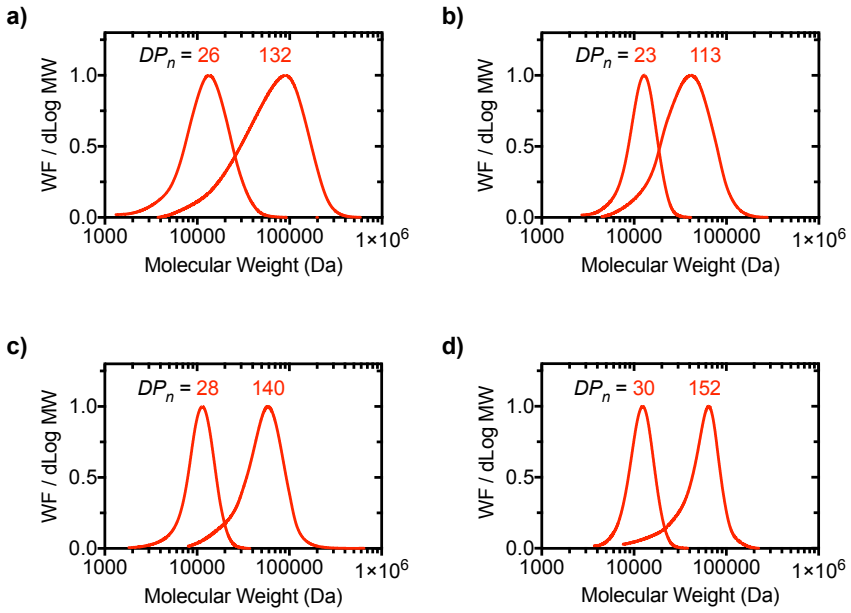

Figure 2.5. Molecular weight distribution plots of **2.5a**$_{10k\text{-}50k}$ (a), **2.5b**$_{10k\text{-}50k}$ (b), **2.5c**$_{10k\text{-}50k}$ (c), **2.5d**$_{10k\text{-}50k}$ (d). Target DP_n is indicated above each trace.

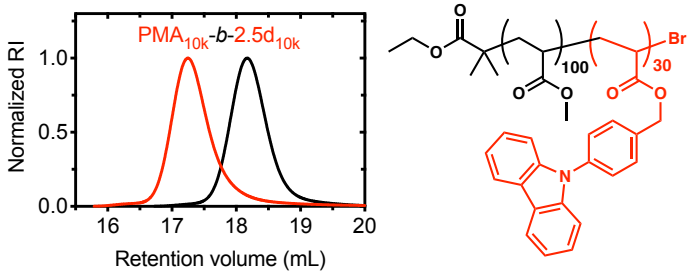

Figure 2.6. GPC chromatogram of *in situ* block copolymer **PMA**$_{10k}$**–2.5d**$_{10k}$ (red) and **PMA**$_{10k}$ homopolymer (black).

2.7 Application to n-type Semiconducting Monomers and Iridium Phosphors

Concurrently, our group sought to develop analogous protocols for the polymerization of electron-transporting (n-type) acrylic monomers and phosphorescent transition-metal complexes.

We disclosed our findings in a pair of separate publications,[182,183] and I describe the key results briefly below.

Electron-transporting materials, frequently containing electron-deficient heterocycles such as pyridines, triazines, oxadiazoles or benzimidazoles, are a critical component of many organic devices, such as organic light-emitting diodes (OLEDs),[184,185] organic thin-film transistors (OTFTs)[186] and organic photovoltaics (OPVs).[187] These represent challenging targets for Cu(0)-RDRP, as in these cases the monomers often possess σ-donating nitrogen atoms, giving polymers capable of acting as polyvalent ligands for the copper species present in the reaction.[188]

We demonstrated the use of Cu(0)-RDRP in the synthesis of polymeric materials based on a series of challenging substrates containing n-type semiconductor moieties (Figure 2.7). Polymerizations gave materials with narrow PDIs ranging from 1.14–1.39 at conversions ≥92%. The polymerization kinetics of these substrates was shown to be complex, which we attributed to the presence of *N*-donor atoms on all of the substrates studied which may interfere with the RDRP equilibria involving Cu(0), Cu(I) and Cu(II) in the reaction. Furthermore, the thermal, optical and electronic properties of the resultant polymers were studied in detail.

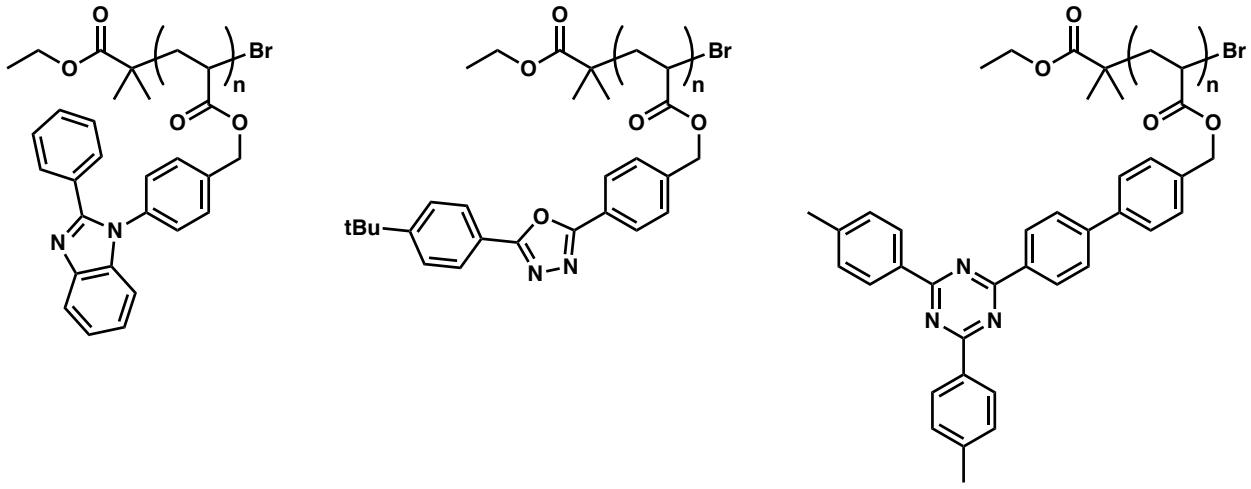

Figure 2.7. Chemical structures of n-type organic acrylate polymers produced by Cu(0) RDRP.

We also reasoned that Cu(0)-RDRP would be ideal for the polymerization of acrylic monomers based on phosphorescent transition-metal complexes. Such complexes, particularly those based on Os, Ir, or Pt, have found widespread use as emitters for OLED displays,[155,189–192] light-emitting electrochemical cells,[193,194] and chemosensors,[195–198] with quantum yields often approaching 100%. Due to the high cost of these materials, a polymerization method that minimizes waste, maximizes yield, and simplifies purification is highly desirable. Thus, we copolymerized red, green, and sky-blue iridium complexes with a carbazole-based host to produce polymers that showed good color purity in the solid state (Figure 2.8). Resulting polymers showed dispersities as low as 1.08 with conversions reaching 93%, providing a low-cost route to phosphorescent metallopolymers with minimal waste. High-molecular-weight polymers with M_n approaching 40 kDa were also successfully prepared, as well as block copolymers by chain extension of methyl acrylate (MA) in one pot.

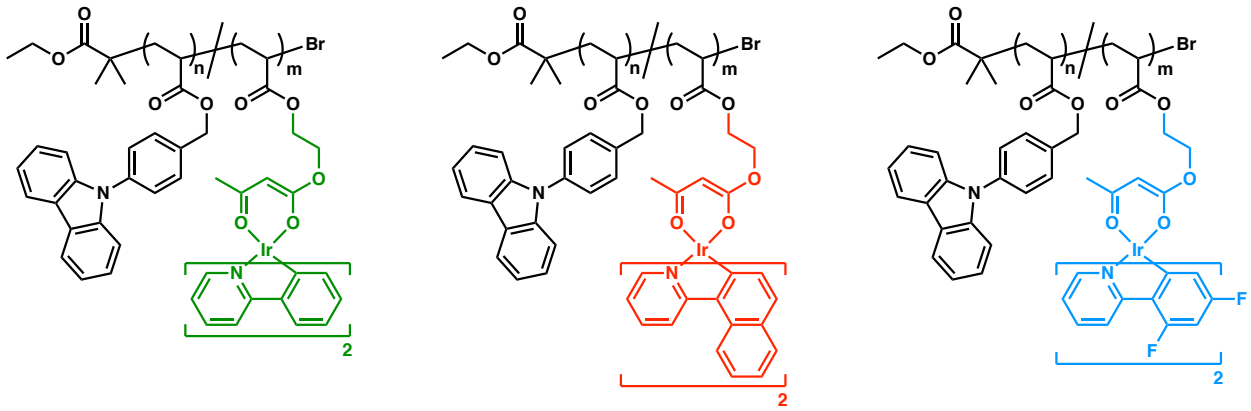

Figure 2.8. Chemical structures of phosphorescent iridium-containing acrylate copolymers produced by Cu(0) RDRP.

2.8 Conclusions

Here we have demonstrated that Cu(0)-RDRP is an effective method for preparing functional acrylate-based polymers with *p*-type organic semiconductors as side chains. It was shown that first-order kinetics are exhibited by these polymers up to ~85% conversion in NMP and ≥93% in DMAc, using Me_6TREN as ligand. Chain-end livingness was also substantially improved in DMAc, facilitating the synthesis of higher molecular weight polymers with M_n approaching 50,000. Moreover, all polymers prepared here show highly reversible one-electron oxidation by cyclic voltammetry and reasonable stability by TGA, making them good candidates for further studies in optoelectronic applications in which triarylamine-based polymers have previously found widespread use. Furthermore, we applied our polymerization method to n-type semiconducting monomers and iridium-containing phosphors. Future investigations will expand upon these methods, with the aim to increase end-group fidelity at higher monomer conversions, towards the synthesis of increasingly complex multiblock copolymers for optoelectronics.

2.9 Experimental Details

General Considerations. All reactions and manipulations were carried out under a nitrogen atmosphere using standard Schlenk or glove box techniques unless otherwise stated. Solvents were obtained from Caledon Laboratories, dried using an Innovative Technologies Inc. solvent purification system, collected under vacuum, and stored under a nitrogen atmosphere over 4 Å molecular sieves. All reagents were purchased from Sigma-Aldrich or Alfa Aesar and used as received unless otherwise stated. Tris[2-(dimethylamino)ethyl]amine (Me_6TREN), ethyl α-bromoisobutyrate (EBiB), and dry dimethylformamide (DMF) were degassed by three freeze-pump-thaw cycles, then stored under a nitrogen atmosphere. 4-(9*H*-carbazol-9-yl)benzaldehyde

(**3d**) was prepared according to literature procedures.[172,173] *N*-methyl-2-pyrrolidone (NMP) and *N*,*N* dimethylacetamide (DMAc) were distilled, then degassed and stored under N_2 atmosphere. CH_2Cl_2 was freshly distilled from P_2O_5 prior to use. Et_3N was dried by distillation on CaH_2 onto activated molecular sieves then degassed and stored under an N_2 atmosphere. The ^1H and $^{13}C\{^1H\}$ nuclear magnetic resonance (NMR) spectra were measured on a Bruker AV III HD 400 MHz spectrometer with chloroform-*d* ($CDCl_3$) or dichloromethane-d_2 (CD_2Cl_2) as the solvent. Absorbance measurements were made on a Cary 60 spectrometer and fluorescence measurements were made on an Edinburgh Instruments FS5 spectrofluorometer. Absolute photoluminescence quantum yields were determined using an Edinburgh Instruments SC–30 Integrating Sphere Module; CH_2Cl_2 was used as the solvent and the optical density at λ_{ex} was kept between 0.05–0.15. Mass spectra were recorded on a Kratos MS-50 instrument using electron impact (EI) ionization.

Gel Permeation Chromatography (GPC). GPC experiments were conducted in chromatography-grade THF at concentrations of 2.5 – 5 mg mL^{-1} using a Malvern OMNISEC GPC instrument equipped with a Viscotek TGuard guard column (CLM3008), and Viscotek T3000 (CLM3003) and T6000 (CLM3006) GPC columns packed with porous poly(styrene-*co*-divinylbenzene) particles regulated at a temperature of 35 °C. Signal response was measured using differential viscometer, differential refractive index, photodiode array and right-angle and low angle light scattering detectors. Calibration was performed using polystyrene standards.

Thermal Analysis. Thermal degradation studies were performed using a NETZSCH TG 209F1 Libra instrument. Samples were placed in an Al_2O_3 crucible and heated at a rate of 10 °C min^{-1}

from 25 to 800 °C under a flow of nitrogen (50 mL min^{-1}). Glass transition temperatures were determined using differential scanning calorimetry (DSC) on a NETZSCH DSC 214 Polyma instrument. The polymer samples were placed in an aluminum pan and heated from 25 to 200 °C at 10 °C min^{-1} under a flow of nitrogen for three heating/cooling cycles.

Electrochemical Methods. Cyclic voltammograms were recorded using a CH Instruments 660D potentiostat at room temperature using a standard three-electrode configuration (working electrode: 2 mm diameter Pt disc; reference electrode: RE-5B Ag/AgCl electrode in saturated aqueous KCl (BASi Inc.), referenced externally to ferrocene/ferrocenium (0.519 V vs Ag/AgCl in CH_2Cl_2);[199] counter electrode: Pt wire) in 0.2 M tetrabutylammonium hexafluorophosphate in dichloromethane. Experiments were run at a scan rate of 100 mV s^{-1} in dry degassed electrolyte solution with ~2 mg mL^{-1} of analyte.

Density Functional Theory (DFT). Calculations were performed using the Gaussian 09 software package. Ground state geometries and energies were calculated at the B3LYP/6-31+g(d) level of theory. To simulate electronic properties of these polymeric materials, analogous versions of each monomer were calculated in which the vinyl end group of the acrylate functionality is replaced with a *sec*-butyl group to more closely mimic the structure of the corresponding polymer chain. If this approximation is not made, the LUMO lies on the acrylate moiety in all cases.

2.9.1 Synthetic Procedures

General Procedure for Cu(0)-RDRP of a polymer with M_n = 10,000:

In a nitrogen atmosphere glovebox, a 4 mL vial capped with a Teflon-lined lid and equipped with a magnetic stir bar was filled with monomer (230 mg), 89.7 μL of a solution of ethyl α-bromoisobutyrate in NMP or DMAc (C_{EBiB} = 50 mg mL^{-1}; EBiB: 4.49 mg, 2.3 x 10^{-2} mmol, 1 eq.), 89.0 μL of a solution of $CuBr_2$/Me_6TREN in NMP or DMAc (C_{Cu} = 3.75 mg mL^{-1}; $CuBr_2$: 0.334 mg, 1.5 x 10^{-3} mmol, 0.065 eq.; Me_6TREN: 0.362 mg, 1.57 x 10^{-3} mmol, 0.068 eq.), and 1,3,5–trimethoxybenzene (3 eq.) as an internal standard. The total polymerization volume was kept to 1.15 mL of solvent. The mixture was stirred at room temperature for 10 minutes to allow all reagents to fully dissolve. A 1.15 cm piece of 18 gauge copper (0) wire was soaked in concentrated HCl for 15 minutes to remove surface impurities, then washed with water followed by acetone, dried *in vacuo* and taken into the glovebox. The wire was added to the mixture to initiate the polymerization. The polymerization was stirred until completion (see Table 1 and Table 4), then quenched by addition of water followed by centrifugation. The polymer was taken up in CH_2Cl_2, dried over $MgSO_4$ and concentrated *in vacuo*. The residue was purified by SEC (Bio-Rad Bio-Beads S-X1 Support) in THF and fractions containing polymer were determined by GPC analysis. All fractions containing polymer were collected and dried *in vacuo* overnight. Alternatively, polymers can be purified by reprecipitation into MeOH (**5a-5c**) or hexanes (**5d**).

Chain extension of methyl acrylate (MA) with 2.5d:

The general procedure for the homopolymerization of a 10k MW polymer by Cu (0)-RDRP was followed as given above. Homopolymerization of MA was allowed to proceed for 8h (~90% conversion by ^{1}H NMR) before addition of a mixture of **5d** (230 mg, 0.70 mmol, 30 eq.), DMAc (1 mL), 103.4 μL of a solution of $CuBr_2$/Me_6TREN in DMAc (C_{Cu} = 3.75 mg mL^{-1}; $CuBr_2$: 0.390 mg, 1.7 x 10^{-3} mmol, 0.065 eq.; Me_6TREN: 0.421 mg, 1.82 x 10^{-3} mmol, 0.068 eq.), and 1.15 cm

Cu(0) wire. Samples were taken at 2 h intervals for a total of 10 h and passed through a short column of neutral alumina to remove dissolved copper salts prior to analysis by ^{1}H NMR and GPC.

General Goldberg Reaction (A):

Modified from a previously reported procedure.[200] Diarylamine (10.0 mmol, 1 eq.), copper (I) iodide (190 mg, 1.0 mmol, 0.1 eq.), and 1,10-phenanthroline (180 mg, 1.0 mmol, 0.1 eq.) were added to a three-neck round bottom flask with an attached condenser and magnetic stir bar. The headspace was evacuated and backfilled with N_2 three times. *p*-xylene (10 mL) and iodobenzene (2.45 g, 12.0 mmol, 1.2 eq) were added and the reaction mixture was heated to reflux. KOH (3.93 g, 70 mmol, 7 eq.) was then ground to a fine powder using a mortar and pestle and added at reflux. The reaction was stirred at reflux until complete by TLC (approximately 24 h), then neutralized with 1 M acetic acid until the aqueous layer reached pH 7. The mixture was then extracted into CH_2Cl_2 (3 x 200 mL), after which the organic fractions were combined, dried over $MgSO_4$, and concentrated *in vacuo*. The crude residue was purified on silica and the product was recrystallized from MeOH.

General Vilsmeier-Haack Formylation (B):

Modified from a previously reported procedure.[200] Triarylamine (10.0 mmol) was added to a 100 mL round bottom flask equipped with a magnetic stir bar. The headspace was evacuated and backfilled with N_2 three times. DMF (6.2 mL, 80 mmol, 8 eq.) and chlorobenzene (12 mL) were added and the flask was heated to 65 ºC in an oil bath. At 65 ºC, $POCl_3$ (5.6 mL, 60 mmol, 6 eq.) was added dropwise to the reaction mixture. The reaction was stirred overnight and then quenched by pouring the solution onto ice. The remaining acid was neutralized with solid K_2CO_3, added in

small portions, until the pH reached 7, and extracted into CH_2Cl_2 (3 x 100 mL). The organic fractions were combined, dried over $MgSO_4$, and concentrated *in vacuo*. The crude residue was purified on silica.

General $NaBH_4$ Reduction (C):

Modified from a previously reported procedure.[201] Pure aldehyde-functionalized compound (10 mmol) was added to a round bottom flask and dissolved in CH_2Cl_2. Once all starting material was dissolved, one part EtOH was added for every three parts CH_2Cl_2. Solid $NaBH_4$ (0.45 g, 12 mmol, 1.2 eq.) was then added to the solution and the reaction was monitored by TLC. When no starting material remained by TLC (approximately 24 h) the reaction was quenched by addition of water followed by extraction using CH_2Cl_2 (3 x 50 mL). The organic fractions were combined, dried over $MgSO_4$, and concentrated *in vacuo*. The crude residue was then purified on a short silica column.

General Acrylation (D):

The alcohol-functionalized compound (10 mmol) and a magnetic stir bar were added to a flame dried round bottom flask which was evacuated and backfilled three times with N_2. CH_2Cl_2 (100 mL) and triethylamine (1.8 mL, 13 mmol, 1.3 eq.) were then added to the round bottom flask and stirred until all solid had dissolved. The reaction flask was cooled to 0 C in an ice bath for 30 minutes, then acryloyl chloride (0.96 mL, 1.2 mmol, 1.2 eq.) was added to the reaction mixture dropwise over 10 minutes. The reaction was then protected from light using foil and allowed to stir in the ice bath for 6, 8 or 24 hrs as indicated below. The reaction was quenched by addition of water and extracted with CH_2Cl_2 (3 x 50 mL). The organic fractions were combined, dried over

$MgSO_4$, and concentrated *in vacuo* without added heat. The crude residue was purified on a short silica column, taking care to elute the product as quickly as possible to avoid decomposition on silica.

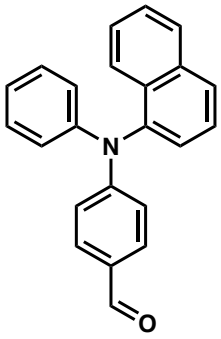

4-(naphthalen-1-yl(phenyl)amino)benzaldehyde (2.3a)

Prepared according to general reaction B, using **2.2a** as the starting material. Purified on silica using CH_2Cl_2. Yield 75%.^{1}H NMR and $^{13}C\{^1H\}$ NMR spectra match literature values.[202]

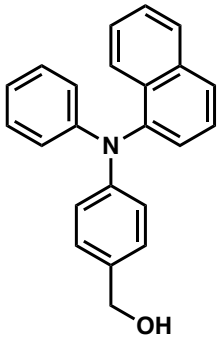

(4-(naphthalen-1-yl(phenyl)amino)phenyl)methanol (2.4a)

Prepared according to general reaction C using **2.3a** as the starting material. Purified on silica using a gradient from 2% to 10% MeOH in CH_2Cl_2. Yield 95%.

^{1}H NMR (400 MHz, Chloroform-*d*): δ 7.92 (ddt, *J* = 16.1, 8.2, 0.9 Hz, 2H), 7.79 (dt, *J* = 8.2, 1.1 Hz, 1H), 7.53 – 7.43 (m, 2H), 7.42 – 7.31 (m, 2H), 7.22 (ddd, *J* = 8.7, 4.7, 2.3 Hz, 4H), 7.08 – 7.00 (m, 4H), 6.99 – 6.93 (m, 1H), 4.63 (s, 2H) ppm.

^{13}C{^{1}H} NMR (101 MHz, Chloroform-*d*): δ 148.4, 147.9, 143.5, 135.4, 134.5, 131.2, 129.0, 128.4, 128.1, 127.3, 126.5, 126.4, 126.3, 126.1, 124.0, 121.8, 121.7, 121.6, 64.8 ppm.

HRMS (EI) *m/z*: [$M^{+\bullet}$] calcd for $[C_{23}H_{19}NO]^{+\bullet}$, 325.14666; found, 325.14626; difference: 1.3 ppm.

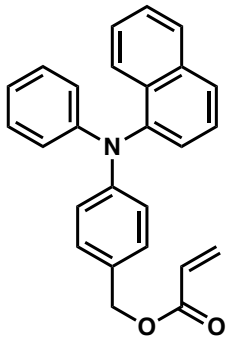

4-(naphthalen-1-yl(phenyl)amino)benzyl acrylate (2.5a)

Prepared according to general reaction D (8 h) using **2.4a** as the starting material. Purified on silica using 6:1 hexanes/ethyl acetate. Yield 97%.

^{1}H NMR (400 MHz, Methylene Chloride-d_2): δ 7.96 (ddd, *J* = 7.6, 4.5, 1.1 Hz, 2H), 7.88 – 7.82 (m, 1H), 7.57 – 7.32 (m, 4H), 7.29 – 7.19 (m, 4H), 7.12 – 7.05 (m, 2H), 7.04 – 6.88 (m, 3H), 6.43 (dd, *J* = 17.3, 1.5 Hz, 1H), 6.18 (dd, *J* = 17.3, 10.4 Hz, 1H), 5.86 (dd, *J* = 10.4, 1.5 Hz, 1H), 5.12 (s, 2H) ppm.

^{13}C{^{1}H} NMR (101 MHz, Methylene Chloride-d_2): δ 166.0, 148.7, 148.2, 143.4, 135.5, 131.4, 130.7, 129.6, 129.3, 128.9, 128.6, 127.5, 126.8, 126.5, 126.3, 124.1, 122.4, 122.3, 121.1, 66.2 ppm.

HRMS (EI) *m/z*: [$M^{+\bullet}$] calcd for $[C_{26}H_{21}NO_2]^{+\bullet}$, 379.15727; found, 379.15723; difference: –0.1 ppm.

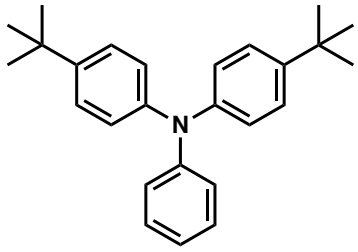

4-(*tert*-butyl)-*N*-(4-(*tert*-butyl)phenyl)-*N*-phenylaniline (2.2b)

Prepared according to general reaction A, using bis(4-(*tert*-butyl)phenyl)amine as the diarylamine. Purified on silica using 1:3 CH_2Cl_2/hexane. Yield 81%. ^{1}H NMR and $^{13}C\{^1H\}$ NMR spectra match literature values. [203]

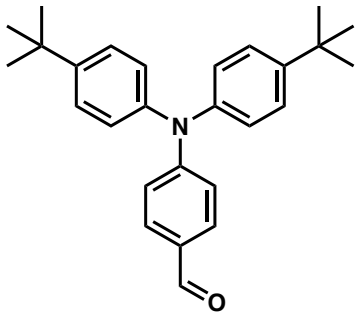

4-(bis(4-(*tert*-butyl)phenyl)amino)benzaldehyde (2.3b)

Prepared according to general reaction B, using **2.2b** as the starting material. Purified on silica using CH_2Cl_2. Yield 95%.^{1}H NMR and $^{13}C\{^1H\}$ NMR spectra match literature values. [204]

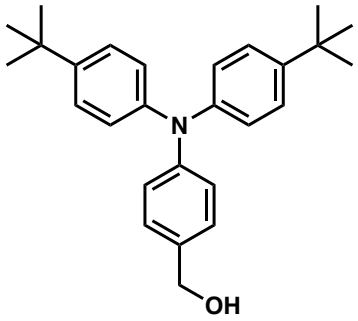

(4-(bis(4-(*tert*-butyl)phenyl)amino)phenyl)methanol (2.4b)

Prepared according to general reaction C using **2.3b** as the starting material. Purified on silica using 1% MeOH in CH_2Cl_2. Yield 90%. ^{1}H NMR and $^{13}C\{^1H\}$ NMR spectra match literature values. [205]

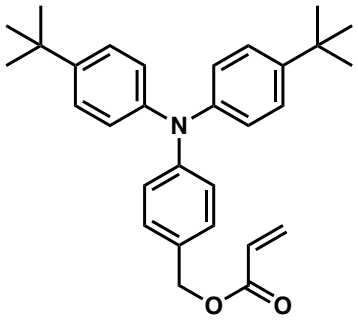

4-(bis(4-(*tert*-butyl)phenyl)amino)benzyl acrylate (2.5b)

Prepared according to general reaction D (24 h) using **2.4b** as the starting material. Purified on silica using CH_2Cl_2. Yield 96%.

^{1}H NMR (400 MHz, Chloroform-*d*): δ 7.39 (s, 1H), 7.33 – 7.20 (m, 6H), 7.10 – 7.00 (m, 6H), 6.48 (dd, J = 17.3, 1.5 Hz, 1H), 6.19 (dd, J = 17.3, 10.4 Hz, 1H), 5.87 (dd, J = 10.4, 1.5 Hz, 1H), 5.16 (s, 2H), 1.34 (s, 18H) ppm.

$^{13}C\{^1H\}$ NMR (101 MHz, Chloroform-*d*): δ 166.2, 148.4, 145.9, 144.9, 130.9, 129.5, 128.6, 128.5, 128.3, 126.1, 124.1, 122.5, 66.3, 34.3, 31.4 ppm.

HRMS (EI) *m/z*: [$M^{+\bullet}$] calcd for $[C_{30}H_{35}NO_2]^{+\bullet}$, 441.26678; found, 441.26711; difference: –0.8 ppm.

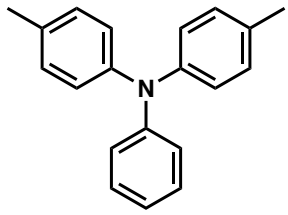

4-methyl-*N*-phenyl-*N*-(*p*-tolyl)aniline (2.2c)

Prepared according to general reaction A, using di-*p*-tolylamine as the diarylamine. Purified on silica using 1:4 CH_2Cl_2/hexane. Yield 62%.^{1}H NMR and $^{13}C\{^1H\}$ NMR spectra match literature values. [202]

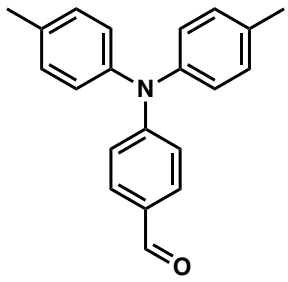

4-(di-*p*-tolylamino)benzaldehyde (2.3c)

Prepared according to general reaction B, using **2.2c** as the starting material. Purified on silica using a gradient from 1:1 CH_2Cl_2/hexane to CH_2Cl_2. Yield 80%.^{1}H NMR and $^{13}C\{^1H\}$ NMR spectra match literature values.[202]

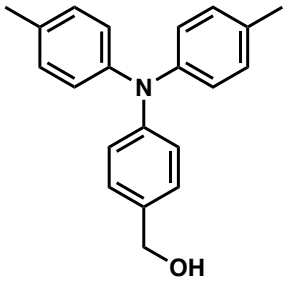

(4-(di-*p*-tolylamino)phenyl)methanol (2.4c)

Prepared according to general reaction C using **2.3c** as the starting material. Purified on silica using CH_2Cl_2. Yield 93%.^{1}H NMR and $^{13}C\{^1H\}$ NMR spectra match literature values.[206]

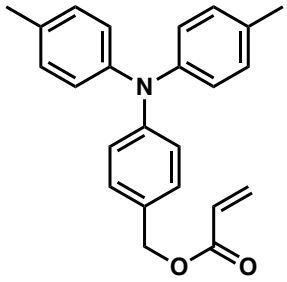

4-(di-*p*-tolylamino)benzyl acrylate (2.5c)

Prepared according to general reaction D (8 h) using **2.4c** as the starting material. Purified on silica using CH_2Cl_2. Yield 73%.

^{1}H NMR (400 MHz, Chloroform-*d*): δ 7.28 – 7.20 (m, 2H), 7.11 (d, *J* = 8.2 Hz, 4H), 7.07 – 6.99 (m, 6H), 6.49 (dd, *J* = 17.3, 1.5 Hz, 1H), 6.21 (dd, *J* = 17.3, 10.4 Hz, 1H), 5.88 (dd, *J* = 10.4, 1.5 Hz, 1H), 5.16 (s, 2H), 2.35 (s, 6H) ppm.

$^{13}C\{^1H\}$ NMR (101 MHz, Chloroform-*d*): δ 166.8, 148.4, 145.1, 132.8, 130.9, 129.9, 129.5, 128.5, 128.4, 124.8, 122.1, 66.3, 20.8 ppm.

HRMS (EI) *m/z*: $[M^{+\bullet}]$ calcd for $[C_{24}H_{23}NO_2]^{+\bullet}$, 357.17293; found, 357.17288; difference: –0.1 ppm.

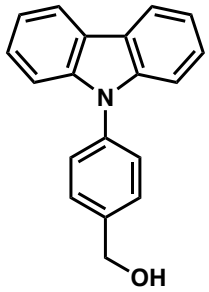

(4-(9*H*-carbazol-9-yl)phenyl)methanol (2.4d)

Prepared according to general reaction C using **2.3d** as the aldehyde. Purified on silica using CH_2Cl_2. Yield 90%. ^{1}H NMR and $^{13}C\{^1H\}$ NMR match literature values.[207]

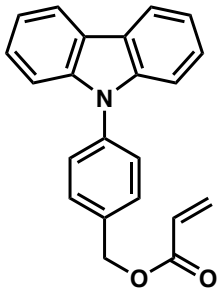

4-(9*H*-carbazol-9-yl)benzyl acrylate (2.5d)

Prepared according to general reaction D (6 h) using **2.4d** as the starting material. Purified on silica using CH_2Cl_2 and recrystallized twice from CH_2Cl_2/hexanes. Yield 96%.

^{1}H NMR (400 MHz, Chloroform-*d*): δ 8.18 (d, J = 7.7 Hz, 2H), 7.63 (q, J = 8.5 Hz, 4H), 7.48 – 7.38 (m, 4H), 7.32 (ddd, J = 8.0, 5.1, 3.1 Hz, 2H), 6.56 (dd, J = 17.3, 1.4 Hz, 1H), 6.27 (dd, J = 17.3, 10.4 Hz, 1H), 5.95 (dd, J = 10.4, 1.4 Hz, 1H), 5.36 (s, 2H) ppm.

$^{13}C\{^1H\}$ (101 MHz, Chloroform-*d*): δ 166.0, 140.8, 137.7, 135.1, 131.5, 129.8, 128.2, 127.2, 126.0, 123.4, 120.3, 120.0, 109.7, 65.8 ppm.

HRMS (EI) *m/z*: $[M^{+\bullet}]$ calcd for $[C_{22}H_{17}NO_2]^{+\bullet}$, 327.12576; found, 327.12593; difference: 0.5 ppm.

Chapter 3: Multiblock Bottlebrush Nanofibers from Organic Electronic Materials

3.1 Introduction

Techniques for the assembly of hierarchical nanostructures from soft matter have opened the door to many new applications of nanotechnology. Methods such as crystallization-driven self-assembly (CDSA),[3,14,18,29,208,209] living supramolecular polymerization,[32,34,210–212] and hierarchical solution self-assembly (HSSA)[8,40,213] have leveraged low-cost solution processing to address scalability challenges, while the complexity of materials prepared in these ways continues to improve. Despite these achievements, synthetic methods in nanotechnology that rely on self-assembly continue to face several challenges. Most importantly, self-assembly can be highly dependent on conditions such as solvent and temperature, which must be kept within certain ranges if the integrity of the nanomaterial is to be maintained. Furthermore, methods for the precise synthesis of soft-matter nanomaterials often require building blocks with highly specific properties. For example, CDSA makes use of polymers amenable to epitaxial crystallization, supramolecular polymerization must precisely balance Van der Waals forces, and HSSA uses building blocks with differing solubilities to achieve complex, well-defined nanomaterials. While each has been used to prepare nanomaterials with impressive complexity and function, the chemical requirements of each technique narrow the potential scope of materials that might be investigated.

We therefore sought methods based on efficient and orthogonal covalent chemistry for preparing nanostructures with well-defined components, which would circumvent many of the challenges associated with nanomaterials synthesis by self-assembly. Bottlebrush copolymers

(BBCPs) are ideally suited for this goal, and have recently emerged as a powerful route to large macromolecules with molecular weights exceeding 10^6 Da.[58,62,65] Consisting of polymeric side-chains attached covalently to a linear backbone, these materials have found numerous applications in photonic crystals,[67,68,214] templating,[215–217] and nanomedicine[74–76,218,219] as a result of their unique physical properties. Due to the steric demands of the side chains, bottlebrush polymers occupy a relatively low-entropy conformational space, adopting extended conformations that limit chain entanglement in solution and the solid state.[55,56] As a result, this class of polymers have recently been used to prepare nanostructures with complex and unique morphologies, including Janus particles,[220] toroids,[221] dumbbells,[222] and brushes with tailored graft distributions.[78,223–225] As a result of their size, bottlebrush polymers also make unique building blocks for larger structures, and have been investigated in self-assembled materials themselves.[81,226,227]

Multiblock bottlebrush copolymers provide a compelling bottom-up approach to the synthesis of hierarchical nanostructures from soft material. Their block-by-block synthesis allows for the preparation of multicompartment structures that remain nanosegregated by virtue of their covalent chemistry, irrespective of environmental conditions such as temperature or solvent. Furthermore, bottlebrush copolymers may be used to form nanostructures from a vast array of monomers, removing the need to consider factors such as crystallization or selective solvation that a self-assembly approach might require. This would facilitate the preparation of hierarchical materials with multiple, complex functionalities difficult to achieve by existing methods.

Here we prepared bottlebrush copolymers which mimic the structure of multilayer organic electronic devices on single polymer chains. Bottlebrush polymers based on polythiophenes have recently shown promise as dielectric materials,[84,85,88] and similar structures composed of multiple organic semiconductors would provide a unique tool for the study of charge transport at nanoscale

junctions.[228,229] Using a series of macromonomers prepared from p- and n-type organic semiconductors, fiber-like nanomaterials of tunable length were prepared with molecular weights from 470 – 2050 kDa. This approach was then used to access diblock nanofibers analogous to organic p-n junctions, which displayed the reversible electrochemistry of each of their components (Figure 3.1). Finally, bottlebrush copolymers were prepared in which individual polymer chains exhibited the multilayer structure of four-component phosphorescent organic light-emitting diodes (OLEDs), such that the photophysical properties of each of the four organic semiconductors could be independently observed.

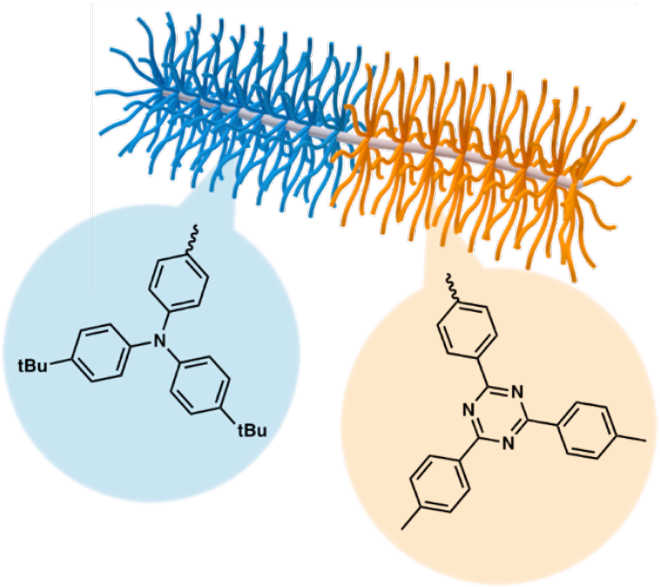

Figure 3.1. Schematic illustration of a diblock bottlebrush copolymer composed of p-type (blue) and n-type (orange) organic semiconductors.

3.2 Results and Discussion

A series of macromonomers (MMs) were first synthesized from acrylates bearing organic semiconductor moieties as side-chains, representative of materials used in the emissive layer (EML), hole-transport layer (HTL) and electron-transport layer (ETL) of organic devices such as

OLEDs or organic thin-film transistors (OTFTs). MMs were prepared *via* direct growth from a norbornene-functionalized initiator via Cu(0) reversible-deactivation radical polymerization (RDRP),[105,106,108] which provides a scalable route to multigram quantities of these materials at room temperature with dispersities (Đ) as low as 1.12 (Figure 3.2). Competing vinyl addition to the norbornene group during the RDRP process can be suppressed by halting the polymerization at conversions ≤ 60%,[230] after which residual monomer can be successfully removed and recycled. Grafting-through ring-opening metathesis polymerization (ROMP) of each macromonomer was then used to give bottlebrushes with target backbone degrees of polymerization (DP_n's) of 100 and 400 from **CzBA-MM**, **ETL-MM** and **tBuHTL-MM**. The grafting-through approach using Grubbs' third-generation catalyst (1.3) was chosen to ensure 100% grafting density of side chains to the bottlebrush backbone, and gave bottlebrushes with $M_n > 2 \times 10^6$ Da (Table 3.1). Consistent with the results of Matson and coworkers,[231] the conversion observed during ROMP decreases and dispersity increases as longer bottlebrushes are targeted, particularly given the considerable steric bulk of the semiconductor side chains employed here. Bottlebrushes formed from **ETL-MM** consistently showed molecular weights higher than those anticipated by theory, perhaps due to interactions from the coordinating nitrogen atoms on the ETL monomer with the ruthenium catalyst.

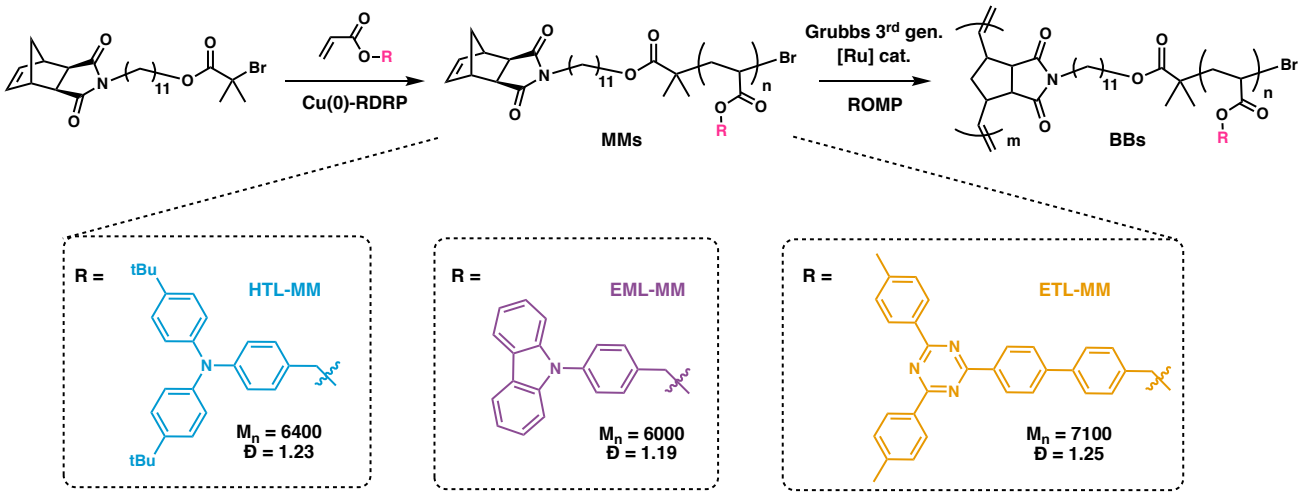

Figure 3.2. Synthesis of norbornene-functionalized macromonomers from a series of organic semiconductors, and their reaction to form bottlebrush polymers by grafting-through ROMP.

We also note that the addition of a C11 spacer between the norbornene-dicarboxamide and the polyacrylate was critical in achieving high backbone DP_n's, as earlier efforts using only a C2 linker gave bottlebrushes with a maximum DP_n of ≈ 50. Importantly, we determined that residual macromomomer can be completely removed from these mixtures by passing the reaction over a reusable methacrylic resin in THF, a critical detail if the properties of individual nanowires are to be electrically interrogated. Atomic force microscopy (AFM) images of bottlebrushes prepared from each of these organic semiconductors on highly oriented pyrolytic graphite (HOPG) substrates are shown in Figure 3, with fiber-like morphologies up to several hundred nanometers in length in each case. All bottlebrushes are fluorescent with emission maxima of 347, 412, and 469 nm and quantum yields of 0.21, 0.02 and 0.56 for **$CzBA_{100}$-BB**, **ETL_{100}-BB** and **$tBuHTL_{100}$-BB** respectively, mirroring the photophysical properties of their respective homopolymers.[182,232]

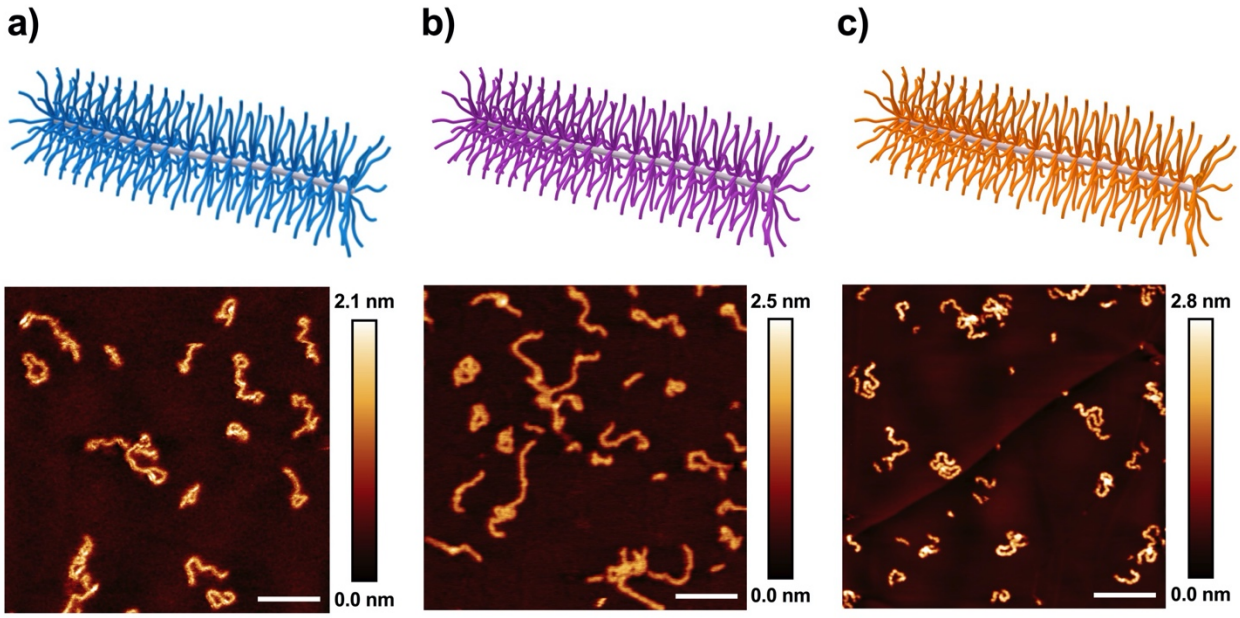

Figure 3.3. Schematic illustrations and AFM height images of a) **tBuHTL$_{400}$-BB**, b) **CzBA$_{400}$-BB** and c) **ETL$_{400}$-BB** (right) on HOPG substrates (scale bars = 200 nm).

Table 3.1. Synthesis of bottlebrush homopolymers.

Entry[a]	$M_{n,\,SEC}$[b] (kDa)	$M_{n,\,theory}$ (kDa)	Đ	Conv. (%)[b]
tBuHTL$_{100}$-BB	570	499	1.14	78
CzBA$_{100}$-BB	701	500	1.17	83
ETL$_{100}$-BB	473	504	1.12	71
tBuHTL$_{400}$-BB	1530	1770	1.35	69
CzBA$_{400}$-BB	1990	2040	1.32	85
ETL$_{400}$-BB	2050	1620	1.31	57

[a]Subscript indicates target DP$_n$.
[b]Determined by SEC in THF after purification by preparatory SEC.

This Cu(0)-RDRP/ROMP strategy was then used to prepare diblock copolymers with structures analogous to nanoscale junctions between chemically distinct organic semiconductors (Figure 3.4). By sequential reaction of macromonomers, diblock BBCPs **(CzBA$_{75}$-*b*-tBuHTL$_{75}$)-**

BB, **(CzBA$_{75}$-*b*-ETL$_{75}$)-BB**, and **(ETL$_{75}$-*b*-tBuHTL$_{75}$)-BB** were successfully prepared. Cyclic voltammetry shows the diblock bottlebrushes to be capable of the reversible reduction and oxidation of their individual components, showing promise for investigating these materials as thin films for ambipolar charge transport or as individual nanoscale diode-like structures. Notably, monomodal molecular weight distributions with dispersities of 1.21 and 1.17 are obtained for **(CzBA$_{75}$-*b*-tBuHTL$_{75}$)-BB** and **(CzBA$_{75}$-*b*-ETL$_{75}$)-BB** respectively, while significant chain death is consistently observed upon addition of the second block for the bulkier **(ETL$_{75}$-*b*-tBuHTL$_{75}$)-BB**. This indicates that the steric bulk of the reactive macronomomers plays a key role in achieving well-defined diblock copolymers from organic semiconductors via ROMP.

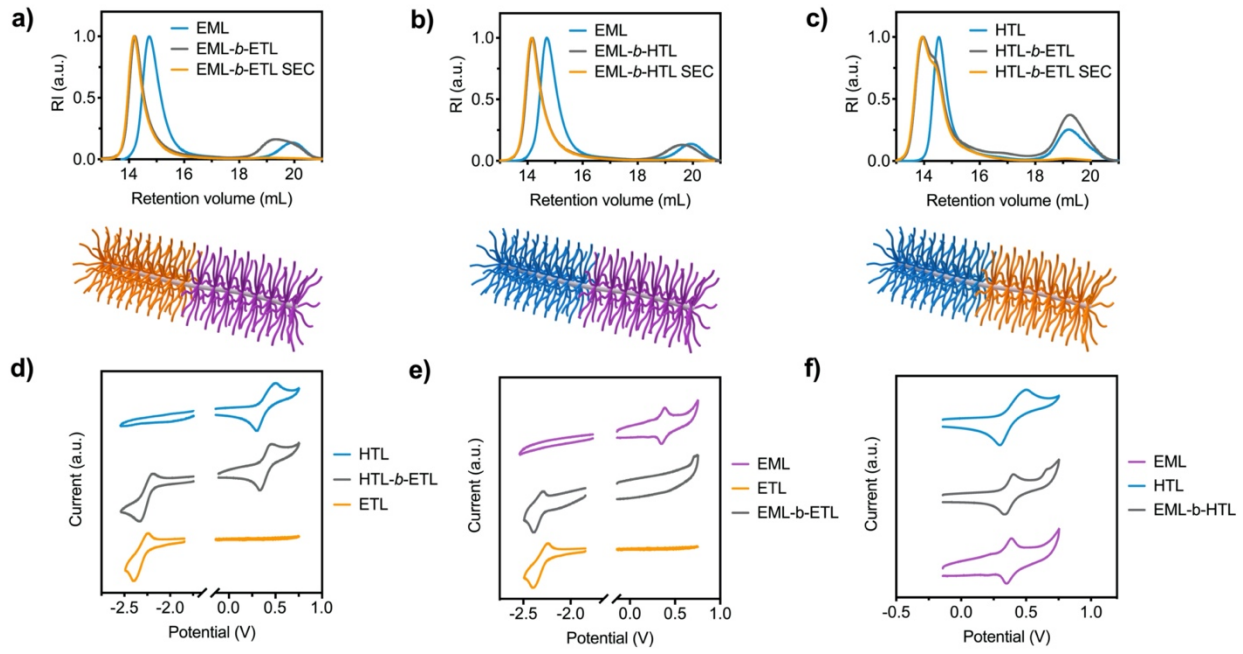

Figure 3.4. Schematics (left) and SEC chromatograms (right) of diblock bottlebrushes (a) **(CzBA$_{75}$-*b*-ETL$_{75}$)-BB** (b) **(CzBA$_{75}$-*b*-tBuHTL$_{75}$)-BB** (c) **(ETL$_{75}$-*b*-tBuHTL$_{75}$)-BB** showing the refractive index (RI) response after the addition of each block, and following purification by preparatory SEC. (d-f) Cyclic voltammograms (CVs) of **(ETL$_{75}$-*b*-tBuHTL$_{75}$)-BB**, **(CzBA$_{75}$-*b*-ETL$_{75}$)-BB** and **(CzBA$_{75}$-*b*-tBuHTL$_{75}$)-BB** relative to $FeCp_2^{0/+}$. CVs of **tBuHTL$_{100}$-BB** (blue), **CzBA$_{100}$-BB** (purple) and **ETL$_{100}$-BB** (orange) are shown for comparison.

To demonstrate the potential of this approach in preparing hierarchical nanostructures from optoelectronic materials, we next prepared triblock BBCPs such that the structure of each individual macromolecule would mimic the design of a four-component OLED, composed of ETL, HTL, a host material, and a phosphorescent iridium dopant. Such nanostructures would allow for control at three levels of hierarchy: 1) the structures of the monomers used; 2) the arrangement of these monomers within macromonomer strands, and 3) the arrangement of macromonomer strands into a multiblock bottlebrush, mimicking the structure of macroscopic devices.

To this end, a fourth macromonomer **IrPPY-MM** was synthesized consisting of **CzBA** doped with 8 wt% of an iridium-containing monomer based on the commonly used OLED emitter $Ir(ppy)_2(acac)$ (M_n = 9300, Đ = 1.22). Sequential ROMP of **ETL-MM**, **IrPPY-MM**, and **tbuHTL-MM** gave **(ETL_{50}-*b*-$IrPPY_{30}$-*b*-$tBuHTL_{50}$)-BB** (Figure 3.5). This material shows bright green phosphorescence (Figures 5e and S12, τ = 5.0 μs) alongside the reversible reduction and oxidation of the ETL and HTL blocks at -2.32 and 0.48 V, respectively. While copolymers consisting of multiple OLED materials have been synthesized previously,[233] **(ETL_{50}-*b*-$IrPPY_{30}$-*b*-$tBuHTL_{50}$)-BB** is composed of individual domains with discrete interfaces that remain nanosegregated due to the unique morphology of the bottlebrush structure (M_n = 296 kDa, Đ = 1.21). Furthermore, the energy levels of the four components of the structure match the typical 'staircase' arrangement of a four-component OLED, (Figure 5b, Table S2) designed to facilitate charge-transport of both electrons and holes from each end of the structure to the active layer at its center. SEC analysis shows that narrow dispersity is maintained at each stage of the polymerization, indicating that separation of the bulky HTL and ETL blocks with the smaller **CzBA** block allows for the synthesis of triblock BBCPs from organic semiconductors with minimal chain death (Table S3).

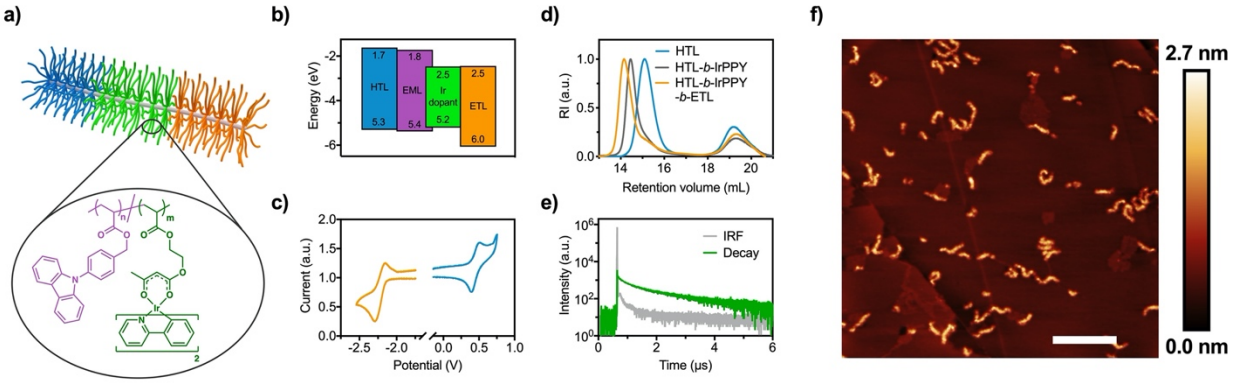

Figure 3.5. (a) Schematic illustration of **(ETL_{50}-*b*-$IrPPY_{30}$-*b*-$tBuHTL_{50}$)-BB**, showing the structure of the IrPPY side chains in the middle block. (b) Energy level diagram for the four components of the triblock BBCP. (c) Cyclic voltammogram of this BBCP showing the reduction of the ETL block (orange) and oxidation of the tBuHTL block (blue). (d) SEC RI chromatograms after the addition of each block. (e) PL decay of the BBCP (λ_{ex} = 340 nm) showing the phosphorescent decay of the Ir dopant. f) AFM height images of these BBCPs on HOPG (scale bar = 200 nm).

3.3 Conclusions

In summary, the grafting-through synthesis of BBCPs has been shown to be an effective route to multiblock structures formed from optoelectronic materials. Multicomponent nanomaterials similar in architecture to block co-micelles can be prepared by covalent chemistry, adapting a cylindrical morphology that does not require environment-dependent self-assembly steps. This work opens the door to research on nanoscale wires and junctions from arbitrary organic semiconductors regardless of their crystallinity or solvophilicity, providing methods for the incorporation of diverse optoelectronic materials into hierarchical nanofibers. Future work will examine the electrical properties of individual wires and multiblock structures by conductive scanning probe microscopy techniques, as well as assess the use of these materials in semiconducting thin films.

3.4 Experimental Details

General Considerations. All reactions and manipulations were carried out under a nitrogen atmosphere using standard Schlenk or glove box techniques unless otherwise stated. Dry solvents were obtained from Caledon Laboratories, dried using an Innovative Technologies Inc. solvent purification system, collected under vacuum, and stored under a nitrogen atmosphere over 4 Å molecular sieves. All reagents were purchased from Sigma-Aldrich or Alfa Aesar and used as received unless otherwise stated. **2.5b**,[232] **2.5d**,[232] **3.1**,[182] **3.2**[183] (see Section 3.4.7), 11-aminoundecan-1-ol,[234] and dichloro[1,3-bis(2,4,6-trimethylphenyl)-2-imidazolidinylidene] (benzylidene)bis(pyridine)ruthenium(II)[122] (**1.3**) were prepared according to literature procedures. *N*-methyl-2-pyrrolidone (NMP) was distilled, then degassed and stored under an N_2 atmosphere. CH_2Cl_2 was freshly distilled from P_2O_5 prior to use. Et_3N was dried by distillation on CaH_2 onto activated molecular sieves then degassed and stored under an N_2 atmosphere. The ^1H and $^{13}C\{^1H\}$ nuclear magnetic resonance (NMR) spectra were measured on a Bruker AV III HD 400 MHz spectrometer with chloroform-*d* ($CDCl_3$) or dichloromethane-d_2 (CD_2Cl_2) as the solvent. Absorbance measurements were made on a Cary 60 spectrometer and fluorescence measurements were made on an Edinburgh Instruments FS5 spectrofluorometer. Absolute photoluminescence quantum yields were determined using an Edinburgh Instruments SC–30 Integrating Sphere Module; toluene was used as the solvent and spectra obtained at concentrations of 0.01 mg mL^{-1}. Mass spectra were recorded on a Kratos MS-50 instrument using electron impact ionization.

Atomic Force Microscopy (AFM). Atomic force microscopy (AFM) images were obtained using an Asylum Instruments Cypher S AFM system in tapping mode at scan rates of 0.1 Hz. Samples were prepared by spin-coating solutions of polymer onto freshly cleaved highly-oriented pyrolytic

graphite (HOPG) at 2500 rpm for 30 s at concentrations of ~0.001 mg mL^{-1}. For best results, 1,2-dichloroethane was used as the solvent for **tBuHTL$_{400}$-BB**, **ETL$_{400}$-BB**, and (**ETL$_{50}$-*b*-IrPPY$_{30}$-*b*-tBuHTL$_{50}$)-BB** while 2:1 chloroform/chlorobenzene was used as the solvent for **CzBA$_{400}$-BB**. Samples were placed in a vacuum oven (60 ºC) for at least 2 h before images were obtained using Mikromasch HQ:NSC14/No Al or HQ:NSC19/No Al probes, with typical resonance frequencies f and spring constants k of (f = 160 kHz, k = 5 N/m) and (f = 65 kHz, k = 0.5 N/m) respectively.

Size Exclusion Chromatography (SEC). SEC experiments were conducted in chromatography-grade THF at concentrations of 0.5 – 2 mg mL^{-1} using a Malvern OMNISEC GPC instrument equipped with a Viscotek TGuard guard column (CLM3008), and Viscotek T3000 (CLM3003) and T6000 (CLM3006) GPC columns packed with porous poly(styrene-*co*-divinylbenzene) particles regulated at a temperature of 35 °C. Signal response was measured using differential viscometer, differential refractive index, photodiode array and right-angle and low angle light scattering detectors. Calibration of interdetector distances was performed using a polystyrene standard from Malvern Inc. Refractive index increments (d*n*/d*c*) were determined using 100% mass recovery methods from Malvern OMNISEC software version 10.2 with each polymer sample being run at least five times to ensure reproducibility of the calculated refractive index increment.

Thermal Analysis. Glass transition temperatures were determined using differential scanning calorimetry (DSC) on a NETZSCH DSC 214 Polyma instrument. The polymer samples were placed in an aluminum pan and heated from 25 to 175 °C at 10 °C min^{-1} under a flow of nitrogen for 3 heating/cooling cycles.

Electrochemical Methods. Cyclic voltammograms were recorded using a BASi Epsilon Eclipse potentiostat at room temperature using a standard three-electrode configuration (working electrode: 3 mm diameter glassy carbon; reference electrode: RE-5B Ag/AgCl electrode in saturated aqueous KCl (BASi Inc.), referenced externally to ferrocene/ferrocenium (0.543 V in 1,2-difluorobenzene);[199] counter electrode: Pt wire) in 0.2 M tetrabutylammonium hexafluorophosphate in 1,2-difluorobenzene. Experiments were run at a scan rate of 100 mV s^{-1} in dry degassed electrolyte solution with ~4 mg mL^{-1} of analyte. Polymers **ETL_{100}-BB**, **$CzBA_{100}$-BB**, and **($CzBA_{75}$-*b*-ETL_{75})-BB** were sparingly soluble and run as saturated solutions.

Density Functional Theory. Calculations were performed using the Gaussian 09 software package.[235] Ground state geometries and energies were calculated at the B3LYP/6-31+g(d) level of theory for all atoms except iridium, for which the LANL2DZ basis set was used. To simulate electronic properties of these polymeric materials, analogous versions of each monomer were calculated in which the vinyl end group of the acrylate functionality was replaced with a *sec*-butyl group to more closely mimic the structure of the corresponding polymer chain. If this approximation is not made, the LUMO lies on the acrylate moiety in all cases.

3.4.1 Synthetic Procedures

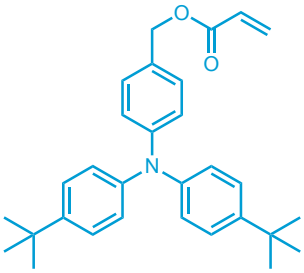

tBuHTL

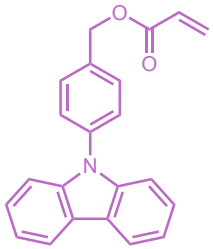

CzBA

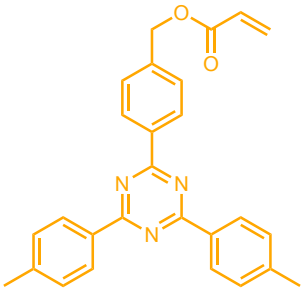

ETL

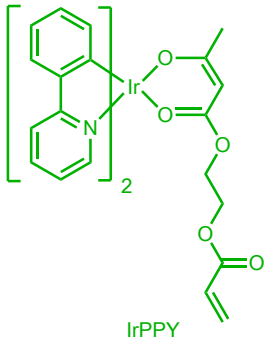

IrPPY

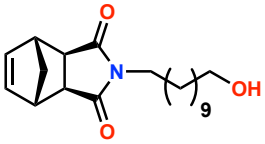

Synthesis of *N*-(hydroxyundecanyl)-*cis*-5-norbornene-*exo*-2,3-dicarboximide (3.3)

Prepared according to a modified literature procedure.[236] A 100 mL round-bottomed flask equipped with a magnetic stir bar, a Dean-Stark trap and a condenser was charged with *cis*-5-norbornene-*exo*-2,3-dicarboxylic anhydride (0.96 g, 5.8 mmol, 1 eq.), 1-aminoundecan-1-ol (1.2 g, 6.4 mmol, 1.1 eq.) and Et_3N (59 mg, 0.58 mmol, 0.1 eq.) and 20 mL toluene. The mixture was heated to reflux and left for 22 h before cooling back to room temperature. The reaction was extracted with CH_2Cl_2 and washed with 0.1 M HCl (20 mL) and brine (20 mL), dried over $MgSO_4$, filtered and concentrated *in vacuo* to yield **3.3** as a yellow oil. Yield = 1.63 g (76 %).

^{1}H NMR (400 MHz, Chloroform-*d*): δ 6.29 (t, J = 1.9 Hz, 2H), 3.65 (t, J = 6.6 Hz, 2H), 3.46 (t, J= 7.3 Hz, 2H), 3.28 (t, J = 1.8 Hz, 2H), 2.68 (d, J = 1.5 Hz, 2H), 1.59 – 1.51 (m, 5H), 1.35 – 1.20 (m, 16H) ppm.

^{13}C{^{1}H} NMR (101 MHz, Chloroform-*d*): δ 178.3, 137.9, 63.2, 47.9, 45.32, 42.8, 38.9, 32.9, 29.6, 29.5, 29.5, 29.5, 29.2, 27.9, 27.0, 25.8 ppm.

HRMS (EI) *m/z*: [$M^{+\bullet}$] calcd for [$C_{20}H_{31}NO_3$]$^{\bullet}$, 333.23039; found, 333.23014; difference: 0.8 ppm.

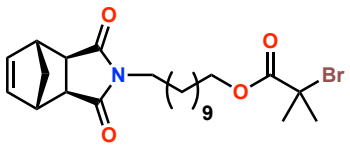

Synthesis of *N*-(undecanyl 2-bromo-2-methylpropionate)-*cis*-5-norbornene-*exo*-2,3-dicarboximide (3.4)

Prepared according to a modified literature procedure.[236] A 100 mL round-bottomed flask equipped with a magnetic stir bar was charged with **3.3** (1.4 g, 4.2 mmol, 1 eq.), Et_3N (59 mg, 0.58 mmol, 0.1 eq) and 50 mL dry CH_2Cl_2. The solution was sparged with N_2 for 10 min and cooled to 0 °C in an ice bath. *α-Bromoisobutyryl bromide* (1.2 g, 6.4 mmol, 1.1eq.) was added dropwise with a syringe over 2 min. The reaction was warmed to room temperature slowly, then left stirring under N_2 overnight. A colour change from light yellow to orange was observed. To quench the reaction 20 mL of H_2O was added. The organic layer was collected and washed with 20 mL brine, dried over $MgSO_4$, filtered and concentrated *in vacuo*. The crude residue was purified with silica gel chromatography (3:1 CH_2Cl_2/Hexanes) to yield **3.4** as a colourless oil. Yield = 0.814 g (84 %).

^{1}H NMR (400 MHz, Chloroform-*d*): δ 6.29 (t, J = 1.9 Hz, 2H), 4.17 (t, J = 6.6 Hz, 2H), 3.46 (d, J = 7.5 Hz, 2H), 3.28 (t, J = 1.8 Hz, 2H), 2.68 (d, J = 1.3 Hz, 2H), 1.94 (s, 6H), 1.67 (dt, J = 8.0, 6.5 Hz, 2H), 1.60 – 1.49 (m, 3H), 1.42 – 1.20 (m, 15H) ppm.

^{13}C{^{1}H} NMR (101 MHz, Chloroform-*d*): δ 178.1, 171.7, 137.8, 66.1, 56.0, 47.8, 45.1, 42.7, 38.7, 30.8, 29.4, 29.4, 29.3, 29.1, 29.1, 28.3, 27.7, 26.9, 25.8 ppm.

HRMS (EI) *m/z*: [$M^{+\bullet}$] calcd for [$C_{24}H_{36}NO_4{}^{79}Br]^{\bullet}$, 481.18277; found, 481.18310; difference: 0.7 ppm.

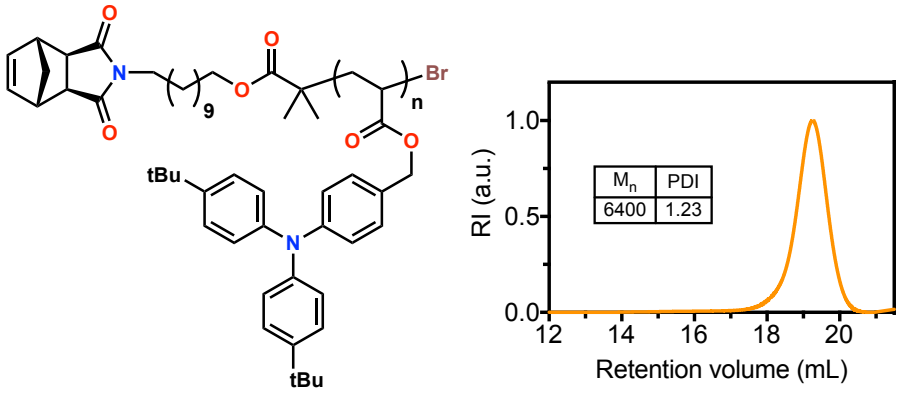

Synthesis of tBuHTL-MM by Cu(0)-RDRP:

In a nitrogen atmosphere glovebox, to a 20 mL vial capped with a Teflon-lined lid and equipped with a magnetic stir bar was added **2.5b** (2.00 g, 4.5 mmol, 23 eq.), 1.93 mL of a solution of **3.4** in NMP (C_{S2} = 50 mg mL^{-1}; **3.4** 96.5 mg, 0.20 mmol, 1 eq.), and 775.0 µL of a solution of $CuBr_2$/Me_6TREN in NMP (C_{Cu} = 3.75 mg mL^{-1}; $CuBr_2$: 2.90 mg, 1.3 x 10^{-2} mmol, 0.065 eq.; Me_6TREN: 3.14 mg, 1.4 x 10^{-2} mmol, 0.068 eq.). The total polymerization volume was kept to 7.3 mL of solvent. The mixture was stirred at room temperature for 10 minutes to allow all reagents to fully dissolve. A 10 cm piece of 18 gauge copper (0) wire was soaked in concentrated HCl for 15 minutes to remove surface impurities, then washed with water followed by acetone, dried *in vacuo* and taken into the glovebox. The wire was added to the mixture to initiate the polymerization. Each hour a 25 µL aliquot was taken and diluted with $CDCl_3$, and the conversion monitored by ^{1}H NMR. At approximately 50 % conversion, the polymerization was quenched by addition of water followed by filtration. The polymer was taken up in CH_2Cl_2, dried over $MgSO_4$ and concentrated *in vacuo*. The residue was purified by preparatory SEC (Bio-Rad Bio-Beads S-X1 Support) in THF and fractions containing polymer were determined by SEC analysis. All fractions containing polymer were collected and dried *in vacuo* overnight. Yield = 950 mg.

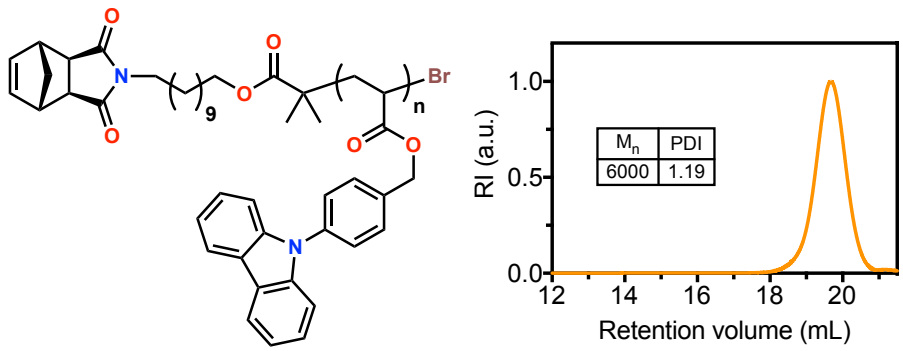

Synthesis of CzBA-MM by Cu(0)-RDRP:

In a nitrogen atmosphere glovebox, to a 20 mL vial capped with a Teflon-lined lid and equipped with a magnetic stir bar was added **2.5d** (2.00 g, 6.1 mmol, 30.5 eq.), 1.93 mL of a solution of **3.4** in NMP (C_{S2} = 50 mg mL^{-1}; **3.4**: 96.5 mg, 0.20 mmol, 1 eq.), and 775.0 µL of a solution of $CuBr_2$/Me_6TREN in NMP (C_{Cu} = 3.75 mg mL^{-1}; $CuBr_2$: 2.90 mg, 1.3 x 10^{-2} mmol, 0.065 eq.; Me_6TREN: 3.14 mg, 1.4 x 10^{-2} mmol, 0.068 eq.). The total polymerization volume was kept to 9.2 mL of solvent. The mixture was stirred at room temperature for 10 minutes to allow all reagents to fully dissolve. A 10 cm piece of 18 gauge copper (0) wire was soaked in concentrated HCl for 15 minutes to remove surface impurities, then washed with water followed by acetone, dried *in vacuo* and taken into the glovebox. The wire was added to the mixture to initiate the polymerization. Each hour a 25 µL aliquot was taken and diluted with $CDCl_3$, and the conversion monitored by ^{1}H NMR. At approximately 50 % conversion, the polymerization was quenched by addition of water followed by filtration. The polymer was taken up in CH_2Cl_2, dried over $MgSO_4$ and concentrated *in vacuo*. The residue was purified by preparatory SEC (Bio-Rad Bio-Beads S-X1 Support) in THF and fractions containing polymer were determined by SEC analysis. All fractions containing polymer were collected and dried *in vacuo* overnight. Yield = 753 mg.

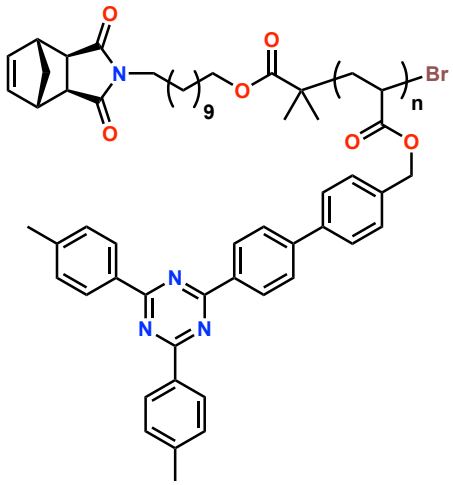

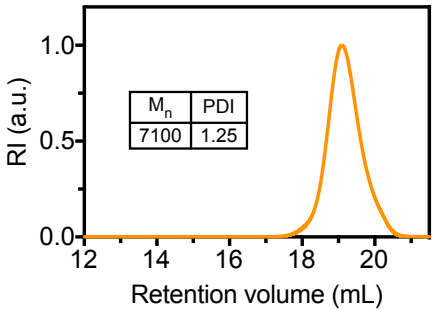

Synthesis of ETL-MM by Cu(0)-RDRP:

In a nitrogen atmosphere glovebox, to a 40 mL vial capped with a Teflon-lined lid and equipped with a magnetic stir bar was added **3.1** (2.00 g, 4.0 mmol, 20 eq.), 1.93 mL of a solution of **3.4** in NMP (C_{S2} = 50 mg mL^{-1}; **3.4**: 96.5 mg, 0.20 mmol, 1 eq.), and 775.0 µL of a solution of $CuBr_2$/Me_6TREN in NMP (C_{Cu} = 3.75 mg mL^{-1}; $CuBr_2$: 2.90 mg, 1.3 x 10^{-2} mmol, 0.065 eq.; Me_6TREN: 3.14 mg, 1.4 x 10^{-2} mmol, 0.068 eq.). The total polymerization volume was kept to 17.3 mL of solvent. The mixture was stirred at room temperature for 10 minutes to allow reagents to dissolve, however the polymerization can be initiated before all **3.1** is in solution. A 20 cm piece of 18 gauge copper (0) wire was soaked in concentrated HCl for 15 minutes to remove surface impurities, then washed with water followed by acetone, dried *in vacuo* and taken into the glovebox. The wire was added to the mixture to initiate the polymerization. Each hour a 25 µL aliquot was taken and diluted with $CDCl_3$, and the conversion monitored by ^{1}H NMR. At approximately 50 % conversion, the polymerization was quenched by addition of water followed by filtration. The polymer was taken up in CH_2Cl_2, dried over $MgSO_4$ and concentrated *in vacuo*. The residue was purified by preparatory SEC (Bio-Rad Bio-Beads S-X1 Support) in THF and

fractions containing polymer were determined by SEC analysis. All fractions containing polymer were collected and dried *in vacuo* overnight. Yield = 973 mg.

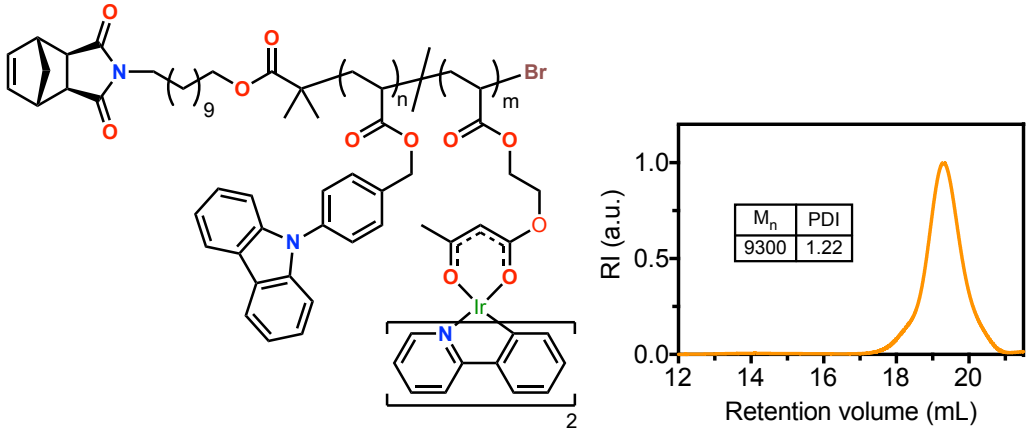

Synthesis of IrPPY-MM by Cu(0)-RDRP:

In a nitrogen atmosphere glovebox, to a 20 mL vial capped with a Teflon-lined lid and equipped with a magnetic stir bar was added **2.5d** (920 mg, 2.8 mmol, 40 eq.), **3.2** (80 mg, 0.114 mmol, 1.1 eq.), 0.966 mL of a solution of **3.4** in NMP (C_{S2} = 50 mg mL^{-1}; **3.4**: 48.3 mg, 0.10 mmol, 1 eq.), and 390.0 µL of a solution of $CuBr_2$/Me_6TREN in NMP (C_{Cu} = 3.75 mg mL^{-1}; $CuBr_2$: 1.45 mg, 6.5 x 10^{-3} mmol, 0.065 eq.; Me_6TREN: 1.5 mg, 6.8 x 10^{-3} mmol, 0.068 eq.). The total polymerization volume was kept to 4.6 mL of solvent. The mixture was stirred at room temperature for 10 minutes to allow all reagents to fully dissolve. A 5 cm piece of 18 gauge copper (0) wire was soaked in concentrated HCl for 15 minutes to remove surface impurities, then washed with water followed by acetone, dried *in vacuo* and taken into the glovebox. The wire was added to the mixture to initiate the polymerization. Each hour a 25 µL aliquot was taken and diluted with $CDCl_3$, and the conversion monitored by ^{1}H NMR. At approximately 60 % conversion, the polymerization was quenched by addition of water followed by filtration. The polymer was taken up in CH_2Cl_2, dried over $MgSO_4$ and concentrated *in vacuo*. The residue was purified by

preparatory SEC (Bio-Rad Bio-Beads S-X1 Support) in THF and fractions containing polymer were determined by SEC analysis. All fractions containing polymer were collected and dried *in vacuo* overnight. Yield = 500 mg.

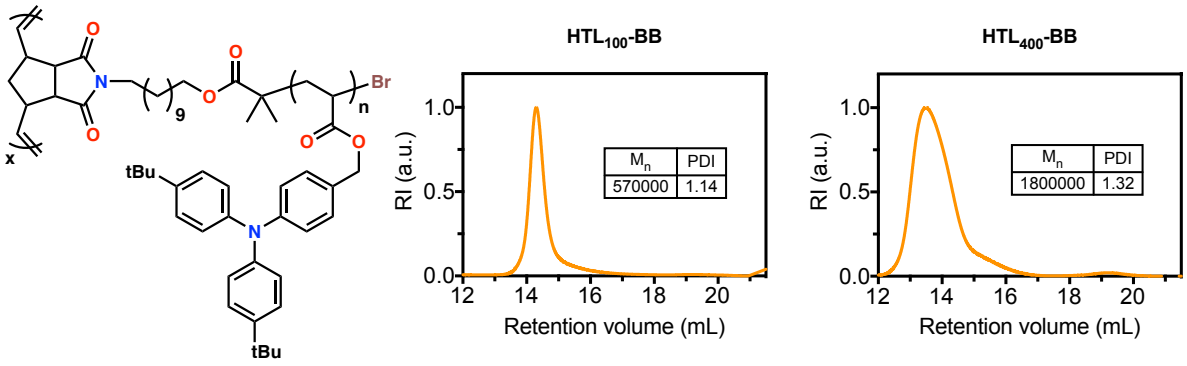

Synthesis of tBuHTL$_{100}$-BB by ROMP:

In a nitrogen atmosphere glovebox, to a 2 mL vial capped with a Teflon-lined lid and equipped with a magnetic stir bar was added **tBuHTL-MM** (100 mg, 1.6 x 10^{-2} mmol, 100 eq.) and 400 µL of THF (dry, degassed, filtered through basic alumina). Using a glass microsyringe 28 µL of a solution of **1.3** in THF ($C_{1.3}$ = 4 mg mL^{-1}; **1.3**: 0.11 mg, 1.3 x 10^{-4} mmol, 1 eq.) was added to the dissolved polymer rapidly in one portion. The mixture was stirred at room temperature for 1 h. Two 5 µL aliquots were taken for ^{1}H NMR and SEC analysis, and the polymerization was removed from the glove box, quenched with one drop of ethyl vinyl ether, and immediately purified by preparatory SEC (Toyopearl HW-55F resin) in THF and fractions containing polymer were determined by SEC analysis. All fractions containing polymer were collected and dried *in vacuo* overnight. Yield = 64 mg.

Synthesis of tBuHTL$_{400}$-BB by ROMP:

Prepared as above, using $C_{1.3}$ = 1 mg mL^{-1}. Yield = 43 mg.

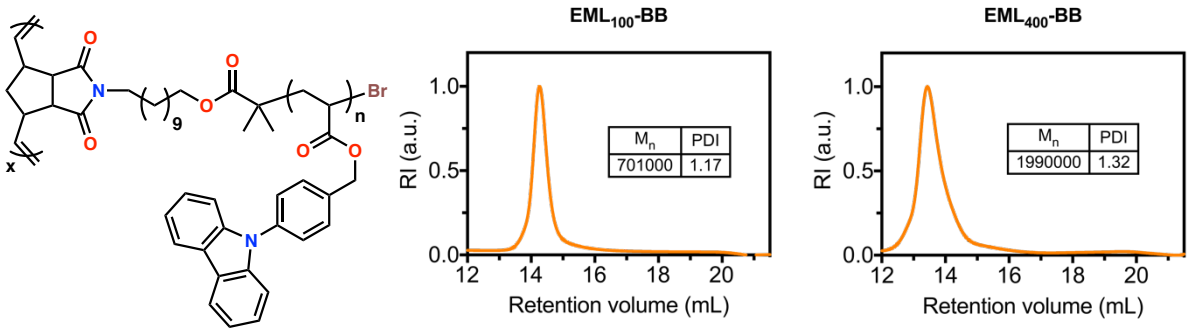

Synthesis of $CzBA_{100}$-BB by ROMP:

In a nitrogen atmosphere glovebox, to a 2 mL vial capped with a Teflon-lined lid and equipped with a magnetic stir bar was added **CzBA-MM** (75 mg, 1.3 x 10^{-2} mmol, 100 eq.) and 187.5 µL of THF (dry, degassed, filtered through basic alumina). Using a glass microsyringe 23 µL of a solution of **1.3** in THF ($C_{\mathbf{1.3}}$ = 4 mg mL^{-1}; **1.3**: 0.092 mg, 1.3 x 10^{-4} mmol, 1 eq.) was added to the dissolved polymer rapidly in one portion. The mixture was stirred at room temperature for 1 h. Two 5 µL aliquots were taken for ^{1}H NMR and SEC analysis, and the polymerization was removed from the glove box, quenched with one drop of ethyl vinyl ether, and immediately purified by preparatory SEC (Toyopearl HW-55F resin) in THF and fractions containing polymer were determined by SEC analysis. All fractions containing polymer were collected and dried *in vacuo* overnight. Yield = 57 mg.

Synthesis of $CzBA_{400}$-BB by ROMP:

Prepared as above, using $C_{\mathbf{1.3}}$ = 1 mg mL^{-1}. Yield = 52 mg.

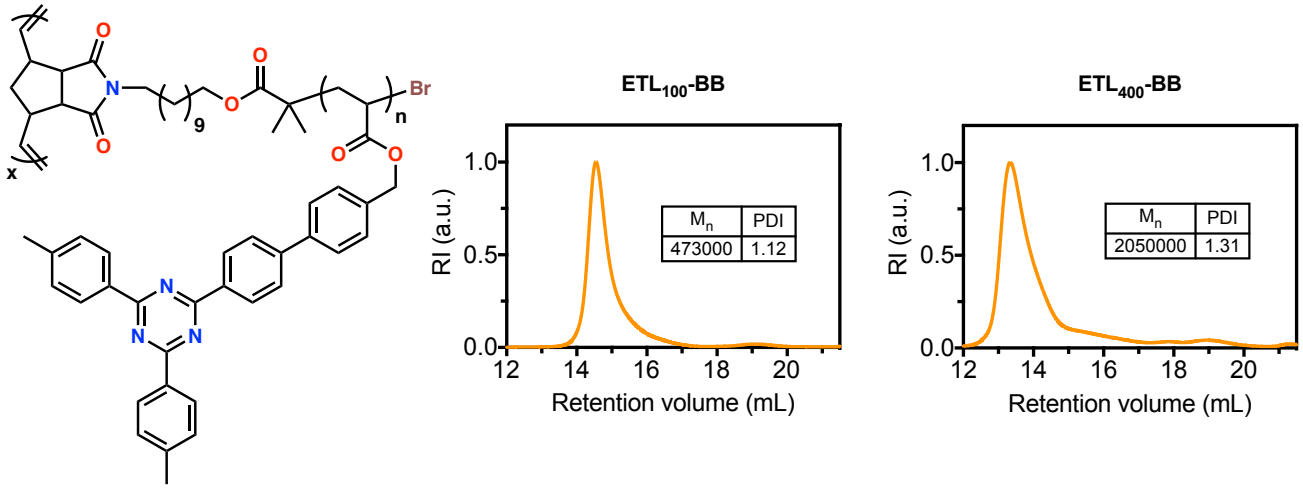

Synthesis of ETL_{100}-BB by ROMP:

In a nitrogen atmosphere glovebox, to a 2 mL vial capped with a Teflon-lined lid and equipped with a magnetic stir bar was added **ETL-MM** (100 mg, 1.4 x 10^{-2} mmol, 100 eq.) and 500 µL of THF (dry, degassed, filtered through basic alumina). Using a glass microsyringe 26 µL of a solution of **1.3** in THF ($C_{\mathbf{1.3}}$ = 4 mg mL^{-1}; **1.3**: 0.10 mg, 1.4 x 10^{-4} mmol, 1 eq.) was added to the dissolved polymer rapidly in one portion. The mixture was stirred at room temperature for 1 h. Two 5 µL aliquots were taken for ^{1}H NMR and SEC analysis, and the polymerization was removed from the glove box, quenched with one drop of ethyl vinyl ether, and immediately purified by preparatory SEC (Toyopearl HW-55F resin) in THF and fractions containing polymer were determined by SEC analysis. All fractions containing polymer were collected and dried *in vacuo* overnight. Yield = 41 mg.

Synthesis of ETL_{400}-BB by ROMP:

Prepared as above, using $C_{\mathbf{1.3}}$ = 1 mg mL^{-1}. Yield = 20 mg.

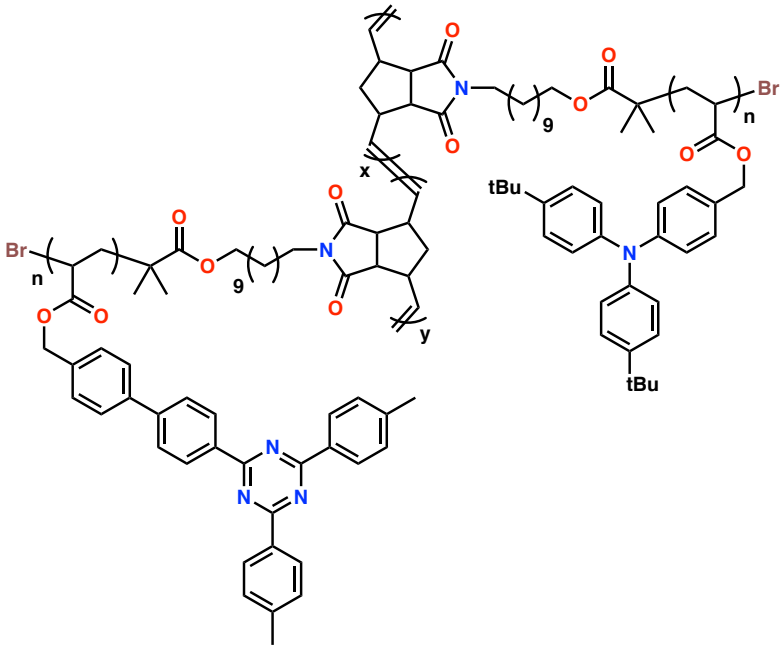

Synthesis of (tBuHTL$_{75}$-*b*-ETL$_{75}$)-BB by ROMP:

In a nitrogen atmosphere glovebox, to a 2 mL vial capped with a Teflon-lined lid and equipped with a magnetic stir bar was added **ETL-MM** (50 mg, 7.0 x 10^{-3} mmol, 75 eq.) and 250 µL of THF (dry, degassed, filtered through basic alumina). Using a glass microsyringe 34 µL of a solution of **1.3** in THF ($C_{1.3}$ = 2 mg mL^{-1}; **1.3**: 0.07 mg, 9.3 x 10^{-5} mmol, 1 eq.) was added to the dissolved polymer rapidly in one portion. The mixture was stirred at room temperature for 1 h. Two 5 µL aliquots were taken for ^{1}H NMR and SEC analysis, before addition of **tBuHTL-MM** (47 mg, 7.0 x 10^{-3} mmol, 75 eq.) dissolved in 250 µL of THF. The mixture was stirred at room temperature for an additional 1 h. Two 5 µL aliquots were taken for ^{1}H NMR and SEC analysis, and the polymerization was removed from the glove box, quenched with one drop of ethyl vinyl ether, and immediately purified by preparatory SEC (Toyopearl HW-55F resin) in THF and fractions containing polymer were determined by SEC analysis. All fractions containing polymer were collected and dried *in vacuo* overnight. Yield = 60 mg.

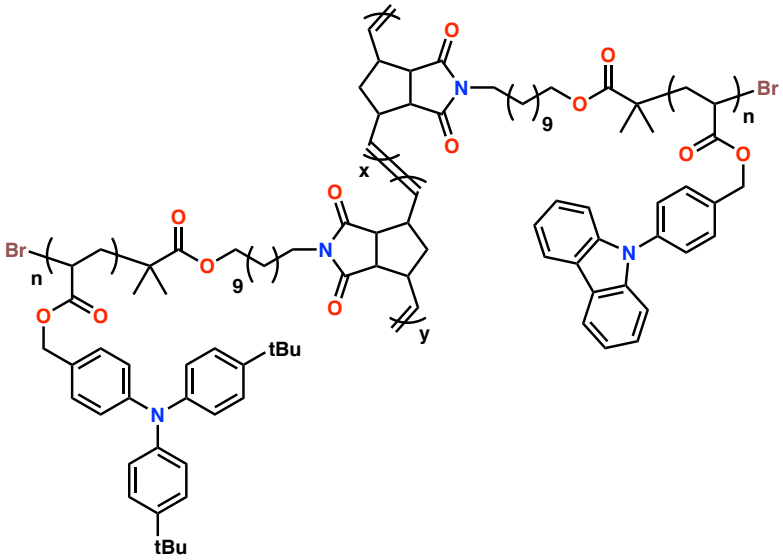

Synthesis of (CzBA$_{75}$-*b*-tBuHTL$_{75}$)-BB by ROMP:

In a nitrogen atmosphere glovebox, to a 2 mL vial capped with a Teflon-lined lid and equipped with a magnetic stir bar was added **CzBA-MM** (53 mg, 8.8 x 10^{-3} mmol, 75 eq.) and 250 µL of THF (dry, degassed, filtered through basic alumina). Using a glass microsyringe 44 µL of a solution of **1.3** in THF ($C_{\mathbf{1.3}}$ = 2 mg mL^{-1}; **1.3**: 0.09 mg, 1.2 x 10^{-4} mmol, 1 eq.) was added to the dissolved polymer rapidly in one portion. The mixture was stirred at room temperature for 1 h. Two 5 µL aliquots were taken for ^{1}H NMR and SEC analysis, before addition of **tBuHTL-MM** (59 mg, 8.8 x 10^{-3} mmol, 75 eq.) dissolved in 250 µL of THF. The mixture was stirred at room temperature for an additional 1 h. Two 5 µL aliquots were taken for ^{1}H NMR and SEC analysis, and the polymerization was removed from the glove box, quenched with one drop of ethyl vinyl ether, and immediately purified by preparatory SEC (Toyopearl HW-55F resin) in THF and fractions containing polymer were determined by SEC analysis. All fractions containing polymer were collected and dried *in vacuo* overnight. Yield = 62 mg.

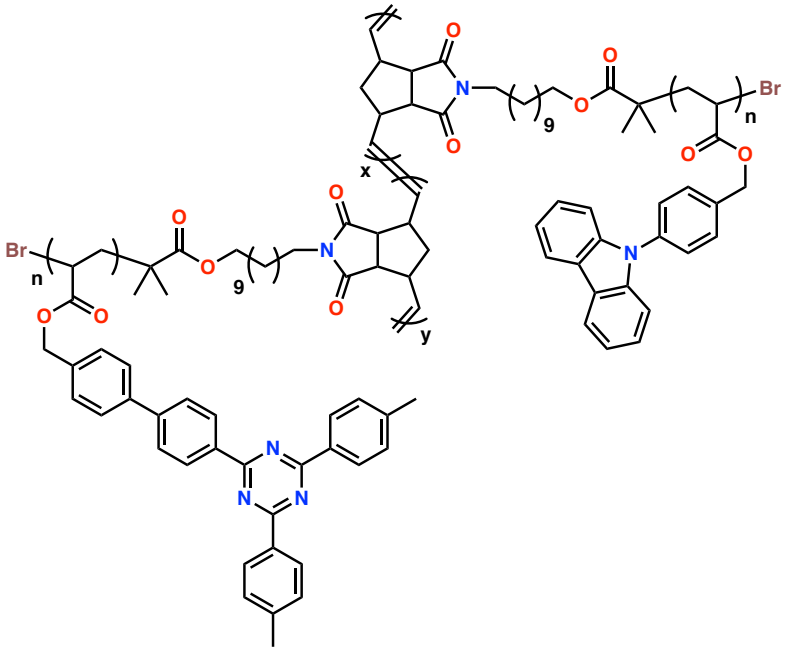

Synthesis of (CzBA$_{75}$-*b*-tBuHTL$_{75}$)-BB by ROMP:

In a nitrogen atmosphere glovebox, to a 2 mL vial capped with a Teflon-lined lid and equipped with a magnetic stir bar was added **CzBA-MM** (47 mg, 7.8 x 10^{-3} mmol, 75 eq.) and 250 µL of THF (dry, degassed, filtered through basic alumina). Using a glass microsyringe 40 µL of a solution of **1.3** in THF ($C_{1.3}$ = 2 mg mL^{-1}; **1.3**: 0.08 mg, 1.0 x 10^{-4} mmol, 1 eq.) was added to the dissolved polymer rapidly in one portion. The mixture was stirred at room temperature for 1 h. Two 5 µL aliquots were taken for ^{1}H NMR and SEC analysis, before addition of **ETL-MM** (55 mg, 7.8 x 10^{-3} mmol, 75 eq.) dissolved in 250 µL of THF. The mixture was stirred at room temperature for an additional 1 h. Two 5 µL aliquots were taken for ^{1}H NMR and SEC analysis, and the polymerization was removed from the glove box, quenched with one drop of ethyl vinyl ether, and immediately purified by preparatory SEC (Toyopearl HW-55F resin) in THF and fractions containing polymer were determined by SEC analysis. All fractions containing polymer were collected and dried *in vacuo* overnight. Yield = 63 mg.

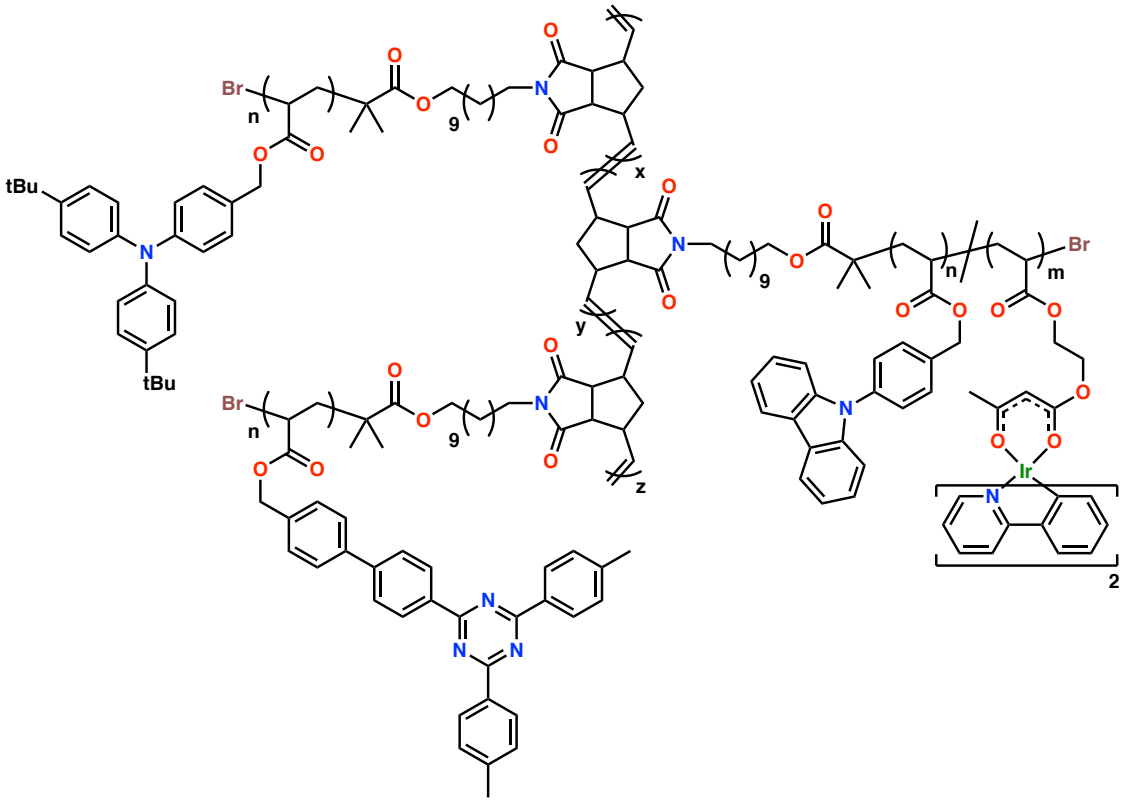

Synthesis of (ETL$_{50}$-*b*-IrPPY$_{30}$-*b*-tBuHTL$_{50}$)-BB by ROMP:

In a nitrogen atmosphere glovebox, to a 2 mL vial capped with a Teflon-lined lid and equipped with a magnetic stir bar was added **ETL-MM** (50 mg, 7.0 x 10^{-3} mmol, 50 eq.) and 250 µL of THF (dry, degassed, filtered through basic alumina). Using a glass microsyringe 26 µL of a solution of **1.3** in THF ($C_{1.3}$ = 4 mg mL^{-1}; **1.3**: 1.0 mg, 1.0 x 10^{-4} mmol, 1 eq.) was added to the dissolved polymer rapidly in one portion. The mixture was stirred at room temperature for 1 h. Two 5 µL aliquots were taken for ^{1}H NMR and SEC analysis, before addition of **IrPPY-MM** (40 mg, 4.3 x 10^{-3} mmol, 30 eq.) dissolved in 250 µL of THF. The mixture was stirred at room temperature for 1 h. Two 5 µL aliquots were taken for ^{1}H NMR and SEC analysis, before addition of **tBuHTL-MM** (47 mg, 7.0 x 10^{-3} mmol, 50 eq.) dissolved in 250 µL of THF. The mixture was

stirred at room temperature for an additional 1 h. Two 5 μL aliquots were taken for ^{1}H NMR and SEC analysis, the polymerization was removed from the glove box and quenched with one drop of ethyl vinyl ether. The polymer was collected and dried *in vacuo* overnight. Yield = 130 mg. 2.5 mg of this polymer was further purified for AFM analysis using the silylated Toyopearl HW-55F resin described below.

Silylation of HW-55F Resin:

To a 250 mL Erlenmeyer flask was added 50 mL of THF-saturated Toyopearl HW-55F resin followed by a further 50 mL of THF. Et_3N (0.80 g, 1.1 mL, 7.9 mmol) and trimethylsilyl chloride (0.86 g, 1 mL, 7.9 mmol) were then added sequentially with gentle mixing. The mixture was left to stand for 16 h, then transferred to a filtration funnel with glass frit and washed with 200 mL THF:EtOH (1:1 v/v) followed by 200 mL THF. This re-usable resin can then be used to purify **(ETL_{50}-*b*-$IrPPY_{30}$-*b*-$tBuHTL_{50}$)-BB** with no observed retention of the iridium complex.

Chapter 4: Aggregation-Induced Energy Transfer in Color-Tunable Multiblock Bottlebrush Nanofibers

4.1 Introduction

Achieving precise control over the assembly of soft materials into multifunctional nanostructures is critical to the discovery of both new phenomena and new applications in nanotechnology. Advancements in self-assembly have led to many impressive examples of each, offering ever-increasing control over nanoparticle shape and composition. Techniques such as crystallization-driven self-assembly (CDSA),[3,14,21,29,208] living supramolecular polymerization,[32,210] and hierarchical solution self-assembly (HSSA)[8,19,81,211,237] offer routes to complex morphologies such as multicompartment spheres,[40,213] scarf-like nanoribbons,[5,6] and supramolecular block copolymers,[35,37–39,238] leveraging low-cost solution processing under ambient conditions. Furthermore, studying such structures has led to the discovery of entirely new phenomena, such as long-range exciton transport through self-assembled nanowires,[18] the use of hydrogel actuators as photonic crystals,[239] or the control of living self-assembly using light.[208] As the complexity and order of nanomaterials prepared by self-assembly improves, the range of applications they can address will only continue to grow.

However, self-assembly approaches for the fabrication of nanomaterials commonly encounter several limitations and addressing these would substantially broaden the potential applications of soft-matter nanotechnology. For instance, the self-assembly of non-centrosymmetric nano-objects with anisotropic shapes remains a significant challenge, despite being entirely routine in molecular synthesis.[240] In addition, many self-assembly methods require building blocks with precisely tuned solvophilicity, crystallinity, or hydrogen-bonding to function,

limiting the scope of nanomaterials that can be prepared in these ways. Finally, self-assembled structures must often be kept within specific temperatures or solvation environments to hold their shapes, losing order or disassembling entirely if these conditions are not maintained. While some of these challenges can be overcome with post-assembly treatments such as chemical crosslinking,[14,241,242] methods for preparing robust, precise, and multifunctional nanostructures from general building blocks remain highly sought after.

Bottom-up approaches to nanomaterials based on covalent chemistry are ideally suited to this goal, and benefit from the use of large building blocks when designing materials with well-defined nanoscale domains. Bottlebrush copolymers (BBCPs) are one example of such an architecture, whereby polymeric side-chains are attached covalently to a linear backbone.[41,58,62,65] Due to the steric demands of the side chains, BBCPs occupy a relatively low-entropy conformational space, adopting extended conformations that limit chain entanglement in solution and the solid state.[55,56] As a result, they have emerged as unique nanostructures with controllable size, shape and function, with molecular weights for individual bottlebrushes commonly exceeding 10^6 Da. Due to their unique morphology, these materials have found numerous applications in photonic crystals,[68,214,243,244] templating,[216,245,246] and nanomedicine.[74–76,219,247] Their block-by-block synthesis allows for the preparation of multicompartment structures that remain segregated on the nanoscale, regardless of solvent or temperature. Furthermore, polymer growth in a single direction provides a convenient route to non-centrosymmetric structures with significant shape anisotropy, without the need for additional crosslinking steps.[14,240]

Using BBCPs as a platform, we described in Chapter 3 that it is possible to prepare nanofibers that mimic the structure of multilayer organic electronic devices on single polymer chains.[248] This approach was used to access nanofibers analogous to organic p−n junctions, as well

as phosphorescent organic light emitting diodes (OLEDs) in which the photophysical properties of each organic semiconductor component could be independently observed. This versatile method now allows us to prepare multicomponent nanofibers with improved complexity, as well as to study how optoelectronic functions interact between and within bottlebrush polymer blocks.

The organization of chromophores into supramolecular and nanoscale structures is critical to enabling the energy and electron-transfer processes found in light-harvesting systems in Nature.[249–251] We reasoned that the well-defined interfaces in BBCPs could not only be used to prepare nanofibers with tunable optoelectronic segments, but also to regulate energy transfer processes between these segments as a function of chain collapse. By installing chromophores in discrete blocks along the length of a bottlebrush nanofiber, these chromophores can be kept outside their Förster distances when the bottlebrush is dissolved and the individual domains are free to expand. When the BBCPs are aggregated by changing the polarity of the solvent, Förster resonance energy transfer (FRET) can be observed with significant accompanying colour change. By combining fluorescent and phosphorescent chromophores on a single bottlebrush, this aggregation-induced energy transfer can be further enhanced, as well as time-resolved.

Herein we prepare a series of bottlebrush copolymers from red, green and blue luminescent macromonomers using a carbazole-based host. These building blocks are then combined to give diblock and triblock luminescent BBCPs, which show aggregation-induced changes in energy transfer from one block to another as the solvent polarity is varied. We then quantify these changes in energy transfer efficiency and inter-chromophore distance upon aggregation and demonstrate that these phenomena can be used to produce solvent-responsive luminescent encoded patterns. Finally, we combine these emissive macromonomers with hole transport and electron transport materials to give pentablock nanofibers mimicking the structure of white light-emitting diodes

with multiple discrete emission zones. This work describes the preparation of robust, ordered nanofibers from up to six distinct optoelectronic materials, combining their properties in ways that can be both reversibly switched and temporally resolved.

4.2 Results and Discussion

We first prepared red, green and blue emissive macromonomers **IrPIQ-MM**, **IrPPY-MM**, and **tBuODA-MM** based on commonly used two-component emissive layers for OLEDs. Using a norbornene-functionalized initiator and a carbazole-based acrylic monomer (**CzBA**) as host material, copolymerization with 8 wt% of emissive material gave macromonomers with tunable colour by Cu(0)-RDRP[105,106,108,182,232] (Figure 4.1). Acrylic monomers based on $Ir(ppy)_2(acac)$, $Ir(piq)_2(acac)$, and the donor-acceptor material 4-(5-([1,1'-biphenyl]-4-yl)-1,3,4-oxadiazol-2-yl)-*N,N*-di-*p*-tolylaniline were used to provide the green, red, and blue macromonomers, respectively (ppy = 2-phenylpyridine, piq = 2-phenylisoquinoline).

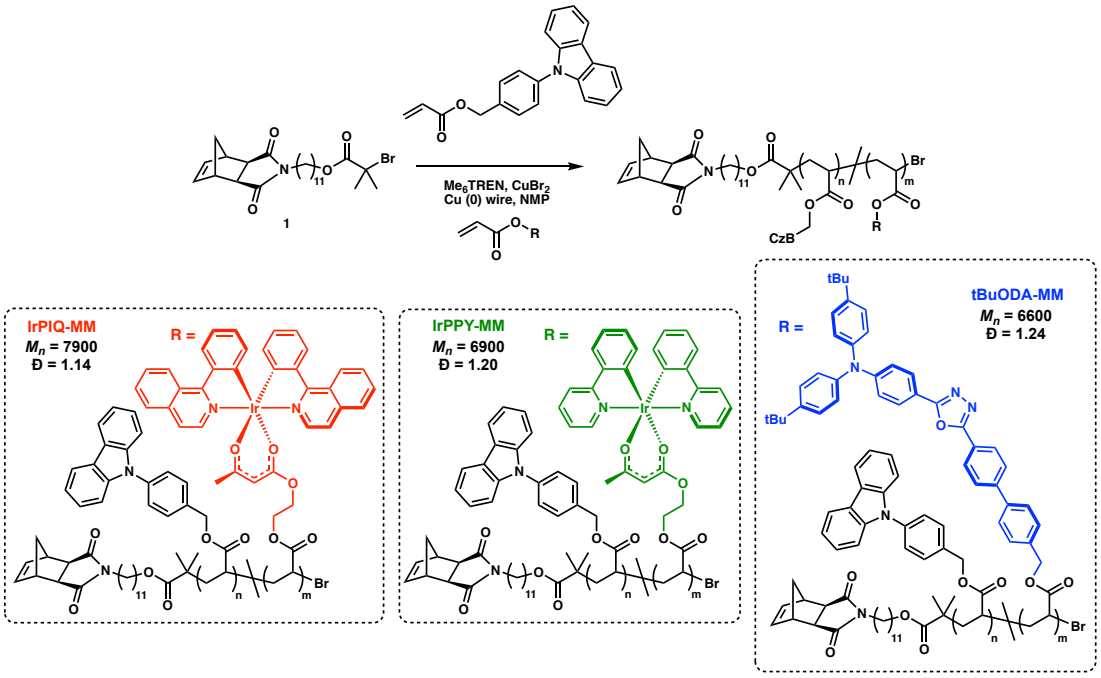

Figure 4.1. Synthesis of red, green and blue emissive norbornene-functionalized macromonomers by Cu(0)-RDRP. CzB = *p*-(*N*-carbazolyl) benzyl. NMP = *N*-methyl-2-pyrrolidone.

We then used grafting-through ring-opening metathesis polymerization (ROMP)[236,252,253] to give bottlebrush polymers with backbone degrees of polymerization of 150. The resulting polymers showed molecular weights between 0.8–1.1 × 10^6 Da with dispersities as low as 1.14. Residual macromomomer was completely removed from these mixtures by passing the products over a reusable methacrylic resin (silylated HW-55F resin, *vide infra*) in THF. Atomic force microscopy (AFM) images of each bottlebrush prepared on an HOPG substrate are shown in Figure 4.2, and fiber-like morphologies approximately 100 nm in length can be seen in each case. All bottlebrushes are photoluminescent with emission maxima of 448, 516, and 624 nm, and Commission internationale de l'eclairage (CIE) 1931 coordinates of (0.16, 0.14), (0.30, 0.62), and (0.66, 0.33). Quantum yields of 0.84, 0.21, and 0.28 (thin films) for **tBuODA**$_{150}$**-BB**, **IrPPY**$_{150}$**-BB**, and **IrPIQ**$_{150}$**-BB** were measured, in agreement with the photophysical properties of their

respective linear homopolymers.[183,254] Per the naming conventions used in this chapter, the suffix -BB denotes that the polymer in question is a bottlebrush, with the subscript indicating the target backbone degree of polymerization.

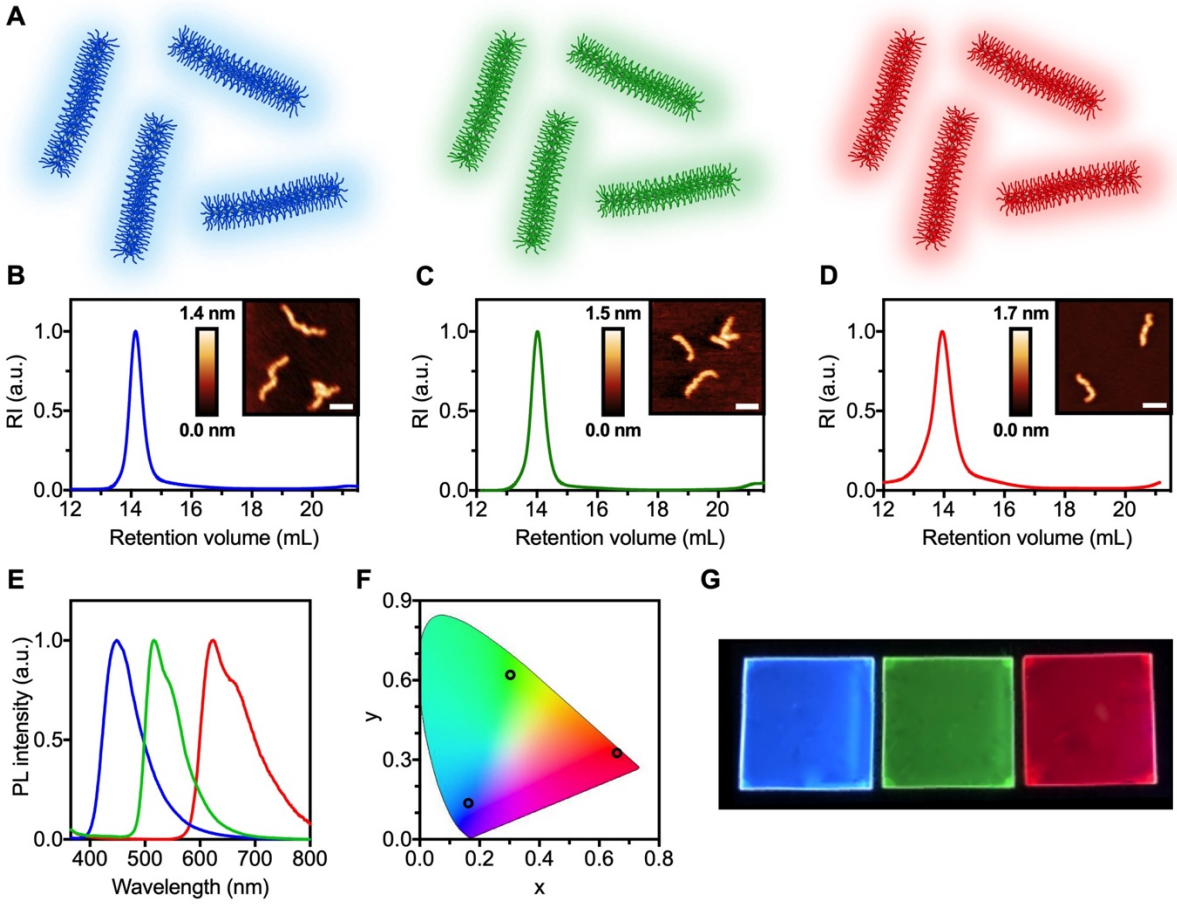

Figure 4.2. a) Schematic illustrations of luminescent bottlebrush polymers. b-d) SEC chromatograms after purification. Inset: AFM height images on HOPG (scale bar = 50 nm). e) Solid state PL spectra, f) CIE 1931chromaticity diagram g) photo of bottlebrush films spin cast on quartz substrates irradiated with 254 nm light. a-g): blue = **tBuODA$_{150}$-BB**, green = **IrPPY$_{150}$-BB,** red = **IrPIQ$_{150}$-BB.**

Table 4.1. Synthesis of bottlebrush polymers.

Entry[a]	M_n, B1[b] (kDa)	DP_n B1[b]	DP_n B2[c]	DP_n B3[c]	$M_{n,total}$ [e] (kDa)	$M_{n,theory}$[a] (kDa)	Đ [b]	Conv. (%)[b]
IrPPY$_{150}$-BB	1040	150	--	--	--	1035	1.20	85
IrPIQ$_{150}$-BB	1100[d]	148[d]	--	--	--	1110	1.39	83
tBuODA$_{150}$-BB	823	125	--	--	--	990	1.17	81
IrPPY$_{100}$-*b*-IrPIQ$_{50}$-BB	460	67	46	--	800	1060	1.14	77
tBuODA$_{75}$-*b*-IrPPY$_{75}$-BB	375	57	59	--	782	1013	1.27	81
tBuODA$_{60}$-*b*-IrPIQ$_{90}$-BB	327	50	77	--	897	1062	1.29	81
tBuODA$_{50}$-*b*-IrPPY$_{50}$-*b*-IrPIQ$_{50}$-BB	231	35	41	41	817	1045	1.29	80

[a]Sample names and listed $M_{n,theory}$ values refer to the theoretical degree of polymerization (DP_n) rather than measured values.
[b] Determined by SEC in THF using triple detection.
[c] Determined by ^{1}H NMR.
[d] Determined by SEC in THF using conventional calibration with **CzBA** standards.[183] Using polystyrene standards, M_n = 237 kDa, DP_n = 62.
[e] Determined by ^{1}H NMR using the degree of polymerization determined for the first block by SEC. B1, B2, B3 = first, second, and third block added. DP_n = degree of polymerization of poly(norbornene) backbone.

Using this grafting-through synthetic strategy, diblock copolymers were then synthesized to give **tBuODA$_{75}$-IrPPY$_{75}$-BB**, **tBuODA$_{60}$-IrPIQ$_{90}$-BB**, and **IrPPY$_{100}$-IrPIQ$_{50}$-BB**, with block ratios chosen to give colours intermediate between the two constituent homopolymers. Incorporating these chromophores along a single BBCP gives two-color structures with a well-defined interface between emission zones, the interaction of which can be controlled by solvent polarity. In dilute solutions of THF, both **tBuODA$_{75}$-IrPPY$_{75}$-BB** and **tBuODA$_{60}$-IrPIQ$_{90}$-BB** exhibit strong blue fluorescence, with minimal emission from the iridium components. As the fraction of water (f_w) in the solution increases from 0 to 98%, phosphorescence from the red and green iridium chromophores increase substantially, with an accompanying decrease in blue fluorescence (Figure 4.3). It should be noted that all materials containing a **tBuODA** block first experience a mild polarity-induced solvatochromatic red shift at low water fraction, consistent

with the charge-transfer character of the **tBuODA** dye. Based on DLS data from **tBuODA$_{75}$-IrPPY$_{75}$-BB** (Figure 4.4), it appears that as the solvent polarity increases, the polymer arms begin to collapse, initiating the formation of small aggregates with approximately 50-100 nm radii, dramatically improving the efficiency of energy transfer from both the **CzBA** host and the blue fluorophore to the iridium-based emitters. The diblock BBCP **IrPPY$_{100}$-IrPIQ$_{50}$-BB** diblock does not experience significant changes in chromaticity upon aggregation, as the intensity of emission is low from both iridium chromophores initially, and increase concomitantly upon aggregation. Finally, we prepared a triblock BBCP containing each of the blue, green and red emitters, giving a structure analogous to an RGB pixel on individual nanofibers (Figure 4.3G-I). Additionally, we determined the polar vectors along which the CIE changes occur (Figure 4.3B,E,H) for each of **tBuODA$_{100}$-IrPPY$_{50}$-BB**, **tBuODA$_{60}$-IrPIQ$_{90}$-BB**, and **tBuODA$_{50}$-IrPPY$_{50}$-IrPIQ$_{50}$-BB**. While the magnitudes of the changes in each case are similar, the angle of these vectors show that the colour change of the triblock lies between that for each of **tBuODA$_{60}$-IrPIQ$_{90}$-BB** and **tBuODA$_{75}$-IrPPY$_{75}$-BB**.

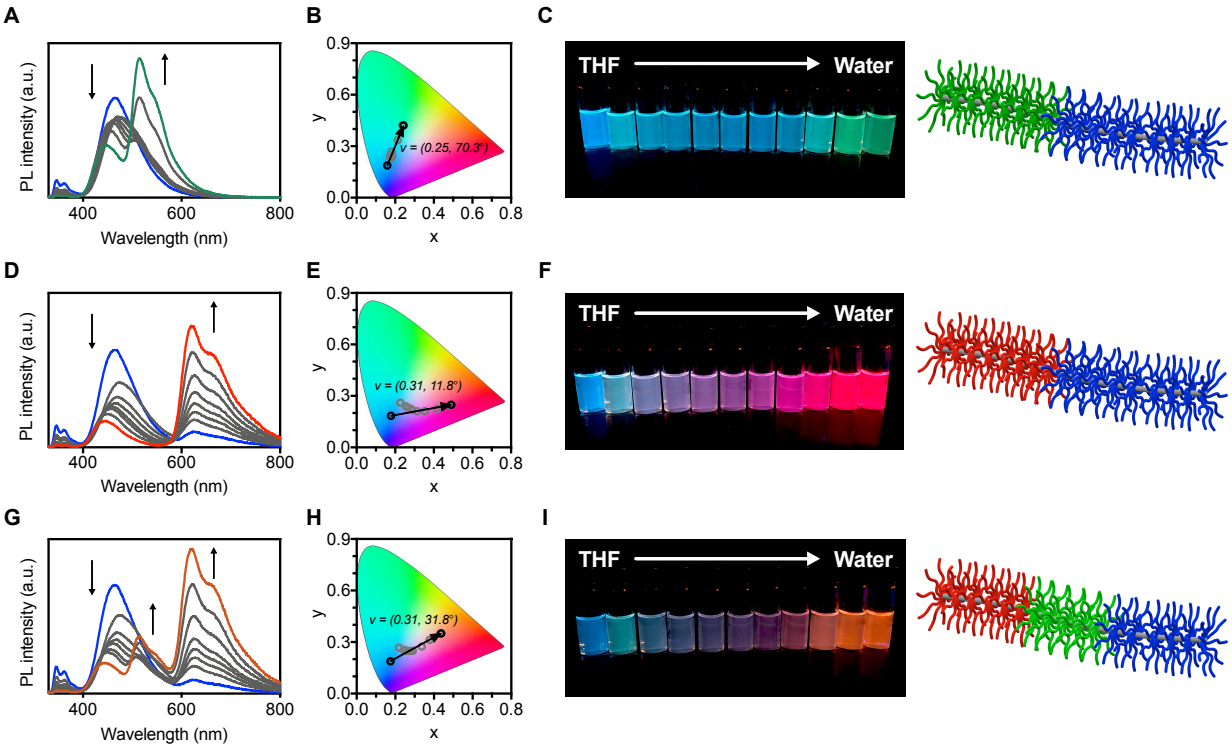

Figure 4.3. PL spectra, chromaticity coordinates, and photographs of 0.01 mg mL^{-1} solutions of **tBuODA$_{100}$-IrPPY$_{50}$-BB** (a-c), **tBuODA$_{60}$-IrPIQ$_{90}$-BB** (d-f), and **tBuODA$_{50}$-IrPPY$_{50}$-IrPIQ$_{50}$-BB** (g-i), with f_w increasing from 0% (blue line) in 10% increments up to 98% (green/red line). λ_{ex} = 365 nm.

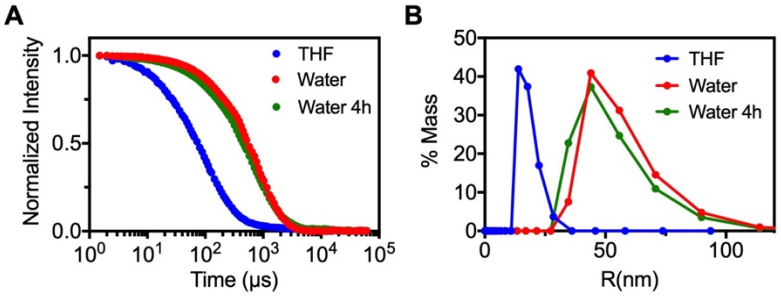

Figure 4.4. Dynamic light scattering data for **tBuODA$_{75}$-*b*-IrPPY$_{75}$-BB** A) autocorrelation function b) plot of Z-average size distribution. The formation of relatively small aggregates can be observed.

These data also present opportunities to study energy transfer processes in these luminescent nanofibers, as well as to quantify how these processes change as a function of aggregation. First, the FRET efficiency for energy transfer *E* from the **CzBA** host to the dopant in each of the **tBuODA**$_{150}$**-BB**, **IrPPY**$_{150}$**-BB**, and **IrPIQ**$_{150}$**-BB** bottlebrushes can be calculated based on equation (1), where F_D' and F_D are the fluorescence intensities of the **CzBA** host with and without an acceptor respectively.

$$E = 1 - \frac{F_D'}{F_D} \tag{1}$$

F_D was measured from the emission spectrum of a homopolymer bottlebrush **CzBA-BB** sythesized previously,[248] at equal concentrations of **CzBA** chromophores (0.01 mg mL^{-1}) and with identical instrument parameters. The donor-acceptor separation distance r and the Förster distance R_0 in each bottlebrush can also be calculated from equations (2) and (3),[255] where κ is the dipole-dipole orientation factor, and Q_D is the quantum yield of the energy donor in the absence of transfer. *J(λ)* is the spectral overlap integral as calculated from equation (4), where $\overline{F_D}$ is the donor emission spectrum normalized to an area of 1, ε_A is the acceptor molar extinction coefficient, and *n* is the refractive index of the solvent.

$$E = \frac{1}{1 + (r/R_0)^6} \tag{2}$$

$$R_0{}^6 = 9.79 \times 10^3 \frac{\kappa^2 Q_D}{n^4} J(\lambda) \tag{3}$$

$$J(\lambda) = \int \overline{F_D}(\lambda)\varepsilon_A(\lambda)\lambda^4 d\lambda \tag{4}$$

For the **tBuODA**$_{150}$**-BB**, **IrPPY**$_{150}$**-BB**, and **IrPIQ**$_{150}$**-BB** bottlebrushes, Q_D = 0.25, n = 1.4, and *J(λ)* was found to be 2.43 × 10^{-14}, 9.45 × 10^{-15}, and 2.50 × 10^{-14} cm^6 mmol^{-1} respectively. κ^2 was

assumed to be 2/3 based on rapid rotational relaxation of the chromophores along the bottlebrush side chains.[255] For these parameters, R_0 was calculated to be 21.3, 18.2 and 21.4 Å, respectively in THF (Figure 4.5a-c). Finally, the rate of energy transfer k_{ET} from **CzBA** to each dopant was calculated based on equation (5) where $k_f + \sum k_i$ was determined from the inverse lifetime of the **CzBA-BB**.

$$E = \frac{k_{ET}}{k_f + k_{ET} + \sum k_i} \tag{5}$$

With detailed data regarding energy transfer in each of the single-emitter bottlebrush nanofibers, it is possible to characterize the energy transfer processes in multichromophore bottlebrushes in detail. Given the good spectral separation between the emission profiles of the **tBuODA** and **IrPIQ** emitters, the **tBuODA**$_{60}$**-IrPIQ**$_{90}$**-BB** system is ideally suited to this quantification (Figure 4.5d-f). It was found that in dilute solutions of THF there is no observable energy transfer from the **tBuODA** emitter to the **IrPIQ** emitter. As the fraction of water in the solution was increased from 0 to 98% however, the energy transfer efficiency increased, with $r = R_0$ at $f_w = 0.5$, and E reaching a final value of 81% at $f_w = 0.98$. In a similar fashion, energy transfer efficiency from the **IrPPY** emitter to the **IrPIQ** emitter in **IrPPY**$_{100}$**-IrPIQ**$_{50}$**-BB** was found to increase from approximately 0 to 60%. Energy transfer efficiencies could not readily be obtained for **tBuODA**$_{75}$**-IrPPY**$_{75}$**-BB** due to the extensive spectral overlap of the **tBuODA** and **IrPPY** emission profiles.

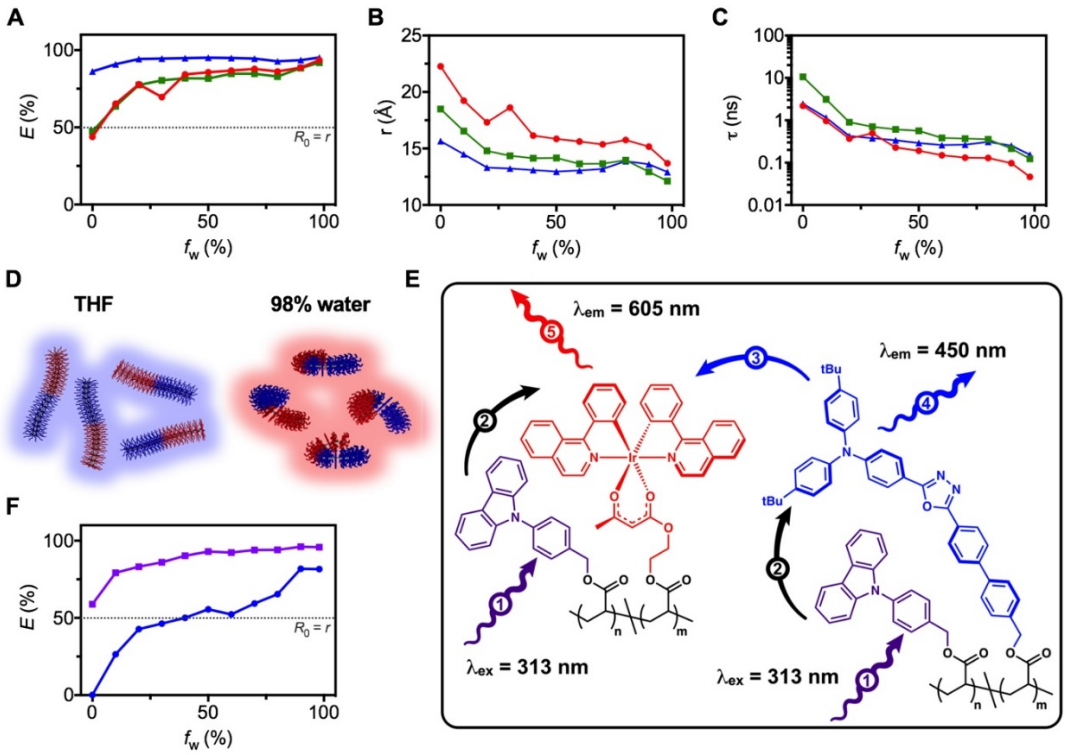

Figure 4.5. a) Energy transfer (ET) efficiency b) inter-chromophore distance, and c) rate of energy transfer as a function of f_w for **tBuODA**$_{150}$**-BB** (blue), **IrPPY**$_{150}$**-BB** (green), and **IrPIQ**$_{150}$**-BB** (red)**.** d) Schematic representation of **tBuODA**$_{60}$**-IrPIQ**$_{90}$**-BB** dissolved in THF (left) and aggregated in 98% water (right). e) ET processes in **tBuODA**$_{60}$**-IrPIQ**$_{90}$**-BB,** where (1) is photoexcitation of **CzBA**, (2) is ET from **CzBA** to **tBuODA** and **IrPIQ**, (3) is ET from **tBuODA** to **IrPIQ**, (4) is PL of **tBuODA**, and (5) is PL of **IrPIQ**. f) ET efficiency vs. f_w for the **CzBA** host to both dopants (purple) and for **tBuODA** to **IrPIQ** (blue).

The combination of fluorescent and phosphorescent components in each block provides further photophysical differentiation as the polymers exclude solvent. The photoluminescence (PL) lifetimes of **tBuODA**$_{150}$**-BB**, **IrPPY**$_{150}$**-BB**, and **IrPIQ**$_{150}$**-BB** in 98% water are 4.1 ns, 2.6 μs and 1.2 μs, respectively. The diblock bottlebrush polymer **tBuODA**$_{60}$**-IrPIQ**$_{90}$**-BB** has a lifetime of 4.0 ns in THF, due to the fluorescent emission of the **tBuODA** block only (Figure 4.6). As the water fraction of the solution is increased up to 98% water, a second lifetime component begins to

appear with a lifetime of 1.2 μs. A similar phenomenon occurs for **tBuODA$_{100}$-IrPPY$_{50}$-BB**, where only one component can be detected initially with a 4.1 ns lifetime and a second component (1.6 μs) appears as more efficient energy transfer begins to occur within and between blocks.

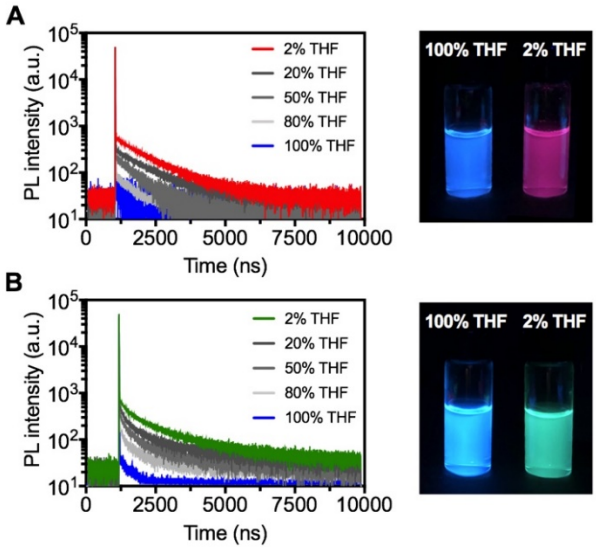

Figure 4.6. Time-dependent PL spectra showing an increase in PL lifetime with aggregation and photograph of 100% THF and 2% THF for a) **tBuODA$_{60}$-*b*-IrPIQ$_{90}$-BB** and b) **tBuODA$_{100}$-*b*-IrPPY$_{50}$-BB.**

Furthermore, the colour change upon aggregation is made more pronounced by the use of phosphorescent acceptor chromophores, which can also be quenched by dissolved O_2 if the bottlebrush is in an extended conformation in solution.[256] When dissolved in THF, the intensity of red phosphorescence in **tBuODA$_{60}$-IrPIQ$_{90}$-BB** is reduced by 65% under an air atmosphere relative to an N_2-sparged solution (Figure 4.7). Aggregation of the polymers in 98% water, however, causes exclusion of O_2, leading to enhanced red phosphorescence even in aerated solution.

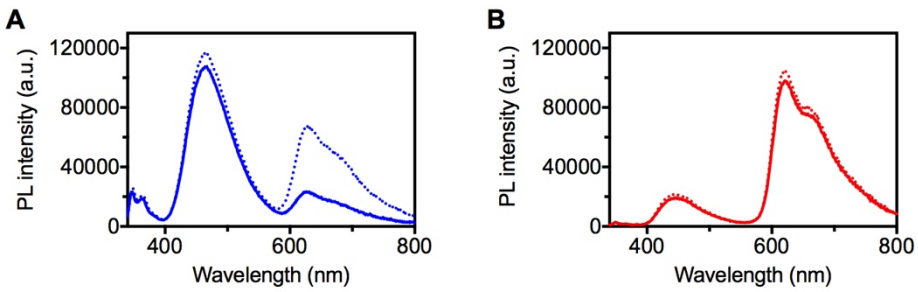

Figure 4.7. PL spectra of **tBuODA$_{60}$-*b*-IrPIQ$_{90}$-BB** at 1 x 10^{-5} M under an air atmosphere (solid) or N_2 atmosphere (dashed) in a) THF and b) water.

The aggregation-induced changes that we observe in our system are similar, yet distinct from aggregation-induced emission (AIE) – a process by which a luminophore is initially non-emissive, but becomes highly luminescent when intramolecular motion is restricted due to aggregation.[257,258] Owing to this property, molecules exhibiting AIE, or AIEgens, have found diverse applications as biological probes,[259,260] chemical sensors,[261–263] OLED materials,[264] and stimuli-responsive compounds.[265] Rather than restricting rotations within a single chromophore, colour changes in these BBCPs are induced by restricting the relative positions of two chromophores on nearby polymer side-chains. The reorganization of nanoscopic domains has recently proven to be an effective strategy for inducing changes in FRET in diverse nanoscale systems, including ionic liquid crystals,[266] surfactant-responsive polymers,[250] and carbon dots.[267] Such materials have applications as reversibly-switchable luminescent inks for use in anti-counterfeiting and encryption,[267] and we envisioned that aggregation in multichromophore BBCPs could be used in a similar fashion. Aggregation-induced colour changes have also been observed in linear polymers,[142] and many polymers containing AIEgens demonstrate AIE.[257] To demonstrate this, the diblock **tBuODA$_{\infty}$-*b*-IrPIQ$_{\infty}$-BB** was dissolved in toluene solution (ca. 0.5 mg mL^{-1}) and

loaded into an empty softliner pen (Molotow, 1 mm brush). This pen was used to draw images that when partially masked reveal unique patterns when exposed to solvent (toluene), or impose fluorescent changes on the image. These changes in emission colour are fully reversible when the substrate is dried (Figure 4.8 and 4.9).

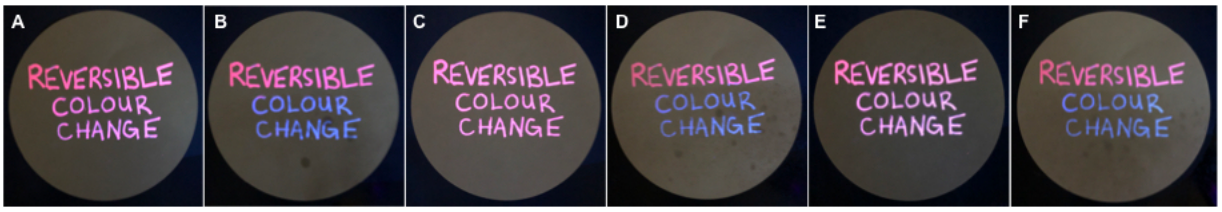

Figure 4.8. Photographs of **tBuODA$_{60}$-*b*-IrPIQ$_{90}$-BB** drawn on filter paper when completely dried (a) and after exposure to toluene spray (b) through a mask. The filter paper was allowed to dry for 2 min to give (c) and exposed to solvent again (d). This process was repeated again to give (e) and (f). The blue fluorescent areas indicate the area affected by the solvent.

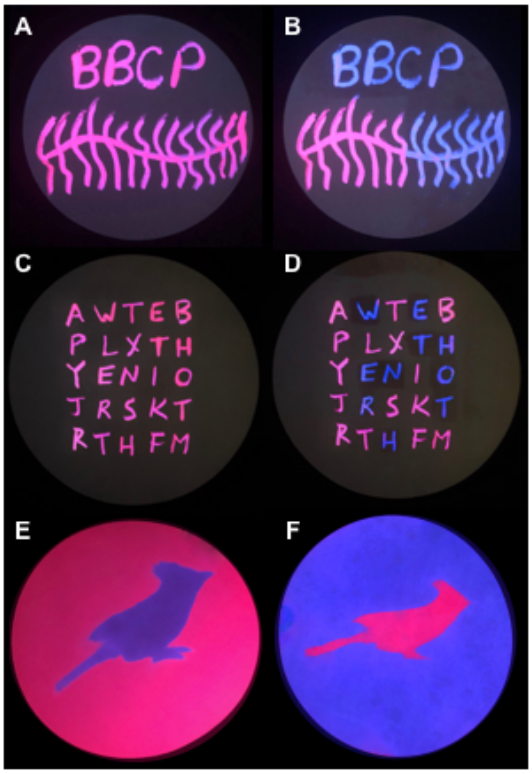

Figure 4.9. Photographs of **tBuODA$_{60}$-*b*-IrPIQ$_{90}$-BB** drawn on filter paper when completely dried (a, c) and after exposure to toluene spray (b, d, e, f) through a mask. The blue fluorescent areas indicate the area affected by the solvent, revealing the fluorescent structure of the bottlebrush in b), the message "WE THE NORTH" in d) and the silouette of a Stellar's Jay in e) and f).[268] λ_{ex} = 254 nm.

In addition to the potential applications above, these BBCPs also allow for the preparation of multicompartment nanofibers which mimic the ordered structure of macroscale optoelectronic devices on single macromolecules, with many of their observable functions. To demonstrate this potential, we prepared linear 'pentablock' nanofibers mimicking the design of a white OLED, with discrete red, green and blue emissive zones. Attributes such as high energy efficiency, diffuse lighting, and an ultrathin form factor have made white OLEDs a promising technology for next-generation solid-state lighting, and they commonly make use of several layers of emissive materials between charge-transporting layers to achieve the desired chromaticity.[269] To this end,

we reasoned that it should be possible to replicate this five-layer structure on a single polymer strand while maintaining discrete interfaces between the blocks. Two additional macromonomers **MeHTL-MM** (M_n = 6400, Đ = 1.12) and **ETL-MM** (M_n = 6800, Đ = 1.19) were synthesized to serve as the hole transport and electron transport layers, based on an electron-rich triarylamine and electron-deficient triazine, respectively. Sequential ROMP of **MeHTL-MM**, **tBuODA-MM**, **IrPPY-MM**, **IrPIQ-MM** and **ETL-MM** gave **MeHTL$_{30}$-*b*-tBuODA$_{30}$-*b*-IrPPY$_{30}$-*b*-IrPIQ$_{30}$-ETL$_{30}$-*b*-BB** (Figure 4.10), incorporating the six distinct optoelectronic functions of a white OLED onto single bottlebrush fibers. SEC analysis reveals narrow dispersity is maintained at each stage of the polymerization with minimal chain death (small shoulder observed at ~15.2 mL) upon addition of each block and only a small amount of residual macromonomer (peak at 19.5 mL), which can be purified using the reusable methacrylic resin discussed previously. Overall the material shows light pink luminescence in the solid state (Figures 4.10d) with CIE coordinates of (0.30, 0.23), alongside the reversible reduction and oxidation of the ETL and MeHTL blocks at -2.11 and 0.55 V relative to ferrocene/ferrocenium ($Fc^{0/+}$), respectively (Figure 4.10e). The result is an ordered nanofiber formed from semiconducting materials, with a structure that previously could only be prepared on the macroscale in solid-state devices. Moving forward, such systems hold potential for the rapid self-assembly of complex multilayer films with synthetically installed order, and for investigations into charge transport at nanoscale interfaces.

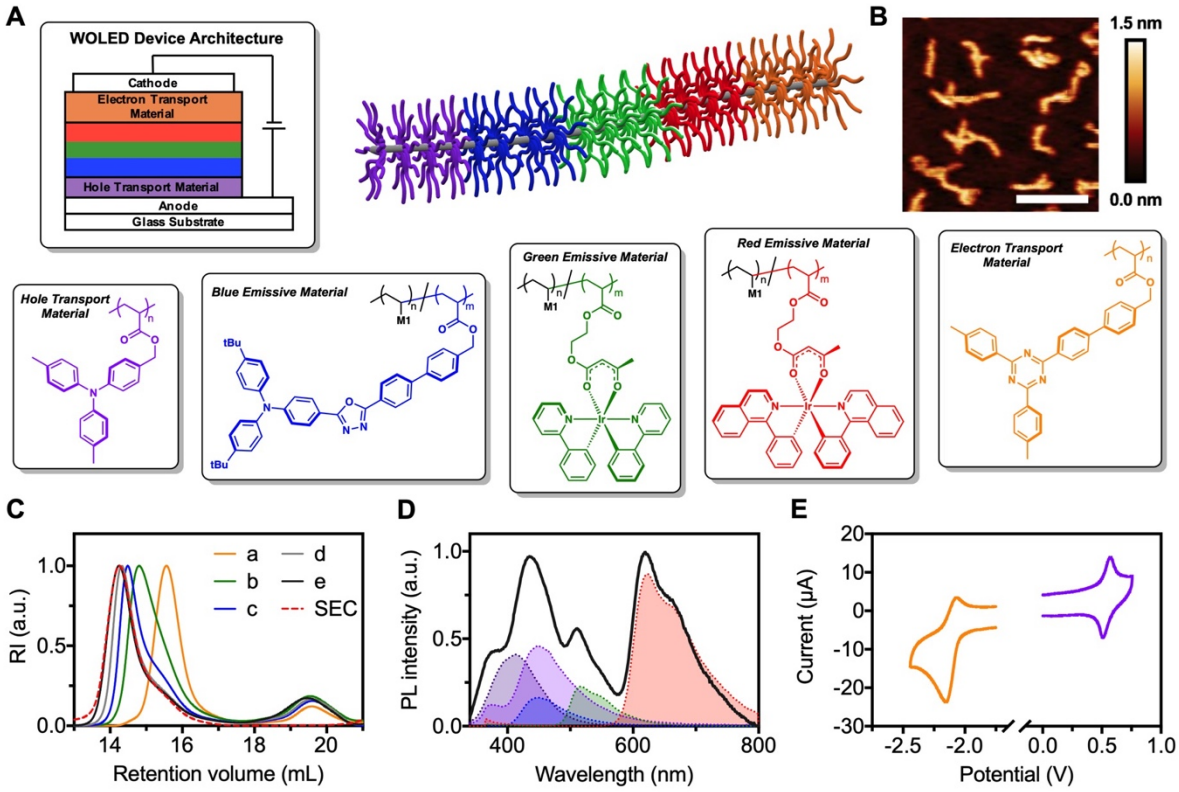

Figure 4.10. a) Schematic illustration of a pentablock bottlebrush consisting of a hole transport material, blue, green and red emitters doped in a carbazole host, and an electron transport material, alongside an archetypical WOLED device configuration. b) AFM height image on HOPG (scale bar = 65 nm) c) SEC chromatogram of the pentablock BB where a-e denote the addition of **MeHTL**, **tBuODA**, **IrPPY**, **IrPIQ**, and **ETL** blocks, respectively and 'SEC' denotes the trace after purification. d) Solid state PL spectrum of **MeHTL**$_{30}$-*b*-**tBuODA**$_{30}$-*b*-**IrPPY**$_{30}$-*b*-**IrPIQ**$_{30}$-**ETL**$_{30}$-*b*-**BB** (black) on glass with emission spectra of **MeHTL** (light purple), **tBuODA** (blue), **IrPPY** (green), **IrPIQ** (red), and **ETL** (dark purple) shown. e) Cyclic voltammogram of the pentablock BBCP showing the reduction of the ETL block (orange) and oxidation of the MeHTL block (purple) vs $Fc^{0/+}$.

4.3 Conclusions

In summary, a series of BBCPs were prepared from red, green and blue luminescent macromonomers, which were then used to prepare multicolour, multiblock nanofibers. Using

solvent polarity as stimulus, efficient energy transfer from the blue fluorophore to the red and green phosphors could be modulated to give aggregation-induced changes in emission colour. Aggregation was further accompanied by changes in the emission lifetime of the nanofiber from the nanosecond to microsecond regime, and changes in energy transfer efficiency and interchromophore distance quantified using a FRET model. Preliminary demonstration of these materials as polarity-sensitive inks for encryption and encoding were also demonstrated using a red/blue fluorescence switch upon exposure to solvent. Finally, the potential complexity of optoelectronic materials accessible with these methods was demonstrated by combining these building blocks with hole- and electron-transporting materials, to give nanofibers with an ordered structure analogous to the device configuration of state-of-the-art white OLEDs. Future work will focus on alignment of the fibers for devices, as well as examining their use as single molecule junctions situated between two electrodes. This work demonstrates that BBCPs can be used to prepare robust, precise and multifunctional nanostructures from general building blocks, with switchable changes in optoelectronic properties from ordered soft nanomaterials.

4.4 Experimental Details

General Considerations. All reactions and manipulations were carried out under a nitrogen atmosphere using standard Schlenk or glove box techniques unless otherwise stated. Dry solvents were obtained from Caledon Laboratories, dried using an Innovative Technologies Inc. solvent purification system, collected under vacuum, and stored under a nitrogen atmosphere over 4 Å molecular sieves. All reagents were purchased from Sigma-Aldrich or Alfa Aesar and used as received unless otherwise stated. **CzBA,**[232] **IrPIQ**,[183] **IrPPY,**[183] **tBuODA**,[254] **HTL-MM**,[248] **ETL-**

MM,[248] ***N*-(undecanyl-2-bromo-2-methylpropionate)-*cis*-5-norbornene-*exo*-2,3-dicarboximide**,[248] **CzBA-BB** (M_n = 1990 kDa, PDI = 1.32)[248] and dichloro[1,3-bis(2,4,6-trimethylphenyl)-2-imidazolidinylidene](benzylidene) bis(pyridine)ruthenium(II)[122] (**G3**) were prepared according to literature procedures. *N*-methyl-2-pyrrolidone (NMP) was distilled, then degassed and stored under an N_2 atmosphere. The ^1H and $^{13}C\{^1H\}$ nuclear magnetic resonance (NMR) spectra were measured on a Bruker AV III HD 400 MHz spectrometer with chloroform-*d* ($CDCl_3$) or dichloromethane-d_2 (CD_2Cl_2) as the solvent and chemical shifts are given in parts per million (ppm). Absorbance measurements were made on a Cary 60 spectrometer and fluorescence measurements were made on an Edinburgh Instruments FS5 spectrofluorometer. Absolute photoluminescence quantum yields were determined using an Edinburgh Instruments SC–30 Integrating Sphere Module; toluene was used as the solvent and spectra obtained at concentrations of 0.01 mg mL^{-1}. Time-resolved fluorescence data were collected using a Horiba Yvon Fluorocube time-correlated single photon counting (TCSPC) apparatus. A 370 nm NanoLED source pulsing at a repetition rate of 100−1000 kHz was used for excitation. Broad- band emission was monitored by a CCD detector at wavelengths > 450 nm using a low-pass filter. Data were fitted using the DAS6 Data Analysis software package. Mass spectra were recorded on a Kratos MS-50 instrument using electron impact ionization.

Dynamic light scattering (DLS). DLS experiments were performed with a DynaPro Titan DLS instrument (Wyatt Technology Corporation) equipped with a 60 mW helium–neon laser (l = 832.15 nm) and thermoelectric temperature controller. Measurements were taken at a 90° scattering angle in a 3 × 3 mm quartz cuvette on solutions that had been equilibrated to 25 °C, and particle sizes determined using quadratic cumulant fits. The laser power was controlled to 8–10%.

The sample solutions were diluted in THF or water prior to analysis. The concentrations of the analyzed sample solutions were 1×10^{-5} M.

Atomic Force Microscopy (AFM). Atomic force microscopy (AFM) images were obtained using an Asylum Instruments Cypher S AFM system in tapping mode at scan rates of 0.1 Hz. Samples were prepared by spin-coating solutions of polymer onto freshly cleaved highly-oriented pyrolytic graphite (HOPG) at 2500 rpm for 30 s at concentrations of ~0.001 mg mL^{-1}. For best results, 1,2-dichloroethane was used as the solvent. Samples were placed in a vacuum oven (60 ºC) for at least 2 h before images were obtained using Mikromasch HQ:NSC14/No Al or HQ:NSC19/No Al probes, with typical resonance frequencies f and spring constants k of (f = 160 kHz, k = 5 N/m) and (f = 65 kHz, k = 0.5 N/m) respectively.

Size Exclusion Chromatography (SEC). SEC experiments were conducted in chromatography-grade THF at concentrations of 0.5 – 2 mg mL^{-1} using a Malvern OMNISEC GPC instrument equipped with a Viscotek TGuard guard column (CLM3008), and Viscotek T3000 (CLM3003) and T6000 (CLM3006) GPC columns packed with porous poly(styrene-*co*-divinylbenzene) particles regulated at a temperature of 35 °C. Signal response was measured using differential viscometer, differential refractive index, photodiode array and right-angle and low angle light scattering detectors. Calibration of interdetector distances was performed using a polystyrene standard from Malvern Inc. Refractive index increments (d*n*/d*c*) were determined using 100% mass recovery methods from Malvern OMNISEC software version 10.2 with each polymer sample being run at least five times to ensure reproducibility of the calculated refractive index increment.

Thermal Analysis. Thermal degradation studies were performed using a NETZSCH TG 209F1 Libra instrument. Samples were placed in an Al_2O_3 crucible and heated at a rate of 10 °C min^{-1} from 25 to 800 °C under a flow of nitrogen (50 mL min^{-1}). Glass transition temperatures were determined using differential scanning calorimetry (DSC) on a NETZSCH DSC 214 Polyma instrument. The polymer samples were placed in an aluminum pan and heated from 30 to 200 °C at 10 °C min^{-1} under a flow of nitrogen for 3 heating/cooling cycles.

Analysis of Aggregation-Induced Colour Change. The diblock **tBuODA$_{60}$-*b*-IrPIQ$_{90}$-BB** has a CIE coordinate of (0.49, 0.24) for its fluorescent emission in THF and (0.17, 0.18) in 2% THF/water mixture when illuminated with 365 nm light. For the polar vector representing this change, we can determine the magnitude and direction using equations (1) and (2).

$$|\overrightarrow{AB}| = \sqrt{(x_2 - x_1) + (y_2 - y_1)} \quad (1)$$

$$\tan\theta = \frac{y_2 - y_1}{x_2 - x_1} \quad (2)$$

Written in ordered pair notation, $v = (r, \theta)$, we obtain a vector (0.32, 11.8) where the first component of the vector is the magnitude r and the second component is the angle θ in degrees. Doing this for **tBuODA$_{75}$-*b*-IrPPY$_{75}$-BB** and **tBuODA$_{50}$-*b*-IrPPY$_{50}$-*b*-IrPIQ$_{50}$-BB,** we obtain vectors (0.25, 70.3) and (0.31, 31.8). While the magnitude of the change in each case remain similar, it is clear from the angles that the colour change of the triblock is intermediate between those of **tBuODA$_{60}$-*b*-IrPIQ$_{90}$-BB** and **tBuODA$_{75}$-*b*-IrPPY$_{75}$-BB**.

4.4.1 Synthetic Procedures

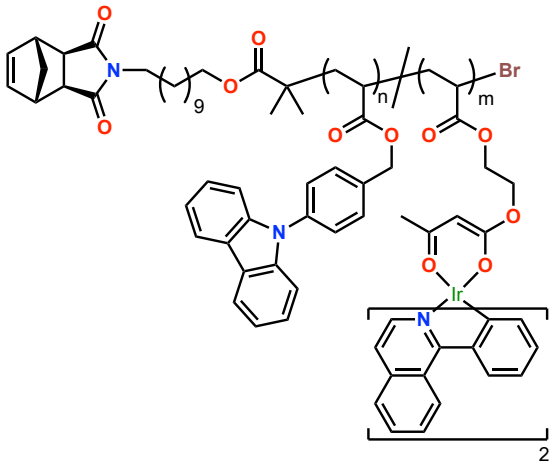

Synthesis of IrPIQ-MM by Cu(0)-RDRP:

In a nitrogen atmosphere glovebox, to a 4 mL vial capped with a Teflon-lined lid and equipped with a magnetic stir bar was added **CzBA** (300 mg, 0.92 mmol, 28 eq.), **IrPIQ** (26 mg, 0.03 mmol, 1.1 eq.), **1** (16 mg, 0.03 mmol, 1 eq.), and 128 µL of a solution of $CuBr_2$/Me_6TREN in NMP (C_{Cu} = 3.75 mg mL^{-1}; $CuBr_2$: 0.48 mg, 2.1 x 10^{-3} mmol, 0.065 eq.; Me_6TREN: 0.50 mg, 2.2 x 10^{-3} mmol, 0.068 eq.). The total polymerization volume was kept to 1.5 mL of solvent. The mixture was stirred at room temperature for 10 minutes to allow all reagents to fully dissolve. A 1.5 cm piece of 18 gauge copper (0) wire was soaked in concentrated HCl for 15 minutes to remove surface impurities, then washed with water followed by acetone, dried *in vacuo* and taken into the glovebox. The wire was added to the mixture to initiate the polymerization. Each hour a 25 µL aliquot was taken and diluted with $CDCl_3$, and the conversion monitored by ^{1}H NMR. At approximately 60 % conversion, the polymerization was quenched by addition of water followed by filtration. The polymer was taken up in CH_2Cl_2, dried over $MgSO_4$ and concentrated *in vacuo*. The residue was purified by preparatory SEC (Bio-Rad Bio-Beads S-X1 Support) in THF and fractions containing polymer were determined by SEC analysis. All fractions containing polymer

were collected and dried *in vacuo* overnight. Yield = 193 mg (56%). M_n = 7400 Da, Đ = 1.14. ^{1}H NMR (400 MHz, chloroform-*d*) δ 9.10 (d, *J* = 6.4 Hz, 0.9H), 9.02 (d, *J* = 8.6 Hz, 0.9H), 8.25 – 7.74 (br, m, 49H), 7.70 – 6.97 (br, m, 227H), 6.86 (t, *J* = 7.5 Hz, 0.9H), 6.63 – 6.51 (m, 1.8H), 6.28 (s, 1.8H), 6.09 (d, *J* = 7.8 Hz, 0.9H), 5.08 (br, m, 44H), 4.18 (br, m, 3H), 3.94 (br, s, 2H), 3.43 (t, *J* = 7.6 Hz, 2H), 3.28 (s, 2H), 2.61 (br, m, 22H), 2.29 – 2.02 (br, m, 13H), 1.88 – 1.44 (br, m, 24H), 1.39 – 0.97 (br, m, 27H). ^{13}C{^{1}H} NMR (101 MHz, chloroform-*d*) δ 174.19, 140.45, 137.81, 134.53, 129.56, 126.95, 125.91, 123.37, 120.26, 120.05, 109.56, 77.24, 68.00, 66.10, 47.78, 45.16, 29.46, 27.75. Fractional protons represent an average of 0.45 IrPIQ units incorporated per polymer chain.

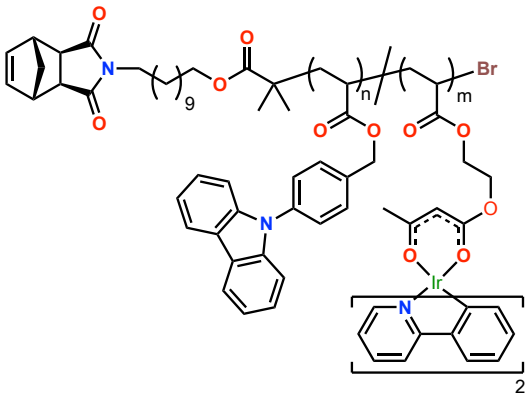

Synthesis of IrPPY-MM by Cu(0)-RDRP:

In a nitrogen atmosphere glovebox, to a 20 mL vial capped with a Teflon-lined lid and equipped with a magnetic stir bar was added **CzBA** (920 mg, 2.8 mmol, 40 eq.), **IrPPY** (80 mg, 0.114 mmol, 1.1 eq.), 0.966 mL of a solution of **1** in NMP (C_{S2} = 50 mg mL^{-1}; **1**: 48.3 mg, 0.10 mmol, 1 eq.), and 390.0 µL of a solution of $CuBr_2$/Me_6TREN in NMP (C_{Cu} = 3.75 mg mL^{-1}; $CuBr_2$: 1.45 mg, 6.5 x 10^{-3} mmol, 0.065 eq.; Me_6TREN: 1.50 mg, 6.8 x 10^{-3} mmol, 0.068 eq.). The total polymerization volume was kept to 4.6 mL of solvent. The mixture was stirred at room temperature for 10 minutes to allow all reagents to fully dissolve. A 5 cm piece of 18 gauge copper (0) wire

was soaked in concentrated HCl for 15 minutes to remove surface impurities, then washed with water followed by acetone, dried *in vacuo* and taken into the glovebox. The wire was added to the mixture to initiate the polymerization. Each hour a 25 μL aliquot was taken and diluted with $CDCl_3$, and the conversion monitored by ^1H NMR. At approximately 60 % conversion, the polymerization was quenched by addition of water followed by filtration. The polymer was taken up in CH_2Cl_2, dried over $MgSO_4$ and concentrated *in vacuo*. The residue was purified by preparatory SEC (Bio-Rad Bio-Beads S-X1 Support) in THF and fractions containing polymer were determined by SEC analysis. All fractions containing polymer were collected and dried *in vacuo* overnight. Yield = 500 mg (48%). M_n = 6900 Da, Đ = 1.20. ^1H NMR (400 MHz, chloroform-*d*) δ 9.29 (dd, *J* = 5.7, 1.5 Hz, 1H), 8.22 – 7.87 (br, m, 45H), 7.77 (td, *J* = 7.8, 1.6 Hz, 1H), 7.68 – 6.99 (br, m, 221H), 6.87 – 6.72 (m, 2H), 6.61 (td, *J* = 7.5, 1.4 Hz, 1H), 6.29 (s, 2H), 5.98 (d, *J* = 7.7 Hz, 1H), 5.30 – 4.84 (br, m, 44H), 4.24 (s, 3H), 3.95 (s, 3H), 3.45 (d, *J* = 7.6 Hz, 2H), 3.28 (s, 2H), 2.63 (br, m, 22H), 2.30 – 2.03 (br, m, 14H), 1.96 – 1.43 (br, m, 24H), 1.36 – 0.98 (br, m, 24H). $^{13}C\{^1H\}$ NMR (101 MHz, chloroform-*d*) δ 140.47, 137.81, 137.67, 134.56, 129.58, 126.97, 125.92, 123.66, 123.38, 120.27, 120.06, 109.57, 66.09, 47.79, 45.17, 41.58, 38.72, 30.36, 29.45, 28.52. Fractional protons represent an average of 0.5 IrPPY units incorporated per polymer chain.

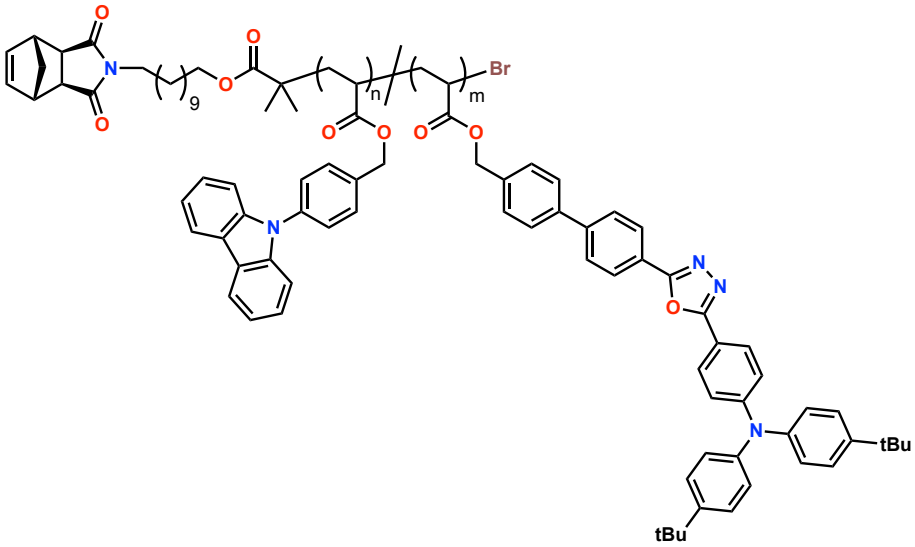

Synthesis of tBuODA-MM by Cu(0)-RDRP:

In a nitrogen atmosphere glovebox, to a 20 mL vial capped with a Teflon-lined lid and equipped with a magnetic stir bar was added **CzBA** (1380 mg, 4.20 mmol, 28 eq.), **tBuODA** (120 mg, 0.17 mmol, 1.1 eq.), **1** (72.5 mg, 0.15 mmol, 1 eq.), and 585 µL of a solution of $CuBr_2$/Me_6TREN in NMP (C_{Cu} = 3.75 mg mL^{-1}; $CuBr_2$: 2.18 mg, 9.8 x 10^{-3} mmol, 0.065 eq.; Me_6TREN: 2.28 mg, 1.0 x 10^{-2} mmol, 0.068 eq.). The total polymerization volume was kept to 7.5 mL of solvent. The mixture was stirred at room temperature for 10 minutes to allow all reagents to fully dissolve. A 7.5 cm piece of 18 gauge copper (0) wire was soaked in concentrated HCl for 15 minutes to remove surface impurities, then washed with water followed by acetone, dried *in vacuo* and taken into the glovebox. The wire was added to the mixture to initiate the polymerization. Each hour a 25 µL aliquot was taken and diluted with $CDCl_3$, and the conversion monitored by ^1H NMR. At approximately 60 % conversion, the polymerization was quenched by addition of water followed by filtration. The polymer was taken up in CH_2Cl_2, dried over $MgSO_4$ and concentrated *in vacuo*. The residue was purified by preparatory SEC (Bio-Rad Bio-Beads S-X1 Support) in THF and fractions containing polymer were determined by SEC analysis. All

fractions containing polymer were collected and dried *in vacuo* overnight. Yield = 868 mg (55%). M_n = 6600 Da, Đ = 1.24. ^{1}H NMR (400 MHz, chloroform-*d*) δ 8.07 (br, m, 42H), 7.66 – 6.90 (m, 210H), 6.29 (s, 2H), 5.11 (br, s, 42H), 4.25 (s, 1H), 3.95 (s, 2H), 3.44 (t, *J* = 7.6 Hz, 2H), 3.28 (s, 2H), 2.63 (br, m, 21H), 2.38 – 2.03 (br, m, 13H), 2.02 – 1.49 (br, m, 39H), 1.40 (br, m, 16H), 1.33 – 0.99 (br, m, 26H). ^{13}C{^{1}H} NMR (101 MHz, chloroform-*d*) δ 140.47, 137.81, 137.65, 134.56, 129.59, 126.97, 126.49, 125.93, 125.49, 123.38, 120.27, 120.06, 109.57, 66.11, 47.79, 45.17, 41.56, 31.46, 29.46. Fractional protons represent an average of 0.9 tBuODA units incorporated per polymer chain.

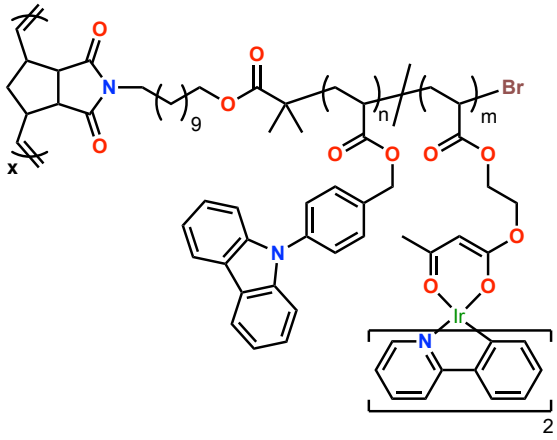

Synthesis of IrPPY$_{150}$-BB by ROMP:

In a nitrogen atmosphere glovebox, to a 2 mL vial capped with a Teflon-lined lid and equipped with a magnetic stir bar was added **IrPPY-MM** (75 mg, 1.1 x 10^{-2} mmol, 150 eq.) and 375 µL of THF (dry, degassed, filtered through basic alumina). Using a glass microsyringe 26 µL of a solution of **G3** in THF (C_{G3} = 2 mg mL^{-1}; **G3**: 0.053 mg, 7.3 x 10^{-5} mmol, 1 eq.) was added to the dissolved polymer rapidly in one portion. The mixture was stirred at room temperature for 1 h. Two 5 µL aliquots were taken for ^{1}H NMR and SEC analysis, and the polymerization was removed from the glove box, quenched with one drop of ethyl vinyl ether, and immediately

purified by preparatory SEC (silylated Toyopearl HW-55F resin) in THF and fractions containing polymer were determined by SEC analysis. All fractions containing polymer were collected and concentrated then precipitated into MeOH and dried *in vacuo* overnight. Yield = 41 mg (55%). M_n = 1040 kDa, Đ = 1.20. ^{1}H NMR (400 MHz, chloroform-*d*) δ 8.47 (s, 1H), 7.95 (br, m, 45H), 7.77 (t, *J* = 7.8 Hz, 1H), 7.20 (br, m, 221H), 6.96 – 6.76 (m, 2H), 6.60 (t, *J* = 7.2 Hz, 2H), 6.16 (s, 1H), 5.02 (br, m, 44H), 4.20 (s, 1H), 4.02 – 3.73 (br, m, 4H), 2.90 – 1.98 (m, 35H), 1.58 (s, 16H), 1.33 – 0.55 (m, 33H).

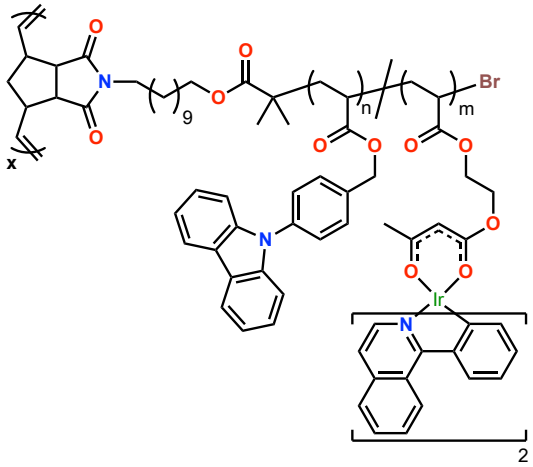

Synthesis of IrPIQ$_{150}$-BB by ROMP:

In a nitrogen atmosphere glovebox, to a 2 mL vial capped with a Teflon-lined lid and equipped with a magnetic stir bar was added **IrPIQ-MM** (75 mg, 1.0 x 10^{-2} mmol, 150 eq.) and 375 µL of THF (dry, degassed, filtered through basic alumina). Using a glass microsyringe 23 µL of a solution of **G3** in THF (C_{G3} = 2 mg mL^{-1}; **G3**: 0.046 mg, 6.3 x 10^{-5} mmol, 1 eq.) was added to the dissolved polymer rapidly in one portion. The mixture was stirred at room temperature for 1 h. Two 5 µL aliquots were taken for ^{1}H NMR and SEC analysis, and the polymerization was removed from the glove box, quenched with one drop of ethyl vinyl ether, and immediately purified by preparatory SEC (silylated Toyopearl HW-55F resin) in THF and fractions containing

polymer were determined by SEC analysis. All fractions containing polymer were collected and concentrated then precipitated into MeOH and dried *in vacuo* overnight. Yield = 36 mg (48%). M_n = 1100 kDa, Đ = 1.39. ^{1}H NMR (400 MHz, chloroform-*d*) δ 9.15 – 8.77 (m, 0.9H), 8.43 (s, 0.9H), 7.94 (br, m, 49H), 7.20 (d, *J* = 78.4 Hz, 227H), 6.85 (t, *J* = 7.3 Hz, 0.9H), 6.56 (m, 1.8H), 6.30 (br, m, 0.9H), 5.01 (br, m, 44H), 4.19 (br, s, 2H), 3.96 – 3.73 (m, 2H), 2.83 – 1.95 (br, m, 37H), 1.59 (br, m, 26H), 1.13 (br, m, 27H).

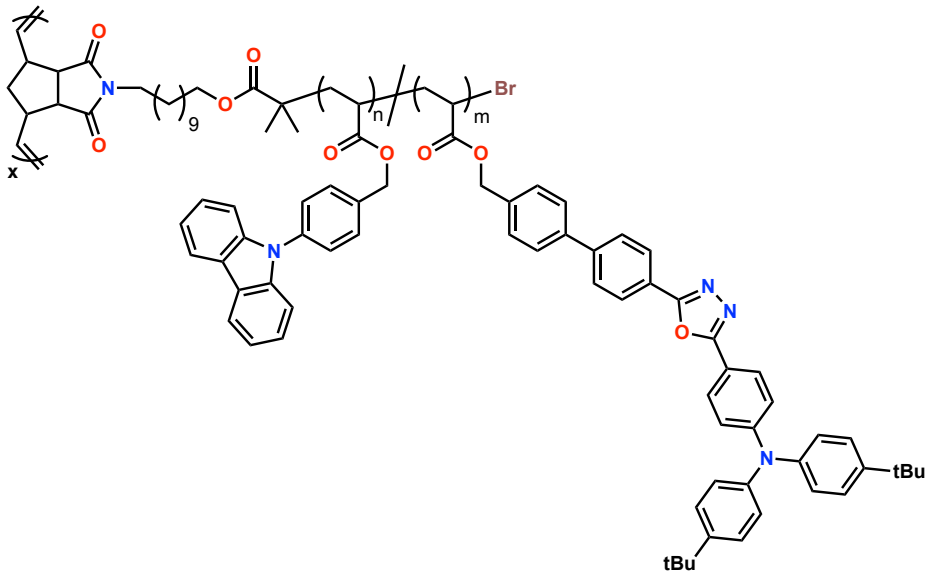

Synthesis of tBuODA$_{150}$-BB by ROMP:

In a nitrogen atmosphere glovebox, to a 2 mL vial capped with a Teflon-lined lid and equipped with a magnetic stir bar was added **tBuODA-MM** (75 mg, 1.1 x 10^{-2} mmol, 150 eq.) and 375 µL of THF (dry, degassed, filtered through basic alumina). Using a glass microsyringe 28 µL of a solution of **G3** in THF (C_{G3} = 2 mg mL^{-1}; **G3**: 0.055 mg, 7.6 x 10^{-5} mmol, 1 eq.) was added to the dissolved polymer rapidly in one portion. The mixture was stirred at room temperature for 1 h. Two 5 µL aliquots were taken for ^{1}H NMR and SEC analysis, and the polymerization was removed from the glove box, quenched with one drop of ethyl vinyl ether, and immediately purified by preparatory SEC (Toyopearl HW-55F resin) in THF and fractions containing polymer

were determined by SEC analysis. All fractions containing polymer were collected and concentrated then precipitated into MeOH and dried *in vacuo* overnight. Yield = 40 mg (53%). M_n = 823 kDa, Đ = 1.17. ^{1}H NMR (400 MHz, chloroform-*d*) δ 7.95 (s, 42H), 7.21 (br, m, 210H), 5.03 (br, s, 42H), 4.20 (br, s, 1H), 4.02 – 3.77 (br, m, 21H), 2.75 – 1.97 (br, m, 13H), 1.59 (br, m, 39H), 1.32 (br, m, 16H), 1.07 (br, m, 26H).

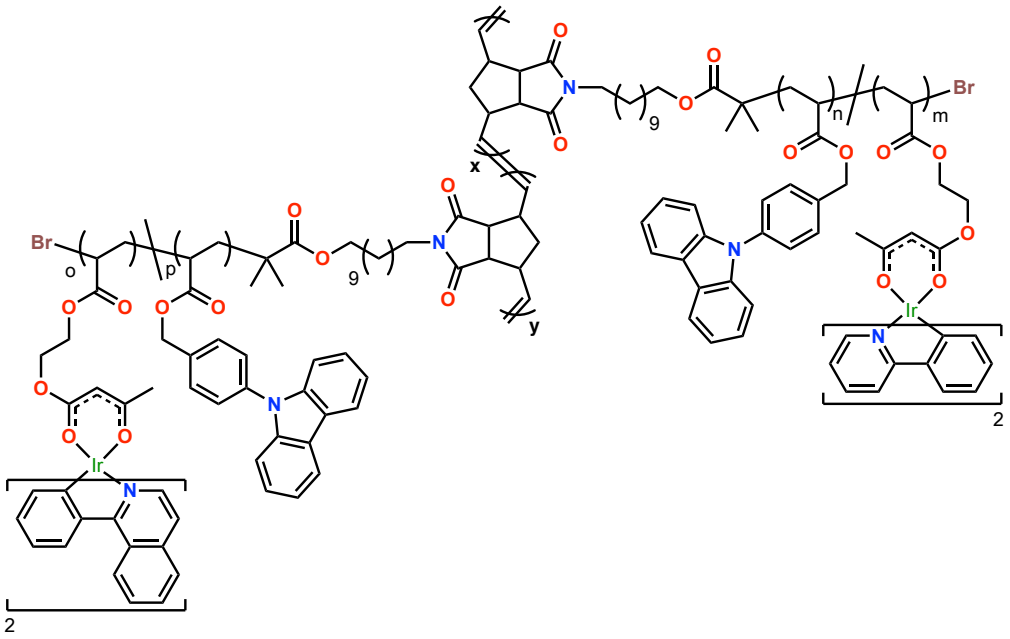

Synthesis of IrPPY$_{100}$-*b*-IrPIQ$_{50}$-BB by ROMP:

In a nitrogen atmosphere glovebox, to a 2 mL vial capped with a Teflon-lined lid and equipped with a magnetic stir bar was added **IrPPY-MM** (60 mg, 8.7 x 10^{-3} mmol, 100 eq.) and 280 µL of THF (dry, degassed, filtered through basic alumina). Using a glass microsyringe 32 µL of a solution of **G3** in THF (C_{G3} = 2 mg mL^{-1}; **G3**: 0.063 mg, 8.7 x 10^{-5} mmol, 1 eq.) was added to the dissolved polymer rapidly in one portion. The mixture was stirred at room temperature for 1 h. Two 5 µL aliquots were taken for ^{1}H NMR and SEC analysis, before addition of **IrPIQ-MM** (34 mg, 4.3 x 10^{-3} mmol, 50 eq.) dissolved in 150 µL of THF. The mixture was stirred at room temperature for an additional 1 h. Two 5 µL aliquots were taken for ^{1}H NMR and SEC analysis,

and the polymerization was removed from the glove box, quenched with one drop of ethyl vinyl ether, and immediately purified by preparatory SEC (silylated Toyopearl HW-55F resin) in THF and fractions containing polymer were determined by SEC analysis. All fractions containing polymer were collected and concentrated then precipitated into MeOH and dried *in vacuo* overnight. Yield = 40 mg (43%). M_n = 800 kDa, Đ = 1.14. ^{1}H NMR (400 MHz, chloroform-*d*) δ 9.06 (br, m, 0.3H), 8.47 (s, 0.6H), 7.95 (br, m, 42H), 7.21 (br, m, 227H), 6.59 (br, m, 2H), 6.16 (s, 0.6H), 5.89 (s, 0.6H), 5.02 (br, s, 40H), 4.20 (br, m, 1H), 3.86 (br, s, 2H), 2.85 – 1.98 (br, m, 33H), 1.59 (br, m, 64H), 1.07 (br, m, 27H).

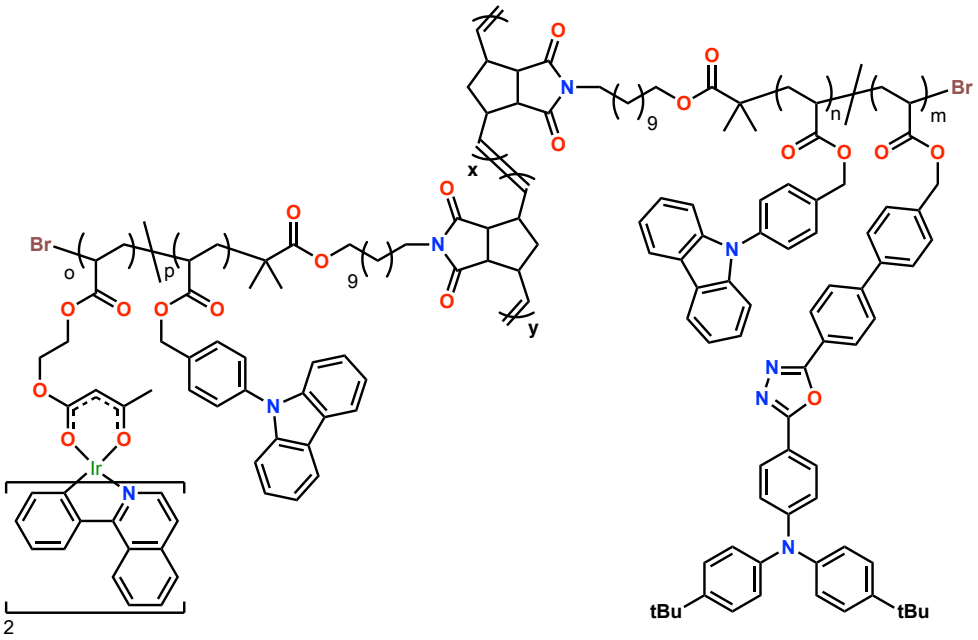

Synthesis of tBuODA$_{100}$-*b*-IrPIQ$_{50}$-BB by ROMP:

In a nitrogen atmosphere glovebox, to a 2 mL vial capped with a Teflon-lined lid and equipped with a magnetic stir bar was added **tBuODA-MM** (30 mg, 4.5 x 10^{-3} mmol, 60 eq.) and 150 µL of THF (dry, degassed, filtered through basic alumina). Using a glass microsyringe 28 µL of a solution of **G3** in THF (C_{G3} = 2 mg mL^{-1}; **G3**: 0.055 mg, 7.6 x 10^{-5} mmol, 1 eq.) was added to the dissolved polymer rapidly in one portion. The mixture was stirred at room temperature for

1 h. Two 5 µL aliquots were taken for ^{1}H NMR and SEC analysis, before addition of **IrPIQ-MM** (34 mg, 4.3 x 10^{-3} mmol, 50 eq.) dissolved in 150 µL of THF. The mixture was stirred at room temperature for an additional 1 h. Two 5 µL aliquots were taken for ^{1}H NMR and SEC analysis, and the polymerization was removed from the glove box, quenched with one drop of ethyl vinyl ether, and immediately purified by preparatory SEC (silylated Toyopearl HW-55F resin) in THF and fractions containing polymer were determined by SEC analysis. All fractions containing polymer were collected and concentrated then precipitated into MeOH and dried *in vacuo* overnight. Yield = 34 mg (53%). M_n = 897 kDa, Đ = 1.29. ^{1}H NMR (400 MHz, chloroform-*d*) δ 9.19 – 8.68 (m, 0.51H), 8.44 (s, 0.25H), 8.29 – 7.72 (br, m, 37H), 7.20 (br, m, 200H), 6.66 – 6.23 (br, m, 1H), 5.18 (br, m, 39H), 4.20 (br, s, 1H), 3.83 (br, s, 2H), 2.84 – 1.98 (br, m, 27H), 1.53 (br, m, 54H), 1.40 – 1.27 (br, m, 9H), 1.24 – 0.71 (br, m, 23H).

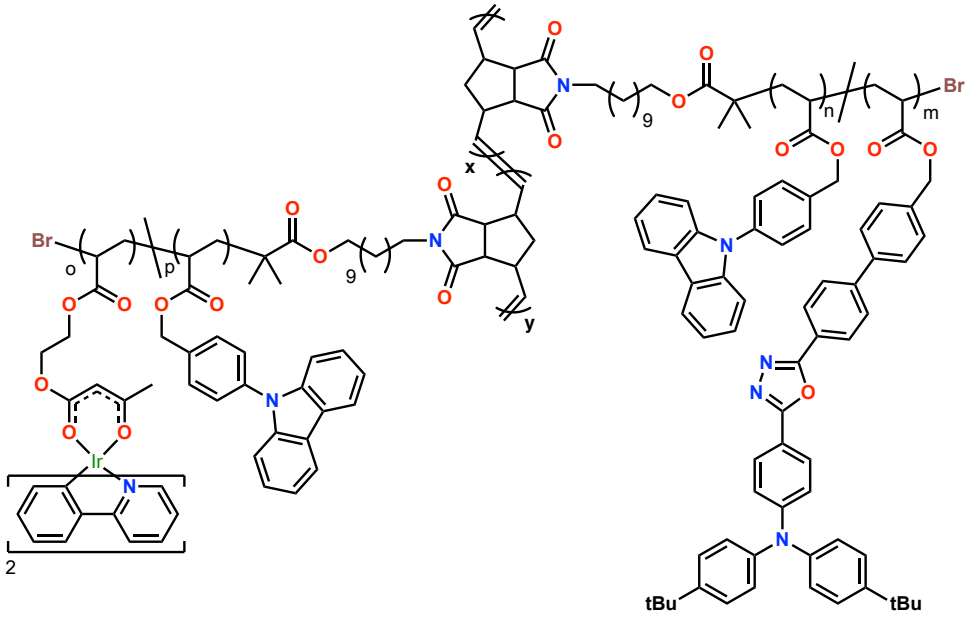

Synthesis of tBuODA$_{75}$-*b*-IrPPY$_{75}$-BB by ROMP:

In a nitrogen atmosphere glovebox, to a 2 mL vial capped with a Teflon-lined lid and equipped with a magnetic stir bar was added **tBuODA-MM** (35 mg, 5.3 x 10^{-3} mmol, 75 eq.) and 185 µL

of THF (dry, degassed, filtered through basic alumina). Using a glass microsyringe 26 μL of a solution of **G3** in THF ($C_{\mathbf{G3}}$ = 2 mg mL^{-1}; **G3**: 0.051 mg, 7.1 x 10^{-5} mmol, 1 eq.) was added to the dissolved polymer rapidly in one portion. The mixture was stirred at room temperature for 1 h. Two 5 μL aliquots were taken for ^{1}H NMR and SEC analysis, before addition of **IrPIQ-MM** (37 mg, 5.3 x 10^{-3} mmol, 75 eq.) dissolved in 185 μL of THF. The mixture was stirred at room temperature for an additional 1 h. Two 5 μL aliquots were taken for ^{1}H NMR and SEC analysis, and the polymerization was removed from the glove box, quenched with one drop of ethyl vinyl ether, and immediately purified by preparatory SEC (silylated Toyopearl HW-55F resin) in THF and fractions containing polymer were determined by SEC analysis. All fractions containing polymer were collected and concentrated then precipitated into MeOH and dried *in vacuo* overnight. Yield = 39 mg (54%). M_n = 782 kDa, Đ = 1.27. ^{1}H NMR (400 MHz, chloroform-*d*) δ 8.42-8.33 (br, s, 0.61H), 7.84 (br, s, 44H), 7.09 (br, m, 246H), 6.49 (br, m, 3H), 6.05 (s, 0.61H), 5.63 (s, 0.61H), 4.92 (br, s, 42H), 4.05 (br, m, 1H), 3.76 (br, s, 2H), 2.27 (br, m, 33H), 1.48 (br, m, 70H), 1.21 (br, m, 11H), 0.96 (br, m, 27H).

Synthesis of tBuODA$_{50}$-*b*-IrPPY$_{50}$-*b*-IrPIQ$_{50}$-BB by ROMP:

In a nitrogen atmosphere glovebox, to a 2 mL vial capped with a Teflon-lined lid and equipped with a magnetic stir bar was added **tBuODA-MM** (29 mg, 4.4 x 10^{-3} mmol, 50 eq.) and 175 μL of THF (dry, degassed, filtered through basic alumina). Using a glass microsyringe 32 μL of a solution of dichloro[1,3-bis(2,4,6-trimethylphenyl)-2-imidazolidinylidene](benzylidene) bis(pyridine)ruthenium(II) (**1.3**) in THF ($C_{\mathbf{1.3}}$ = 2 mg mL^{-1}; **1.3**: 0.064 mg, 8.9 x 10^{-5} mmol, 1 eq.) was added to the dissolved polymer rapidly in one portion. The mixture was stirred at room temperature for 25 min. Two 5 μL aliquots were taken for ^{1}H NMR and SEC analysis, before

addition of **IrPPY-MM** (30 mg, 4.4 x 10^{-3} mmol, 50 eq.) dissolved in 175 µL of THF. The mixture was stirred at room temperature for an additional 25 min. Two 5 µL aliquots were taken for ^{1}H NMR and SEC analysis, before addition of **IrPIQ-MM** (35 mg, 4.4 x 10^{-3} mmol, 50 eq.) dissolved in 175 µL of THF. Two 5 µL aliquots were taken for ^{1}H NMR and SEC analysis, and the polymerization was removed from the glove box, quenched with one drop of ethyl vinyl ether, and immediately purified by preparatory SEC (silylated Toyopearl HW-55F resin) in THF and fractions containing polymer were determined by SEC analysis. All fractions containing polymer were collected and concentrated then precipitated into MeOH and dried *in vacuo* overnight. Yield = 56 mg (60%). M_n = 817 kDa, Đ = 1.29. ^{1}H NMR (400 MHz, chloroform-*d*) δ 9.29 – 8.70 (br, m, 0.6H), 8.46 (br, s, 0.6H), 7.95 (br, s, 60H), 7.21 (br, m, 311H), 6.57 (br, m, 2H), 5.81 (br, m, 1H), 5.02 (br, s, 58H), 4.20 (br, m, 1H), 3.87 (br, s, 3H), 2.38 (br, m, 43H), 1.59 (br, m, 81H), 1.40 – 1.27 (br, m, 12H), 1.26 – 0.86 (br, m, 36H).

Synthesis of MeHTL$_{30}$-*b*-tBuODA$_{30}$-*b*-IrPPY$_{30}$-*b*-IrPIQ$_{30}$-*b*-ETL$_{30}$-BB by ROMP:

In a nitrogen atmosphere glovebox, to a 2 mL vial capped with a Teflon-lined lid and equipped with a magnetic stir bar was added **MeHTL-MM** (25 mg, 3.9 x 10^{-3} mmol, 30 eq.) and 175 µL of THF (dry, degassed, filtered through basic alumina). Using a glass microsyringe 47 µL of a solution of **1.3** in THF ($C_{\mathbf{1.3}}$ = 2 mg mL^{-1}; **1.3**: 0.095 mg, 1.3 x 10^{-4} mmol, 1 eq.) was added to the dissolved polymer rapidly in one portion. The mixture was stirred at room temperature for 5 min. Two 5 µL aliquots were taken for ^{1}H NMR and SEC analysis, before addition of **tBuODA-MM** (29 mg, 3.9 x 10^{-3} mmol, 30 eq.) dissolved in 175 µL of THF. The mixture was stirred at room temperature for an additional 10 min. Two 5 µL aliquots were taken for ^{1}H NMR and SEC analysis, before addition of **IrPPY-MM** (27 mg, 3.9 x 10^{-3} mmol, 30 eq.) dissolved in 175 µL of

THF. The mixture was stirred at room temperature for an additional 20 min. Two 5 μL aliquots were taken for ^{1}H NMR and SEC analysis, before addition of **IrPIQ-MM** (29 mg, 3.9 x 10^{-3} mmol, 30 eq.) dissolved in 175 μL of THF. The mixture was stirred at room temperature for an additional 35 min. Two 5 μL aliquots were taken for ^{1}H NMR and SEC analysis, before addition of **ETL-MM** (27 mg, 3.9 x 10^{-3} mmol, 30 eq.) dissolved in 175 μL of THF. The mixture was stirred at room temperature for an additional 1 h. Two 5 μL aliquots were taken for ^{1}H NMR and SEC analysis, and the polymerization was removed from the glove box, quenched with one drop of ethyl vinyl ether, and immediately purified by preparatory SEC (silylated Toyopearl HW-55F resin) in THF and fractions containing polymer were determined by SEC analysis. All fractions containing polymer were collected and concentrated then precipitated into MeOH and dried *in vacuo* overnight. Yield = 65 mg (48%). M_n = 827 kDa, Đ = 1.33, DP_n B1/B2/B3/B4/B5 = 26/26/26/26/17. ^{1}H NMR (400 MHz, chloroform-*d*) δ 9.28 (t, *J* = 6.2 Hz, 0.3H), 8.77 (br, s, 0.3H), 8.59 – 8.16 (br, m, 38H), 7.97 (br, m, 52H), 7.20 (br, m, 446H), 6.64 – 6.50 (br, m, 2H), 6.15 – 5.91 (br, m, 2H), 5.78 (br, m, 2H), 4.93 (br, m, 85H), 4.15 (br, m, 6H), 3.88 (br, s, 8H), 2.47 (br, m, 25H), 2.34 – 1.96 (br, s, 118H), 1.53 (br, m, 89H), 1.34 (br, m, 10H), 1.30 – 0.86 (br, m, 77H).

Silylation of HW-55F Resin:

To a 250 mL Erlenmeyer flask was added 250 mL of THF-saturated Toyopearl HW-55F resin followed by a further 250 mL of THF. Et_3N (4.0 g, 5.5 mL, 39.5 mmol) and trimethylsilyl chloride (4.3 g, 5 mL, 39.5 mmol) were then added sequentially with gentle mixing. The mixture was left to stand for 16 h, then transferred to a filtration funnel with glass frit and washed with 500 mL THF:EtOH (1:1 v/v) followed by 500 mL THF. This re-usable resin can then be used to purify Ir(acac)-containing polymers with no observed retention of the iridium complex.

Chapter 5: Donor–Acceptor Materials Exhibiting Thermally Activated Delayed Fluorescence Using a Planarized *N*-Phenylbenzimidazole Acceptor

5.1 Introduction

The discovery of thermally activated delayed fluorescence (TADF) has revolutionized organic light-emitting diode (OLED) technology, enabling the fabrication of OLEDs with 100% internal quantum efficiencies using purely organic emitters.[127–131] Capable of converting triplet excitons to singlets through reverse intersystem crossing (RISC), TADF compounds have attracted significant recent attention as robust, efficient and scalable emissive materials.[132–136] Though applications in OLEDs have been the primary driver of TADF research to date, these materials have also found use in fluorescence lifetime imaging[270,271] and oxygen sensing.[272] To achieve efficient RISC, TADF materials are typically designed to minimize the energy difference between the lowest triplet (T_1) and lowest singlet (S_1) excited states, termed ΔE_{ST}.

While T_1 states are substantially lower in energy than their S_1 counterparts in the vast majority of molecules, a small ΔE_{ST} can be achieved by minimizing the Pauli repulsion (or exchange energy) between ground and excited state electrons. In practical terms, this is commonly achieved by designing materials with minimal overlap between their HOMO and LUMO, such that the electrons of the frontier orbitals will occupy different regions of space when the material is excited. This is often obtained by the coupling of donor and acceptor units in a twisted conformation,[137,139,140] sometimes using steric bulk to ensure that the π systems of the donor and acceptor remain orthogonal.[138] This type of conformation also results in emitters with large transition dipoles and significant charge-transfer character, including broad emission bands and large Stokes shifts.

More recently, several studies have demonstrated that molecular rigidification can lead to narrower emission spectra, higher quantum yields and enhanced stability in luminescent materials, primarily as a result of suppressed vibrational motion.[144,145] For example, Yamaguchi and coworkers utilized the idea of structural constraint to create an extremely photo-stable phosphole-based dye for multiple-acquisition stimulated emission depletion (STED) imaging.[273,274] Furthermore, they synthesized a series of planarized 9-phenylanthracene derivatives, in which the planar and rigid structure induced effective π-conjugation and reduced the nonradiative decay process from the excited state, resulting in red-shifted absorptions, increased molar absorption coefficients, and intense fluorescence.[275–279] Hatakeyama and coworkers have also leveraged an organoboron compound, possessing two nitrogen atoms, in a rigid polycyclic aromatic framework to produce ultrapure blue TADF emitters in this fashion.[130,144,145]

Deep blue or violet TADF emitters pose a particular synthetic challenge, in light of the large Stokes shifts typically caused by the common donor-acceptor conformation of TADF materials.[254,280–285] To realize deep blue emission a wide energy gap >2.75 eV is required, therefore an electron acceptor with a shallow LUMO is ideal. Imidazole and benzimidazole are attractive electron acceptors for this reason, and many imidazole-based blue fluorescent emitters have been reported with PLQYs near unity and high OLED efficiencies.[286–289] However, there are few reports in which imidazole-containing compounds have exhibited TADF. In 2018, Wang and coworkers[290] reported highly efficient green organic light emitting diodes with phenanthroimidazole-based TADF emitters, and shortly after Kido and coworkers reported a series of imidazo[1,2-f]phenanthridine-based sky-blue TADF compounds.[291]

Herein we report the design of a planarized 1-phenylbenzimidazole chromophore which has been linked via a methylene bridge at the 2 and 7 positions of the phenyl ring and the

benzimidazole, respectively (Figure 5.1). This fused imidazole/acridine chromophore (IMAC, formally 6,6-dimethyl-6H-imidazo[4,5,1-de]acridine) was then used to prepare donor-π-acceptor materials using six different donor moieties commonly used in organic electronics, including phenoxazine (PXZ), phenothiazine (PTZ), 9,9-dimethylacridan (ACR), and carbazole (CZ). Several of these molecules exhibit TADF with deep blue to green emission colours, and quantum yields of up to 0.99. These compounds should find application in the emitting layer of OLEDs, either as the emitter or as ambipolar host materials.

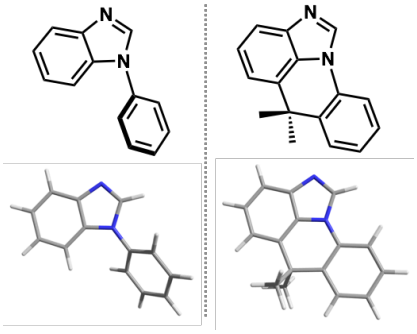

Figure 5.1. Optimized structure for 1-phenyl-1H-benzo[d]imidazole (left) and 6,6-dimethyl-6H-imidazo[4,5,1-de]acridine (right).

5.2 Results and Discussion

5.2.1 Synthesis and solid-state structure

Synthesis of the IMAC acceptor fragment began with a double Grignard addition to methyl anthranilate using MeMgBr to give tertiary alcohol **5.1**, which was then protected using 1,1'-carbonyldiimidazole to give carbamate **5.2** (Scheme 5.1). Nucleophilic aromatic substitution of *o*-nitrofluorobenzene with **5.2** was then used to obtain **5.3** in 70% yield. Hydrolysis of the carbamate was achieved in the presence of NaOH, followed by electrophilic aromatic substitution in the presence of H_3PO_4 to form the nitrosylated acridine **5.5**. Reduction of the nitro group to a primary

amine was achieved using Pd/C and hydrazine, yielding **5.6** quantitatively and giving a planarized, *ortho*-diamine which can be used to prepare benzimidazoles from a variety of aldehydes. Finally, a series of phenylaldehyde-linked donors were coupled with **5.6** via I_2-mediated intramolecular C-H amidation to synthesize the target donor-π-acceptor compounds in yields ranging from 56% to 65%. The identity of final compounds was confirmed by ^{1}H and $^{13}C\{^{1}H\}$ NMR, as well as high resolution mass spectrometry (HRMS).

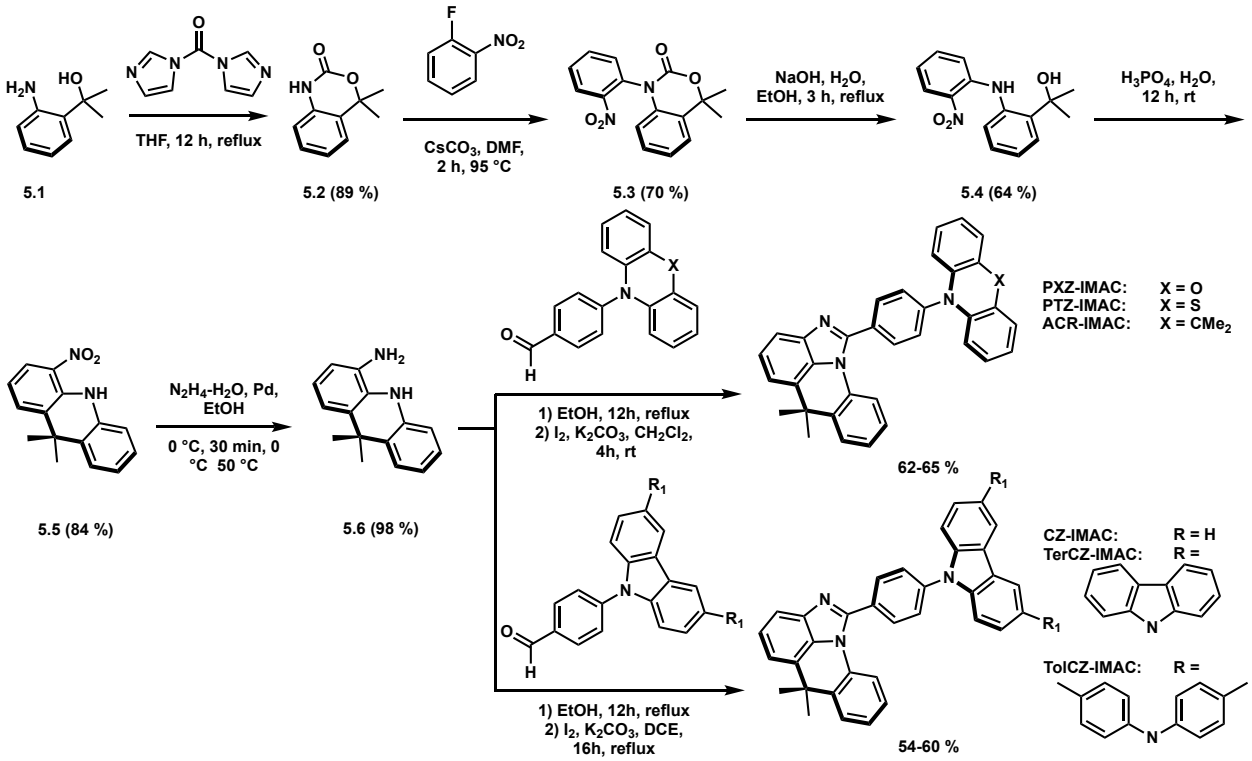

Scheme 5.1. Synthesis of IMAC compounds.

Single crystals of **PXZ-IMAC, PTZ-IMAC**, **ACR-IMAC**, and **CZ-IMAC** were obtained from a mixture of CH_2Cl_2 and hexanes by slow evaporation (Figure 5.2). The solid-state structures indicate the donor groups are twisted with respect to the phenyl ring giving very large dihedral angles of 81.3 and 82.4° for **PXZ-IMAC** and **ACR-IMAC**, respectively. **PTZ-IMAC** and **CZ-**

IMAC have more moderated twisting with dihedral angles of 69.3 and 60.0°, respectively. Such twisted structures typically result from the steric repulsion of hydrogen atoms in the phenyl and heteroaromatic units. Further, it results in effective spatial separation of the HOMO and LUMO and reduction of ΔE_{ST}. There also exists a moderate twist between the imidazole plane and the phenyl ring resulting in dihedral angles between 52.5–57.5°. **PXZ-IMAC, PTZ-IMAC**, and **ACR-IMAC** all pack in the P21/c space group, while **CZ-IMAC** packs in the P-1 space group. Additionally, the **CZ-IMAC** derivative is the only compound to co-crystallize with solvent (CH_2Cl_2).

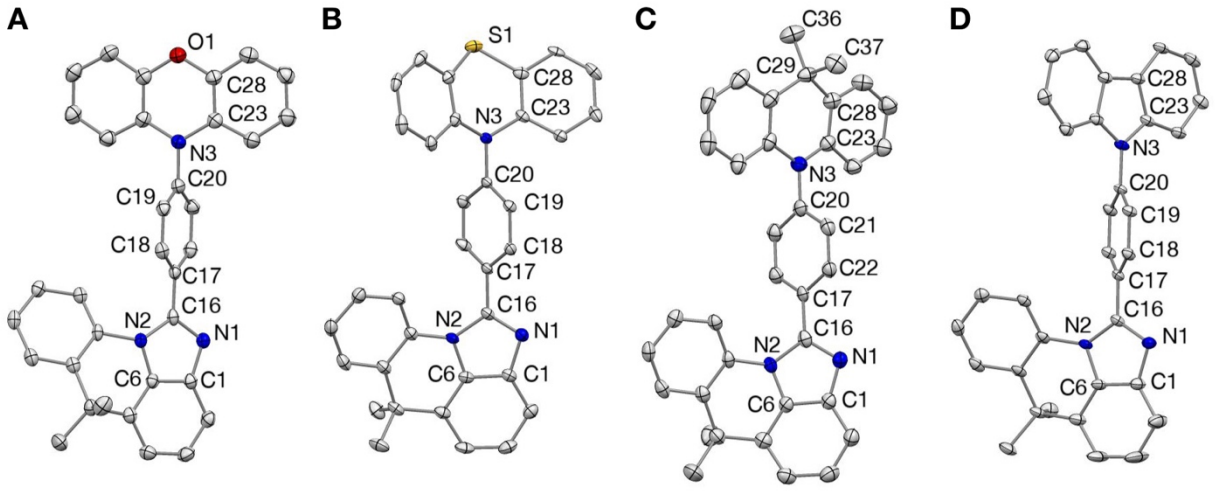

Figure 5.2. Crystal structures of (A) **PXZ-IMAC**, (B) **PTZ-IMAC**, (C) **ACR-IMAC**, and (D) **CZ-IMAC** depicted with 50 % thermal ellipsoids. Hydrogen atoms and co-crystallized solvent molecules omitted for clarity. Selected bond lengths (Å): **PXZ-IMAC**; N1–C16 1.319(2), N2–C16 1.397(3), N3–C20 1.437(3) **PTZ-IMAC**; N1–C16 1.318(3), N2–C16 1.396(2), N3–C20 1.437(2) **ACR-IMAC**; N1–C16 1.326(3), N2–C16 1.400(3), N3–C20 1.436(3) **CZ-IMAC**; N1–C16 1.318(3), N2–C16 1.392(2), N3–C20 1.428(2). Selected torsion angles (°): **PXZ-IMAC**; N1–C16–C17–C18 135.0(2), C19–C20–N3–C23 98.7(2) **PTZ-IMAC**; N1–C16–C17–C18 57.5(3), C19–C20–N3–C23 69.3(2) **ACR-IMAC**; N1–C16–C17–C18 134.2(2), C19–C20–N3–C23 97.6(3) **CZ-IMAC**; N1–C16–C17–C18 52.5(3), C19–C20–N3–C23 120.0(2).

5.2.2 Photophysical and Electrochemical Properties

UV-vis absorption and photoluminescence (PL) spectra of this series of compounds in toluene solution (1×10^{-5} M) are shown in Figure 5.3. Absorption maxima are between 293 and 308 nm and all compounds have broad, featureless emission spectra consistent with a charge-transfer excited state. Based on TD-DFT calculations we attribute the lowest energy transition in all cases to the HOMO to LUMO transition. TD-DFT predicts **PXZ-IMAC**, **PTZ-IMAC**, **ACR-IMAC**, and **TolCZ-IMAC** to all have lowest energy transitions above 395 nm, significantly higher than the **CZ-IMAC** or **TerCZ-IMAC** derivatives (Table 5.1). However, the oscillator strengths are calculated to be 0.0004 (extremely low) for the **PTZ-IMAC** and 0.0002 for the **ACR-IMAC** derivatives, slightly higher at 0.0142 for the **PXZ-IMAC** derivative and much higher at 0.2792 for the **TolCZ-IMAC** derivative, consistent with apparent intensities observed in their experimental spectra. All compounds showed strong positive solvatochromism in the fluorescence spectra, with significant red shifts in polar relative to nonpolar solvents. The effect was most pronounced for **TolCZ-IMAC** and **PNX-IMAC**, with red shifts of 176 (5861 cm^{-1}) and 157 nm (5510 cm^{-1}) going from hexanes to MeCN, respectively. **CZ-IMAC** had the least dramatic shift of 3676 cm^{-1} going from 378 to 439 nm as the solvent polarity was increased from hexanes to MeCN. For simplicity Stokes shifts discussed in this paper are the apparent shifts from the largest absorption band to the emission maxima. It has previously been reported that chromophores containing *N*-phenylphenothiazine can adopt two conformations, termed quasi-axial and quasi-equatorial, differing in the relative orientations of the phenothiazine moiety and the phenyl ring.[292–295] Such conformers often result in dual emission properties, as is observed in **PTZ-IMAC**, with peaks at ~400 and ~530 nm and may also explain its low photoluminescence quantum yield (PLQY, Φ).

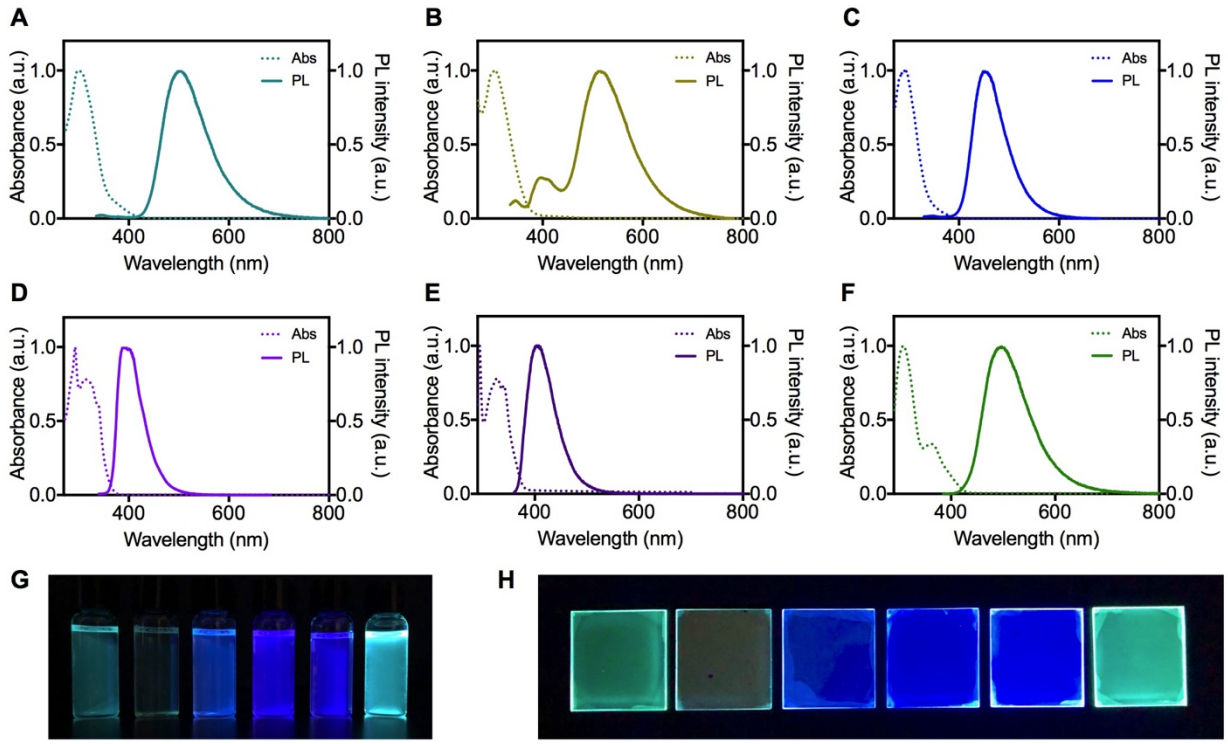

Figure 5.3. UV-vis spectra measured in CH_2Cl_2 at 1×10^{-5} M and PL spectra measured in toluene solution at 0.05 to 0.15 optical density for (A) **PXZ-IMAC**, (B) **PTZ-IMAC**, (C) **ACR-IMAC**, (D) **CZ-IMAC**, (E) **TerCZ-IMAC**, and (F) **TolCZ-IMAC**. Photographs of the series of compounds in toluene (G) and as 10 wt% films in DPEPO (H) irradiated with 365 nm light.

Table 5.1. TD-DFT results for the HOMO to LUMO transition in IMAC compounds.

Entry	Total Energy (Hartree)[a]	λ (nm)[b]	ΔE (eV) [b]	f[b]
PXZ-IMAC	–1548.40	448	2.77	0.0142
PTZ-IMAC	–1879.30	397	3.12	0.0004
ACR-IMAC	–1591.06	405	3.06	0.0002
CZ-IMAC	–1473.28	339	3.65	0.5135
TerCZ-IMAC	–2504.65	362	3.43	0.3028
TolCZ-IMAC	–2664.05	424	2.93	0.2792

[a]Calculated total energy of the optimized structures in S_0. [b]Calculated with TDA-DFT on neutral condition optimized structures in S_1.

In order to probe the delayed fluorescence behavior of the series of compounds, transient photoluminescence decay curves for each compound doped in bis[2-(diphenylphosphino)phenyl] ether oxide (DPEPO) films (10 wt%) were measured at room temperature. DPEPO was chosen since it is a large band gap material commonly used to host blue TADF materials in OLEDs. As shown in Figure 5.4 and summarized in Table 5.2, the doped films of **PXZ-IMAC**, **PTZ-IMAC**, **ACR-IMAC**, and **TolCZ-IMAC** showed clear long-lived exponential decays at 300 K. **PXZ-IMAC** exhibits a two-component short lifetime of 4.2 ns and 13.8 ns and a long lifetime of 1390 μs, and these are 2.1 ns, 10.1 ns and 228 μs for **PTZ-IMAC**. **ACR-IMAC** and **TolCZ-IMAC** had lifetimes of 5.7 ns, 14.2 ns, 127 μs and 4.4 ns, 13.1 ns, 1194 μs, respectively. The two-component nature of the short lifetimes is likely a result of the film consisting of both an IMAC emitter and DPEPO host, thus there is possibility for direct excitation of the emitter as well as for energy transfer from the host to emitter. The short lifetime component was attributed to relaxation from S_1 to S_0, and the delayed component was assigned to thermal up-conversion of excitons from T_1

to S_1, followed by relaxation from S_1 to S_0. PL decay curves were measured for **PXZ-IMAC**, **PTZ-IMAC**, **ACR-IMAC**, and **TolCZ-IMAC** at 77 K and in all cases the delayed component was suppressed, confirming the thermal dependence (Figure 5.5). Time-resolved emission spectra of all compounds were obtained in 2-MeTHF solution measured at 77 K (Figure 5.6) in order to determine the singlet-triplet gap for each compound. Singlet-triplet gaps were also calculated for each compound according to Adachi's method.[131,296] We also note that the delayed fluorescence lifetimes for **TolCZ-IMAC** and **PXZ-IMAC** are much longer than those of **PTZ-IMAC** and **ACR-IMAC**, while their solid-state quantum yields are significantly higher (Table 5.2). Films of **CZ-IMAC** and **TerCZ-IMAC** had no observable delayed component under these conditions, consistent with DFT calculations indicating these compounds possess a larger ΔE_{ST} (*vide infra*).

Table 5.2. Photophysical properties of IMAC compounds.

Entry	$\lambda_{max,\ abs}$[a]	$\lambda_{max,\ em}$[b]	Φ Solution[b]/Solid[c]	CIE[b]	τ_p (ns)[c]	τ_d (μs)[c]
PXZ-IMAC	298	502	0.31/0.71	(0.23, 0.43)	4.2, 13.8	1390
PTZ-IMAC	303	515	0.08/0.05	(0.27, 0.44)	2.1, 10.1	228
ACR-IMAC	293	450	0.34/0.51	(0.15, 0.12)	5.7, 14.2	127
CZ-IMAC	293	394	0.99/0.85	(0.16, 0.03)	1.9, 28.2	–
TerCZ-IMAC	294	401	0.94/0.61	(0.16, 0.04)	2.9, 17.2	–
TolCZ-IMAC	308	496	0.85/0.45	(0.21, 0.39)	4.4, 13.1	1194

[a]Measured in CH_2Cl_2. [b]Measured in degassed toluene with an optical density between 0.05 and 0.15. [c]Measured as films doped in DPEPO at 10 wt % under vacuum. DPEPO: Bis[2-(diphenylphosphino)phenyl] ether oxide.

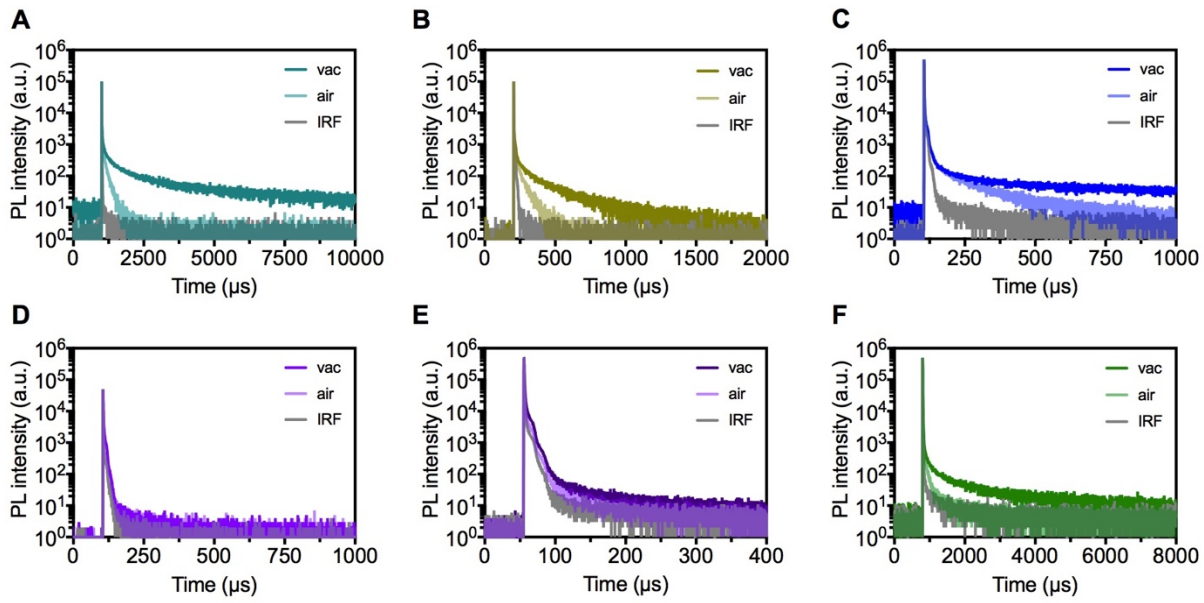

Figure 5.4. PL decay curves for (A) **PXZ-IMAC**, (B) **PTZ-IMAC**, (C) **ACR-IMAC**, (D) **CZ-IMAC**, (E) **TerCZ-IMAC**, and (F) **TolCZ-IMAC** doped in 10 wt % DPEPO films at 300 K.

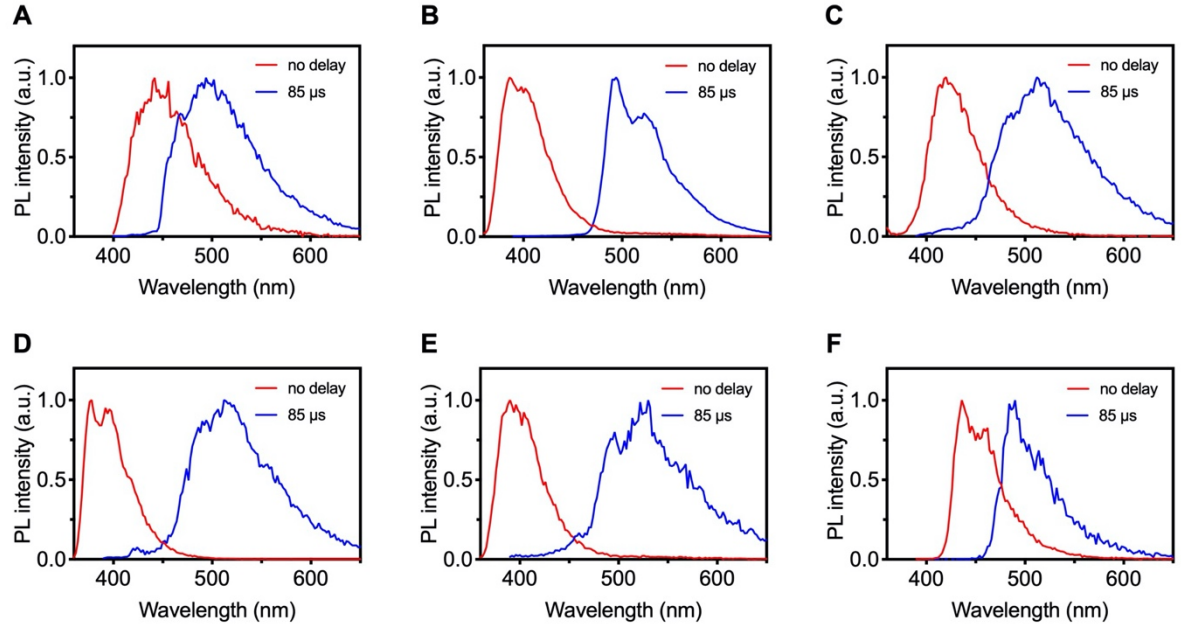

Figure 5.5. Time-resolved emission spectra of (a) **PXZ-IMAC**, (b) **PTZ-IMAC**, (c) **ACR-IMAC**, (d) **CZ-IMAC**, (e) **TerCZ-IMAC**, and (f) **TolCZ-IMAC** in 2-MeTHF measured at 77 K.

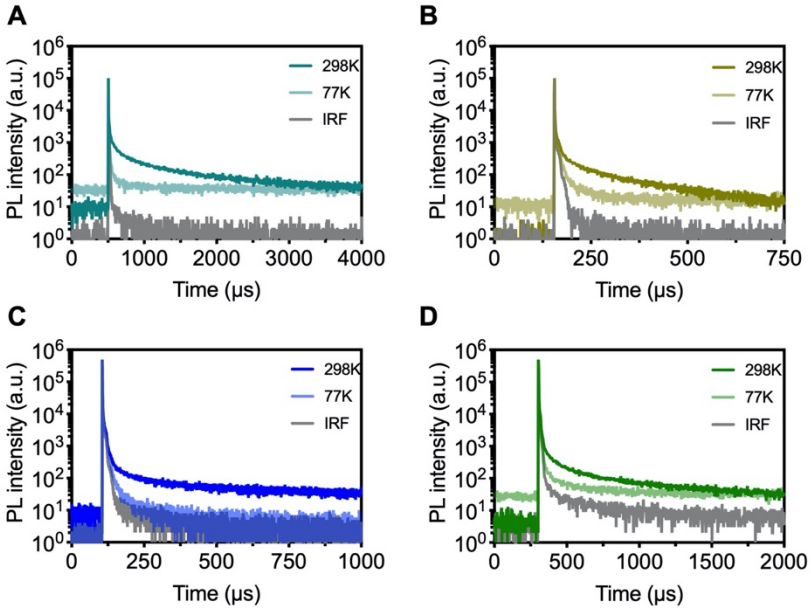

Figure 5.6. PL decay curves of (a) **PXZ-IMAC**, (b) **PTZ-IMAC**, (c) **ACR-IMAC**, and (d) **TolCZ-IMAC** doped in 10 wt % DPEPO films measured at 298 K and 77 K.

The electrochemical properties and energy levels of these compounds were investigated by cyclic voltammetry in DMF using a conventional three electrode system. All compounds have a reversible one-electron reduction at approximately –2.50 eV (Table 5.3) relative to the $FeCp^{0/+}$ redox couple, arising from the IMAC unit. These are in reasonable agreement with similar donor-acceptor compounds containing benzimidazole.[289] The LUMO energy levels of the compounds were calculated to be approximately –1.4 eV. **TolCZ-IMAC** had the lowest oxidation potential at 0.21 eV, followed closely by **PXZ-IMAC** at 0.28 eV and **PTZ-IMAC** at 0.31 eV. **CZ-IMAC** and **ACR-IMAC** had significantly higher oxidation potentials at 0.49 and 0.51 eV, respectively. Oxidation of the **TerCZ-IMAC** could not be achieved within the solvent window of DMF, though a reduction peak was still observed for this compound.

Table 5.3. Calculated and experimental electronic properties of the series of IMAC compounds.

Compound	$E_{1/2}^{ox}$[a]	$E_{1/2}^{red}$[a]	HOMO (eV)		LUMO (eV)		E_g (eV)		ΔE_{ST} (eV)	
			Calc.	Exp.[b]	Calc.	Exp.[b]	Calc.	Exp.	Calc.	Exp.[d/e]
PXZ-IMAC	0.28	–2.52	–4.66	–5.08	–1.47	–2.28	2.77	2.92	0.03	0.29/0.27
PTZ-IMAC	0.31	–2.52	–4.98	–5.11	–1.46	–2.28	3.12	3.32	0.04	0.25/0.76
ACR-IMAC	0.51	–2.52	–4.90	–5.31	–1.41	–2.28	3.06	3.15	0.01	0.21/0.25
CZ-IMAC	0.49	–2.54	–5.37	–5.29	–1.40	–2.26	3.65	3.41	0.60	-/0.71
TerCZ-IMAC	–	–2.45	–5.18	–5.61[c]	–1.61	–2.35	3.43	3.35[c]	0.31	-/0.66
TolCZ-IMAC	0.21	–2.48	–4.50	–5.01	–1.40	–2.32	2.93	2.92	0.17	0.27/0.28

[a]In DMF relative to $FeCp^{0/+}$.
[b]Calculated from $E_{1/2}^{ox}$ relative to the $FeCp^{0/+}$ HOMO level (–4.80 eV).
[c]Calculated from the LUMO level and the optical energy gap, E_g. E_g was determined from the intersection point of the normalized emission and absorption spectra.
[d]Determined from the measurements of quantum yield and lifetime of the fluorescence and TADF components (Table S2) according to Adachi's method.[131,296]
[e]Determined from the high energy band edge of the phosphorescence spectrum in 2-MeTHF at 10^{-5} M at 77 K.

5.2.3 Theoretical Calculations

Quantum chemical calculations using density functional theory (DFT) with the PBE0/6-31+G(d) method/basis set in Gaussian 09 software were performed to obtain insight into the molecular conformation and electronic structures of these emissive materials. The calculation results, showing the optimized structure and HOMO/LUMO distribution of each compound, are given in Figure 5.7. Significant separation of the HOMO and LUMO is present for all compounds, with the HOMO mainly distributed on the donor group and the LUMO centered on the IMAC acceptor. **CZ-IMAC** was an exception to this trend, with the **IMAC** unit contributing significantly to the HOMO – consistent with the lack of observed delayed fluorescence for this material. We next

calculated the S_1 and T_1 excited state energies using the Tamm-Dancoff approximation to time-dependent density functional theory (TD-DFT). The calculated ΔE_{ST} values were <0.04 eV for **PXZ-IMAC**, **PTZ-IMAC**, and **ACR-IMAC**, consistent with their apparent TADF behavior. **CZ-IMAC** was calculated to have quite a large ΔE_{ST} of 0.60 eV, most likely due to the very weak donating ability of the CZ donor moiety leading to substantial overlap of the HOMO and LUMO on the **IMAC** fragment. **TerCZ-IMAC** and **TolCZ-IMAC** were calculated to have gaps of 0.31 and 0.17 eV, respectively. These values are small enough that efficient TADF should be possible. While the calculated ΔE_{ST} values support the observance of TADF, there exist substantial differences between the calculated and experimentally determined ΔE_{ST} values for all compounds. Due to charge-transfer nature of these materials, a gap-tuned range-separated hybrid functional like ωB97XD* might be used in the future to provide a more accurate estimation.[297]

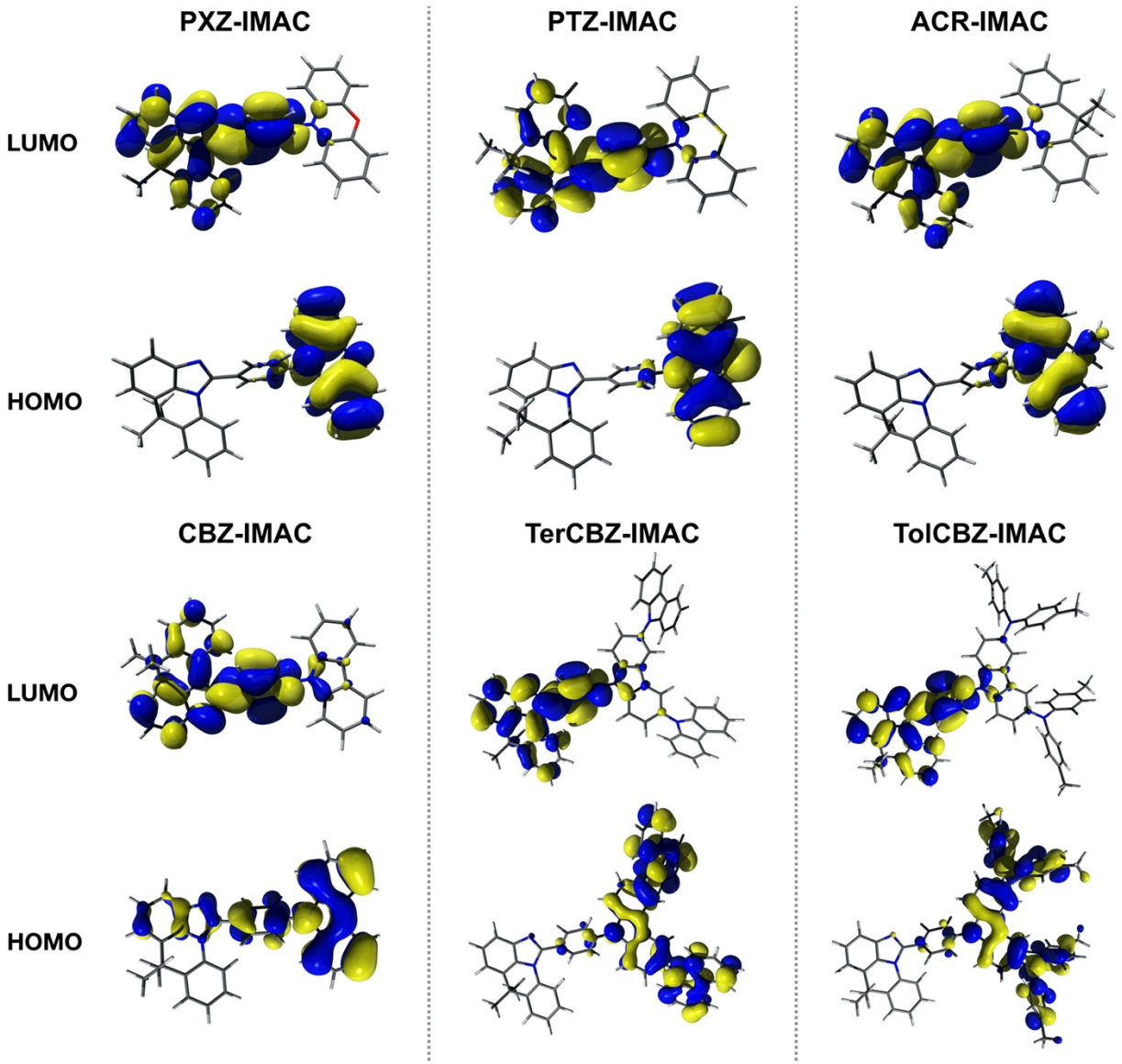

Figure 5.7. Optimized structures, and HOMO and LUMO distributions for the series of IMAC-containing compounds.

5.3 Conclusions

In summary, a planarized IMAC acceptor fragment was prepared and used to synthesize six donor-π-acceptor type emissive materials. Four of these donor-π-acceptor molecules exhibit TADF with deep blue to green emission colour in the solid state and photoluminescence quantum yields of up to 0.85 in solution. Additionally, two fluorescent emitters were prepared with carbazole and

tercarbazole donor moieties and quantum yields of 0.94 and 0.99, respectively. Theoretical calculations established the donor-acceptor character of the molecules, as well as indicated small ΔE_{ST} values for the compounds which exhibited delayed fluorescence. The results provide a promising opportunity for the design and synthesis of highly efficient TADF materials based on IMAC derivatives.

5.4 Experimental Details

General Considerations. All reactions and manipulations were carried out under a nitrogen atmosphere using standard Schlenk or glove box techniques unless otherwise stated. Dry solvents were obtained from Caledon Laboratories, dried using an Innovative Technologies Inc. solvent purification system, collected under vacuum, and stored under a nitrogen atmosphere over 4 Å molecular sieves. All reagents were purchased from Sigma-Aldrich, Cambridge Isotope Laboratories, Alfa Aesar or Tokyo Chemical Institute and used as received unless otherwise stated. Syntheses of the following compounds have been previously reported: **5.1**,[298] 4-(10*H*-phenoxazin-10-yl)benzaldehyde,[299] 4-(10*H*-phenothiazin-10-yl)benzaldehyde,[295] 4-(9*H*-carbazol-9-yl)benzaldehyde,[173] 4-(9'*H*-[9,3':6',9''-tercarbazol]-9'-yl)benzaldehyde,[300] and 9-benzyl-3,6-diiodo-9*H*-carbazole.[300] The ^{1}H and $^{13}C\{^{1}H\}$ nuclear magnetic resonance (NMR) spectra were measured on a Bruker AV III HD 400 MHz spectrometer with chloroform-*d* ($CDCl_3$), methylene chloride-d_2 (CD_2Cl_2), benzene-d_6 (C_6D_6) or dimethylsulfoxide-d_6 (DMSO-d_6) as the solvent. The chemical shift data are reported in units of δ (ppm) relative to residual solvent. Absorbance measurements were made on a Cary 60 spectrometer and fluorescence measurements were made on an Edinburgh Instruments FS5 spectrofluorometer. Absolute photoluminescence quantum yields were determined using an Edinburgh Instruments SC–30 Integrating Sphere Module;

toluene was used as the solvent and spectra obtained at approximately 10^{-5} M unless otherwise stated. Photoluminescence decay characteristics of the film samples were investigated under vacuum conditions using an Edinburgh Instruments FS5 spectrofluorometer and SC-80 sample holder. The fast decay component was recorded using time-correlated single photon counting in conjunction with a 313 nm EPLED excitation source, while the slow decay component was recorded using multichannel scaling with a pulsed Xe flash lamp source. Low temperature time-resolved emission spectra were measured on a Horiba PTI QM-400 spectrometer equipped with a Continuum PL8000 nanosecond YAG laser, operating at 355 nm, 10 Hz, and 1-2 mJ/pulse. Mass spectra were recorded on a Kratos MS-50 instrument using electron impact ionization. Melting points (mp) were determined using a Barnstead Electrotherm 1001D/1001 Mel-Temp capillary melting point apparatus equipped with a Fluke 51-II digital thermometer.

Electrochemical Methods. Cyclic voltammograms were recorded using a BASi Epsilon Eclipse potentiostat at room temperature using a standard three-electrode configuration (working electrode: 3 mm diameter glassy carbon; reference electrode: RE-5B Ag/AgCl electrode in saturated aqueous KCl (BASi Inc.), referenced externally to ferrocene/ferrocenium (0.543 V in DMF);[199] counter electrode: Pt wire) in 0.1 M tetrabutylammonium hexafluorophosphate in DMF. Experiments were run at a scan rate of 100 mV s^{-1} in dry degassed electrolyte solution with ~1 mg mL^{-1} of analyte.

Density Functional Theory. Calculations were performed using the Gaussian 09 software package.[235] Ground state geometries and energies were calculated at the PBE0/6-31+G(d) level of theory. The singlet and triplet states were calculated by the Tamm-Dancoff approximation to time-dependent density functional theory (TD-DFT) with the PBE0 functional at the same basis set

level. Molecular orbitals were visualized using Avogadro version 1.20 and rendered using POV-Ray version 3.7.0.

5.4.1 Synthetic Procedures

Synthesis of 4,4-dimethyl-1,4-dihydro-2H-benzo[d][1,3]oxazin-2-one (5.2). A mixture of *N,N'*-carbonyldiimidazole (24.4 g, 150 mmol) and 2-(2-aminophenyl)propan-2-ol (**1)** (18.0 g, 119 mmol) in THF (500 mL) was refluxed for 16 h. The solvent was evaporated under reduced pressure to give a yellow oil, which was redissolved in CH_2Cl_2 and washed with saturated aqueous NH_4Cl, 2 N HCl solution, and brine. The organic layer was dried over anhydrous $MgSO_4$ and concentrated to afford a yellow solid. Yield = 17.8 g (85%). mp. = 106.5-108.6 °C. ^{1}H NMR (400 MHz, DMSO-d_6): δ 10.20 (s, 1H), 7.32 – 7.19 (m, 2H), 7.04 (td, J = 7.6, 1.2 Hz, 1H), 6.91 (dd, J = 7.9, 1.1 Hz, 1H), 1.62 (s, 6H). ^{13}C NMR (101 MHz, DMSO-d_6): δ 150.7, 134.7, 128.6, 126.2, 123.4, 122.6, 114.0, 81.3, 27.6. HRMS (EI) *m/z*: [$M^{+\bullet}$] calcd for $[C_{10}H_{11}NO_2]^{+\bullet}$, 177.07898; found, 177.07862; difference: –2.02 ppm.

Synthesis of 4,4-dimethyl-1-(2-nitrophenyl)-1,4-dihydro-2H-benzo[d][1,3]oxazin-2-one (5.3). A mixture of **5.2** (17.8 g, 100 mmol), 1-fluoro-2-nitrobenzene (15.7 g, 111 mmol) and $CsCO_3$ (39.1 g, 121 mmol) in DMF (250 mL) was heated to 95 °C for 16 h. After cooling to room temperature, the reaction was poured into 500 mL of water and extracted with EtOAc (5 × 100 mL). The combined organic layer was washed with water and brine, dried over anhydrous $MgSO_4$, concentrated to give a bright yellow oil, and then purified through silica gel column chromatography (Hexanes/EtOAc 4:1, R_f = 0.02 gradient to Hexanes/EtOAc 1:1) to afford a yellow solid. mp. = 89.8-91.7 °C. Yield = 21.1 g (70 %). ^{1}H NMR (400 MHz, DMSO-d_6): δ 8.29 (dd, J = 8.2, 1.5 Hz, 1H), 7.96 (td, J = 7.7, 1.5 Hz, 1H), 7.83 (td, J = 7.8, 1.4 Hz, 1H), 7.76 (dd, J

= 7.9, 1.4 Hz, 1H), 7.47 (dd, *J* = 7.6, 1.6 Hz, 1H), 7.22 (dtd, *J* = 24.3, 7.6, 1.4 Hz, 2H), 6.31 (dd, *J* = 8.0, 1.2 Hz, 1H), 1.81 (s, 3H), 1.78 (s, 3H). ^{13}C NMR (101 MHz, DMSO-d_6): δ 149.6, 146.9, 136.4, 135.4, 131.9, 130.6, 130.2, 128.9, 127.7, 125.8, 123.8, 123.8, 114.6, 82.0, 28.1, 27.1. HRMS (EI) *m/z*: [$M^{+\bullet}$] calcd for $[C_{16}H_{14}N_2O_4]^{+\bullet}$, 298.09536; found, 298.09503; difference: –1.08 ppm.

Synthesis of 2-{2-[(2-nitrophenyl)amino]phenyl}propan-2-ol (5.4). A mixture of **5.3** (21.0 g, 70.4 mmol) and 5% aqueous NaOH (10 g NaOH in 200 mL water) in EtOH (300 mL) was heated to reflux for 16 h. The reaction mixture turned from light yellow to dark red. The solvent was partially removed under reduced pressure before the mixture was poured into 500 mL of water, sonicated for 15 min, and the resulting bright orange powder collected by vacuum filtration. Yield = 12.4 g (64 %). mp. = 129.5-131.0 °C. ^{1}H NMR (400 MHz, DMSO-d_6): δ 10.06 (s, 1H), 8.05 (dd, *J* = 8.5, 1.4 Hz, 1H), 7.85 (dt, *J* = 7.6, 1.1 Hz, 1H), 7.53 – 7.45 (m, 1H), 7.29 – 7.15 (m, 2H), 7.10 – 6.93 (m, 2H), 1.58 (s, 6H). ^{13}C NMR (101 MHz, DMSO-d_6): δ 135.5, 135.0, 133.0, 132.9, 131.7, 129.0, 127.1, 125.4, 123.9, 122.8, 118.9, 116.2, 36.2, 31.4. HRMS (EI) *m/z*: [$M^{+\bullet}$] calcd for $[C_{15}H_{16}N_2O_3]^{+\bullet}$, 272.11609; found, 272.11664; difference: 2.03 ppm.

Synthesis of 9,9-dimethyl-4-nitro-9,10-dihydroacridine (5.5). A suspension of **5.4** (12.4 g, 45.5 mmol) in H_3PO_4 (200 mL) was stirred for 16 h. The reaction mixture turned from orange to dark red. The mixture was poured into water (500 mL) and the resulting bright red powder collected by vacuum filtration. Yield = 9.7 g (84 %). mp. = 134.1-135.6 °C. ^{1}H NMR (400 MHz, DMSO-d_6): δ 10.05 (s, 1H), 8.04 (dd, *J* = 8.5, 1.5 Hz, 1H), 7.83 (dt, *J* = 7.5, 1.1 Hz, 1H), 7.48 (dd, *J* = 7.8, 1.3 Hz, 1H), 7.27 – 7.15 (m, 2H), 7.05 (ddd, *J* = 8.4, 7.1, 1.5 Hz, 1H), 6.99 (dd, *J* = 8.5, 7.5 Hz, 1H), 1.56 (s, 6H). ^{13}C NMR (101 MHz, DMSO-d_6): δ 135.5, 135.0, 133.0, 132.8, 131.6, 129.0, 127.1,

125.4, 123.9, 122.8, 118.9, 116.1, 36.2, 31.4. HRMS (EI) *m/z*: [$M^{+\bullet}$] calcd for [$C_{15}H_{14}N_2O_2$]$^{+\bullet}$, 254.10553; found, 254.10452; difference: –3.96 ppm.

Synthesis of 9,9-dimethyl-9,10-dihydroacridin-4-amine (5.6). A mixture of **5.5** (143 mg, 0.562 mmol) in EtOH (5 mL) was cooled to 0 °C and placed under a flow of N_2 gas. Pd/C (6 mg, 0.06 mmol) was added to the stirred solution followed by very slow addition of N_2H_4. The mixture was stirred for 30 min then slowly allowed to warm to room temperature (care was taken to ensure the reaction vessel was not over-pressurizing) followed by heating to 50 °C. After 2 h the reaction was cooled to room temperature and subsequently filtered using EtOH to rinse. The filtrate was collected and concentrated to give a black solid. Yield = 123 g (99 %). mp. = 108.2-110.6 °C. ^{1}H NMR (400 MHz, DMSO-d_6): δ 7.80 (s, 1H), 7.34 (d, *J* = 7.8 Hz, 1H), 7.07 (t, *J* = 7.5 Hz, 1H), 6.94 (dd, *J* = 8.0, 1.3 Hz, 1H), 6.82 (t, *J* = 7.5 Hz, 1H), 6.70 (d, *J* = 7.7 Hz, 1H), 6.63 (t, *J* = 7.7 Hz, 1H), 6.53 (dd, *J* = 7.6, 1.4 Hz, 1H), 4.87 (s, 2H), 1.48 (s, 6H). ^{13}C NMR (101 MHz, DMSO-d_6): δ 139.1, 133.3, 128.1, 128.1, 126.3, 125.5, 125.1, 119.8, 119.4, 113.8, 113.7, 112.6, 35.6, 30.7. HRMS (EI) *m/z*: [$M^{+\bullet}$] calcd for [$C_{15}H_{16}N_2$]$^{+\bullet}$, 224.13135; found, 224.13112; difference: –1.00 ppm.

Synthesis of 10-[4-(6,6-dimethyl-6H-imidazo[4,5,1-de]acridin-1-yl)phenyl]-10H-phenoxazine (PXZ-IMAC). A mixture of **5.6** (100 mg, 0.446 mmol) and 4-(10*H*-phenoxazin-10-yl)benzaldehyde (141 mg, 0.491 mmol) in EtOH (10 mL) was refluxed for 16 h. The solvent was evaporated under reduced pressure to give a yellow oil, which was redissolved in CH_2Cl_2 (10 mL), followed by the sequential addition of iodine (135 mg, 0.532 mmol) and K_2CO_3 (185 mg, 1.34 mmol). The reaction mixture was stirred at reflux temperature for another 16 h. Upon completion of the reaction, it was quenched with 5% $Na_2S_2O_3$ (20 mL) and then extracted with CH_2Cl_2 (10

mL × 3). The combined organic layer was washed with brine (20 mL), dried over anhydrous $MgSO_4$, concentrated, and then purified through silica gel column chromatography (1:1, hexanes:CH_2Cl_2, R_f = 0.25) to afford a yellow/green solid. Yield = 136 mg (62 %). X-ray quality crystals were obtained from the slow evaporation of a solution of **PXZ-IMAC** in CH_2Cl_2/hexanes. mp. = 221.2-223.1 °C. ^{1}H NMR (400 MHz, methylene chloride-d_2): δ 8.14 – 8.06 (m, 2H), 7.69 (ddd, J = 18.5, 7.8, 1.4 Hz, 2H), 7.64 – 7.59 (m, 2H), 7.51 – 7.36 (m, 2H), 7.34 – 7.23 (m, 2H), 7.14 (ddd, J = 8.5, 7.4, 1.5 Hz, 1H), 6.83 – 6.65 (m, 6H), 6.24 – 6.10 (m, 2H), 1.82 (s, 6H). ^{13}C NMR (101 MHz, methylene chloride-d_2): δ 150.4, 144.4, 141.3, 141.0, 136.7, 134.4, 133.7, 133.4, 132.9, 131.9, 131.7, 130.7, 128.4, 127.0, 125.9, 125.0, 123.8, 122.0, 119.1, 117.1, 116.9, 115.8, 113.8, 38.0, 33.0. HRMS (EI) *m/z*: [$M^{+\bullet}$] calcd for $[C_{34}H_{25}N_3O_1]^{+\bullet}$, 491.19976; found, 491.19866; difference: –2.24 ppm.

Synthesis of 10-[4-(6,6-dimethyl-6H-imidazo[4,5,1-de]acridin-1-yl)phenyl]-10H-phenothiazine (PTZ-IMAC). A mixture of **5.6** (100 mg, 0.446 mmol) and 4-(10*H*-phenothiazin-10-yl)benzaldehyde (149 mg, 0.491 mmol) in EtOH (10 mL) was refluxed for 16 h. The solvent was evaporated under reduced pressure to give a reddish oil, which was redissolved in CH_2Cl_2 (10 mL), followed by the sequential addition of iodine (135 mg, 0.532 mmol) and K_2CO_3 (185 mg, 1.34 mmol). The reaction mixture was stirred at reflux temperature for another 16 h. Upon completion of the reaction, it was quenched with 5% $Na_2S_2O_3$ (20 mL) and then extracted with CH_2Cl_2 (10 mL × 3). The combined organic layer was washed with brine (20 mL), dried over anhydrous $MgSO_4$, concentrated, and then purified through silica gel column chromatography (CH_2Cl_2, R_f = 0.15) to afford a yellow solid. Yield = 148 mg (65 %). X-ray quality crystals were obtained from the slow evaporation of a solution of **PTZ-IMAC** in CH_2Cl_2/hexanes. mp. = 259.8-261.1 °C. ^{1}H

NMR (400 MHz, methylene chloride-d_2): δ 8.05 – 7.97 (m, 2H), 7.70 (dd, J = 7.9, 1.5 Hz, 1H), 7.66 (dd, J = 7.7, 1.1 Hz, 1H), 7.60 – 7.53 (m, 2H), 7.48 – 7.38 (m, 2H), 7.35 (dd, J = 8.3, 1.3 Hz, 1H), 7.30 – 7.20 (m, 3H), 7.12 (tdd, J = 7.8, 6.0, 1.6 Hz, 3H), 7.02 (td, J = 7.5, 1.3 Hz, 2H), 6.74 (dd, J = 8.1, 1.3 Hz, 2H), 1.82 (s, 6H). ^{13}C NMR (101 MHz, methylene chloride-d_2): δ 150.7, 144.1, 143.8, 141.3, 136.7, 133.8, 132.2, 132.0, 131.2, 130.7, 128.3, 127.8, 127.7, 127.5, 127.0, 125.8, 124.9, 124.3, 124.0, 119.3, 119.0, 117.0, 1167.0, 38.0, 32.9. HRMS (EI) *m/z*: [$M^{+\bullet}$] calcd for $[C_{34}H_{25}N_3S_1]^{+\bullet}$, 507.17692; found, 507.17579; difference: –2.22 ppm.

Synthesis of 1-[4-(9,9-dimethylacridin-10(9H)-yl)phenyl]-6,6-dimethyl-6H-imidazo[4,5,1-de]acridine (ACR-IMAC). A mixture of **5.6** (100 mg, 0.446 mmol) and 4-(9,9-dimethylacridin-10(9*H*)-yl)benzaldehyde (**5.10**) (154 mg, 0.491 mmol) in EtOH (10 mL) was refluxed for 16 h. The solvent was evaporated under reduced pressure to give a yellow oil, which was redissolved in CH_2Cl_2 (10 mL), followed by the sequential addition of iodine (135 mg, 0.532 mmol) and K_2CO_3 (185 mg, 1.34 mmol). The reaction mixture was stirred at reflux temperature for the 16 h. Upon completion of the reaction, it was quenched with 5% $Na_2S_2O_3$ (20 mL) and then extracted with CH_2Cl_2 (10 mL × 3). The combined organic layer was washed with brine (20 mL), dried over anhydrous $MgSO_4$, concentrated, and then purified through silica gel column chromatography (CH_2Cl_2, R_f = 0.2) to afford an off white solid. Yield = 144 mg (63 %). X-ray quality crystals were obtained from the slow evaporation of a solution of **ACR-IMAC** in CH_2Cl_2/hexanes. mp. = 246.5-247.6 °C. ^{1}H NMR (400 MHz, methylene chloride-d_2): δ 8.05 – 7.92 (m, 2H), 7.55 (ddd, J = 12.9, 7.8, 1.3 Hz, 2H), 7.49 – 7.43 (m, 2H), 7.40 (dd, J = 7.7, 1.6 Hz, 2H), 7.35 – 7.19 (m, 3H), 7.13 (td, J = 7.6, 1.3 Hz, 1H), 7.01 (ddd, J = 8.6, 7.3, 1.5 Hz, 1H), 6.95 (ddd, J = 8.3, 7.2, 1.6 Hz, 2H), 6.87 (td, J = 7.4, 1.3 Hz, 2H), 6.36 (dd, J = 8.2, 1.3 Hz, 2H), 1.68 (s, 6H), 1.61 (s, 6H). ^{13}C NMR (101

MHz, methylene chloride-d_2): δ 150.6, 143.3, 141.3, 141.1, 136.8, 133.8, 133.1, 132.7, 132.2, 132.0, 130.8, 130.7, 128.4, 127.0, 126.8, 125.9, 125.7, 125.0, 121.3, 119.1, 117.1, 117.0, 114.6, 38.0, 36.4, 33.0, 31.3. HRMS (EI) *m/z*: [$M^{+\bullet}$] calcd for $[C_{37}H_{31}N_3]^{+\bullet}$, 517.25180; found, 517.25084; difference: –1.86 ppm.

Synthesis of 1-[4-(9H-carbazol-9-yl)phenyl]-6,6-dimethyl-6H-imidazo[4,5,1-de]acridine (CZ-IMAC). A mixture of **5.6** (100 mg, 0.446 mmol) and 4-(9*H*-carbazol-9-yl)benzaldehyde (135 mg, 0.498 mmol) in EtOH (10 mL) was refluxed for 16 h. The solvent was evaporated under reduced pressure to give a yellow oil, which was redissolved in CH_2Cl_2 (10 mL), followed by the sequential addition of iodine (135 mg, 0.532 mmol) and K_2CO_3 (185 mg, 1.34 mmol). The reaction mixture was stirred at reflux temperature for the 16 h. Upon completion of the reaction, it was quenched with 5% $Na_2S_2O_3$ (20 mL) and then extracted with CH_2Cl_2 (10 mL × 3). The combined organic layer was washed with brine (20 mL), dried over anhydrous $MgSO_4$, concentrated, and then purified through silica gel column chromatography (1 % MeOH in CH_2Cl_2, R_f = 0.20) to afford a light pink solid. The solid was dissolved in a minimal amount of CH_2Cl_2 and layered with hexane to give large X-ray quality crystals of **CZ-IMAC**. Yield = 118 mg (56%). mp. = 254.1-255.8 °C. ^{1}H NMR (400 MHz, DMSO-d_6): δ 8.33 (d, J = 7.8 Hz, 2H), 8.13 (d, J = 8.1 Hz, 2H), 7.93 (d, J = 8.1 Hz, 2H), 7.68 – 7.59 (m, 3H), 7.59 – 7.47 (m, 3H), 7.44 (t, J = 7.7 Hz, 1H), 7.38 (t, J = 7.4 Hz, 2H), 7.33 – 7.19 (m, 3H), 1.77 (s, 6H). ^{13}C NMR (101 MHz, DMSO-d_6): δ 149.7, 140.2, 139.8, 138.5, 135.8, 132.7, 131.4, 131.1, 130.8, 130.1, 128.4, 127.0, 126.9, 126.4, 125.7, 124.6, 123.0, 120.6, 120.4, 118.9, 116.4, 116.1, 109.8, 37.3, 32.6. HRMS (EI) *m/z*: [$M^{+\bullet}$] calcd for $[C_{34}H_{25}N_3]^{+\bullet}$, 475.20485; found, 475.20331; difference: –3.24 ppm.

*Synthesis of 1-[4-(9'H-[9,3':6',9''-tercarbazol]-9'-yl)phenyl]-6,6-dimethyl-6H-imidazo[4,5,1-de]acridine (**TerCZ-IMAC**).* A mixture of **5.6** (58.0 mg, 0.259 mmol) and 4-(9'*H*-[9,3':6',9''-tercarbazol]-9'-yl)benzaldehyde (170 mg, 0.283 mmol) in EtOH (10 mL) and 1,2-dichloroethane (10 mL) was refluxed for 16 h. The solvent was evaporated under reduced pressure to give a reddish oil, which was redissolved in 1,2-dichloroethane (10 mL), followed by the sequential addition of iodine (92 mg, 0.36 mmol) and K_2CO_3 (108 mg, 0.781 mmol). The reaction mixture was stirred at reflux temperature for another 16 h. Upon completion of the reaction, it was quenched with 5% $Na_2S_2O_3$ (20 mL) and then extracted with CH_2Cl_2 (10 mL × 3). The combined organic layer was washed with brine (20 mL), dried over anhydrous $MgSO_4$, concentrated, and then purified through silica gel column chromatography (CH_2Cl_2, R_f = 0.25) to afford an off-white solid. Yield = 131 mg (58 %). mp. = 243.5-245.4 °C. ^{1}H NMR (400 MHz, methylene chloride-d_2): δ 8.35 (d, J = 2.0 Hz, 2H), 8.23 – 8.14 (m, 6H), 8.03 – 7.97 (m, 2H), 7.88 (d, J = 8.7 Hz, 2H), 7.74 – 7.63 (m, 4H), 7.49 – 7.37 (m, 11H), 7.28 (m, 5H), 7.18 (m, 1H), 1.81 (s, 6H) ppm. ^{13}C NMR (101 MHz, methylene chloride-d_2): δ 150.5, 142.3, 141.5, 141.0, 139.3, 137.0, 134.0, 132.9, 132.2, 131.2, 131.0, 128.7, 127.8, 127.3, 126.9, 126.5, 126.2, 125.3, 124.9, 123.7, 120.8, 120.3, 120.3, 119.4, 117.3, 117.2, 112.1, 110.3, 38.2, 33.1 ppm. HRMS (EI) *m/z*: [$M^{+\bullet}$] calcd for $[C_{58}H_{39}N_5]^{+\bullet}$, 805.32055; found, 805.31727; difference: –3.28 ppm.

*Synthesis of 9-[4-(6,6-dimethyl-6H-imidazo[4,5,1-de]acridin-1-yl)phenyl]-N^3,N^3,N^6,N^6-tetra(p-tolyl)-9H-carbazole-3,6-diamine (**TolCZ-IMAC**).* A mixture of **5.6** (74.0 mg, 0.330 mmol) and 4-[3,6-bis(di-*p*-tolylamino)-9*H*-carbazol-9-yl]benzaldehyde (**5.7**) (300 mg, 0.453 mmol) in EtOH (10 mL) and 1,2-dichloroethane (10 mL) was refluxed for 16 h. The solvent was evaporated under reduced pressure to give a reddish oil, which was redissolved in 1,2-dichloroethane (10 mL),

followed by the sequential addition of iodine (117 mg, 0.461 mmol) and K_2CO_3 (137 mg, 0.991 mmol). The reaction mixture was stirred at reflux temperature for another 16 h. Upon completion of the reaction, it was quenched with 5% $Na_2S_2O_3$ (20 mL) and then extracted with EtOAc (10 mL × 3). The combined organic layer was washed with brine (20 mL), dried over anhydrous $MgSO_4$, concentrated, and then purified through silica gel column chromatography (1:1, hexanes:CH_2Cl_2, R_f = 0.30) to afford a green solid. Yield = 170 mg (60 %). mp. = 193.4-195.6 °C. ^{1}H NMR (400 MHz, benzene-d_6): δ 8.04–7.97 (m, 3H), 7.94 – 7.88 (m, 2H), 7.48–7.29 (m, 17H), 7.10–6.98 (m, 9H), 2.24 (s, 12H), 1.68 (s, 6H) ppm. ^{13}C NMR (101 MHz, benzene-d_6): δ 150.5, 147.0, 142.2, 142.0, 139.4, 138.2, 136.5, 134.1, 132.3, 131.8, 131.7, 131.1, 130.1, 128.4, 128.1, 127.9, 126.8, 126.6, 126.4, 125.5, 125.2, 125.1, 123.3, 118.9, 118.8, 117.9, 117.1, 111.3, 37.8, 32.5, 20.7 ppm. HRMS (EI) *m/z*: [$M^{+\bullet}$] calcd for $[C_{62}H_{51}N_5]^{+\bullet}$, 865.41445; found, 865.41440; difference: –0.04 ppm.

*9-Benzyl-N^3,N^3,N^6,N^6-tetra(p-tolyl)-9H-carbazole-3,6-diamine (**5.7**).* Ditolylamine (11.7 g, 59.0 mmol), 9-benzyl-3,6-diiodo-9*H*-carbazole (10.0 g, 19.8 mmol), K_2CO_3 (21.7 g, 157.0 mmol), Cu powder (5.07 g, 79.7 mmol), and 18-crown-6 (1.04 g, 3.93 mmol) were added to a flame dried 500 mL round bottom flask equipped with a magnetic stir bar and reflux condenser. The vessel was evacuated and refilled with N_2 three times before addition of dry, degassed *o*-dichlorobenzene (150 mL). The reaction mixture was heated to reflux and left stirring for 120 h. The reaction mixture was allowed to cool to room temperature, filtered to remove K_2CO_3, and concentrated under reduced pressure. The brown residue was dissolved in CH_2Cl_2 and washed with water three times. The organic layer was collected, dried with $MgSO_4$, filtered and concentrated under reduced pressure. The solid was dissolved in CH_2Cl_2 and further purified by reprecipitation into hexanes

(three times) to afford a yellow powder. Yield = 11.65 g (91 %). mp. = 132.4-134.2 °C. ^{1}H NMR (400 MHz, DMSO-d_6): δ 7.81 (d, J = 2.1 Hz, 2H), 7.59 (d, J = 8.8 Hz, 2H), 7.37–7.20 (m, 5H), 7.15 (dd, J = 8.7, 2.2 Hz, 2H), 7.01 (d, J = 8.1 Hz, 8H), 6.91–6.72 (m, 8H), 5.61 (s, 2H), 2.22 (s, 12H). ^{13}C NMR (101 MHz, DMSO-d_6): δ 145.9, 139.5, 137.8, 130.3, 129.7, 128.6, 127.4, 126.9, 125.4, 122.9, 122.1, 118.3, 110.6, 45.9, 20.2. HRMS (EI) *m/z*: [$M^{+\bullet}$] calcd for $[C_{47}H_{41}N_3]^{+\bullet}$, 647.33005; found, 667.32831; difference: –2.68 ppm.

*N^3,N^3,N^6,N^6-tetra(p-tolyl)-9H-carbazole-3,6-diamine (**5.8**).* $AlCl_3$ (16.8 g, 126.0 mmol) was suspended in dry, degassed anisole (15 mL) and cooled to 0 °C with stirring. In a separated flask **5.7** (11.7 g, 18.0 mmol) was taken up in anisole (50 mL) and then transferred into the $AlCl_3$ solution, resulting in a colour change from yellow to dark brown. Upon heating the reaction to 70 °C the reaction became clear. After 16 h the reaction mixture was poured into water (250 mL) and extracted with toluene (3 × 50 mL). The organic layers were collected, dried over $MgSO_4$, filtered and concentrated under reduced pressure. The mixture was purified through silica gel column chromatography (hexanes/CH_2Cl_2 2:1, R_f = 0.25) to afford an off-white solid. Yield = 8.33 g (83 %). mp. = 258.9-260.8 °C. ^{1}H NMR (400 MHz, benzene-d_6): δ 7.77 (d, J = 2.1 Hz, 2H), 7.32 (dd, J = 8.6, 2.1 Hz, 2H), 7.16–7.10 (m, 8H), 6.91 (m, 10H), 6.44 (s, 1H), 2.11 (s, 12H). ^{13}C NMR (101 MHz, benzene-d_6): δ 147.2, 140.9, 137.5, 130.8, 130.1, 126.2, 124.8, 123.1, 119.2, 111.8, 20.7. HRMS (EI) *m/z*: [$M^{+\bullet}$] calcd for $[C_{40}H_{35}N_3]^{+\bullet}$, 557.28310; found, 557.28241; difference: –1.23 ppm.

*4-{3,6-Bis[di(p-tolyl)amino]-9H-carbazol-9-yl}benzaldehyde (**5.9**).* **5.8** (500 mg, 0.896 mmol), K_3PO_4 (1.00 g, 4.50 mmol) and DMF (33 mL) were combined in a 100 mL round bottom flask

equipped with a magnetic stir bar and reflux condenser. The reaction was heated to 150 °C before addition of 4-fluorobenzaldehyde (0.30 mL, 2.70 mmol). After stirring for 16 h the reaction mixture was allowed to cool to room temperature, filtered to remove K_3PO_4, and concentrated under reduced pressure. The brown mixture was purified through silica gel column chromatography (hexanes/CH_2Cl_2 1:1, R_f = 0.15) to afford a bright yellow solid. Yield = 340 mg (48 %). mp. = 141.1-143.0 °C. ^{1}H NMR (400 MHz, benzene-d_6): δ 9.66 (s, 1H), 7.83 (d, J = 2.1 Hz, 2H), 7.56–7.49 (m, 2H), 7.29 (dd, J = 8.8, 2.1 Hz, 2H), 7.17 (m, 4H), 7.16–7.08 (m, 8H), 6.93 (d, J = 8.2 Hz, 8H), 2.11 (s, 12H). ^{13}C NMR (101 MHz, benzene-d_6): δ 190.0, 146.9, 143.0, 142.4, 137.7, 134.9, 131.3, 131.2, 130.7, 126.4, 126.3, 125.5, 123.3, 118.8, 111.1, 20.7. HRMS (EI) *m/z*: $[M^{+\bullet}]$ calcd for $[C_{47}H_{39}N_3O]^{+\bullet}$, 661.30931; found, 661.30651; difference: –4.24 ppm.

*4-(9,9-Dimethyl-10(9H)-acridinyl)benzaldehyde (**5.10**)*.[301] To a 3-neck, 3 litre round bottom flask was added acridine (26.0 g, 124 mmol), K_3PO_4 (132 g, 621 mmol), and 2.15 L of DMF as well as a magnetic stir bar. A reflux condenser was attached to the flask, then the reaction mixture was heated to reflux. Once refluxing, 4-fluorobenzaldehyde (26.7 mL, 248 mmol) was added to the reaction mixture gradually. The reaction mixture was stirred overnight. After confirmation of the completion of the reaction by TLC, the crude reaction mixture was filtered to remove excess K_3PO_4. The filtrate was then concentrated under reduced pressure then dissolved in 500 mL ethyl acetate. This organic layer was washed three times with 250 mL of deionized water, dried over $MgSO_4$, filtered and concentrated under reduced pressure. The crude mixture was purified by column chromatography using a gradient of hexane and CH_2Cl_2 (100% hexane to 100% CH_2Cl_2) on silica. Yield = 38.3 g (98%). ^{1}H NMR (400 MHz, chloroform-*d*): δ 10.16 (s, 1H), 8.17 (d, J = 8.4 Hz, 2H), 7.58 (d, J = 8.3 Hz, 2H), 7.55–7.49 (m, 2H), 7.03 (m, 4H), 6.42–6.35 (m, 2H), 1.73

(s, 6H). ^{13}C NMR (101 MHz, chloroform-*d*): δ 191.2, 147.5, 140.4, 135.4, 132.2, 131.4, 130.8, 126.4, 125.4, 121.5, 114.9, 36.2, 30.9. HRMS (ESI) *m/z*: [M+H] calcd. for $[C_{22}H_{19}NO]+H$, 314.1544; found, 314.1545; difference: 0.3 ppm.

Chapter 6: Deep-Blue Fluorophores with Imidazoacridine Acceptors: Enhancing Photostablility and Two-Photon Fluorescence using Structural Constraint

6.1 Introduction

Fluorescent dyes for use in biological applications have attracted significant research attention for more than three decades. Near-infrared dyes have garnered particular interest as their absorption range (650-900 nm) allows for deep penetration into tissues and avoids the influence of bioautofluorescence.[302] As dyes emitting efficiently in this range remain scarce, an alternative approach utilizes two-photon excited fluorescence (2PEF), a third-order non-linear optical process whereby a molecule is electronically excited by simultaneous absorption of a pair of photons.[303] In a two-photon process the energy absorbed is proportional to the square of the incident light intensity, providing spatial selectivity in three dimensions with one-wavelength resolution. Beyond imaging applications,[304,305] materials with large 2PEF cross sections are also useful for optical power limiting[306,307] and 3D optical data storage.[308,309]

Common requirements for fluorescent dyes in all of these applications are high two-photon cross-sections, high photoluminescent quantum yields (PLQYs), and stability to repeated excitation. Molecular rigidification has recently emerged as a powerful strategy for meeting these goals, providing fluorophores with narrower emission spectra, higher quantum yields, and increased resistance to photobleaching compared to analogues lacking the same structural constraints.[275] The suppression of vibrational/rotational motion in such fluorophores is believed to reduce or eliminate many of the decomposition pathways available to these molecules in their excited states. For example, Yamaguchi and coworkers designed and synthesized a series of ultra-

photostable dyes for multiple-acquisition stimulated emission depletion (STED) imaging by incorporating a rigid carbon bridge into a naphthophosphole *P*-oxide fluorophore.[273,274] This strategy has also been applied to boron-, nitrogen-, phosphorus-, and silicon-containing polycyclic aromatic materials to give conformationally locked fluorophores with increased π-conjugation, red-shifted absorptions, increased molar absorption coefficients, and intense fluorescence.[275–279] Adachi and coworkers have also observed high electroluminescence quantum efficiencies in fully fused, planar and rigid acridone ring systems with high chemical stability based on excited-state intramolecular proton transfer (ESIPT).[310] In a recent report, Hatakeyama and coworkers developed a series of fused boron- and nitrogen-containing polycyclic aromatic emitters, leveraging a unique property known as the multiple resonance effect to produce efficient thermally activated delayed fluorescence (TADF).[130,144,145] Many of these materials also exhibit narrow emission bands and enhanced colour purity, which are desirable in nearly all applications in which fluorescent materials are used.

In addition to increased stability, planarization has been shown to be an effective means to increase the 2PEF cross section of materials.[275] Liu, Lai and coworkers developed dendritic systems based on the locked planarity of hexamethylazatriangulene (HMAT) moieties yielding a fourfold increase in 2PEF cross section relative to analogous nonplanar triarylamines.[311–313] Müllen, Perry, Brédas and coworkers examined the effects of planarization by comparing the properties of a donor-acceptor series of molecules, one in which triarylamine phenyl groups were free to rotate and another, planar structure in which the rings were locked.[314] Our group also recently reported that HMAT-functionalized benzothiadiazole exhibits red fluorescence with a high 2PEF cross section of 230 GM, while also exhibiting high photostability.[315]

Deep blue or violet fluorescent emitters are increasingly sought after for applications in biological and chemical sensing,[316,317] electroluminescent devices,[285,287,318,319] and organic lasers.[320,321] To realize emission in this region a wide energy gap >3.0 eV is required, and thus an electron acceptor with a shallow LUMO is ideal. Imidazole and benzimidazole are attractive for this purpose, with several examples of high PLQY blue fluorescent emitters recently reported.[266,286–289,322] Despite these advances, the search for deep-blue luminescent materials that are both stable and efficient remains a particular challenge.

Herein we report the synthesis of donor-acceptor dyes based on benzimidazole acceptors and triphenylamine donors, employing structural constraint to improve quantum yield, photostability, and two-photon cross-section. **tBuTPA-PBI** is composed of a di-*tert*-butyl triphenylamine (tBuTPA) donor and *N*-phenylbenzimidazole (PBI) acceptor, representing a flexible structure with numerous rotational degrees of freedom (Figure 6.1). **tBuTPA-IMAC** contains a rigidified 6,6-dimethyl-6*H*-imidazo[4,5,1-*de*]acridine (IMAC) acceptor unit and **HMAT-IMAC** contains rigidified hexamethylazatriangulene (HMAT) and IMAC units. These dyes all exhibit deep blue emission with PLQYs of 95-100%. In addition to photophysical and electrochemical characterization, the photostability of this series of compounds was probed, revealing **HMAT-IMAC** to have vastly improved photostability. Further, 2PEF cross sections were measured for all three dyes, increasing with increasing planarity of the fluorophores.

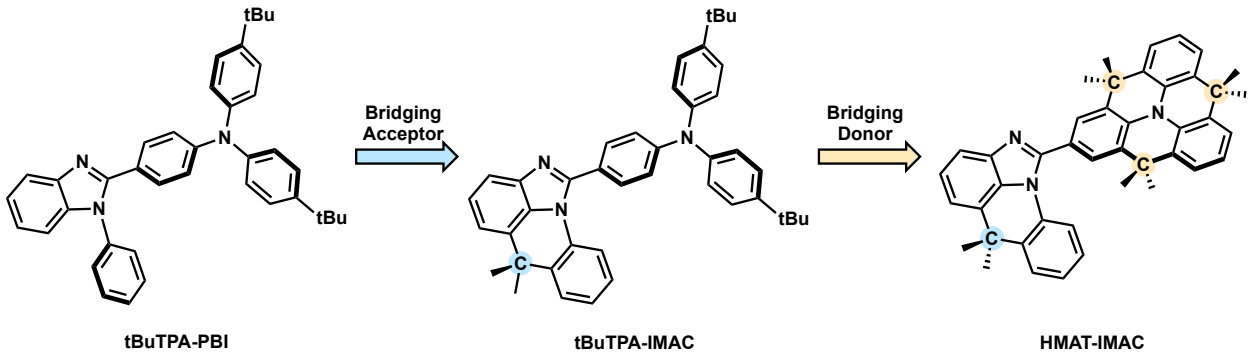

Figure 6.1. Chemical structures of **tBuTPA-PBI**, **tBuTPA-IMAC**, and **HMAT-IMAC**.

6.2 Results and Discussion

Compound **6.1** was purchased from MilliporeSigma, while compounds **6.2**,[323] **6.3**,[232] and **6.4**[312] were synthesized according to previously reported procedures. Synthesis of **tBuTPA-PBI** was achieved by the coupling of **6.1** with **6.3** via an I_2-mediated intramolecular C−H amidation (Figure 6.2).[323,324] In a similar fashion **tBuTPA-IMAC** and **HMAT-IMAC** were synthesized by coupling the respective phenylaldehyde-linked triarylamine (**6.3** or **6.4**) with 9,9-dimethyl-9,10-dihydroacridin-4-amine (**6.2**). The identity of final compounds was confirmed by ^{1}H and $^{13}C\{^{1}H\}$ NMR, as well as high resolution mass spectrometry (HRMS).

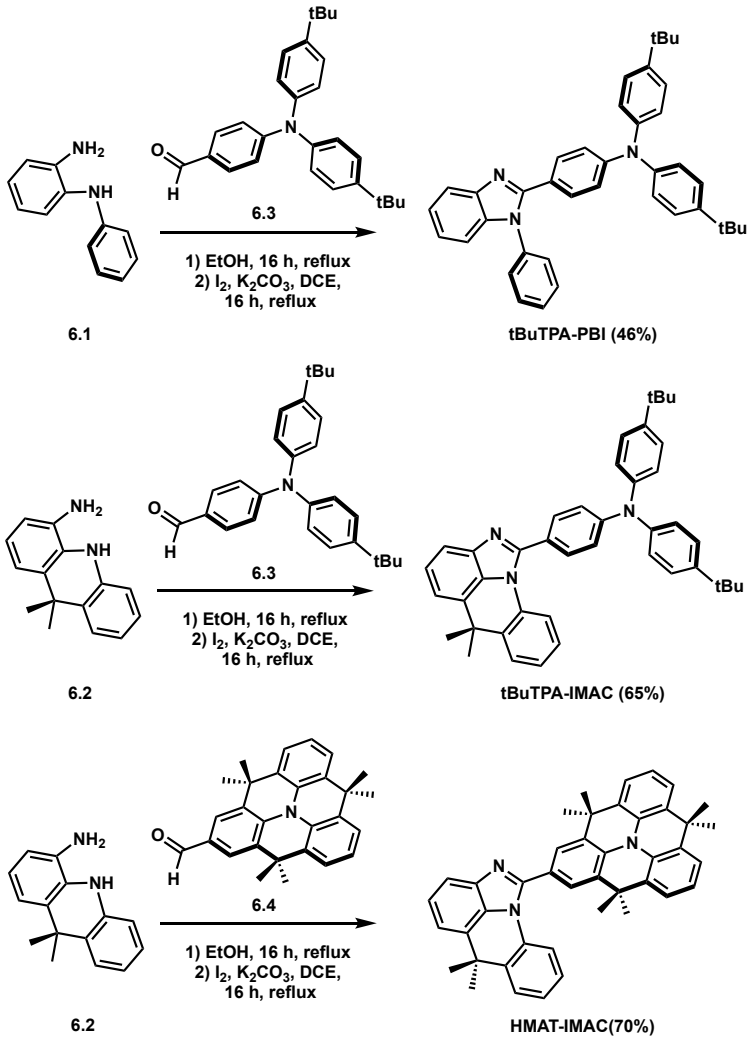

Figure 6.2. Synthesis of **tBuTPA-PBI**, **tBuTPA-IMAC**, and **HMAT-IMAC**.

The molecular conformation and electronic structures of these materials was first probed by performing quantum chemical calculations using density functional theory (DFT) with the PBE0/6-31+G(d) method/basis set (Figure 6.3). **tBuTPA-PBI** exhibited a large dihedral angle of 60° between the *N*-phenyl and benzimidazole moieties, as well as significant torsion (*ca.* 66°) on the three phenyl groups of the triarylamine. In **tBuTPA-IMAC** the *N*-phenyl and benzimidazole groups are locked with a dimethylmethylene bridge, affording the fused IMAC acceptor. This

increases the conjugation of the π-system, resulting in red-shifted absorption, increased molar absorptivity, and intense fluorescence.[278] **HMAT-IMAC** also includes a planarized donor, yet steric interaction between nearby hydrogen atoms on the HMAT and IMAC fragments results in donor-acceptor dihedral angle of 34°. While the HOMO and LUM O are mainly distributed over the donor and acceptor moieties respectively, significant conjugation between the two groups is observed.

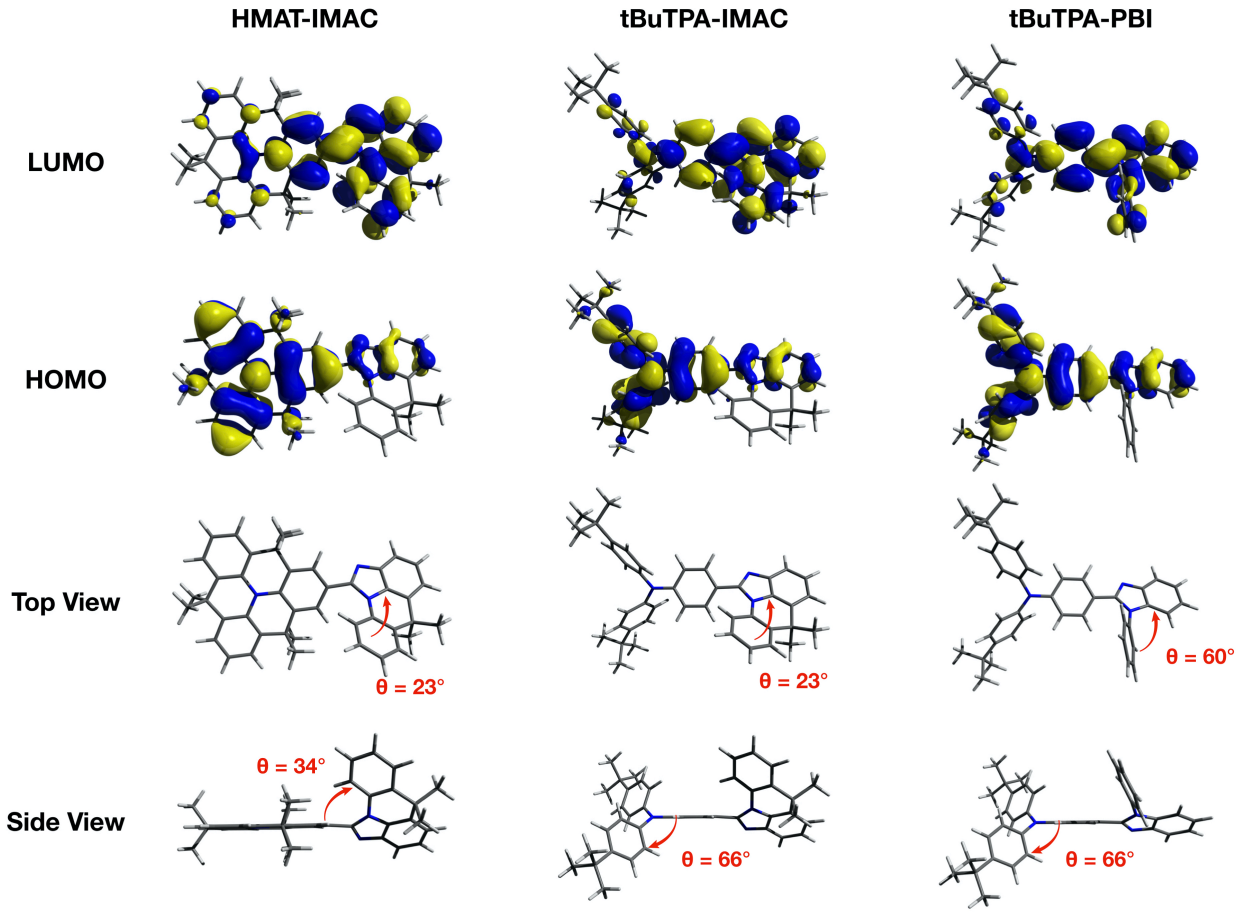

Figure 6.3. Optimized structures and HOMO/LUMO orbital diagrams for **tBuTPA-PBI**, **tBuTPA-IMAC**, and **HMAT-IMAC**. Selected angles θ are indicated with red arrows.

UV-vis absorption and photoluminescence (PL) spectra of **tBuTPA-PBI**, **tBuTPA-IMAC**, and **HMAT-IMAC** in toluene solution (1×10^{-5} M) are shown in Figure 6.4. **tBuTPA-PBI**, **tBuTPA-IMAC**, and **HMAT-IMAC** all have broad, featureless emission spectra consistent with a charge-transfer excited state with $\lambda_{max,\ abs}$ = 356, 353, and 366 nm, respectively (Table 6.1). Based on TD-DFT calculations we attribute the lowest energy transition in all cases to the HOMO to LUMO transition. TD-DFT further predicts oscillator strengths of 0.96, 0.89, and 0.56 for **tBuTPA-PBI**, **tBuTPA-IMAC** and **HMAT-IMAC**, respectively. All have intense fluorescence in the blue/violet region with $\lambda_{max,\ em}$ = 419, 442, and 432 nm, respectively (Figure 6.4, Table 6.1). Significant red shifts in polar relative to nonpolar solvents indicate all compounds possess strong solvatochromism in their fluorescence spectra. The effect was most pronounced for **tBuTPA-IMAC**, with a red shift of 4133 cm^{-1} in hexane relative to MeCN followed by **tBuTPA-PBI** and **HMAT-IMAC** (3706 and 2781 cm^{-1} respectively). **tBuTPA-PBI**, **tBuTPA-IMAC**, and **HMAT-IMAC** exhibit spectra which have full-width at half maxima (FWHM) of 57, 64, and 58 nm, respectively. Photoluminescence decay curves for each compound were measured in toluene solution at room temperature, giving lifetimes between 1.99-2.55 ns.

The electrochemical properties and energy levels of these compounds were investigated by cyclic voltammetry in DMF using a conventional three-electrode system. **tBuTPA-PBI** and **tBuTPA-IMAC** exhibited quasi-reversible one-electron oxidation events at 1.03 V relative to ferrocene/ferrocenium ($FeCp^{0/+}$) attributed to the triphenylamine moiety. Similarly, **HMAT-IMAC** exhibits quasi-reversible one-electron oxidation at 0.98 V ascribed to the HMAT component. **tBuTPA-IMAC** and **HMAT-IMAC** exhibit quasi-reversible one-electron reduction events at –2.14 and –2.08 V respectively arising from the IMAC unit, which is in reasonable agreement with similar donor-acceptor compounds containing benzimidazole (Figure 6.4C).[289]

Reduction of the **tBuTPA-PBI** was not observed. The LUMO energy levels of all three compounds were calculated to be approximately –1.10 V.

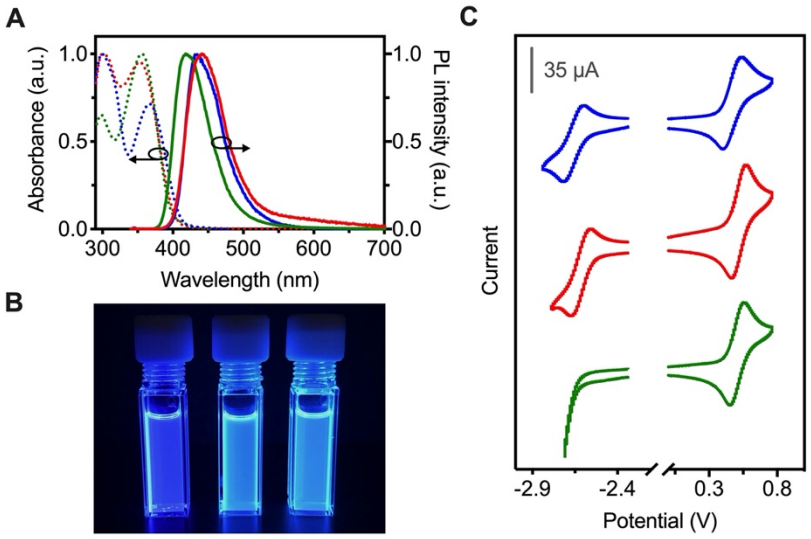

Figure 6.4. (A) UV-vis spectra measured in CH_2Cl_2 at 1×10^{-5} M and PL spectra measured in toluene solution at 1×10^{-5} M, for **tBuTPA-PBI** (green), **tBuTPA-IMAC** (red), and **HMAT-IMAC** (blue). (B) Photographs of the series of compounds in toluene irradiated with 365 nm light (from left to right **tBuTPA-PBI**, **tBuTPA-IMAC**, and **HMAT-IMAC**). (C) Cyclic voltammograms of these compounds relative to $FeCp_2^{0/+}$.

Table 6.1. Photophysical properties of IMAC compounds.

Entry	$\lambda_{max,\ abs}$ [a]	$\lambda_{max,\ em}$ [b]	ε (10^4 M^{-1} cm^{-1}) [a]	Φ_F [b]	CIE [b]	τ_p (ns) [b]
tBuTPA-PBI	356	419	2.63	0.97	(0.16, 0.05)	1.99
tBuTPA-IMAC	353	442	2.80	1.00	(0.17, 0.09)	2.55
HMAT-IMAC	366	432	1.71	0.95	(0.15, 0.06)	2.33

[a]Measured in toluene. [b]Measured in degassed toluene with an optical density between 0.05 and 0.15 (approximately 1×10^{-5} M).

The photostability of **tBuTPA-PBI**, **tBuTPA-IMAC**, and **HMAT-IMAC** were next evaluated in DMSO (Figure 6.5). Photoirradiation of the **tBuTPA-PBI** and **tBuTPA-IMAC** solutions for 90 min with a 350 nm excitation source (intensity estimated at 98 mW at the sample)

resulted in 81 and 78% photobleaching, respectively. In contrast, only 21% of **HMAT-IMAC** photobleached under the same irradiation conditions, demonstrating the improved photostability of the HMAT derivative. As such, **HMAT-IMAC** may be a promising candidate for application in imaging, where the stability of blue dyes has conventionally been problematic. The enhanced stability of **HMAT-IMAC** can be attributed to the improved stability of the triarylamine C-N bonds as a result of the emitters overall structural rigidification.[325,326] Stability enhancement of the transient radical cation at the nitrogen atom in the HMAT structure may have an additional stabilizing effect.

We also examined the two-photon cross-section of these compounds to assess their suitability for applications in 2PEF imaging (Figure 6.5B). All three compounds show high two-photon cross-sections at approximately 730 nm (710 nm is the wavelength limit of our laser). **tBuTPA-PBI** has the smallest cross-section of 450 GM. **tBuTPA-IMAC** has a slightly higher cross-section of 526 GM and **HMAT-IMAC** has a much larger cross-section of 696 GM, a 54% increase from the analogue lacking added rigidification. These cross-section values are similar in magnitude to other HMAT-based chromophores with comparable size and molecular weight.[311,313–315]

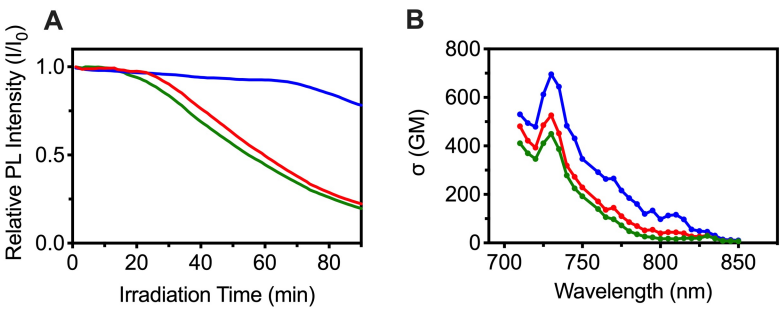

Figure 6.5. (A) Photostability for **tBuTPA-PBI** (green), **tBuTPA-IMAC** (red), and **HMAT-IMAC** (blue). (B) Two-photon absorption for **tBuTPA-PBI**, **tBuTPA-IMAC**, and **HMAT-IMAC**.

Water-soluble polymer dots (Pdots) have recently been demonstrated as useful nanoparticle-based materials for biological sensing and imaging applications.[327–330] Capable of encapsulating a high density of chromophores, Pdots can act as fluorescent probes with extremely high brightness with remarkable signal-to-noise ratios. Furthermore, Pdots can be functionalized with binding groups or therapeutic cargo to afford multifunctional probes capable of selective tissue labeling and drug delivery. With this in mind, we next explored the encapsulation of our fluorescent dyes in water-soluble Pdots to investigate their utility in imaging applications.

Encapsulation was performed using a modified nanoprecipitation procedure, with poly(styrene-co-maleic anhydride) (PSMA) as the amphiphilic copolymer (Figure 6.6A).[331] Briefly, a THF solution containing both the dye and PSMA was rapidly injected into a larger volume of water under sonication. THF was removed and the solution was concentrated by rotary evaporation. The hydrodynamic size of the resulting Pdots in solution was determined by nanoparticle tracking analysis (NTA). Representative data for **HMAT-IMAC** Pdots is shown in Figure 6B, revealing an average particle diameter of 96.3 ± 9.0 nm. NTA data for **tBuTPA-PBI** and **tBuTPA-IMAC** Pdots indicated average particle diameters of 96.4 ± 2.1 and 110.8 ± 1.7 nm,

respectively. The emission maxima of **tBuTPA-PBI**, **tBuTPA-IMAC**, and **HMAT-IMAC** red-shift from 419 to 510 nm, 442 to 526 nm, and 432 to 528 nm, respectively when encapsulated (Figure 6.6C), attributable to solvatochromic effects.

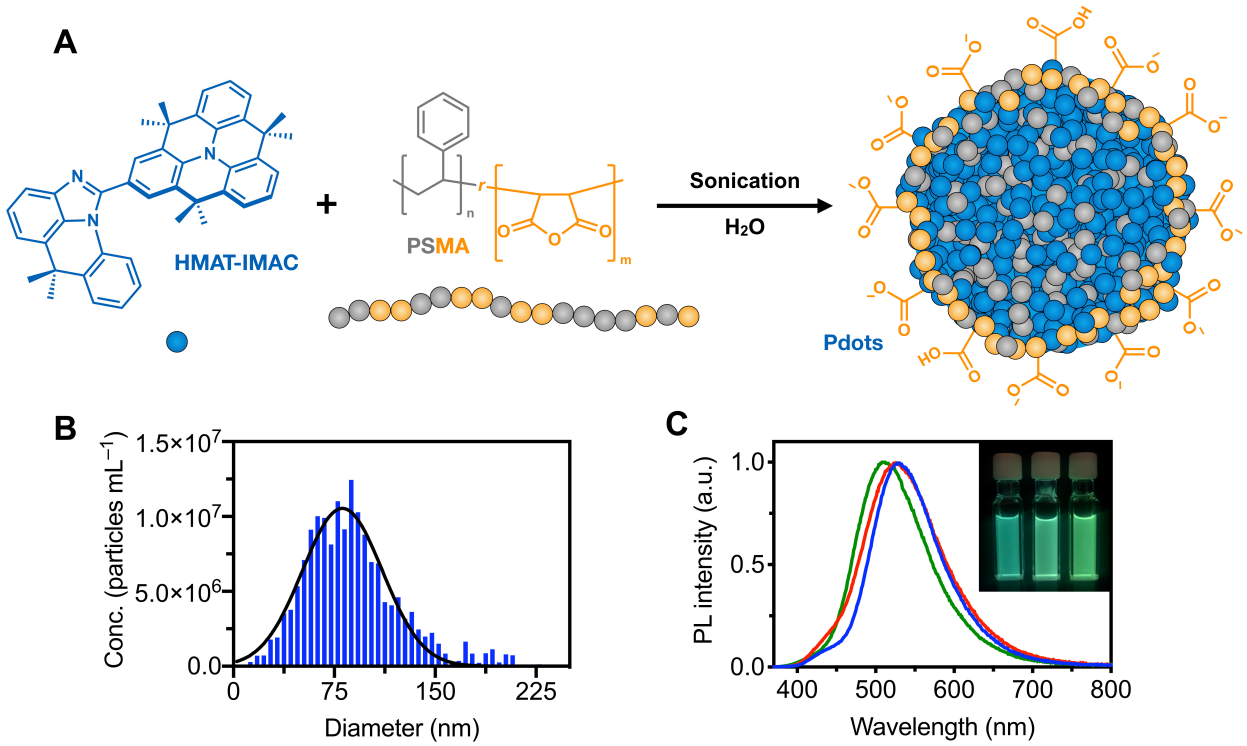

Figure 6.6. (A) Schematic of **HMAT-IMAC** dye encapsulation in the amphiphilic polymer PSMA to produce water-soluble Pdots. (B) Size distribution of polymer dots of **HMAT-IMAC** in aqueous solution (blue) with curve fit (solid black line) at 0.25 μg mL^{-1}. (C) Normalized photoluminescence of **tBuTPA-PBI** (green), **tBuTPA-IMAC** (red), and **HMAT-IMAC** (blue) in PSMA in water at 0.01 mg mL^{-1}, with photographs of these solutions (inset) under 365 nm irradiation.

6.3 Conclusions

In summary, we have reported a series of novel donor-acceptor dyes based on benzimidazole acceptors and triphenylamine donors exhibiting deep blue emission with PLQY near unity. Their photophysical and electrochemical properties have been characterized and

density functional theory calculations have been employed to better understand their structure-property relationships. Furthermore, the photostability of **tBuTPA-PBI**, **tBuTPA-IMAC**, and **HMAT-IMAC** were measured in solution, revealing substantially improved photostability for **HMAT-IMAC** as a result of reduced intramolecular motion. Finally, 2PEF cross-sections were found to be high for all three dyes, increasing with the degree of structural constraint. Overall, this work provides a framework for the development of high-stability benzimidazole-containing dyes for two-photon imaging. Future studies will examine the adaptation of these materials for application in biological systems.

6.4 Experimental Details

General Considerations. All reactions and manipulations were carried out under a nitrogen atmosphere using standard Schlenk or glove box techniques unless otherwise stated. Dry solvents were obtained from Caledon Laboratories, dried using an Innovative Technologies Inc. solvent purification system, collected under vacuum, and stored under a nitrogen atmosphere over 4 Å molecular sieves. All reagents were purchased from Sigma-Aldrich, Cambridge Isotope Laboratories, Alfa Aesar or Tokyo Chemical Institute and used as received unless otherwise stated. Syntheses of the following compounds have been previously reported: **6.2**,[323] **6.3**,[232] **6.4**.[312] The ^{1}H and $^{13}C\{^{1}H\}$ nuclear magnetic resonance (NMR) spectra were measured on a Bruker AV III HD 400 MHz spectrometer with methylene chloride-d_2 (CD_2Cl_2) as the solvent. The chemical shift data are reported in units of δ (ppm) relative to residual solvent. Absorbance measurements were made on a Cary 60 spectrometer and fluorescence measurements were made on an Edinburgh Instruments FS5 spectrofluorometer. Absolute photoluminescence quantum yields were determined using an Edinburgh Instruments SC–30 Integrating Sphere Module; toluene was used

as the solvent and spectra obtained at approximately 10^{-5} M unless otherwise stated. Two-photon cross-sections (σ_2) were calculated using the two-photon excited fluorescence method. Two-photon cross-section (σ_2) values from 710−850 nm were measured with an inverted two-photon fluorescence scanning microscope (Zeiss LSM 510 MP). Samples (3 mL) were measured in quartz cuvettes and concentrations were adjusted to give similar 2PEF intensities (**tBuTPA-PBI**, 2.0 × 10^{-2} mg mL^{-1}; **tBuTPA-IMAC**, 2.0 × 10^{-2} mg mL^{-1}; **HMAT-IMAC**, 2.0 × 10^{-2} mg mL^{-1} in toluene) and Rhodamine B in MeOH (1.0 × 10^{-1} mg mL^{-1} in MeOH) was used as the reference. The cuvette was illuminated at a depth of 0.6 mm from the bottom of the cuvette and imaged with a 10x/0.3 objective lens and femtosecond laser with a tuning range of 710-850 nm. The dichroic mirror had a cut-off at 660 nm. The square-dependence of the fluorescence intensity on laser power was periodically confirmed for all measured and σ_2 was calculated using the quantum yield obtained from one-photon excitation experiments. Photoluminescence decay characteristics were investigated under a nitrogen atmosphere using an Edinburgh Instruments FS5 spectrofluorometer and SC-80 sample holder. The fast decay component was recorded using time-correlated single photon counting in conjunction with a 313 nm EPLED excitation source. Mass spectra were recorded on a Kratos MS-50 instrument using electron impact ionization.

Photobleaching. Photobleaching measurements were performed on an inverted microscope. Sample aliquots (5 μL) were measured in a clear flat-bottom 1536-well plate (Greiner Bio One, Kremsmünster, Austria) with the wells covered with universal optical sealing tape (#6575, Corning). Sample concentrations were adjusted to obtain similar initial fluorescence intensities (**tBuTPA-PBI**, 1.0 × 10^{-3} mg mL^{-1}; **tBuTPA-IMAC**, 1.0 × 10^{-3} mg mL^{-1}; **HMAT-IMAC**, 1.0 × 10^{-3} mg mL^{-1} in in DMSO. A 2 × 2 array of wells was illuminated and imaged with a 4× objective

lens (NA 0.16). The excitation filter was 350/50 (center wavelength and bandwidth in nm), the dichroic mirror had a cut-off at 425 nm, and no emission filter was used. The excitation power was estimated to be ~98 mW at the sample. Samples were continuously illuminated using the above conditions and images were acquired at 1 min intervals for 90 min and analyzed using ImageJ8 software with the Time Series Analyzer V3 plugin. The initial intensity for each sample was normalized to a value of one.

Electrochemical Methods. Cyclic voltammograms were recorded using a BASi Epsilon Eclipse potentiostat at room temperature using a standard three-electrode configuration (working electrode: 3 mm diameter glassy carbon; reference electrode: RE-5B Ag/AgCl electrode in saturated aqueous KCl (BASi Inc.), referenced externally to ferrocene/ferrocenium (0.543 V in DMF);[199] counter electrode: Pt wire) in 0.1 M tetrabutylammonium hexafluorophosphate in DMF. Experiments were run at a scan rate of 100 mV s^{-1} in dry degassed electrolyte solution with ~1 mg mL^{-1} of analyte.

Density Functional Theory. Calculations were performed using the Gaussian 09 software package.[235] Ground state geometries and energies were calculated at the PBE0/6-31+G(d) level of theory. The singlet states were calculated by the Tamm-Dancoft approximation to time-dependent density functional theory (TD-DFT) with the PBE0 functional at the same basis set level. Molecular orbitals were visualized using Avogadro version 1.20 and rendered using POV-Ray version 3.7.0.

6.4.1 Synthetic Procedures

*Synthesis of 4-(tert-butyl)-N-(4-(tert-butyl)phenyl)-N-(4-(1-phenyl-1H-benzo[d]imidazol-2-yl)phenyl)aniline (**tBuTPA-PBI**).* A mixture of *N*-phenyl-*o*-phenylenediamine (**6.1**) (200 mg, 1.09 mmol) and **6.3** (460 mg, 1.19 mmol) in EtOH (10 mL) was refluxed for 16 h. The solvent was evaporated under reduced pressure to give a yellow oil, which was redissolved in 1,2-dichloroethane (20 mL), followed by the sequential addition of iodine (390 mg, 1.53 mmol) and K_2CO_3 (450 mg, 3.27 mmol). The reaction mixture was stirred at reflux temperature for the 16 h. Upon completion of the reaction, it was quenched with 5% $Na_2S_2O_3$ (30 mL) and then extracted with CH_2Cl_2 (20 mL × 3). The combined organic layer was washed with brine (30 mL), dried over anhydrous $MgSO_4$, concentrated, and then purified through silica gel column chromatography (5% EtOAc in hexanes, R_f = 0.15) to afford an off white solid. Yield = 275 mg (46 %). ^{1}H NMR (400 MHz, Methylene Chloride-d_2) δ 7.81 (dt, J = 8.0, 1.0 Hz, 1H), 7.63 – 7.50 (m, 3H), 7.47 – 7.39 (m, 4H), 7.38 – 7.30 (m, 5H), 7.30 – 7.19 (m, 2H), 7.13 – 7.05 (m, 4H), 6.92 – 6.86 (m, 2H), 1.36 (s, 18H) ppm. ^{13}C NMR (101 MHz, Methylene Chloride-d_2) δ 152.8, 149.6, 147.4, 144.6, 143.6, 137.9, 137.8, 130.3, 130.2, 128.9, 128.0, 126.7, 125.6, 123.0, 122.9, 122.1, 120.0, 119.5, 110.5, 34.7, 31.5. HRMS (EI) *m/z*: [$M^{+\bullet}$] calcd for $[C_{39}H_{39}N_3]^{+\bullet}$, 549.31440; found, 549.31357; difference: –0.82 ppm.

*Synthesis of 4-(tert-butyl)-N-(4-(tert-butyl)phenyl)-N-(4-(6,6-dimethyl-6H-imidazo[4,5,1-de]acridin-1-yl)phenyl)aniline (**tBuTPA-IMAC**).* A mixture of **6.2** (200 mg, 0.89 mmol) and **6.3** (380 mg, 0.98 mmol) in EtOH (10 mL) was refluxed for 16 h. The solvent was evaporated under reduced pressure to give a yellow oil, which was redissolved in 1,2-dichloroethane (20 mL), followed by the sequential addition of iodine (320 mg, 1.25 mmol) and K_2CO_3 (320 mg, 2.67

mmol). The reaction mixture was stirred at reflux temperature for the 16 h. Upon completion of the reaction, it was quenched with 5% $Na_2S_2O_3$ (30 mL) and then extracted with CH_2Cl_2 (20 mL × 3). The combined organic layer was washed with brine (30 mL), dried over anhydrous $MgSO_4$, concentrated, and then purified through silica gel column chromatography (5% EtOAc in hexanes, R_f = 0.15) to afford an off white solid. Yield = 343 mg (65 %). ^{1}H NMR (400 MHz, Methylene Chloride-d_2) δ 7.71 – 7.61 (m, 3H), 7.59 (dd, J = 7.8, 1.0 Hz, 1H), 7.48 – 7.32 (m, 7H), 7.27 – 7.11 (m, 8H), 1.79 (s, 6H), 1.39 (s, 18H). ^{13}C NMR (101 MHz, Methylene Chloride-d_2) δ 151.8, 150.3, 147.5, 144.7, 141.4, 136.6, 134.2, 132.0, 130.7, 130.5, 128.1, 126.9, 126.8, 125.5, 124.6, 124.6, 120.7, 118.4, 117.1, 116.7, 37.9, 34.7, 32.8, 31.6. HRMS (EI) *m/z*: [$M^{+\bullet}$] calcd for $[C_{42}H_{43}N_3]^{+\bullet}$, 589.34570; found, 589.34738; difference: 1.68 ppm.

*Synthesis of 2-(6,6-dimethyl-6H-imidazo[4,5,1-de]acridin-1-yl)-4,4,8,8,12,12-hexamethyl-8,12-dihydro-4H-benzo[9,1]quinolizino[3,4,5,6,7-defg]acridine (**HMAT-IMAC**).* A mixture of **6.2** (155 mg, 0.69 mmol) and **6.4** (300 mg, 0.76 mmol) in EtOH (10 mL) was refluxed for 16 h. The solvent was evaporated under reduced pressure to give a yellow oil, which was redissolved in 1,2-dichloroethane (20 mL), followed by the sequential addition of iodine (245 mg, 0.97 mmol) and K_2CO_3 (285 mg, 2.07 mmol). The reaction mixture was stirred at reflux temperature for the 16 h. Upon completion of the reaction, it was quenched with 5% $Na_2S_2O_3$ (30 mL) and then extracted with CH_2Cl_2 (20 mL × 3). The combined organic layer was washed with brine (30 mL), dried over anhydrous $MgSO_4$, concentrated, and then purified through silica gel column chromatography (5% EtOAc in hexanes, R_f = 0.20) to afford a yellow solid. Yield = 300 mg (70 %). ^{1}H NMR (400 MHz, Methylene Chloride-d_2) δ 7.86 (s, 2H), 7.68 (dd, J = 8.0, 1.5 Hz, 1H), 7.64 (dd, J = 7.8, 1.0 Hz, 1H), 7.49 (ddd, J = 9.2, 7.7, 1.6 Hz, 4H), 7.43 (t, J = 7.6 Hz, 1H), 7.37 (ddd, J = 8.4, 5.9, 1.1 Hz,

2H), 7.26 – 7.18 (m, 3H), 7.03 (ddd, J = 8.5, 7.2, 1.5 Hz, 1H), 1.82 (s, 6H), 1.73 (s, 6H), 1.71 (s, 12H). ^{13}C NMR (101 MHz, Methylene Chloride-d_2) δ 151.9, 141.4, 136.6, 134.0, 133.8, 131.8, 130.6, 130.5, 130.5, 130.3, 128.2, 126.9, 126.8, 125.6, 125.4, 124.7, 124.3, 124.0, 123.8, 118.6, 117.1, 116.7, 37.9, 36.0, 35.9, 33.7, 33.2, 25.6. HRMS (EI) *m/z*: [$M^{+\bullet}$] calcd for $[C_{43}H_{39}N_3]^{+\bullet}$, 597.31440; found, 597.31320; difference: –2.01 ppm.

Pdot Synthesis. Pdots were synthesized by the nanoprecipitation method. Briefly, a 5.0 mL solution of **tBuTPA-PBI**, **tBuTPA-IMAC** or **HMAT-IMAC** and PSMA (20 and 4 μg/ mL, respectively) in THF was briefly sonicated and then rapidly injected into water (10 mL) under sonication. THF was removed, and the solution was concentrated to ∼5 mL by rotary evaporation.

Chapter 7: Conclusions and Future Work

This thesis describes the preparation of organic semiconductors with novel optoelectronic properties and morphologies. Significant strides have now been made toward ordered, multicomponent nanowires by covalent synthesis. Using bottlebrush polymers, highly complex non-centrosymmetric materials have been generated with control over composition at multiple levels of structural hierarchy. By controlling the identity of the monomers used, the organization of these monomers in polymeric side chains, and the ordering of these polymeric side chains along the bottlebrush backbone, distinct photophysical properties can be achieved. The thesis also described work to address interesting problems of closely related fields, including the efficient synthesis of planar TADF materials and stable organic fluorophores.

Chapter 2 described a series of acrylic monomers based on p-type organic semiconductor motifs commonly found in organic electronic devices. These monomers were polymerized by Cu(0)-RDRP, the kinetics of which are described in detail. The title polymers were obtained in high yield with low polydispersities and display first-order polymerization kinetics up to high (>90%) monomer conversion. The optical, electrochemical and thermal properties for each of these p-type materials are also described. All polymers prepared here showed highly reversible one-electron oxidation by cyclic voltammetry and reasonable stability by TGA, making them good candidates for further studies in applications as p-type materials for organic electronics, including organic light-emitting diodes (OLEDs), solar cells, and organic thin-film transistors. Future investigations will also focus on improving the polymerization of these materials into high molecular weight multiblock copolymers that can be used for self-assembly.

Chapter 3 described methods for the preparation of fiber-like nanomaterials that mimic the multilayer structure of organic electronic devices on individual polymer chains. By combining

Cu(0)-RDRP and ROMP, narrowly dispersed multiblock bottlebrush fibers were prepared from materials commonly used as the hole transport, electron transport, and host materials in organic electronics. This strategy was used to construct nanofibers with the structure of phosphorescent OLEDs on single macromolecules, such that the photophysical properties of each component of an OLED can be independently observed. Moving forward, such systems hold potential for the rapid self-assembly of complex multilayer films with synthetically installed order, and for investigations into charge transport at nanoscale interfaces. For the majority of these materials, macroscopic device applications have not yet been examined. The ultrahigh molecular weight and high grafting density offered by the bottlebrush architecture makes direct comparisons with linear homopolymers composed of the same organic electronic units a promising next step. There is also substantial evidence in literature documenting the ability of BBCPs to assemble into lamellar structures in the solid state.[69] One could thus envisage orienting diblock, and potentially even multiblock BBCPs normal to an electrode substrate in order to generate well-defined multilayer films in a single step. Finally, the use of conductive AFM could be used to directly measure block-by-block conductivity in each semiconducting block, with the goal of demonstrating charge transport in a single bottlebrush chain.

Chapter 4 described the synthesis of a series of bottlebrush copolymers from red, green, and blue luminescent macromonomers, which were then used to prepare multiblock organic nanofibers structurally analogous to nanoscale RGB pixels. By segregating optoelectronic functionality into discrete blocks along a nanofiber, their photophysical properties could be controlled to give properties that are difficult to achieve by other means. Changes in energy transfer efficiency and interchromophore distance were quantified using a FRET model. Preliminary demonstration of these materials as polarity-sensitive inks for encryption and encoding were also

demonstrated using a red/blue fluorescence switch upon exposure to solvent. Finally, the potential complexity of optoelectronic materials accessible with these methods was demonstrated by preparing organic nanofibers with ordered structures mimicking those of multilayer white OLEDs. In the future, incorporating blocks that swell or contract when exposed to various external stimuli could make these BBCPs useful in ratiometric fluorescent sensing, as energy transfer between brush arms is modulated by the applied stimulus. Due to their large domain sizes, BBCPs can also readily self-assemble into photonic crystal films, with selective reflection of colour within the visible spectrum. In this way, chromophore-containing BBCPs could potentially be explored as laser gain media, giving optical amplification in a similar fashion to chiral liquid crystals or colloidal crystals doped with fluorescent dyes.[332]

Chapter 5 described the design of an *N*-phenylbenzimidazole constrained in a coplanar fashion with a methylene tether (IMAC) that was used to prepare a series of emitters exhibiting thermally activated delayed fluorescence (TADF). The twisted conformation between donor and acceptor in these molecules resulted in effective spatial separation of the HOMO and LUMO and small singlet−triplet energy gaps. Crystallographic properties, electronic structures, thermal stabilities, photophysical properties, and energy levels were studied systematically. In the immediate future, quantum efficiencies could be tested for OLEDs fabricated using these molecules. Additionally, we have recently began to study these molecules in the context of photocatalysis. Photoredox catalysts have recently become important tools in organic synthesis, facilitating a number of difficult, high-energy organic transformations.[333–336] Owing to the high triplet energies present in our IMAC-containing molecules and their high quantum yields, they should perform well as organic photocatalysts.

Chapter 6 described the synthesis of three donor-acceptor fluorescent dyes based on benzimidazole acceptors and triphenylamine donors, which exhibit deep blue emission. We demonstrated that restriction of rotational freedom greatly reduced the rate of photobleaching, particularly in the donor unit. Locking these chromophores into planar configurations also improved their cross-section for two-photon excited fluorescence (2PEF). Proof-of concept studies incorporating these dyes into water-soluble polymer dots suitable for biological imaging was also demonstrated. The stability of deep blue fluorophores for imaging applications is a persistent challenge due to the high excitation energy required, and here we presented a strategy for stabilizing such dyes while retaining colour purity and high quantum yield. Beyond imaging applications, materials with large 2PEF cross sections are also useful for optical power limiting and 3D optical data storage. Common requirements for fluorescent dyes in all of these applications are high two-photon cross-sections, high luminescent quantum yields, and stability to repeated excitation. Here we realized these goals through the design of molecules with rigidified donor and acceptor units. Future studies will examine the adaptation of these materials for application in biological systems. For example, derivatives of these materials could be synthesized which incorporate functional groups, such as dimethylamino or sulfonic acid residues, on the periphery of the molecule to impart water solubility.

The drive for miniaturization in the areas of optics, electronics and diagnostic technology has also led to intense interest in the preparation of nanomaterials with well-defined patterns of emission colour. Much focus over the past decades, including the focus of this thesis, has been on understanding the synthesis and properties of such nanostructures. However, the biggest challenge facing the field currently is that the usefulness of these materials in applications is yet to be fully demonstrated. I believe the following three points represent the most promising areas to apply

semiconducting BBCPs: 1) Due to their large domain sizes, BBCPs can also readily self-assemble into photonic crystal films, and could thus be applied as laser gain media; 2) One could envisage assembling multiblock BBCPs normal to an electrode substrate in order to generate well-defined multilayer films to produce nanoscopic OLED devices in a single step; 3) Due to their small size and potentially high density of encoded information multiblock BBCPs tagged with various chromophores and biological directing groups could find application in multiplexed cellular diagnostics. Investigation into the applications noted above will facilitate a rapid expansion in the field of BBCP nanostructures.

References

(1) Qiu, H.; Gao, Y.; Boott, C. E.; Gould, O. E. C.; Harniman, R. L.; Miles, M. J.; Webb, S. E. D.; Winnik, M. A.; Manners, I. Uniform Patchy and Hollow Rectangular Platelet Micelles from Crystallizable Polymer Blends. *Science* **2016**, *352*, 697–701.

(2) Nazemi, A.; He, X.; MacFarlane, L. R.; Harniman, R. L.; Hsiao, M.-S.; Winnik, M. A.; Faul, C. F. J.; Manners, I. Uniform "Patchy" Platelets by Seeded Heteroepitaxial Growth of Crystallizable Polymer Blends in Two Dimensions. *J. Am. Chem. Soc.* **2017**, *139*, 4409–4417.

(3) Inam, M.; Cambridge, G.; Pitto-Barry, A.; Laker, Z. P. L.; Wilson, N. R.; Mathers, R. T.; Dove, A. P.; O'Reilly, R. K. 1D vs. 2D Shape Selectivity in the Crystallization-Driven Self-Assembly of Polylactide Block Copolymers. *Chem. Sci.* **2017**, *8*, 4223–4230.

(4) Yang, S.; Kang, S.-Y.; Choi, T.-L. Morphologically Tunable Square and Rectangular Nanosheets of a Simple Conjugated Homopolymer by Changing Solvents. *J. Am. Chem. Soc.* **2019**, *141*, 19138–19143.

(5) Ieong, N. S.; Gadt, T.; Cambridge, G.; Winnik, M. A.; Manners, I. Complex Micelle Architectures from Polyferrocene Diblock Copolymers Using Living, Crystallization-Driven Supramolecular Polymerisations. *Nat. Mater.* **2009**, *100*, 516.

(6) Fan, B.; Wang, R.-Y.; Wang, X.-Y.; Xu, J.-T.; Du, B.-Y.; Fan, Z.-Q. Crystallization-Driven Co-Assembly of Micrometric Polymer Hybrid Single Crystals and Nanometric Crystalline Micelles. *Macromolecules* **2017**, *50*, 2006–2015.

(7) Gädt, T.; Ieong, N. S.; Cambridge, G.; Winnik, M. A.; Manners, I. Complex and Hierarchical Micelle Architectures from Diblock Copolymers Using Living, Crystallization-Driven Polymerizations. *Nat. Mater.* **2009**, *8*, 144–150.

(8) Gröschel, A. H.; Walther, A.; Löbling, T. I.; Schacher, F. H.; Schmalz, H.; Müller, A. H. E. Guided Hierarchical Co-Assembly of Soft Patchy Nanoparticles. *Nature* **2013**, *503*, 247–251.

(9) Qiu, H.; Hudson, Z. M.; Winnik, M. A.; Manners, I. Multidimensional Hierarchical Self-Assembly of Amphiphilic Cylindrical Block Comicelles. *Science* **2015**, *347*, 1329–1332.

(10) Jia, C.; Lin, Z.; Huang, Y.; Duan, X. Nanowire Electronics: From Nanoscale to Macroscale. *Chem. Rev.* **2019**, *119*, 9074–9135.

(11) Yan, R.; Gargas, D.; Yang, P. Nanowire Photonics. *Nat. Photonics* **2009**, *3*, 569–576.

(12) Shikha, S.; Salafi, T.; Cheng, J.; Zhang, Y. Versatile Design and Synthesis of Nano-Barcodes. *Chem. Soc. Rev.* **2017**, *46*, 7054–7093.

(13) He, F.; Gädt, T.; Manners, I.; Winnik, M. A. Fluorescent "Barcode" Multiblock Co-Micelles via the Living Self-Assembly of Di- and Triblock Copolymers with a Crystalline Core-Forming Metalloblock. *J. Am. Chem. Soc.* **2011**, *133*, 9095–9103.

(14) Hudson, Z. M.; Lunn, D. J.; Winnik, M. A.; Manners, I. Colour-Tunable Fluorescent Multiblock Micelles. *Nat. Commun.* **2014**, *5*, 3372.

(15) Jeon, Y. S.; Shin, H. M.; Kim, Y. J.; Nam, D. Y.; Park, B. C.; Yoo, E.; Kim, H.-R.; Kim, Y. K. Metallic Fe–Au Barcode Nanowires as a Simultaneous T Cell Capturing and Cytokine Sensing Platform for Immunoassay at the Single-Cell Level. *ACS Appl. Mater. Interfaces* **2019**, *11*, 23901–23908.

(16) Rasouli, R.; Barhoum, A.; Bechelany, M.; Dufresne, A. Nanofibers for Biomedical and Healthcare Applications. *Macromol. Biosci.* **2019**, *19*, 1800256.

(17) Patolsky, F.; Zheng, G.; Lieber, C. M. Nanowire Sensors for Medicine and the Life Sciences. *Nanomedicine* **2006**, *1*, 51–65.

(18) Jin, X.; Price, M. B.; Finnegan, J. R.; Boott, C. E.; Richter, J. M.; Rao, A.; Menke, S. M.; Friend, R. H.; Whittell, G. R.; Manners, I. Long-Range Exciton Transport in Conjugated Polymer Nanofibers Prepared by Seeded Growth. *Science* **2018**, *360*, 897–900.

(19) Groschel, A. H.; Muller, A. H. E. Self-Assembly Concepts for Multicompartment Nanostructures. *Nanoscale* **2015**, *7*, 11841–11876.

(20) Massey, J.; Power, K. N.; Manners, I.; Winnik, M. A. Self-Assembly of a Novel Organometallic−Inorganic Block Copolymer in Solution and the Solid State: Nonintrusive Observation of Novel Wormlike Poly(Ferrocenyldimethylsilane)- b -Poly(Dimethylsiloxane) Micelles. *J. Am. Chem. Soc.* **1998**, *120*, 9533–9540.

(21) Gilroy, J. B.; Gädt, T.; Whittell, G. R.; Chabanne, L.; Mitchels, J. M.; Richardson, R. M.; Winnik, M. A.; Manners, I. Monodisperse Cylindrical Micelles by Crystallization-Driven Living Self-Assembly. *Nat. Chem.* **2010**, *2*, 566–570.

(22) Sun, L.; Petzetakis, N.; Pitto-Barry, A.; Schiller, T. L.; Kirby, N.; Keddie, D. J.; Boyd, B. J.; O'Reilly, R. K.; Dove, A. P. Tuning the Size of Cylindrical Micelles from Poly(L-lactide)-b-poly(Acrylic Acid) Diblock Copolymers Based on Crystallization-Driven Self-Assembly. *Macromolecules* **2013**, *46*, 9074–9082.

(23) Arno, M. C.; Inam, M.; Coe, Z.; Cambridge, G.; Macdougall, L. J.; Keogh, R.; Dove, A. P.; O'Reilly, R. K. Precision Epitaxy for Aqueous 1D and 2D Poly(ε-Caprolactone) Assemblies. *J. Am. Chem. Soc.* **2017**, *139*, 16980–16985.

(24) Schöbel, J.; Karg, M.; Rosenbach, D.; Krauss, G.; Greiner, A.; Schmalz, H. Patchy Wormlike Micelles with Tailored Functionality by Crystallization-Driven Self-Assembly: A Versatile Platform for Mesostructured Hybrid Materials. *Macromolecules* **2016**, *49*, 2761–2771.

(25) Schmalz, H.; Schmelz, J.; Drechsler, M.; Yuan, J.; Walther, A.; Schweimer, K.; Mihut, A. M. Thermo-Reversible Formation of Wormlike Micelles with a Microphase-Separated Corona from a Semicrystalline Triblock Terpolymer. *Macromolecules* **2008**, *41*, 3235–3242.

(26) Patra, S. K.; Ahmed, R.; Whittell, G. R.; Lunn, D. J.; Dunphy, E. L.; Winnik, M. A.; Manners, I. Cylindrical Micelles of Controlled Length with a π-Conjugated Polythiophene Core via Crystallization-Driven Self-Assembly. *J. Am. Chem. Soc.* **2011**, *133*, 8842–8845.

(27) Tao, D.; Feng, C.; Cui, Y.; Yang, X.; Manners, I.; Winnik, M. A.; Huang, X. Monodisperse Fiber-like Micelles of Controlled Length and Composition with an Oligo(p -Phenylenevinylene) Core via "Living" Crystallization-Driven Self-Assembly. *J. Am. Chem. Soc.* **2017**, *139*, 7136–7139.

(28) Kynaston, E. L.; Nazemi, A.; MacFarlane, L. R.; Whittell, G. R.; Faul, C. F. J.; Manners, I. Uniform Polyselenophene Block Copolymer Fiberlike Micelles and Block Co-Micelles via Living Crystallization-Driven Self-Assembly. *Macromolecules* **2018**, *51*, 1002–1010.

(29) Li, X.; Wolanin, P. J.; MacFarlane, L. R.; Harniman, R. L.; Qian, J.; Gould, O. E. C. C.; Dane, T. G.; Rudin, J.; Cryan, M. J.; Schmaltz, T.; Frauenrath, H.; Winnik, M. A.; Faul, C. F. J. J.; Manners, I. Uniform Electroactive Fibre-like Micelle Nanowires for Organic Electronics. *Nat. Commun.* **2017**, *8*, 15909.

(30) Hasegawa, M.; Iyoda, M. Conducting Supramolecular Nanofibers and Nanorods. *Chem. Soc. Rev.* **2010**, *39*, 2420.

(31) Rest, C.; Kandanelli, R.; Fernández, G. Strategies to Create Hierarchical Self-Assembled Structures via Cooperative Non-Covalent Interactions. *Chem. Soc. Rev.* **2015**, *44*, 2543–2572.

(32) Ogi, S.; Sugiyasu, K.; Manna, S.; Samitsu, S.; Takeuchi, M. Living Supramolecular Polymerization Realized through a Biomimetic Approach. *Nat. Chem.* **2014**, *6*, 188–195.

(33) Wagner, W.; Wehner, M.; Stepanenko, V.; Ogi, S.; Würthner, F. Living Supramolecular Polymerization of a Perylene Bisimide Dye into Fluorescent J-Aggregates. *Angew. Chem. Int Ed.* **2017**, *129*, 16224–16228.

(34) Endo, M.; Fukui, T.; Jung, S. H.; Yagai, S.; Takeuchi, M.; Sugiyasu, K. Photoregulated Living Supramolecular Polymerization Established by Combining Energy Landscapes of Photoisomerization and Nucleation–Elongation Processes. *J. Am. Chem. Soc.* **2016**, *138*, 14347–14353.

(35) Adelizzi, B.; J. Van Zee, N.; N. J. de Windt, L.; R. A. Palmans, A.; W. Meijer, E.; Van Zee, N. J.; de Windt, L. N. J.; Palmans, A. R. A. A.; Meijer, E. W. The Future of Supramolecular Copolymers Unveiled by Reflecting on Covalent Copolymerization. *J. Am. Chem. Soc.* **2019**, *141*, 6110−6121.

(36) De Greef, T. F. A.; Smulders, M. M. J.; Wolffs, M.; Schenning, A. P. H. J.; Sijbesma, R. P.; Meijer, E. W. Supramolecular Polymerization. *Chem. Rev.* **2009**, *109*, 5687–5754.

(37) Jung, S. H.; Bochicchio, D.; Pavan, G. M.; Takeuchi, M.; Sugiyasu, K. A Block Supramolecular Polymer and Its Kinetically Enhanced Stability. *J. Am. Chem. Soc.* **2018**, *140*, 10570–10577.

(38) Adelizzi, B.; Aloi, A.; Markvoort, A. J.; Ten Eikelder, H. M. M.; Voets, I. K.; Palmans, A. R. A.; Meijer, E. W. Supramolecular Block Copolymers under Thermodynamic Control. *J. Am. Chem. Soc.* **2018**, *140*, 7168–7175.

(39) Wagner, W.; Wehner, M.; Stepanenko, V.; Würthner, F. Supramolecular Block Copolymers by Seeded Living Polymerization of Perylene Bisimides. *J. Am. Chem. Soc.*

2019, *141*, 12044–12054.

(40) Löbling, T. I.; Borisov, O.; Haataja, J. S.; Ikkala, O.; Gröschel, A. H.; Müller, A. H. E. Rational Design of ABC Triblock Terpolymer Solution Nanostructures with Controlled Patch Morphology. *Nat. Commun.* **2016**, *7*, 12097.

(41) Foster, J. C.; Varlas, S.; Couturaud, B.; Coe, Z.; O'Reilly, R. K.; O'Reilly, R. K. Getting into Shape: Reflections on a New Generation of Cylindrical Nanostructures' Self-Assembly Using Polymer Building Blocks. *J. Am. Chem. Soc.* **2019**, *141*, 2742–2753.

(42) Charleux, B.; Delaittre, G.; Rieger, J.; D'Agosto, F. Polymerization-Induced Self-Assembly: From Soluble Macromolecules to Block Copolymer Nano-Objects in One Step. *Macromolecules* **2012**, *45*, 6753–6765.

(43) Tan, J.; Liu, D.; Bai, Y.; Huang, C.; Li, X.; He, J.; Xu, Q.; Zhang, L. Enzyme-Assisted Photoinitiated Polymerization-Induced Self-Assembly: An Oxygen-Tolerant Method for Preparing Block Copolymer Nano-Objects in Open Vessels and Multiwell Plates. *Macromolecules* **2017**, *50*, 5798–5806.

(44) Yeow, J.; Boyer, C. Photoinitiated Polymerization-Induced Self-Assembly (Photo-PISA): New Insights and Opportunities. *Adv. Sci.* **2017**, *4*.

(45) D'Agosto, F.; Rieger, J.; Lansalot, M. RAFT-Mediated Polymerization-Induced Self-Assembly. *Angew. Chem. Int. Ed.* **2019**, 2–27.

(46) Foster, J. C.; Varlas, S.; Blackman, L. D.; Arkinstall, L. A.; O'Reilly, R. K. Ring-Opening Metathesis Polymerization in Aqueous Media Using a Macroinitiator Approach. *Angew. Chem. Int Ed.* **2018**, *130*, 10832–10836.

(47) Wright, D. B.; Touve, M. A.; Thompson, M. P.; Gianneschi, N. C. Aqueous-Phase Ring-Opening Metathesis Polymerization-Induced Self-Assembly. *ACS Macro Lett.* **2018**, *7*,

401–405.

(48) Zhang, W.-J.; Hong, C.-Y.; Pan, C.-Y. Efficient Fabrication of Photosensitive Polymeric Nano-Objects via an Ingenious Formulation of RAFT Dispersion Polymerization and Their Application for Drug Delivery. *Biomacromolecules* **2017**, *18*, 1210–1217.

(49) Bagheri, A.; Boyer, C.; Lim, M. Synthesis of Light-Responsive Pyrene-Based Polymer Nanoparticles via Polymerization-Induced Self-Assembly. *Macromol. Rapid Commun.* **2019**, *40*, 1–7.

(50) Mitchell, D. E.; Lovett, J. R.; Armes, S. P.; Gibson, M. I. Combining Biomimetic Block Copolymer Worms with an Ice-Inhibiting Polymer for the Solvent-Free Cryopreservation of Red Blood Cells. *Angew. Chem. Int. Ed.* **2016**, *55*, 2801–2804.

(51) Foster, J. C.; Varlas, S.; Couturaud, B.; Jones, J. R.; Keogh, R.; Mathers, R. T.; O'Reilly, R. K. Predicting Monomers for Use in Polymerization-Induced Self-Assembly. *Angew. Chem. Int Ed.* **2018**, *130*, 15959–15963.

(52) Hirschberg, J. H. K. K.; Brunsveld, L.; Ramzi, A.; Vekemans, J. A. J. M.; Sijbesma, R. P.; Meijer, E. W. Helical Self-Assembled Polymers from Cooperative Stacking of Hydrogen-Bonded Pairs. *Nature* **2000**, *407*, 167–170.

(53) Van Zee, N. J.; Adelizzi, B.; Mabesoone, M. F. J.; Meng, X.; Aloi, A.; Zha, R. H.; Lutz, M.; Filot, I. A. W.; Palmans, A. R. A.; Meijer, E. W. Potential Enthalpic Energy of Water in Oils Exploited to Control Supramolecular Structure. *Nature* **2018**, *558*, 100–103.

(54) Lu, J.; Owen, S. C.; Shoichet, M. S. Stability of Self-Assembled Polymeric Micelles in Serum. *Macromolecules* **2011**, *44*, 6002–6008.

(55) Paturej, J.; Sheiko, S. S.; Panyukov, S.; Rubinstein, M. Molecular Structure of Bottlebrush Polymers in Melts. *Sci. Adv.* **2016**, *2*, e1601478.

(56) Daniel, W. F. M. M.; Burdyńska, J.; Vatankhah-Varnoosfaderani, M.; Matyjaszewski, K.; Paturej, J.; Rubinstein, M.; Dobrynin, A. V.; Sheiko, S. S. Solvent-Free, Supersoft and Superelastic Bottlebrush Melts and Networks. *Nat. Mater.* **2016**, *15*, 183–189.

(57) Sunday, D. F.; Chang, A. B.; Liman, C. D.; Gann, E.; Delongchamp, D. M.; Thomsen, L.; Matsen, M. W.; Grubbs, R. H.; Soles, C. L. Self-Assembly of ABC Bottlebrush Triblock Terpolymers with Evidence for Looped Backbone Conformations. *Macromolecules* **2018**, *51*, 7178–7185.

(58) Verduzco, R.; Li, X.; Pesek, S. L.; Stein, G. E. Structure, Function, Self-Assembly, and Applications of Bottlebrush Copolymers. *Chem. Soc. Rev.* **2015**, *44*, 2405–2420.

(59) Sheiko, S. S.; Sumerlin, B. S.; Matyjaszewski, K. Cylindrical Molecular Brushes: Synthesis, Characterization, and Properties. *Prog. Polym. Sci.* **2008**, *33*, 759–785.

(60) Feng, C.; Li, Y.; Yang, D.; Hu, J.; Zhang, X.; Huang, X. Well-Defined Graft Copolymers: From Controlled Synthesis to Multipurpose Applications. *Chem. Soc. Rev.* **2011**, *40*, 1282–1295.

(61) Chen, Y. Shaped Hairy Polymer Nanoobjects. *Macromolecules* **2012**, *45*, 2619–2631.

(62) Müllner, M.; Müller, A. H. E. Cylindrical Polymer Brushes – Anisotropic Building Blocks, Unimolecular Templates and Particulate Nanocarriers. *Polymer* **2016**, *98*, 389–401.

(63) Rzayev, J. Molecular Bottlebrushes: New Opportunities in Nanomaterials Fabrication. *ACS Macro Lett.* **2012**, *1*, 1146–1149.

(64) Lee, H.; Pietrasik, J.; Sheiko, S. S.; Matyjaszewski, K. Stimuli-Responsive Molecular Brushes. *Prog. Polym. Sci.* **2010**, *35*, 24–44.

(65) Pelras, T.; Mahon, C. S.; Müllner, M. Synthesis and Applications of Compartmentalised

Molecular Polymer Brushes. *Angew. Chem. Int. Ed.* **2018**, *57*, 6982–6994.

(66) Pelras, T.; Mahon, C. S.; Nonappa; Ikkala, O.; Gröschel, A. H.; Müllner, M. Polymer Nanowires with Highly Precise Internal Morphology and Topography. *J. Am. Chem. Soc.* **2018**, *140*, 12736–12740.

(67) Chae, C.-G.; Yu, Y.-G.; Seo, H.-B.; Kim, M.-J.; Grubbs, R. H.; Lee, J.-S. Experimental Formulation of Photonic Crystal Properties for Hierarchically Self-Assembled POSS–Bottlebrush Block Copolymers. *Macromolecules* **2018**, *51*, 3458–3466.

(68) Miyake, G. M.; Weitekamp, R. A.; Piunova, V. A.; Grubbs, R. H. Synthesis of Isocyanate-Based Brush Block Copolymers and Their Rapid Self-Assembly to Infrared-Reflecting Photonic Crystals. *J. Am. Chem. Soc.* **2012**, *134*, 14249–14254.

(69) Liberman-Martin, A. L.; Chu, C. K.; Grubbs, R. H. Application of Bottlebrush Block Copolymers as Photonic Crystals. *Macromol. Rapid Commun.* **2017**, *38*, 1700058.

(70) Macfarlane, R. J.; Kim, B.; Lee, B.; Weitekamp, R. A.; Bates, C. M.; Lee, S. F.; Chang, A. B.; Delaney, K. T.; Fredrickson, G. H.; Atwater, H. A.; Grubbs, R. H. Improving Brush Polymer Infrared One-Dimensional Photonic Crystals via Linear Polymer Additives. *J. Am. Chem. Soc.* **2014**, *136*, 17374–17377.

(71) Miyake, G. M.; Piunova, V. A.; Weitekamp, R. A.; Grubbs, R. H. Precisely Tunable Photonic Crystals From Rapidly Self-Assembling Brush Block Copolymer Blends. *Angew. Chem. Int. Ed.* **2012**, *51*, 11246–11248.

(72) Song, D.-P.; Li, C.; Colella, N. S.; Lu, X.; Lee, J.-H.; Watkins, J. J. Thermally Tunable Metallodielectric Photonic Crystals from the Self-Assembly of Brush Block Copolymers and Gold Nanoparticles. *Adv. Opt. Mater.* **2015**, *3*, 1169–1175.

(73) Geng, Y.; Dalhaimer, P.; Cai, S.; Tsai, R.; Tewari, M.; Minko, T.; Discher, D. E. Shape

Effects of Filaments versus Spherical Particles in Flow and Drug Delivery. *Nat. Nanotechnol.* **2007**, *2*, 249–255.

(74) Sowers, M. A.; McCombs, J. R.; Wang, Y.; Paletta, J. T.; Morton, S. W.; Dreaden, E. C.; Boska, M. D.; Ottaviani, M. F.; Hammond, P. T.; Rajca, A.; Johnson, J. A. Redox-Responsive Branched-Bottlebrush Polymers for in Vivo MRI and Fluorescence Imaging. *Nat. Commun.* **2014**, *5*, 5460.

(75) Müllner, M.; Yang, K.; Kaur, A.; New, E. J. Aspect-Ratio-Dependent Interaction of Molecular Polymer Brushes and Multicellular Tumour Spheroids. *Polym. Chem.* **2018**, *9*, 3461–3465.

(76) Unsal, H.; Onbulak, S.; Calik, F.; Er-Rafik, M.; Schmutz, M.; Sanyal, A.; Rzayev, J. Interplay between Molecular Packing, Drug Loading, and Core Cross-Linking in Bottlebrush Copolymer Micelles. *Macromolecules* **2017**, *50*, 1342–1352.

(77) Bates, C. M.; Chang, A. B.; Momčilović, N.; Jones, S. C.; Grubbs, R. H. ABA Triblock Brush Polymers: Synthesis, Self-Assembly, Conductivity, and Rheological Properties. *Macromolecules* **2015**, *48*, 4967–4973.

(78) Jiang, L.; Nykypanchuk, D.; Ribbe, A. E.; Rzayev, J. One-Shot Synthesis and Melt Self-Assembly of Bottlebrush Copolymers with a Gradient Compositional Profile. *ACS Macro Lett.* **2018**, *7*, 619–623.

(79) Cho, S.; Son, J.; Kim, I.; Ahn, H.; Jang, H.-S.; Joo, S. H.; Park, K. H.; Lee, E.; Kim, Y.; Ahn, S. Asymmetric Polystyrene-Polylactide Bottlebrush Random Copolymers: Synthesis, Self-Assembly and Nanoporous Structures. *Polymer* **2019**, *175*, 49–56.

(80) Wang, Y.; Shao, F.; Sauvé, E. R.; Tonge, C. M.; Hudson, Z. M. Self-Assembly of Giant Bottlebrush Block Copolymer Surfactants from Luminescent Organic Electronic

Materials. *Soft Matter* **2019**, *15*, 5421–5430.

(81) Li, Z.; Ma, J.; Lee, N. S.; Wooley, K. L. Dynamic Cylindrical Assembly of Triblock Copolymers by a Hierarchical Process of Covalent and Supramolecular Interactions. *J. Am. Chem. Soc.* **2011**, *133*, 1228–1231.

(82) Mougnier, S.; Brochon, C.; Cloutet, E.; Fleury, G.; Cramail, H.; Hadziioannou, G. Design of Well-Defined Monofunctionalized Poly(3-Hexylthiophene)s: Toward the Synthesis of Semiconducting Graft Copolymers. *Macromol. Rapid Commun.* **2012**, *33*, 703–709.

(83) Heinrich, C. D.; Thelakkat, M. Poly-(3-Hexylthiophene) Bottlebrush Copolymers with Tailored Side-Chain Lengths and High Charge Carrier Mobilities. *J. Mater. Chem. C* **2016**, *4*, 5370–5378.

(84) Yin, X.; Qiao, Y.; Gadinski, M. R.; Wang, Q.; Tang, C. Flexible Thiophene Polymers: A Concerted Macromolecular Architecture for Dielectrics. *Polym. Chem.* **2016**, *7*, 2929–2933.

(85) Ahn, S.; Nam, J.; Zhu, J.; Lee, E.; Michael Kilbey, S. Solution Self-Assembly of Poly(3-Hexylthiophene)–Poly(Lactide) Brush Copolymers: Impact of Side Chain Arrangement. *Polym. Chem.* **2018**, *9*, 3279–3286.

(86) Wang, J.; Lu, C.; Mizobe, T.; Ueda, M.; Chen, W.-C.; Higashihara, T. Synthesis and Characterization of All-Conjugated Graft Copolymers Comprised of n-Type or p-Type Backbones and Poly(3-Hexylthiophene) Side Chains. *Macromolecules* **2013**, *46*, 1783–1793.

(87) Zeigler, D. F.; Mazzio, K. A.; Luscombe, C. K. Fully Conjugated Graft Copolymers Comprising a P-Type Donor–Acceptor Backbone and Poly(3-Hexylthiophene) Side Chains Synthesized Via a “Graft Through” Approach. *Macromolecules* **2014**, *47*, 5019–

5028.

(88) Obhi, N. K.; Peda, D. M.; Kynaston, E. L.; Seferos, D. S. Exploring the Graft-To Synthesis of All-Conjugated Comb Copolymers Using Azide–Alkyne Click Chemistry. *Macromolecules* **2018**, *51*, 2969–2978.

(89) Gao, D.; Hollinger, J.; Seferos, D. S. Selenophene–Thiophene Block Copolymer Solar Cells with Thermostable Nanostructures. *ACS Nano* **2012**, *6*, 7114–7121.

(90) Gao, D.; Hollinger, J.; Jahnke, A. A.; Seferos, D. S. Influence of Selenophene–Thiophene Phase Separation on Solar Cell Performance. *J. Mater. Chem. A* **2014**, *2*, 6058–6063.

(91) Hawker, C. J.; Bosman, A. W.; Harth, E. New Polymer Synthesis by Nitroxide Mediated Living Radical Polymerizations. *Chem. Rev.* **2001**, *101*, 3661–3688.

(92) Kato, M.; Kamigaito, M.; Sawamoto, M.; Higashimura, T. Polymerization of Methyl Methacrylate with the Carbon Tetrachloride/Dichlorotris-(Triphenylphosphine)Ruthenium(II)/Methylaluminum Bis(2,6-Di-Tert-Butylphenoxide) Initiating System: Possibility of Living Radical Polymerization. *Macromolecules* **1995**, *28*, 1721–1723.

(93) Wang, J.-S.; Matyjaszewski, K. Controlled/"living" Radical Polymerization. Atom Transfer Radical Polymerization in the Presence of Transition-Metal Complexes. *J. Am. Chem. Soc.* **1995**, *117*, 5614–5615.

(94) Chiefari, J.; Chong, Y. K. (Bill); Ercole, F.; Krstina, J.; Jeffery, J.; Le, T. P. T.; Mayadunne, R. T. A.; Meijs, G. F.; Moad, C. L.; Moad, G.; Rizzardo, E.; Thang, S. H. Living Free-Radical Polymerization by Reversible Addition−Fragmentation Chain Transfer: The RAFT Process. *Macromolecules* **1998**, *31*, 5559–5562.

(95) Matyjaszewski, K.; Tsarevsky, N. V. Nanostructured Functional Materials Prepared by

Atom Transfer Radical Polymerization. *Nat. Chem.* **2009**, *1*, 276.

(96) Braunecker, W. A.; Matyjaszewski, K. Controlled/Living Radical Polymerization: Features, Developments, and Perspectives. *Prog. Polym. Sci.* **2007**, *32*, 93–146.

(97) Greszta, D.; Mardare, D.; Matyjaszewski, K. "Living" Radical Polymerization. 1. Possibilities and Limitations. *Macromolecules* **1994**, *27*, 638–644.

(98) Matyjaszewski, K. Atom Transfer Radical Polymerization (ATRP): Current Status and Future Perspectives. *Macromolecules* **2012**, *45*, 4015–4039.

(99) Fischer, H. The Persistent Radical Effect: A Principle for Selective Radical Reactions and Living Radical Polymerizations. *Chem. Rev.* **2001**, *101*, 3581–3610.

(100) Matyjaszewski, K.; Jakubowski, W.; Min, K.; Tang, W.; Huang, J.; Braunecker, W. A.; Tsarevsky, N. V. Diminishing Catalyst Concentration in Atom Transfer Radical Polymerization with Reducing Agents. *Proc. Natl. Acad. Sci.* **2006**, *103*, 15309–15314.

(101) Jakubowski, W.; Matyjaszewski, K. Activators Regenerated by Electron Transfer for Atom-Transfer Radical Polymerization of (Meth)Acrylates and Related Block Copolymers. *Angew. Chem. Int Ed.* **2006**, *118*, 4594–4598.

(102) Magenau, A. J. D.; Strandwitz, N. C.; Gennaro, A.; Matyjaszewski, K. Electrochemically Mediated Atom Transfer Radical Polymerization. *Science* **2011**, *332*, 81–84.

(103) Tasdelen, M. A.; Uygun, M.; Yagci, Y. Photoinduced Controlled Radical Polymerization in Methanol. *Macromol. Chem. Phys.* **2010**, *211*, 2271–2275.

(104) Fors, B. P.; Hawker, C. J. Control of a Living Radical Polymerization of Methacrylates by Light. *Angew. Chem. Int. Ed.* **2012**, *51*, 8850–8853.

(105) Konkolewicz, D.; Wang, Y.; Krys, P.; Zhong, M.; Isse, A. A.; Gennaro, A.; Matyjaszewski, K. SARA ATRP or SET-LRP. End of Controversy? *Polym. Chem.* **2014**,

5, 4396–4417.

(106) Alsubaie, F.; Anastasaki, A.; Nikolaou, V.; Simula, A.; Nurumbetov, G.; Wilson, P.; Kempe, K.; Haddleton, D. M. Investigating the Mechanism of Copper(0)-Mediated Living Radical Polymerization in Organic Media. *Macromolecules* **2015**, *48*, 5517–5525.

(107) Alsubaie, F.; Anastasaki, A.; Nikolaou, V.; Simula, A.; Nurumbetov, G.; Wilson, P.; Kempe, K.; Haddleton, D. M. Investigating the Mechanism of Copper(0)-Mediated Living Radical Polymerization in Aqueous Media. *Macromolecules* **2015**, *48*, 6421–6432.

(108) Anastasaki, A.; Nikolaou, V.; Nurumbetov, G.; Wilson, P.; Kempe, K.; Quinn, J. F.; Davis, T. P.; Whittaker, M. R.; Haddleton, D. M. Cu(0)-Mediated Living Radical Polymerization: A Versatile Tool for Materials Synthesis. *Chem. Rev.* **2016**, *116*, 835–877.

(109) Rosen, B. M.; Percec, V. Single-Electron Transfer and Single-Electron Transfer Degenerative Chain Transfer Living Radical Polymerization. *Chem. Rev.* **2009**, *109*, 5069–5119.

(110) Whitfield, R.; Anastasaki, A.; Nikolaou, V.; Jones, G. R.; Engelis, N. G.; Discekici, E. H.; Fleischmann, C.; Willenbacher, J.; Hawker, C. J.; Haddleton, D. M. Universal Conditions for the Controlled Polymerization of Acrylates, Methacrylates, and Styrene via Cu(0)-RDRP. *J. Am. Chem. Soc.* **2017**, *139*, 1003–1010.

(111) Matyjaszewski, K.; Coca, S.; Gaynor, S. G.; Wei, M.; Woodworth, B. E. Zerovalent Metals in Controlled/"Living" Radical Polymerization. *Macromolecules* **1997**, *30*, 7348–7350.

(112) Boyer, C.; Corrigan, N. A.; Jung, K.; Nguyen, D.; Nguyen, T.-K.; Adnan, N. N. M.; Oliver, S.; Shanmugam, S.; Yeow, J. Copper-Mediated Living Radical Polymerization

(Atom Transfer Radical Polymerization and Copper(0) Mediated Polymerization): From Fundamentals to Bioapplications. *Chem. Rev.* **2016**, *116*, 1803–1949.

(113) Anastasaki, A.; Nikolaou, V.; Haddleton, D. M. Cu(0)-Mediated Living Radical Polymerization: Recent Highlights and Applications; a Perspective. *Polym. Chem.* **2016**, *7*, 1002–1026.

(114) Anastasaki, A.; Waldron, C.; Wilson, P.; Boyer, C.; Zetterlund, P. B.; Whittaker, M. R.; Haddleton, D. High Molecular Weight Block Copolymers by Sequential Monomer Addition via Cu(0)-Mediated Living Radical Polymerization (SET-LRP): An Optimized Approach. *ACS Macro Lett.* **2013**, *2*, 896–900.

(115) Magenau, A. J. D.; Kwak, Y.; Matyjaszewski, K. ATRP of Methacrylates Utilizing CuIIX2/L and Copper Wire. *Macromolecules* **2010**, *43*, 9682–9689.

(116) Sutthasupa, S.; Shiotsuki, M.; Sanda, F. Recent Advances in Ring-Opening Metathesis Polymerization, and Application to Synthesis of Functional Materials. *Polym. J.* **2010**, *42*, 905–915.

(117) Schwab, P.; Grubbs, R. H.; Ziller, J. W. Synthesis and Applications of RuCl 2 (CHR‘)(PR 3) 2 : The Influence of the Alkylidene Moiety on Metathesis Activity. *J. Am. Chem. Soc.* **1996**, *118*, 100–110.

(118) Schwab, P.; France, M. B.; Ziller, J. W.; Grubbs, R. H. A Series of Well-Defined Metathesis Catalysts–Synthesis of[RuCl2(=CHR′)(PR3)2] and Its Reactions. *Angew. Chemie Int. Ed. English* **1995**, *34*, 2039–2041.

(119) Scholl, M.; Ding, S.; Lee, C. W.; Grubbs, R. H. Synthesis and Activity of a New Generation of Ruthenium-Based Olefin Metathesis Catalysts Coordinated with 1,3-Dimesityl-4,5-Dihydroimidazol-2-Ylidene Ligands §. *Org. Lett.* **1999**, *1*, 953–956.

(120) Love, J. A.; Morgan, J. P.; Trnka, T. M.; Grubbs, R. H. A Practical and Highly Active Ruthenium-Based Catalyst That Effects the Cross Metathesis of Acrylonitrile. *Angew. Chem. Int. Ed.* **2002**, *41*, 4035–4037.

(121) Choi, T.-L.; Grubbs, R. H. Controlled Living Ring-Opening-Metathesis Polymerization by a Fast-Initiating Ruthenium Catalyst. *Angew. Chem. Int. Ed.* **2003**, *42*, 1743–1746.

(122) Sanford, M. S.; Love, J. A.; Grubbs, R. H. A Versatile Precursor for the Synthesis of New Ruthenium Olefin Metathesis Catalysts. *Organometallics* **2001**, *20*, 5314–5318.

(123) Tang, C. W.; Vanslyke, S. A. Organic Electroluminescent Diodes. *Appl. Phys. Lett.* **1987**, *51*, 913–915.

(124) Adachi, C.; Baldo, M. A.; Thompson, M. E.; Forrest, S. R. Nearly 100% Internal Phosphorescence Efficiency in an Organic Light-Emitting Device. *J. Appl. Phys.* **2001**, *90*, 5048–5051.

(125) Baldo M. A.; O'Brien D. F.; You Y.; Shoustikov A.; Sibley S.; Thompson M. E.; Forrest S. R. Highly Efficient Phosphorescent Emission from Organic Electroluminescent Devices. *Nature* **1998**, *395*, 151–154.

(126) Baldo, M. A.; Thompson, M. E.; Forrest, S. R. Phosphorescent Materials for Application to Organic Light Emitting Devices. *Pure Appl. Chem.* **1999**, *71*, 2095–2106.

(127) Uoyama, H.; Goushi, K.; Shizu, K.; Nomura, H.; Adachi, C. Highly Efficient Organic Light-Emitting Diodes from Delayed Fluorescence. *Nature* **2012**, *492*, 234–238.

(128) Wong, M. Y.; Zysman-Colman, E. Purely Organic Thermally Activated Delayed Fluorescence Materials for Organic Light-Emitting Diodes. *Adv. Mater.* **2017**, *29*, 1605444.

(129) Yang, Z.; Mao, Z.; Xie, Z.; Zhang, Y.; Liu, S.; Zhao, J.; Xu, J.; Chi, Z.; Aldred, M. P.

Recent Advances in Organic Thermally Activated Delayed Fluorescence Materials. *Chem. Soc. Rev.* **2017**, *46*, 915–1016.

(130) Nakanotani, H.; Furukawa, T.; Hosokai, T.; Hatakeyama, T.; Adachi, C. Light Amplification in Molecules Exhibiting Thermally Activated Delayed Fluorescence. *Adv. Opt. Mater.* **2017**, *5*, 1700051.

(131) Kaji, H.; Suzuki, H.; Fukushima, T.; Shizu, K.; Suzuki, K.; Kubo, S.; Komino, T.; Oiwa, H.; Suzuki, F.; Wakamiya, A.; Murata, Y.; Adachi, C. Purely Organic Electroluminescent Material Realizing 100% Conversion from Electricity to Light. *Nat. Commun.* **2015**, *6*, 8476.

(132) Kim, J. H.; Yun, J. H.; Lee, J. Y. Recent Progress of Highly Efficient Red and Near-Infrared Thermally Activated Delayed Fluorescent Emitters. *Adv. Opt. Mater.* **2018**, *6*, 1800255.

(133) Huang, T.; Jiang, W.; Duan, L. Recent Progress in Solution Processable TADF Materials for Organic Light-Emitting Diodes. *J. Mater. Chem. C* **2018**, *6*, 5577–5596.

(134) Wex, B.; Kaafarani, B. R. Perspective on Carbazole-Based Organic Compounds as Emitters and Hosts in TADF Applications. *J. Mater. Chem. C* **2017**, *5*, 8622–8653.

(135) Tao, Y.; Yuan, K.; Chen, T.; Xu, P.; Li, H.; Chen, R.; Zheng, C.; Zhang, L.; Huang, W. Thermally Activated Delayed Fluorescence Materials towards the Breakthrough of Organoelectronics. *Adv. Mater.* **2014**, *26*, 7931–7958.

(136) Liang, X.; Tu, Z. L.; Zheng, Y. X. Thermally Activated Delayed Fluorescence Materials: Towards Realization of High Efficiency through Strategic Small Molecular Design. *Chem. Eur. J.* **2019**, *25*, 5623–5642.

(137) Sharma, N.; Spuling, E.; Mattern, C. M.; Li, W.; Fuhr, O.; Tsuchiya, Y.; Adachi, C.;

Bräse, S.; Samuel, I. D. W.; Zysman-Colman, E. Turn on of Sky-Blue Thermally Activated Delayed Fluorescence and Circularly Polarized Luminescence (CPL) via Increased Torsion by a Bulky Carbazolophane Donor. *Chem. Sci.* **2019**, *10*, 6689–6696.

(138) Liu, Y.; Li, C.; Ren, Z.; Yan, S.; Bryce, M. R. All-Organic Thermally Activated Delayed Fluorescence Materials for Organic Light-Emitting Diodes. *Nat. Rev. Mater.* **2018**, *3*, 18020.

(139) Kawasumi, K.; Wu, T.; Zhu, T.; Chae, H. S.; Van Voorhis, T.; Baldo, M. A.; Swager, T. M. Thermally Activated Delayed Fluorescence Materials Based on Homoconjugation Effect of Donor–Acceptor Triptycenes. *J. Am. Chem. Soc.* **2015**, *137*, 11908–11911.

(140) Tsujimoto, H.; Ha, D.-G.; Markopoulos, G.; Chae, H. S.; Baldo, M. A.; Swager, T. M. Thermally Activated Delayed Fluorescence and Aggregation Induced Emission with Through-Space Charge Transfer. *J. Am. Chem. Soc.* **2017**, *139*, 4894–4900.

(141) Chen, X.-L.; Jia, J.-H.; Yu, R.; Liao, J.-Z.; Yang, M.-X.; Lu, C.-Z. Combining Charge-Transfer Pathways to Achieve Unique Thermally Activated Delayed Fluorescence Emitters for High-Performance Solution-Processed, Non-Doped Blue OLEDs. *Angew. Chem. Int. Ed.* **2017**, *56*, 15006–15009.

(142) Hu, J.; Li, Q.; Wang, X.; Shao, S.; Wang, L.; Jing, X.; Wang, F. Developing Through-Space Charge Transfer Polymers as a General Approach to Realize Full-Color and White Emission with Thermally Activated Delayed Fluorescence. *Angew. Chem. Int. Ed.* **2019**, *58*, 8405–8409.

(143) Shao, S.; Hu, J.; Wang, X.; Wang, L.; Jing, X.; Wang, F. Blue Thermally Activated Delayed Fluorescence Polymers with Nonconjugated Backbone and Through-Space Charge Transfer Effect. *J. Am. Chem. Soc.* **2017**, *139*, 17739–17742.

(144) Hirai, H.; Nakajima, K.; Nakatsuka, S.; Shiren, K.; Ni, J.; Nomura, S.; Ikuta, T.; Hatakeyama, T. One-Step Borylation of 1,3-Diaryloxybenzenes Towards Efficient Materials for Organic Light-Emitting Diodes. *Angew. Chem. Int. Ed.* **2015**, *54*, 13581–13585.

(145) Hatakeyama, T.; Shiren, K.; Nakajima, K.; Nomura, S.; Nakatsuka, S.; Kinoshita, K.; Ni, J.; Ono, Y.; Ikuta, T. Ultrapure Blue Thermally Activated Delayed Fluorescence Molecules: Efficient HOMO-LUMO Separation by the Multiple Resonance Effect. *Adv. Mater.* **2016**, *28*, 2777–2781.

(146) Pershin, A.; Hall, D.; Lemaur, V.; Sancho-Garcia, J.-C. C.; Muccioli, L.; Zysman-Colman, E.; Beljonne, D.; Olivier, Y. Highly Emissive Excitons with Reduced Exchange Energy in Thermally Activated Delayed Fluorescent Molecules. *Nat. Commun.* **2019**, *10*, 3–7.

(147) Suresh, S. M.; Duda, E.; Hall, D.; Yao, Z.; Bagnich, S.; Slawin, A. M. Z.; Bässler, H.; Beljonne, D.; Buck, M.; Olivier, Y.; Köhler, A.; Zysman-Colman, E. A Deep Blue B,N-Doped Heptacene Emitter That Shows Both Thermally Activated Delayed Fluorescence and Delayed Fluorescence by Triplet–Triplet Annihilation. *J. Am. Chem. Soc.* **2020**, *142*, 6588–6599.

(148) Hüttner, S.; Sommer, M.; Steiner, U.; Thelakkat, M. Organic Field Effect Transistors from Triarylamine Side-Chain Polymers. *Appl. Phys. Lett.* **2010**, *96*, 73503.

(149) Bellmann, E.; Shaheen, S. E.; Thayumanavan, S.; Barlow, S.; Grubbs, R. H.; Marder, S. R.; Kippelen, B.; Peyghambarian, N. New Triarylamine-Containing Polymers as Hole Transport Materials in Organic Light-Emitting Diodes: Effect of Polymer Structure and Cross-Linking on Device Characteristics. *Chem. Mater.* **1998**, *10*, 1668–1676.

(150) Snaith, H. J.; Whiting, G. L.; Sun, B.; Greenham, N. C.; Huck, W. T. S.; Friend, R. H.

Self-Organization of Nanocrystals in Polymer Brushes. Application in Heterojunction Photovoltaic Diodes. *Nano Lett.* **2005**, *5*, 1653–1657.

(151) Whiting, G. L.; Snaith, H. J.; Khodabakhsh, S.; Andreasen, J. W.; Breiby, D. W.; Nielsen, M. M.; Greenham, N. C.; Friend, R. H.; Huck, W. T. S. Enhancement of Charge-Transport Characteristics in Polymeric Films Using Polymer Brushes. *Nano Lett.* **2006**, *6*, 573–578.

(152) Niu, Y.-H.; Liu, M. S.; Ka, J.-W.; Bardeker, J.; Zin, M. T.; Schofield, R.; Chi, Y.; Jen, A. K.-Y. Crosslinkable Hole-Transport Layer on Conducting Polymer for High-Efficiency White Polymer Light-Emitting Diodes. *Adv. Mater.* **2007**, *19*, 300–304.

(153) Griniene, R.; Tavgeniene, D.; Baranauskyte, U.; Xie, Z.; Zhang, B.; Gelzinis, A.; Grigalevicius, S. New Electroactive Polymers with Electronically Isolated 3,6,9-Triarylcarbazole Units as Efficient Hole Transporting Materials for Organic Light Emitting Diodes. *Opt. Mater.* **2017**, *66*, 230–235.

(154) Shih, H.-K.; Chu, Y.-L.; Chang, F.-C.; Zhu, C.-Y.; Kuo, S.-W. A Cross-Linkable Triphenylamine Derivative as a Hole Injection/Transporting Material in Organic Light-Emitting Diodes. *Polym. Chem.* **2015**, *6*, 6227–6237.

(155) Page, Z. A.; Narupai, B.; Pester, C. W.; Bou Zerdan, R.; Sokolov, A.; Laitar, D. S.; Mukhopadhyay, S.; Sprague, S.; McGrath, A. J.; Kramer, J. W.; Trefonas, P.; Hawker, C. J. Novel Strategy for Photopatterning Emissive Polymer Brushes for Organic Light Emitting Diode Applications. *ACS Cent. Sci.* **2017**, *3*, 654–661.

(156) Li, H.; Luo, H.; Cao, Z.; Gu, Z.; Shen, P.; Zhao, B.; Chen, H.; Yu, G.; Tan, S. Synthesis and Photovoltaic Performances of Conjugated Copolymers with 4{,}7-Dithien-5-Yl-2{,}1{,}3-Benzothiadiazole and Di(p-Tolyl)Phenylamine Side Groups. *J. Mater. Chem.* **2012**, *22*, 22913–22921.

(157) Zhang, Z.-G.; Zhang, S.; Min, J.; Chui, C.; Zhang, J.; Zhang, M.; Li, Y. Conjugated Side-Chain Isolated Polythiophene: Synthesis and Photovoltaic Application. *Macromolecules* **2012**, *45*, 113–118.

(158) Li, J.; Deng, X.; Zhang, Z.; Wang, Y.; Liu, Y.; He, K.; Huang, Y.; Tao, Q.; Quan, L.; Zhu, W. Tuning Photovoltaic Performance of 9,9-Dioctylfluorene-Alt-5,7-Bis(Thiophen-2-Yl)-2,3-Biphenylthieno[3,4-b]Pyrazine Copolymeric Derivatives by Attaching Additional Donor Units in Pendant Phenyl Ring. *J. Polym. Sci. Part A Polym. Chem.* **2012**, *50*, 4686–4694.

(159) Bian, L.; Yang, D.; Yin, L.; Zhang, J.; Tang, W. Carbazole-Substituted Triphenylamine and Diketopyrrolopyrrole Alternating Copolymer for Photovoltaic Cells. *Macromol. Chem. Phys.* **2013**, *214*, 2136–2143.

(160) Wang, J.; Liu, K.; Ma, L.; Zhan, X. Triarylamine: Versatile Platform for Organic, Dye-Sensitized, and Perovskite Solar Cells. *Chem. Rev.* **2016**, *116*, 14675–14725.

(161) Cho, S. Y.; Ko, J. M.; Jung, J.-Y.; Lee, J. Y.; Choi, D. H.; Lee, C. High-Performance Organic Thin Film Transistors Based on Inkjet-Printed Polymer/TIPS Pentacene Blends. *Org. Electron.* **2012**, *13*, 1329–1339.

(162) Lechmann, M. C.; Kessler, D.; Gutmann, J. S. Functional Templates for Hybrid Materials with Orthogonal Functionality. *Langmuir* **2009**, *25*, 10202–10208.

(163) Williams, P. E.; Moughton, A. O.; Patterson, J. P.; Khodabakhsh, S.; O'Reilly, R. K. Exploring RAFT Polymerization for the Synthesis of Bipolar Diblock Copolymers and Their Supramolecular Self-Assembly. *Polym. Chem.* **2011**, *2*, 720–729.

(164) Zorn, M.; Bae, W. K.; Kwak, J.; Lee, H.; Lee, C.; Zentel, R.; Char, K. Quantum Dot−Block Copolymer Hybrids with Improved Properties and Their Application to

Quantum Dot Light-Emitting Devices. *ACS Nano* **2009**, *3*, 1063–1068.

(165) Kessler, D.; Lechmann, M. C.; Noh, S.; Berger, R.; Lee, C.; Gutmann, J. S.; Theato, P. Surface Coatings Based on Polysilsesquioxanes: Solution-Processible Smooth Hole-Injection Layers for Optoelectronic Applications. *Macromol. Rapid Commun.* **2009**, *30*, 1238–1242.

(166) Häussler, M.; Lok, Y. P.; Chen, M.; Jasieniak, J.; Adhikari, R.; King, S. P.; Haque, S. A.; Forsyth, C. M.; Winzenberg, K.; Watkins, S. E.; Rizzardo, E.; Wilson, G. J. Benzothiadiazole-Containing Pendant Polymers Prepared by RAFT and Their Electro-Optical Properties. *Macromolecules* **2010**, *43*, 7101–7110.

(167) Page, Z. A.; Chiu, C.-Y.; Narupai, B.; Laitar, D. S.; Mukhopadhyay, S.; Sokolov, A.; Hudson, Z. M.; Bou Zerdan, R.; McGrath, A. J.; Kramer, J. W.; Barton, B. E.; Hawker, C. J. Highly Photoluminescent Nonconjugated Polymers for Single-Layer Light Emitting Diodes. *ACS Photonics* **2017**, *4*, 631–641.

(168) Bertrand, O.; Ernould, B.; Boujioui, F.; Vlad, A.; Gohy, J.-F. Synthesis of Polymer Precursors of Electroactive Materials by SET-LRP. *Polym. Chem.* **2015**, *6*, 6067–6072.

(169) Shirota, Y. Photo- and Electroactive Amorphous Molecular Materials-Molecular Design{,} Syntheses{,} Reactions{,} Properties{,} and Applications. *J. Mater. Chem.* **2005**, *15*, 75–93.

(170) Tao, Y.; Yang, C.; Qin, J. Organic Host Materials for Phosphorescent Organic Light-Emitting Diodes. *Chem. Soc. Rev.* **2011**, *40*, 2943–2970.

(171) Li, J.; Liu, D.; Li, Y.; Lee, C.-S.; Kwong, H.-L.; Lee, S. A High Tg Carbazole-Based Hole-Transporting Material for Organic Light-Emitting Devices. *Chem. Mater.* **2005**, *17*, 1208–1212.

(172) Xu, T.; Lu, R.; Liu, X.; Chen, P.; Qiu, X.; Zhao, Y. Synthesis and Characterization of Subporphyrins with Dendritic Carbazole Arms. *European J. Org. Chem.* **2008**, *2008*, 1065–1071.

(173) Hu, B.; Zhuge, F.; Zhu, X.; Peng, S.; Chen, X.; Pan, L.; Yan, Q.; Li, R.-W. Nonvolatile Bistable Resistive Switching in a New Polyimide Bearing 9-Phenyl-9H-Carbazole Pendant. *J. Mater. Chem.* **2012**, *22*, 520–526.

(174) Lligadas, G.; Grama, S.; Percec, V. Single-Electron Transfer Living Radical Polymerization Platform to Practice, Develop, and Invent. *Biomacromolecules* **2017**, *18*, 2981–3008.

(175) Grama, S.; Lejnieks, J.; Enayati, M.; Smail, R. B.; Ding, L.; Lligadas, G.; Monteiro, M. J.; Percec, V. Searching for Efficient SET-LRP Systems via Biphasic Mixtures of Water with Carbonates{,} Ethers and Dipolar Aprotic Solvents. *Polym. Chem.* **2017**, *8*, 5865–5874.

(176) Moreno, A.; Grama, S.; Liu, T.; Galia, M.; Lligadas, G.; Percec, V. SET-LRP Mediated by TREN in Biphasic Water-Organic Solvent Mixtures Provides the Most Economical and Efficient Process. *Polym. Chem.* **2017**, *8*, 7559–7574.

(177) Lligadas, G.; Rosen, B. M.; Monteiro, M. J.; Percec, V. Solvent Choice Differentiates SET-LRP and Cu-Mediated Radical Polymerization with Non-First-Order Kinetics. *Macromolecules* **2008**, *41*, 8360–8364.

(178) Lligadas, G.; Rosen, B. M.; Bell, C. A.; Monteiro, M. J.; Percec, V. Effect of Cu(0) Particle Size on the Kinetics of SET-LRP in DMSO and Cu-Mediated Radical Polymerization in MeCN at 25 °C. *Macromolecules* **2008**, *41*, 8365–8371.

(179) Lligadas, G.; Percec, V. SET-LRP of Acrylates in the Presence of Radical Inhibitors. *J. Polym. Sci. Part A Polym. Chem.* **2008**, *46*, 3174–3181.

(180) Soliman, S. M. A.; Nouvel, C.; Babin, J.; Six, J.-L. O-Nitrobenzyl Acrylate Is Polymerizable by Single Electron Transfer-Living Radical Polymerization. *J. Polym. Sci. Part A Polym. Chem.* **2014**, *52*, 2192–2201.

(181) Wu, C.; Chiu, D. T. Highly Fluorescent Semiconducting Polymer Dots for Biology and Medicine. *Angew. Chem. Int. Ed.* **2013**, *52*, 3086–3109.

(182) Tonge, C. M.; Sauvé, E. R.; Paisley, N. R.; Heyes, J. E.; Hudson, Z. M. Polymerization of Acrylates Based on N-Type Organic Semiconductors Using Cu(0)-RDRP. *Polym. Chem.* **2018**, *9*, 3359–3367.

(183) Christopherson, C. J.; Hackett, Z. S.; Sauvé, E. R.; Paisley, N. R.; Tonge, C. M.; Mayder, D. M.; Hudson, Z. M. Synthesis of Phosphorescent Iridium-Containing Acrylic Monomers and Their Room-Temperature Polymerization by Cu(0)-RDRP. *J. Polym. Sci. Part A Polym. Chem.* **2018**, *56*, 2539–2546.

(184) Wang, J. F.; Jabbour, G. E.; Mash, E. A.; Anderson, J.; Zhang, Y.; Lee, P. A.; Armstrong, N. R.; Peyghambarian, N.; Kippelen, B. Oxadiazole Metal Complex for Organic Light-Emitting Diodes. *Adv. Mater.* **1999**, *11*, 1266–1269.

(185) Kulkarni, A. P.; Tonzola, C. J.; Babel, A.; Jenekhe, S. A. Electron Transport Materials for Organic Light-Emitting Diodes. *Chem. Mater.* **2004**, *16*, 4556–4573.

(186) Sun, B.; Hong, W.; Yan, Z.; Aziz, H.; Li, Y. Record High Electron Mobility of 6.3 Cm 2 V −1 s −1 Achieved for Polymer Semiconductors Using a New Building Block. *Adv. Mater.* **2014**, *26*, 2636–2642.

(187) Facchetti, A. Polymer Donor–Polymer Acceptor (All-Polymer) Solar Cells. *Mater. Today* **2013**, *16*, 123–132.

(188) Bose, K. S.; Patel, C. C. Cu(II) Complexes of 1-Benzyl-2-Phenyl-Benzimidazole. *J. Inorg.*

Nucl. Chem. **1970**, *32*, 1141–1146.

(189) Sasabe, H.; Kido, J. Recent Progress in Phosphorescent Organic Light-Emitting Devices. *European J. Org. Chem.* **2013**, *2013*, 7653–7663.

(190) Suzuri, Y.; Oshiyama, T.; Ito, H.; Hiyama, K.; Kita, H. Phosphorescent Cyclometalated Complexes for Efficient Blue Organic Light-Emitting Diodes. *Sci. Technol. Adv. Mater.* **2014**, *15*, 054202.

(191) Yang, X.; Zhou, G.; Wong, W.-Y. Functionalization of Phosphorescent Emitters and Their Host Materials by Main-Group Elements for Phosphorescent Organic Light-Emitting Devices. *Chem. Soc. Rev.* **2015**, *44*, 8484–8575.

(192) Longhi, E.; De Cola, L. *Iridium (III) in Optoelectronic and Photonics Applications*; Zysman-Colman, E., Ed.; Wiley: Hoboken, New Jersey, 2017.

(193) Martir, D. R.; Momblona, C.; Pertegás, A.; Cordes, D. B.; Slawin, A. M. Z.; Bolink, H. J.; Zysman-Colman, E. Chiral Iridium(III) Complexes in Light-Emitting Electrochemical Cells: Exploring the Impact of Stereochemistry on the Photophysical Properties and Device Performances. *ACS Appl. Mater. Interfaces* **2016**, *8*, 33907–33915.

(194) Martínez-Alonso, M.; Cerdá, J.; Momblona, C.; Pertegás, A.; Junquera-Hernández, J. M.; Heras, A.; Rodríguez, A. M.; Espino, G.; Bolink, H.; Ortí, E. Highly Stable and Efficient Light-Emitting Electrochemical Cells Based on Cationic Iridium Complexes Bearing Arylazole Ancillary Ligands. *Inorg. Chem.* **2017**, *56*, 10298–10310.

(195) Ma, D.-L.; Lin, S.; Wang, W.; Yang, C.; Leung, C.-H. Luminescent Chemosensors by Using Cyclometalated Iridium(<scp>iii</Scp>) Complexes and Their Applications. *Chem. Sci.* **2017**, *8*, 878–889.

(196) Hu, Y.; Li, Y.; Joung, J. F.; Yin, J.; Park, S.; Yoon, J.; Hyun, M. H. Iridium Complex

Bearing Urea Groups as a Phosphorescent Chemosensor for Chiral Anion Recognition. *Sensors Actuators B Chem.* **2017**, *241*, 224–229.

(197) Liu, S.; Xu, A.; Chen, Z.; Ma, Y.; Yang, H.; Shi, Z.; Zhao, Q. Phosphorescent Ion-Paired Iridium(III) Complex for Ratiometric and Time-Resolved Luminescence Imaging of Intracellular Biothiols. *Opt. Express* **2016**, *24*, 28247.

(198) Mei, Q.; Shi, Y.; Hua, Q.; Tong, B. Phosphorescent Chemosensor for Hg 2+ Based on an Iridium(Iii) Complex Coordinated with 4-Phenylquinazoline and Carbazole Dithiocarbamate. *RSC Adv.* **2015**, *5*, 74924–74931.

(199) Aranzaes, J. R.; Daniel, M.-C.; Astruc, D. Metallocenes as References for the Determination of Redox Potentials by Cyclic Voltammetry - Permethylated Iron and Cobalt Sandwich Complexes, Inhibition by Polyamine Dendrimers, and the Role of Hydroxy-Containing Ferrocenes. *Can. J. Chem.* **2006**, *84*, 288–299.

(200) Wang, H.-Y.; Chen, G.; Xu, X.-P.; Ji, S.-J. Synthesis and Properties of the Bipolar Triphenylamine-Benzimidazole Derivatives. *Aust. J. Chem.* **2010**, *63*, 712–718.

(201) Yu, X.; Ci, Z.; Liu, T.; Feng, X.; Wang, C.; Ma, T.; Bao, M. Influence of Different Electron Acceptors in Organic Sensitizers on the Performance of Dye-Sensitized Solar Cells. *Dye. Pigment.* **2014**, *102*, 126–132.

(202) Chou, P.-Y.; Chou, H.-H.; Chen, Y.-H.; Su, T.-H.; Liao, C.-Y.; Lin, H.-W.; Lin, W.-C.; Yen, H.-Y.; Chen, I.-C.; Cheng, C.-H. Efficient Delayed Fluorescence via Triplet-Triplet Annihilation for Deep-Blue Electroluminescence. *Chem. Commun.* **2014**, *50*, 6869–6871.

(203) Faccini, M.; Balakrishnan, M.; Diemeer, M. B. J.; Hu, Z.; Clays, K.; Asselberghs, I.; Leinse, A.; Driessen, A.; Reinhoudt, D. N.; Verboom, W. Enhanced Poling Efficiency in Highly Thermal and Photostable Nonlinear Optical Chromophores. *J. Mater. Chem.* **2008**,

18, 2141–2149.

(204) Klimavicz, J. S.; Mike, J. F.; Bhuwalka, A.; Tomlinson, A. L.; Jeffries-EL, M. Synthesis of Benzobisoxazole-Based D-π-A-π-D Organic Chromophores with Variable Optical and Electronic Properties. *Pure Appl. Chem.* **2012**, *84*, 991–1004.

(205) Barlow, S.; Risko, C.; Odom, S. A.; Zheng, S.; Coropceanu, V.; Beverina, L.; Brédas, J.-L.; Marder, S. R. Tuning Delocalization in the Radical Cations of 1,4-Bis[4-(Diarylamino)Styryl]Benzenes, 2,5-Bis[4-(Diarylamino)Styryl]Thiophenes, and 2,5-Bis[4-(Diarylamino)Styryl]Pyrroles through Substituent Effects. *J. Am. Chem. Soc.* **2012**, *134*, 10146–10155.

(206) Gao, W.; Shirong, W.; Yin, X.; Li, X.; Xianggao, L. Study on Synthesis and Properties of Novel Luminescent Hole Transporting Materials Based on N,N′-Di(p-Tolyl)-N,N′-Diphenyl-1,1′-Biphenyl-4,4′-Diamine Core. *Dye. Pigment.* **2013**, *97*, 92–99.

(207) Hwang, A.-R.; Han, W.-S.; Wee, K.-R.; Kim, H. Y.; Cho, D. W.; Min, B. K.; Nam, S. W.; Pac, C.; Kang, S. O. Photodynamic Behavior of Heteroleptic Ir(III) Complexes with Carbazole-Functionalized Dendrons Associated with Efficient Electron Transfer Processes. *J. Phys. Chem. C* **2012**, *116*, 1973–1986.

(208) Shin, S.; Menk, F.; Kim, Y.; Lim, J.; Char, K.; Zentel, R.; Choi, T.-L. Living Light-Induced Crystallization-Driven Self-Assembly for Rapid Preparation of Semiconducting Nanofibers. *J. Am. Chem. Soc.* **2018**, *140*, 6088–6094.

(209) Li, X.; Gao, Y.; Boott, C. E.; Winnik, M. A.; Manners, I. Non-Covalent Synthesis of Supermicelles with Complex Architectures Using Spatially Confined Hydrogen-Bonding Interactions. *Nat. Commun.* **2015**, *6*, 8127.

(210) Armao, J. J.; Nyrkova, I.; Fuks, G.; Osypenko, A.; Maaloum, M.; Moulin, E.; Arenal, R.;

Gavat, O.; Semenov, A.; Giuseppone, N. Anisotropic Self-Assembly of Supramolecular Polymers and Plasmonic Nanoparticles at the Liquid–Liquid Interface. *J. Am. Chem. Soc.* **2017**, *139*, 2345–2350.

(211) Adhikari, B.; Yamada, Y.; Yamauchi, M.; Wakita, K.; Lin, X.; Aratsu, K.; Ohba, T.; Karatsu, T.; Hollamby, M. J.; Shimizu, N.; Takagi, H.; Haruki, R.; Adachi, S.; Yagai, S. Light-Induced Unfolding and Refolding of Supramolecular Polymer Nanofibres. *Nat. Commun.* **2017**, *8*, 15254.

(212) Venkata Rao, K.; Miyajima, D.; Nihonyanagi, A.; Aida, T. Thermally Bisignate Supramolecular Polymerization. *Nat. Chem.* **2017**, *9*, 1133.

(213) Gröschel, A. H.; Walther, A.; Löbling, T. I.; Schmelz, J.; Hanisch, A.; Schmalz, H.; Müller, A. H. E. Facile, Solution-Based Synthesis of Soft, Nanoscale Janus Particles with Tunable Janus Balance. *J. Am. Chem. Soc.* **2012**, *134*, 13850–13860.

(214) Sveinbjornsson, B. R.; Weitekamp, R. A.; Miyake, G. M.; Xia, Y.; Atwater, H. A.; Grubbs, R. H. Rapid Self-Assembly of Brush Block Copolymers to Photonic Crystals. *Proc. Natl. Acad. Sci.* **2012**, *109*, 14332–14336.

(215) Jiang, B.; He, Y.; Li, B.; Zhao, S.; Wang, S.; He, Y.-B.; Lin, Z. Polymer-Templated Formation of Polydopamine-Coated SnO2 Nanocrystals: Anodes for Cyclable Lithium-Ion Batteries. *Angew. Chem. Int. Ed.* **2017**, *56*, 1869–1872.

(216) Pang, X.; He, Y.; Jung, J.; Lin, Z. 1D Nanocrystals with Precisely Controlled Dimensions, Compositions, and Architectures. *Science* **2016**, *353*, 1268–1272.

(217) Yuan, J.; Xu, Y.; Walther, A.; Bolisetty, S.; Schumacher, M.; Schmalz, H.; Ballauff, M.; Müller, A. H. E. Water-Soluble Organo-Silica Hybrid Nanowires. *Nat. Mater.* **2008**, *7*, 718.

(218) Lu, X.; Tran, T.-H.; Jia, F.; Tan, X.; Davis, S.; Krishnan, S.; Amiji, M. M.; Zhang, K. Providing Oligonucleotides with Steric Selectivity by Brush-Polymer-Assisted Compaction. *J. Am. Chem. Soc.* **2015**, *137*, 12466–12469.

(219) Fouz, M. F.; Mukumoto, K.; Averick, S.; Molinar, O.; McCartney, B. M.; Matyjaszewski, K.; Armitage, B. A.; Das, S. R. Bright Fluorescent Nanotags from Bottlebrush Polymers with DNATipped Bristles. *ACS Cent. Sci.* **2015**, *1*, 431–438.

(220) Kawamoto, K.; Zhong, M.; Gadelrab, K. R.; Cheng, L.-C.; Ross, C. A.; Alexander-Katz, A.; Johnson, J. A. Graft-through Synthesis and Assembly of Janus Bottlebrush Polymers from A-Branch-B Diblock Macromonomers. *J. Am. Chem. Soc.* **2016**, *138*, 11501–11504.

(221) Schappacher, M.; Deffieux, A. Synthesis of Macrocyclic Copolymer Brushes and Their Self-Assembly into Supramolecular Tubes. *Science* **2008**, *319*, 1512–1515.

(222) Li, A.; Li, Z.; Zhang, S.; Sun, G.; Policarpio, D. M.; Wooley, K. L. Synthesis and Direct Visualization of Dumbbell-Shaped Molecular Brushes. *ACS Macro Lett.* **2012**, *1*, 241–245.

(223) Lin, T.-P.; Chang, A. B.; Chen, H.-Y.; Liberman-Martin, A. L.; Bates, C. M.; Voegtle, M. J.; Bauer, C. A.; Grubbs, R. H. Control of Grafting Density and Distribution in Graft Polymers by Living Ring-Opening Metathesis Copolymerization. *J. Am. Chem. Soc.* **2017**, *139*, 3896–3903.

(224) Kim, K. O.; Choi, T.-L. Synthesis of Dendronized Polymers via Macromonomer Approach by Living ROMP and Their Characterization: From Rod-Like Homopolymers to Block and Gradient Copolymers. *Macromolecules* **2013**, *46*, 5905–5914.

(225) Chang, A. B.; Lin, T.-P.; Thompson, N. B.; Luo, S.-X.; Liberman-Martin, A. L.; Chen, H.-Y.; Lee, B.; Grubbs, R. H. Design, Synthesis, and Self-Assembly of Polymers with

Tailored Graft Distributions. *J. Am. Chem. Soc.* **2017**, *139*, 17683–17693.

(226) Fenyves, R.; Schmutz, M.; Horner, I. J.; Bright, F. V.; Rzayev, J. Aqueous Self-Assembly of Giant Bottlebrush Block Copolymer Surfactants as Shape-Tunable Building Blocks. *J. Am. Chem. Soc.* **2014**, *136*, 7762–7770.

(227) Su, L.; Heo, G. S.; Lin, Y.-N.; Dong, M.; Zhang, S.; Chen, Y.; Sun, G.; Wooley, K. L. Syntheses of Triblock Bottlebrush Polymers through Sequential ROMPs: Expanding the Functionalities of Molecular Brushes. *J. Polym. Sci. Part A Polym. Chem.* **2017**, *55*, 2966–2970.

(228) Ling, J.; Zheng, Z.; Köhler, A.; Müller, A. H. E. Rod-Like Nano-Light Harvester. *Macromol. Rapid Commun.* **2013**, *35*, 52–55.

(229) Xia, J.; Busby, E.; Sanders, S. N.; Tung, C.; Cacciuto, A.; Sfeir, M. Y.; Campos, L. M. Influence of Nanostructure on the Exciton Dynamics of Multichromophore Donor–Acceptor Block Copolymers. *ACS Nano* **2017**, *11*, 4593–4598.

(230) Cheng, C.; Khoshdel, E.; Wooley, K. L. ATRP from a Norbornenyl-Functionalized Initiator: Balancing of Complementary Reactivity for the Preparation of α-Norbornenyl Macromonomers/ω-Haloalkyl Macroinitiators. *Macromolecules* **2005**, *38*, 9455–9465.

(231) Radzinski, S. C.; Foster, J. C.; Chapleski, R. C.; Troya, D.; Matson, J. B. Bottlebrush Polymer Synthesis by Ring-Opening Metathesis Polymerization: The Significance of the Anchor Group. *J. Am. Chem. Soc.* **2016**, *138*, 6998–7004.

(232) Sauvé, E. R.; Tonge, C. M.; Paisley, N. R.; Cheng, S.; Hudson, Z. M. Cu(0)-RDRP of Acrylates Based on p-Type Organic Semiconductors. *Polym. Chem.* **2018**, *9*, 1397–1403.

(233) Poulsen, D. A.; Kim, B. J.; Ma, B.; Zonte, S. C.; Fréchet, J. M. J. Site Isolation in Phosphorescent Bichromophoric Block Copolymers Designed for White

Electroluminescence. *Adv. Mater.* **2009**, *22*, 77–82.

(234) Terashima, T.; Mes, T.; De Greef, T. F. A.; Gillissen, M. A. J.; Besenius, P.; Palmans, A. R. A.; Meijer, E. W. Single-Chain Folding of Polymers for Catalytic Systems in Water. *J. Am. Chem. Soc.* **2011**, *133*, 4742–4745.

(235) Frisch, M. J. et al. Gaussian 09, Revision D.01. *Gaussian Inc.* **2009**.

(236) Xia, Y.; Kornfield, J. A.; Grubbs, R. H. Efficient Synthesis of Narrowly Dispersed Brush Polymers via Living Ring-Opening Metathesis Polymerization of Macromonomers. *Macromolecules* **2009**, *42*, 3761–3766.

(237) Elsabahy, M.; Heo, G. S.; Lim, S.-M.; Sun, G.; Wooley, K. L. Polymeric Nanostructures for Imaging and Therapy. *Chem. Rev.* **2015**, *115*, 10967–11011.

(238) Pal, A.; Malakoutikhah, M.; Leonetti, G.; Tezcan, M.; Colomb-Delsuc, M.; Nguyen, V. D.; van der Gucht, J.; Otto, S. Controlling the Structure and Length of Self-Synthesizing Supramolecular Polymers through Nucleated Growth and Disassembly. *Angew. Chem. Int. Ed.* **2015**, *54*, 7852–7856.

(239) Klinger, D.; Wang, C. X.; Connal, L. A.; Audus, D. J.; Jang, S. G.; Kraemer, S.; Killops, K. L.; Fredrickson, G. H.; Kramer, E. J.; Hawker, C. J. A Facile Synthesis of Dynamic, Shape-Changing Polymer Particles. *Angew. Chem. Int. Ed.* **2014**, *53*, 7018–7022.

(240) Rupar, P. A.; Chabanne, L.; Winnik, M. A.; Manners, I. Non-Centrosymmetric Cylindrical Micelles by Unidirectional Growth. *Science* **2012**, *337*, 559–562.

(241) Wang, J.; Shen, Y.; Kessel, S.; Fernandes, P.; Yoshida, K.; Yagai, S.; Kurth, D. G.; Möhwald, H.; Nakanishi, T. Self-Assembly Made Durable: Water-Repellent Materials Formed by Cross-Linking Fullerene Derivatives. *Angew. Chem. Int. Ed.* **2009**, *48*, 2166–2170.

(242) O'Reilly, R. K.; Hawker, C. J.; Wooley, K. L. Cross-Linked Block Copolymer Micelles: Functional Nanostructures of Great Potential and Versatility. *Chem. Soc. Rev.* **2006**, *35*, 1068.

(243) Zhang, T.; Yang, J.; Yu, X.; Li, Y.; Yuan, X.; Zhao, Y.; Lyu, D.; Men, Y.; Zhang, K.; Ren, L. Handwritable One-Dimensional Photonic Crystals Prepared from Dendronized Brush Block Copolymers. *Polym. Chem.* **2019**, 1519–1525.

(244) Chae, C. G.; Yu, Y. G.; Seo, H. Bin; Kim, M. J.; Kishore, M. Y. L. N.; Lee, J. S. Molecular and Kinetic Design for the Expanded Control of Molecular Weights in the Ring-Opening Metathesis Polymerization of Norbornene-Substituted Polyhedral Oligomeric Silsesquioxanes. *Polym. Chem.* **2018**, *9*, 5179–5189.

(245) Müllner, M.; Lunkenbein, T.; Breu, J.; Caruso, F.; Müller, A. H. E. Template-Directed Synthesis of Silica Nanowires and Nanotubes from Cylindrical Core-Shell Polymer Brushes. *Chem. Mater.* **2012**, *24*, 1802–1810.

(246) Jiang, B.; He, Y. B.; Li, B.; Zhao, S.; Wang, S.; He, Y. B.; Lin, Z. Polymer-Templated Formation of Polydopamine-Coated SnO2 Nanocrystals: Anodes for Cyclable Lithium-Ion Batteries. *Angew. Chem. Int. Ed.* **2017**, *56*, 1869–1872.

(247) Tan, X.; Li, B. B.; Lu, X.; Jia, F.; Santori, C.; Menon, P.; Li, H.; Zhang, B.; Zhao, J. J.; Zhang, K. Light-Triggered, Self-Immolative Nucleic Acid-Drug Nanostructures. *J. Am. Chem. Soc.* **2015**, *137*, 6112–6115.

(248) Tonge, C. M.; Sauvé, E. R.; Cheng, S.; Howard, T. A.; Hudson, Z. M. Multiblock Bottlebrush Nanofibers from Organic Electronic Materials. *J. Am. Chem. Soc.* **2018**, *140*, 11599–11603.

(249) Hennebicq, E.; Pourtois, G.; Scholes, G. D.; Herz, L. M.; Russell, D. M.; Silva, C.;

Setayesh, S.; Grimsdale, A. C.; Müllen, K.; Brédas, J.-L. L.; Beljonne, D. Exciton Migration in Rigid-Rod Conjugated Polymers: An Improved Förster Model. *J. Am. Chem. Soc.* **2005**, *127*, 4744–4762.

(250) Malik, A. H.; Hussain, S.; Iyer, P. K. Aggregation-Induced FRET via Polymer–Surfactant Complexation: A New Strategy for the Detection of Spermine. *Anal. Chem.* **2016**, *88*, 7358–7364.

(251) Praveen, V. K.; George, S. J.; Varghese, R.; Vijayakumar, C.; Ajayaghosh, A. Self-Assembled π-Nanotapes as Donor Scaffolds for Selective and Thermally Gated Fluorescence Resonance Energy Transfer (FRET). *J. Am. Chem. Soc.* **2006**, *128*, 7542–7550.

(252) Xia, Y.; Olsen, B. D.; Kornfield, J. A.; Grubbs, R. H. Efficient Synthesis of Narrowly Dispersed Brush Copolymers and Study of Their Assemblies: The Importance of Side Chain Arrangement. *J. Am. Chem. Soc.* **2009**, *131*, 18525–18532.

(253) Jha, S.; Dutta, S.; Bowden, N. B. Synthesis of Ultralarge Molecular Weight Bottlebrush Polymers Using Grubbs' Catalysts. *Macromolecules* **2004**, *37*, 4365–4374.

(254) Tonge, C. M.; Yuan, F.; Lu, Z.-H.; Hudson, Z. M. Cu(0)-RDRP as an Efficient and Low-Cost Synthetic Route to Blue-Emissive Polymers for OLEDs. *Polym. Chem.* **2019**, *19*, 3288–3297.

(255) Lakowicz, J. R. *Principles of Fluorescence Spectroscopy*, Third Edit.; Springer US: Boston, MA, 2006.

(256) Duan, P.; Yanai, N.; Nagatomi, H.; Kimizuka, N. Photon Upconversion in Supramolecular Gel Matrixes: Spontaneous Accumulation of Light-Harvesting Donor–Acceptor Arrays in Nanofibers and Acquired Air Stability. *J. Am. Chem. Soc.* **2015**, *137*, 1887–1894.

(257) Mei, J.; Leung, N. L. C.; Kwok, R. T. K.; Lam, J. W. Y.; Tang, B. Z. Aggregation-Induced Emission: Together We Shine, United We Soar! *Chem. Rev.* **2015**, *115*, 11718–11940.

(258) Gao, H.; Zhang, X.; Chen, C.; Li, K.; Ding, D. Unity Makes Strength: How Aggregation-Induced Emission Luminogens Advance the Biomedical Field. *Adv. Biosyst.* **2018**, *2*, 1800074.

(259) Wang, D.; Lee, M. M. S.; Xu, W.; Shan, G.; Zheng, X.; Kwok, R. T. K.; Lam, J. W. Y.; Hu, X.; Tang, B. Z. Boosting Non-Radiative Decay to Do Useful Work: Development of a Multi-Modality Theranostic System from an AIEgen. *Angew. Chem. Int Ed.* **2019**, *131*, 5684–5688.

(260) Hu, F.; Xu, S.; Liu, B. Photosensitizers with Aggregation-Induced Emission: Materials and Biomedical Applications. *Adv. Mater.* **2018**, *30*, 1801350.

(261) Gao, M.; Tang, B. Z. Fluorescent Sensors Based on Aggregation-Induced Emission: Recent Advances and Perspectives. *ACS Sensors* **2017**, *2*, 1382–1399.

(262) Kwok, R. T. K.; Leung, C. W. T.; Lam, J. W. Y.; Tang, B. Z. Biosensing by Luminogens with Aggregation-Induced Emission Characteristics. *Chem. Soc. Rev.* **2015**, *44*, 4228–4238.

(263) Feng, Q.; Li, Y.; Wang, L.; Li, C.; Wang, J.; Liu, Y.; Li, K.; Hou, H. Multiple-Color Aggregation-Induced Emission (AIE) Molecules as Chemodosimeters for PH Sensing. *Chem. Commun.* **2016**, *52*, 3123–3126.

(264) Guo, J.; Li, X.-L.; Nie, H.; Luo, W.; Gan, S.; Hu, S.; Hu, R.; Qin, A.; Zhao, Z.; Su, S.-J.; Tang, B. Z. Achieving High-Performance Nondoped OLEDs with Extremely Small Efficiency Roll-Off by Combining Aggregation-Induced Emission and Thermally

Activated Delayed Fluorescence. *Adv. Funct. Mater.* **2017**, *27*, 1606458.

(265) Xu, S.; Liu, T.; Mu, Y.; Wang, Y.-F.; Chi, Z.; Lo, C.-C.; Liu, S.; Zhang, Y.; Lien, A.; Xu, J. An Organic Molecule with Asymmetric Structure Exhibiting Aggregation-Induced Emission, Delayed Fluorescence, and Mechanoluminescence. *Angew. Chem. Int. Ed.* **2015**, *54*, 874–878.

(266) Ren, Y.; Kan, W. H.; Thangadurai, V.; Baumgartner, T. Bio-Inspired Phosphole-Lipids: From Highly Fluorescent Organogels to Mechanically Responsive FRET. *Angew. Chem. Int. Ed.* **2012**, *51*, 3964–3968.

(267) Yang, H.; Liu, Y.; Guo, Z.; Lei, B.; Zhuang, J.; Zhang, X.; Liu, Z.; Hu, C. Hydrophobic Carbon Dots with Blue Dispersed Emission and Red Aggregation-Induced Emission. *Nat. Commun.* **2019**, *10*, 1789.

(268) "We The North" Is the Slogan of the Toronto Raptors Basketball Team, Who Won Their First NBA Championship in 2019. The Stellar's Jay Is the Provincial Bird of British Columbia, Canada.

(269) Chang, Y.-L.; Song, Y.; Wang, Z.; Helander, M. G.; Qiu, J.; Chai, L.; Liu, Z.; Scholes, G. D.; Lu, Z. Highly Efficient Warm White Organic Light-Emitting Diodes by Triplet Exciton Conversion. *Adv. Funct. Mater.* **2013**, *23*, 705–712.

(270) Zhang, Q.; Xu, S.; Li, M.; Wang, Y.; Zhang, N.; Guan, Y.; Chen, M.; Chen, C.-F.; Hu, H.-Y. Rationally Designed Organelle-Specific Thermally Activated Delayed Fluorescence Small Molecule Organic Probes for Time-Resolved Biological Applications. *Chem. Commun.* **2019**, *55*, 5639–5642.

(271) Li, T.; Yang, D.; Zhai, L.; Wang, S.; Zhao, B.; Fu, N.; Wang, L.; Tao, Y.; Huang, W. Thermally Activated Delayed Fluorescence Organic Dots (TADF Odots) for Time-

Resolved and Confocal Fluorescence Imaging in Living Cells and In Vivo. *Adv. Sci.* **2017**, *4*, 1600166.

(272) Li, X.; Baryshnikov, G.; Deng, C.; Bao, X.; Wu, B.; Zhou, Y.; Ågren, H.; Zhu, L. A Three-Dimensional Ratiometric Sensing Strategy on Unimolecular Fluorescence–Thermally Activated Delayed Fluorescence Dual Emission. *Nat. Commun.* **2019**, *10*, 731.

(273) Wang, C.; Fukazawa, A.; Taki, M.; Sato, Y.; Higashiyama, T.; Yamaguchi, S. A Phosphole Oxide Based Fluorescent Dye with Exceptional Resistance to Photobleaching: A Practical Tool for Continuous Imaging in STED Microscopy. *Angew. Chem. Int. Ed.* **2015**, *54*, 15213–15217.

(274) Wang, C.; Taki, M.; Sato, Y.; Fukazawa, A.; Higashiyama, T.; Yamaguchi, S. Super-Photostable Phosphole-Based Dye for Multiple-Acquisition Stimulated Emission Depletion Imaging. *J. Am. Chem. Soc.* **2017**, *139*, 10374–10381.

(275) Hirai, M.; Tanaka, N.; Sakai, M.; Yamaguchi, S. Structurally Constrained Boron-, Nitrogen-, Silicon-, and Phosphorus-Centered Polycyclic π-Conjugated Systems. *Chem. Rev.* **2019**, *119*, 8291–8331.

(276) Kushida, T.; Shirai, S.; Ando, N.; Okamoto, T.; Ishii, H.; Matsui, H.; Yamagishi, M.; Uemura, T.; Tsurumi, J.; Watanabe, S.; Takeya, J.; Yamaguchi, S. Boron-Stabilized Planar Neutral π-Radicals with Well-Balanced Ambipolar Charge-Transport Properties. *J. Am. Chem. Soc.* **2017**, *139*, 14336–14339.

(277) Kushida, T.; Yamaguchi, S. A Radical Anion of Structurally Constrained Triphenylborane. *Organometallics* **2013**, *32*, 6654–6657.

(278) Iwahara, H.; Kushida, T.; Yamaguchi, S. A Planarized 9-Phenylanthracene: A Simple Electron-Donating Building Block for Fluorescent Materials. *Chem. Commun.* **2016**, *52*,

1124–1127.

(279) Zhou, Z.; Wakamiya, A.; Kushida, T.; Yamaguchi, S. Planarized Triarylboranes: Stabilization by Structural Constraint and Their Plane-to-Bowl Conversion. *J. Am. Chem. Soc.* **2012**, *134*, 4529–4532.

(280) Chen, W.-C.; Lee, C.-S.; Tong, Q.-X. Blue-Emitting Organic Electrofluorescence Materials: Progress and Prospective. *J. Mater. Chem. C* **2015**, *3*, 10957–10963.

(281) Yang, X.; Xu, X.; Zhou, G. Recent Advances of the Emitters for High Performance Deep-Blue Organic Light-Emitting Diodes. *J. Mater. Chem. C* **2015**, *3*, 913–944.

(282) Hirata, S.; Sakai, Y.; Masui, K.; Tanaka, H.; Lee, S. Y.; Nomura, H.; Nakamura, N.; Yasumatsu, M.; Nakanotani, H.; Zhang, Q.; Shizu, K.; Miyazaki, H.; Adachi, C. Highly Efficient Blue Electroluminescence Based on Thermally Activated Delayed Fluorescence. *Nat. Mater.* **2015**, *14*, 330–336.

(283) Zhu, M.; Yang, C. Blue Fluorescent Emitters: Design Tactics and Applications in Organic Light-Emitting Diodes. *Chem. Soc. Rev.* **2013**, *42*, 4963–4976.

(284) Ahn, D. H.; Kim, S. W.; Lee, H.; Ko, I. J.; Karthik, D.; Lee, J. Y.; Kwon, J. H. Highly Efficient Blue Thermally Activated Delayed Fluorescence Emitters Based on Symmetrical and Rigid Oxygen-Bridged Boron Acceptors. *Nat. Photonics* **2019**, *13*, 540–546.

(285) Lee, J.-H.; Chen, C.-H.; Lee, P.-H.; Lin, H.-Y.; Leung, M.; Chiu, T.-L.; Lin, C.-F. Blue Organic Light-Emitting Diodes: Current Status, Challenges, and Future Outlook. *J. Mater. Chem. C* **2019**, *7*, 5874–5888.

(286) Chen, W. C.; Yuan, Y.; Ni, S. F.; Zhu, Z. L.; Zhang, J.; Jiang, Z. Q.; Liao, L. S.; Wong, F. L.; Lee, C. S. Highly Efficient Deep-Blue Electroluminescence from a Charge-Transfer Emitter with Stable Donor Skeleton. *ACS Appl. Mater. Interfaces* **2017**, *9*, 7331–7338.

(287) Chen, W. C.; Yuan, Y.; Ni, S. F.; Tong, Q. X.; Wong, F. L.; Lee, C. S. Achieving Efficient Violet-Blue Electroluminescence with CIE:Y <0.06 and EQE >6% from Naphthyl-Linked Phenanthroimidazole-Carbazole Hybrid Fluorophores. *Chem. Sci.* **2017**, *8*, 3599–3608.

(288) Jeong, S.; Kim, M.-K.; Kim, S. H.; Hong, J.-I. Efficient Deep-Blue Emitters Based on Triphenylamine-Linked Benzimidazole Derivatives for Nondoped Fluorescent Organic Light-Emitting Diodes. *Org. Electron.* **2013**, *14*, 2497–2504.

(289) Chen, W.-C.; Zhu, Z.-L.; Lee, C.-S. Organic Light-Emitting Diodes Based on Imidazole Semiconductors. *Adv. Opt. Mater.* **2018**, *6*, 1800258.

(290) Huang, Z.; Xiang, S.; Zhang, Q.; Lv, X.; Ye, S.; Guo, R.; Wang, L.; Lv, X.; Xiang, S.; Huang, Z.; Wang, L. Highly Efficient Green Organic Light Emitting Diodes with Phenanthroimidazole-Based Thermally Activated Delayed Fluorescence Emitters. *J. Mater. Chem. C* **2018**, *6*, 2379–2386.

(291) Ohsawa, T.; Sasabe, H.; Watanabe, T.; Nakao, K.; Komatsu, R.; Hayashi, Y.; Hayasaka, Y.; Kido, J. A Series of Imidazo[1,2-f]Phenanthridine-Based Sky-Blue TADF Emitters Realizing EQE of over 20%. *Adv. Opt. Mater.* **2019**, *7*, 1801282.

(292) Li, C.; Liang, J.; Liang, B.; Li, Z.; Cheng, Z.; Yang, G.; Wang, Y. An Organic Emitter Displaying Dual Emissions and Efficient Delayed Fluorescence White OLEDs. *Adv. Opt. Mater.* **2019**, *7*, 1801667.

(293) Etherington, M. K.; Franchello, F.; Gibson, J.; Northey, T.; Santos, J.; Ward, J. S.; Higginbotham, H. F.; Data, P.; Kurowska, A.; Dos Santos, P. L.; Graves, D. R.; Batsanov, A. S.; Dias, F. B.; Bryce, M. R.; Penfold, T. J.; Monkman, A. P. Regio- and Conformational Isomerization Critical to Design of Efficient Thermally-Activated

Delayed Fluorescence Emitters. *Nat. Commun.* **2017**, *8*, 14987.

(294) Chen, D.-G.; Lin, T.-C.; Chen, Y.-A.; Chen, Y.-H.; Lin, T.-C.; Chen, Y.-T.; Chou, P.-T. Revisiting Dual Intramolecular Charge-Transfer Fluorescence of Phenothiazine-Triphenyltriazine Derivatives. *J. Phys. Chem. C* **2018**, *122*, 12215–12221.

(295) Xue, P.; Ding, J.; Chen, P.; Wang, P.; Yao, B.; Sun, J.; Sun, J.; Lu, R. Mechanical Force-Induced Luminescence Enhancement and Chromism of a Nonplanar D–A Phenothiazine Derivative. *J. Mater. Chem. C* **2016**, *4*, 5275–5280.

(296) Zhang, Q.; Kuwabara, H.; Potscavage, W. J.; Huang, S.; Hatae, Y.; Shibata, T.; Adachi, C. Anthraquinone-Based Intramolecular Charge-Transfer Compounds: Computational Molecular Design, Thermally Activated Delayed Fluorescence, and Highly Efficient Red Electroluminescence. *J. Am. Chem. Soc.* **2014**, *136*, 18070–18081.

(297) Mayder, D. M.; Tonge, C. M.; Hudson, Z. M. Thermally Activated Delayed Fluorescence in 1,3,4-Oxadiazoles with π-Extended Donors. *J. Org. Chem.* **2020**, *85*, 11094–11103.

(298) Arisawa, M.; Fujii, Y.; Kato, H.; Fukuda, H.; Matsumoto, T.; Ito, M.; Abe, H.; Ito, Y.; Shuto, S. One-Pot Ring-Closing Metathesis/1,3-Dipolar Cycloaddition through Assisted Tandem Ruthenium Catalysis: Synthesis of a Dye with Isoindolo[2,1-a]Quinoline Structure. *Angew. Chem. Int. Ed.* **2013**, *52*, 1003–1007.

(299) Chen, Y.; Peng, Z.; Tao, Y.; Wang, Z.; Lu, P.; Wang, Y. Polymorphism-Dependent Emissions of Two Phenoxazine Derivatives. *Dye. Pigment.* **2019**, *161*, 44–50.

(300) Liu, H.; Cheng, G.; Hu, D.; Shen, F.; Lv, Y.; Sun, G.; Yang, B.; Lu, P.; Ma, Y. A Highly Efficient, Blue-Phosphorescent Device Based on a Wide-Bandgap Host/FIrpic: Rational Design of the Carbazole and Phosphine Oxide Moieties on Tetraphenylsilane. *Adv. Funct. Mater.* **2012**, *22*, 2830–2836.

(301) Tonge, C. M.; Hudson, Z. M. Interface-Dependent Aggregation-Induced Delayed Fluorescence in Bottlebrush Polymer Nanofibers. *J. Am. Chem. Soc.* **2019**, *141*, 13970–13976.

(302) Yu, F.; Li, P.; Li, G.; Zhao, G.; Chu, T.; Han, K. A Near-IR Reversible Fluorescent Probe Modulated by Selenium for Monitoring Peroxynitrite and Imaging in Living Cells. *J. Am. Chem. Soc.* **2011**, *133*, 11030–11033.

(303) Terenziani, F.; Katan, C.; Badaeva, E.; Tretiak, S.; Blanchard-Desce, M. Enhanced Two-Photon Absorption of Organic Chromophores: Theoretical and Experimental Assessments. *Adv. Mater.* **2008**, *20*, 4641–4678.

(304) Niu, G.; Zhang, R.; Kwong, J. P. C.; Lam, J. W. Y.; Chen, C.; Wang, J.; Chen, Y.; Feng, X.; Kwok, R. T. K.; Sung, H. H. Y.; Williams, I. D.; Elsegood, M. R. J.; Qu, J.; Ma, C.; Wong, K. S.; Yu, X.; Tang, B. Z. Specific Two-Photon Imaging of Live Cellular and Deep-Tissue Lipid Droplets by Lipophilic AIEgens at Ultralow Concentration. *Chem. Mater.* **2018**, *30*, 4778–4787.

(305) Situ, B.; Gao, M.; He, X.; Li, S.; He, B.; Guo, F.; Kang, C.; Liu, S.; Yang, L.; Jiang, M.; Hu, Y.; Tang, B. Z.; Zheng, L. A Two-Photon AIEgen for Simultaneous Dual-Color Imaging of Atherosclerotic Plaques. *Mater. Horizons* **2019**, *6*, 546–553.

(306) Tang, C.; Zheng, Q.; Zhu, H.; Wang, L.; Chen, S.-C.; Ma, E.; Chen, X. Two-Photon Absorption and Optical Power Limiting Properties of Ladder-Type Tetraphenylene Cored Chromophores with Different Terminal Groups. *J. Mater. Chem. C* **2013**, *1*, 1771–1780.

(307) Lin, T.-C.; Chen, Y.-F.; Hu, C.-L.; Hsu, C.-S. Two-Photon Absorption and Optical Power Limiting Properties in Femtosecond Regime of Novel Multi-Branched Chromophores Based on Tri-Substituted Olefinic Scaffolds. *J. Mater. Chem.* **2009**, *19*, 7075–7080.

(308) Strickler, J. H.; Webb, W. W. Three-Dimensional Optical Data Storage in Refractive Media by Two-Photon Point Excitation. *Opt. Lett.* **1991**, *16*, 1780–1782.

(309) Cumpston, B. H.; Ananthavel, S. P.; Barlow, S.; Dyer, D. L.; Ehrlich, J. E.; Erskine, L. L.; Heikal, A. A.; Kuebler, S. M.; Lee, I.-Y. S.; McCord-Maughon, D.; Qin, J.; Röckel, H.; Rumi, M.; Wu, X.-L.; Marder, S. R.; Perry, J. W. Two-Photon Polymerization Initiators for Three-Dimensional Optical Data Storage and Microfabrication. *Nature* **1999**, *398*, 51–54.

(310) Mamada, M.; Inada, K.; Komino, T.; Potscavage, W. J.; Nakanotani, H.; Adachi, C. Highly Efficient Thermally Activated Delayed Fluorescence from an Excited-State Intramolecular Proton Transfer System. *ACS Cent. Sci.* **2017**, *3*, 769–777.

(311) Fang, Z.; Webster, R. D.; Samoc, M.; Lai, Y.-H. Tuning Two-Photon Absorption Cross-Sections for Triphenylamine Derivatives. *RSC Adv.* **2013**, *3*, 17914–17917.

(312) Fang, Z.; Chellappan, V.; Webster, R. D.; Ke, L.; Zhang, T.; Liu, B.; Lai, Y.-H. Bridged-Triarylamine Starburst Oligomers as Hole Transporting Materials for Electroluminescent Devices. *J. Mater. Chem.* **2012**, *22*, 15397–15404.

(313) Fang, Z.; Zhang, X.; Hing Lai, Y.; Liu, B. Bridged Triphenylamine Based Molecules with Large Two-Photon Absorption Cross Sections in Organic and Aqueous Media. *Chem. Commun.* **2009**, No. 8, 920–922.

(314) Makarov, N. S.; Mukhopadhyay, S.; Yesudas, K.; Brédas, J.-L.; Perry, J. W.; Pron, A.; Kivala, M.; Müllen, K. Impact of Electronic Coupling, Symmetry, and Planarization on One- and Two-Photon Properties of Triarylamines with One, Two, or Three Diarylboryl Acceptors. *J. Phys. Chem. A* **2012**, *116*, 3781–3793.

(315) Paisley, N. R.; Tonge, C. M.; Mayder, D. M.; Thompson, K. A.; Hudson, Z. M. Tunable

Benzothiadiazole-Based Donor–Acceptor Materials for Two-Photon Excited Fluorescence. *Mater. Chem. Front.* **2020**, *4*, 555–566.

(316) Shinar, J.; Shinar, R. Organic Light-Emitting Devices (OLEDs) and OLED-Based Chemical and Biological Sensors: An Overview. *J. Phys. D. Appl. Phys.* **2008**, *41*, 133001.

(317) Landgraf, S. Use of Ultrabright LEDs for the Determination of Static and Time-Resolved Florescence Information of Liquid and Solid Crude Oil Samples. *J. Biochem. Biophys. Methods* **2004**, *61*, 125–134.

(318) Reddy, S. S.; Sree, V. G.; Cho, W.; Jin, S. H. Achieving Pure Deep-Blue Electroluminescence with CIE Y≤0.06 via a Rational Design Approach for Highly Efficient Non-Doped Solution-Processed Organic Light-Emitting Diodes. *Chem. Asian J.* **2016**, *11*, 3275–3282.

(319) Shan, T.; Liu, Y.; Tang, X.; Bai, Q.; Gao, Y.; Gao, Z.; Li, J.; Deng, J.; Yang, B.; Lu, P.; Ma, Y. Highly Efficient Deep Blue Organic Light-Emitting Diodes Based on Imidazole: Significantly Enhanced Performance by Effective Energy Transfer with Negligible Efficiency Roll-Off. *ACS Appl. Mater. Interfaces* **2016**, *8*, 28771–28779.

(320) Wei, Q.; Li, Y.; Liu, J.; Fang, Q.; Li, J.; Yan, X.; Xie, L.; Qian, Y.; Xia, R.; Huang, W. A High Performance Deep Blue Organic Laser Gain Material. *Adv. Opt. Mater.* **2017**, *5*, 1601003.

(321) Kuehne, A. J. C.; Gather, M. C. Organic Lasers: Recent Developments on Materials, Device Geometries, and Fabrication Techniques. *Chem. Rev.* **2016**, *116*, 12823–12864.

(322) Zhao, D.; Hu, J.; Wu, N.; Huang, X.; Qin, X.; Lan, J.; You, J. Regiospecific Synthesis of 1,2-Disubstituted (Hetero)Aryl Fused Imidazoles with Tunable Fluorescent Emission.

Org. Lett. **2011**, *13*, 6516–6519.

(323) Sauvé, E. R.; Paeng, J.; Yamaguchi, S.; Hudson, Z. M. Donor–Acceptor Materials Exhibiting Thermally Activated Delayed Fluorescence Using a Planarized N - Phenylbenzimidazole Acceptor. *J. Org. Chem.* **2020**, *85*, 108–117.

(324) Hu, Z.; Zhao, T.; Wang, M.; Wu, J.; Yu, W.; Chang, J. I2-Mediated Intramolecular C-H Amidation for the Synthesis of N-Substituted Benzimidazoles. *J. Org. Chem.* **2017**, *82*, 3152–3158.

(325) Ward, J. S.; Kukhta, N. A.; dos Santos, P. L.; Congrave, D. G.; Batsanov, A. S.; Monkman, A. P.; Bryce, M. R. Delayed Blue Fluorescence via Upper-Triplet State Crossing from C–C Bonded Donor–Acceptor Charge Transfer Molecules with Azatriangulene Cores. *Chem. Mater.* **2019**, *31*, 6684–6695.

(326) Song, W.; Lee, J. Y. Degradation Mechanism and Lifetime Improvement Strategy for Blue Phosphorescent Organic Light-Emitting Diodes. *Adv. Opt. Mater.* **2017**, *5*, 1600901.

(327) Ding, D.; Goh, C. C.; Feng, G.; Zhao, Z.; Liu, J.; Liu, R.; Tomczak, N.; Geng, J.; Tang, B. Z.; Ng, L. G.; Liu, B. Ultrabright Organic Dots with Aggregation-Induced Emission Characteristics for Real-Time Two-Photon Intravital Vasculature Imaging. *Adv. Mater.* **2013**, *25*, 6083–6088.

(328) Massey, M.; Wu, M.; Conroy, E. M.; Algar, W. R. Mind Your P's and Q's: The Coming of Age of Semiconducting Polymer Dots and Semiconductor Quantum Dots in Biological Applications. *Curr. Opin. Biotechnol.* **2015**, *34*, 30–40.

(329) Liou, S.-Y.; Ke, C.-S.; Chen, J.-H.; Luo, Y.-W.; Kuo, S.-Y.; Chen, Y.-H.; Fang, C.-C.; Wu, C.-Y.; Chiang, C.-M.; Chan, Y.-H. Tuning the Emission of Semiconducting Polymer Dots from Green to Near-Infrared by Alternating Donor Monomers and Their

Applications for in Vivo Biological Imaging. *ACS Macro Lett.* **2016**, *5*, 154–157.

(330) Yu, J.; Rong, Y.; Kuo, C.-T.; Zhou, X.-H.; Chiu, D. T. Recent Advances in the Development of Highly Luminescent Semiconducting Polymer Dots and Nanoparticles for Biological Imaging and Medicine. *Anal. Chem.* **2017**, *89*, 42–56.

(331) Lix, K.; Tran, M. V.; Massey, M.; Rees, K.; Sauvé, E. R.; Hudson, Z. M.; Algar, W. R. Dextran Functionalization of Semiconducting Polymer Dots and Conjugation with Tetrameric Antibody Complexes for Bioanalysis and Imaging. *ACS Appl. Bio Mater.* **2020**, *3*, 432–440.

(332) Furumi, S. Self-Assembled Organic and Polymer Photonic Crystals for Laser Applications. *Polym. J.* **2013**, *45*, 579–593.

(333) MacKenzie, I. A.; Wang, L.; Onuska, N. P. R.; Williams, O. F.; Begam, K.; Moran, A. M.; Dunietz, B. D.; Nicewicz, D. A. Discovery and Characterization of an Acridine Radical Photoreductant. *Nature* **2020**, *580*, 76–80.

(334) Feng, K.; Quevedo, R. E.; Kohrt, J. T.; Oderinde, M. S.; Reilly, U.; White, M. C. Late-Stage Oxidative C(Sp 3)–H Methylation. *Nature* **2020**, *580*, 621–627.

(335) Vega-Peñaloza, A.; Mateos, J.; Companyó, X.; Escudero-Casao, M.; Dell'Amico, L. A Rational Approach to Organo-Photocatalysis: Novel Designs and Structure-Property Relationships. *Angew. Chem. Int. Ed.* **2021**, *60*, 1082–1097.

(336) Oderinde, M. S.; Mao, E.; Ramirez, A.; Pawluczyk, J.; Jorge, C.; Cornelius, L. A. M.; Kempson, J.; Vetrichelvan, M.; Pitchai, M.; Gupta, A.; Gupta, A. K.; Meanwell, N. A.; Mathur, A.; Dhar, T. G. M. Synthesis of Cyclobutane-Fused Tetracyclic Scaffolds via Visible-Light Photocatalysis for Building Molecular Complexity. *J. Am. Chem. Soc.* **2020**, *142*, 3094–3103.

Appendices

Appendix A : NMR spectra for Chapter 2

A.1 2.5a

^{1}H NMR spectrum of **2.5a** in CD_2Cl_2.

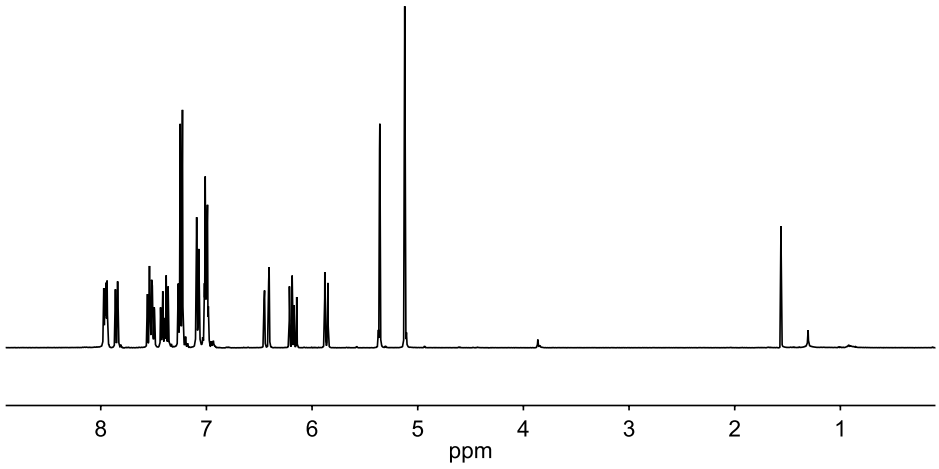

A.2 2.5b

^{1}H NMR spectrum of **2.5b** in $CDCl_3$.

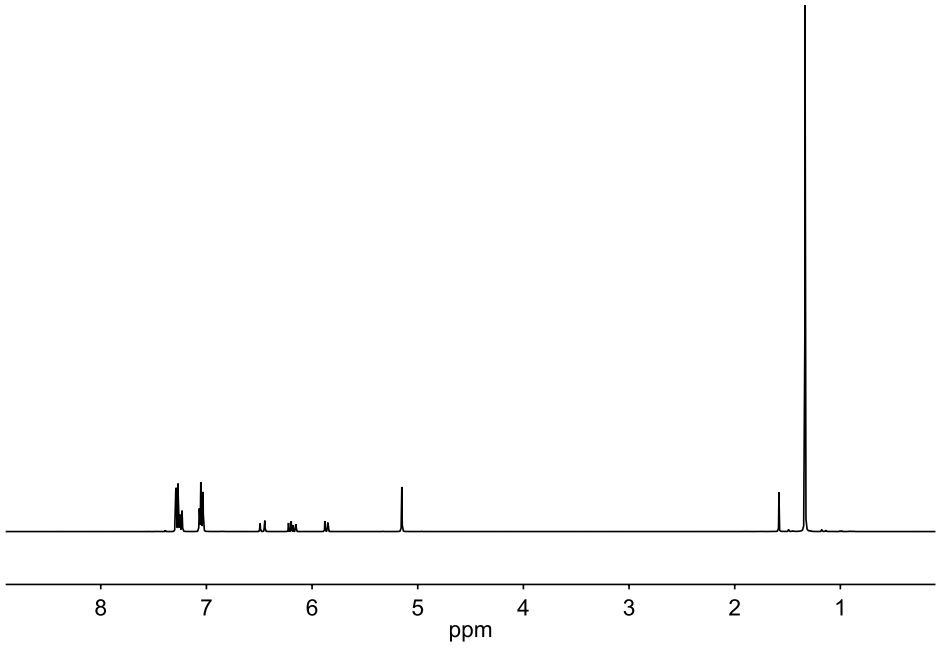

A.3 2.5c

^{1}H NMR spectrum of **2.5c** in $CDCl_3$.

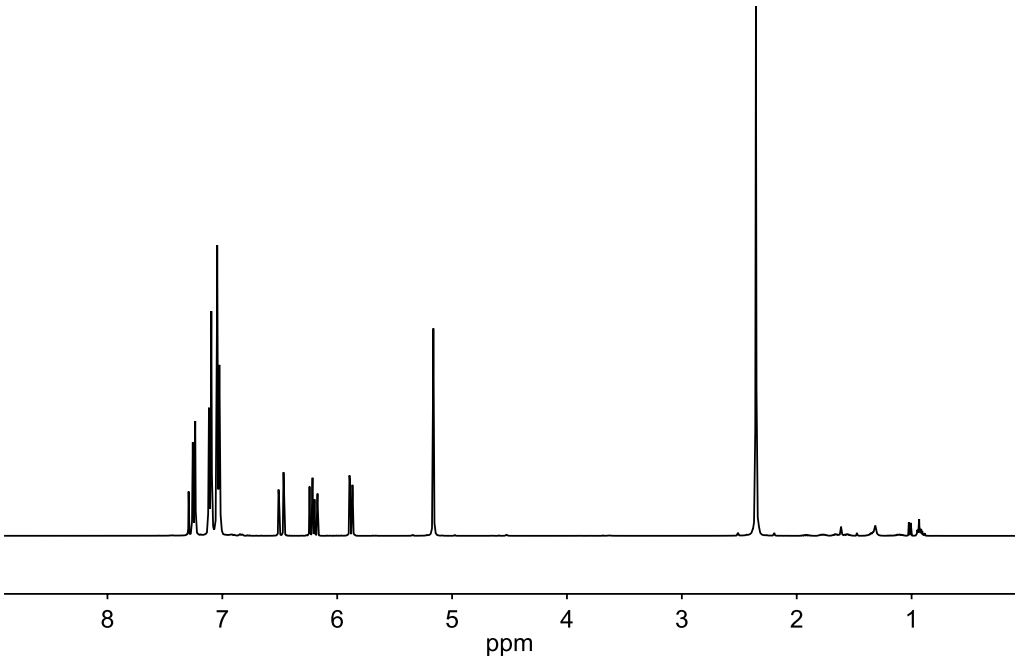

A.4 2.5d

^{1}H NMR spectrum of **2.5d** in $CDCl_3$.

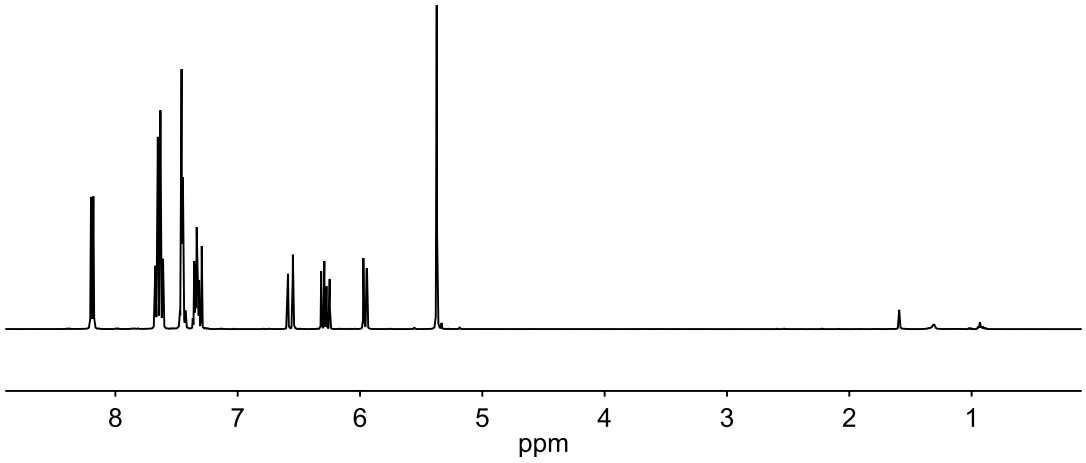

A.5 2.5a$_{10k}$

^{1}H NMR spectrum of **2.5a$_{10k}$** in $CDCl_3$. * = THF

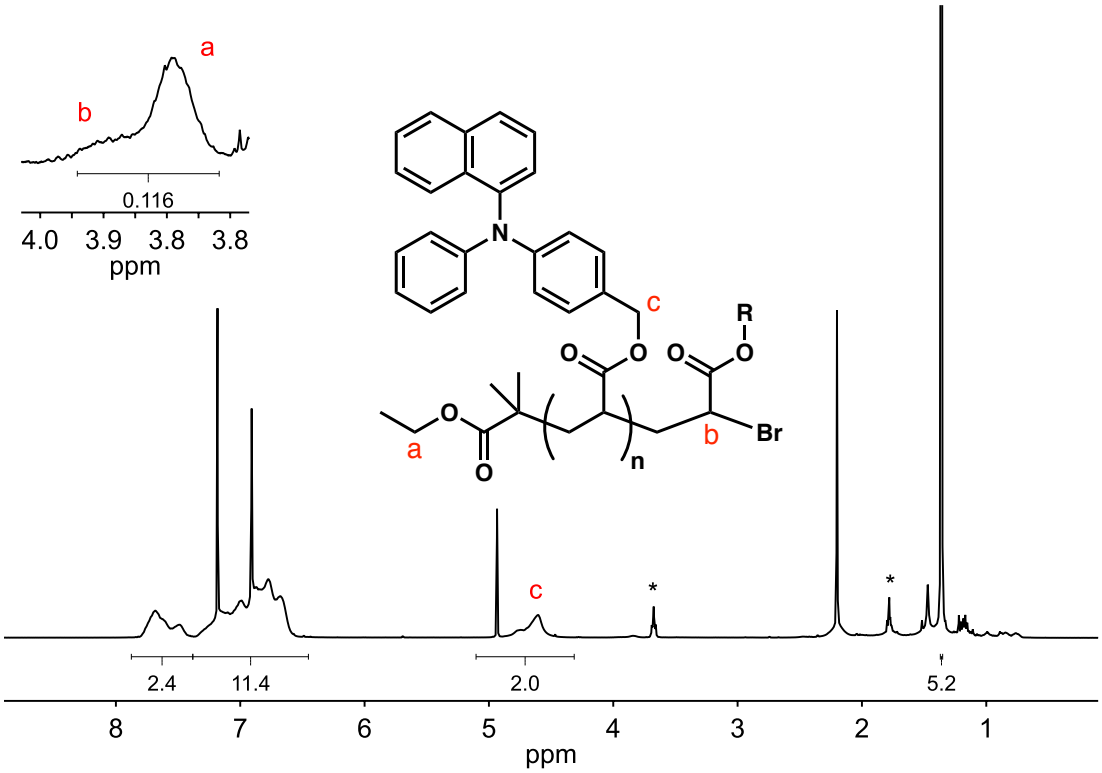

A.6 2.5b$_{10k}$

^{1}H NMR spectrum of **2.5b$_{10k}$** in $CDCl_3$. * = THF

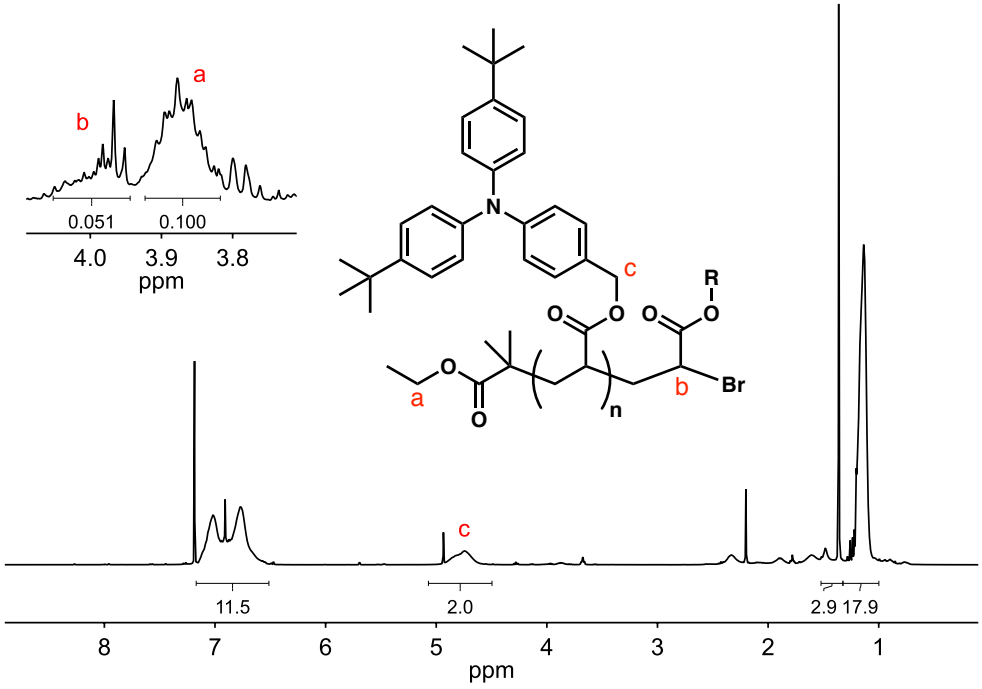

A.7 2.5c$_{10k}$

^{1}H NMR spectrum of **2.5d$_{10k}$** in $CDCl_3$. * = THF

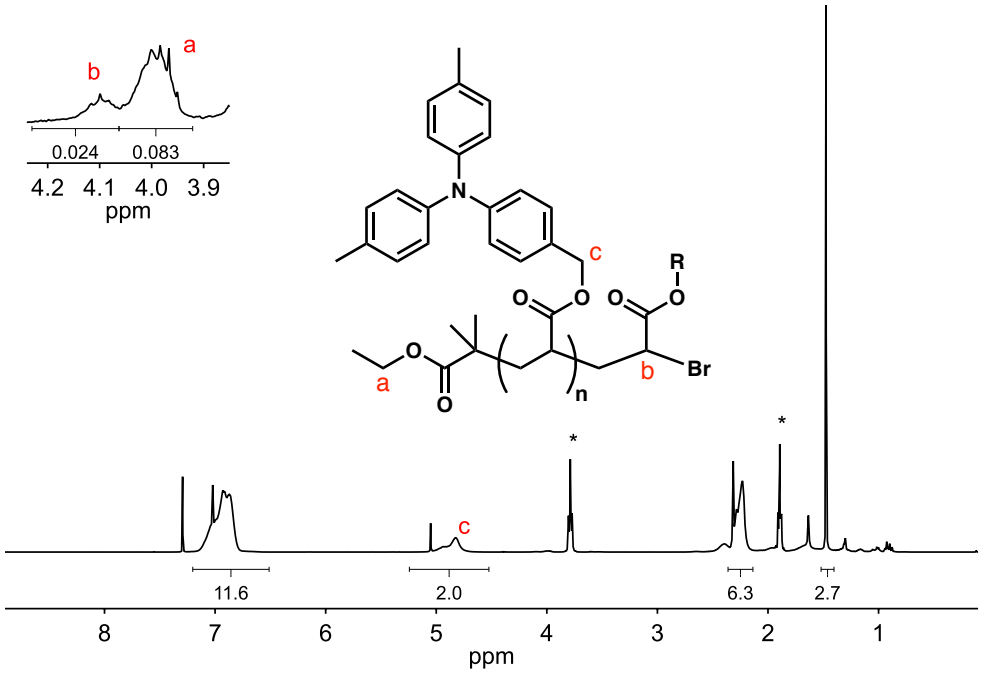

A.8 $2.5d_{10k}$

^{1}H NMR spectrum of **$2.5d_{10k}$** in $CDCl_3$. * = THF

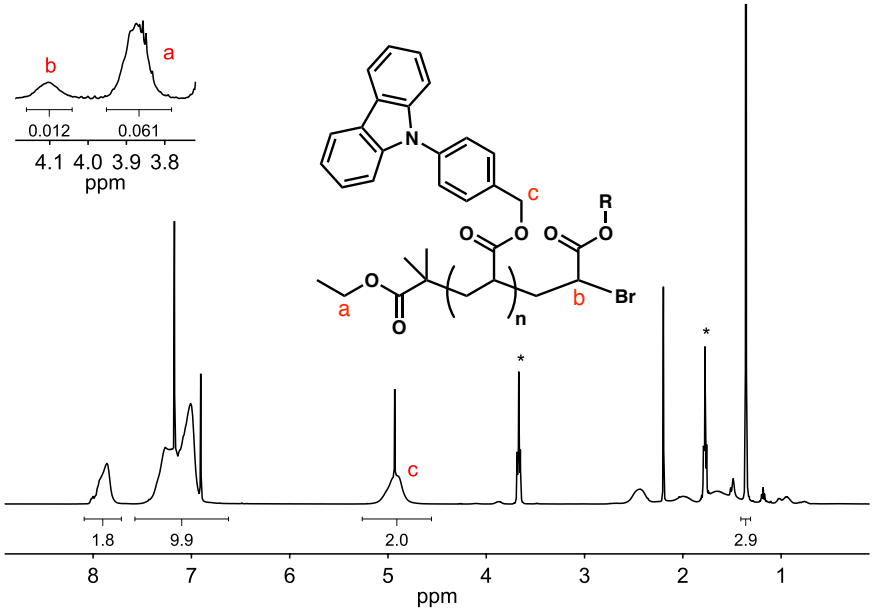

Appendix B : NMR spectra for Chapter 3

B.1 HTL-MM

^{1}H NMR spectrum of **HTL-MM** in $CDCl_3$.

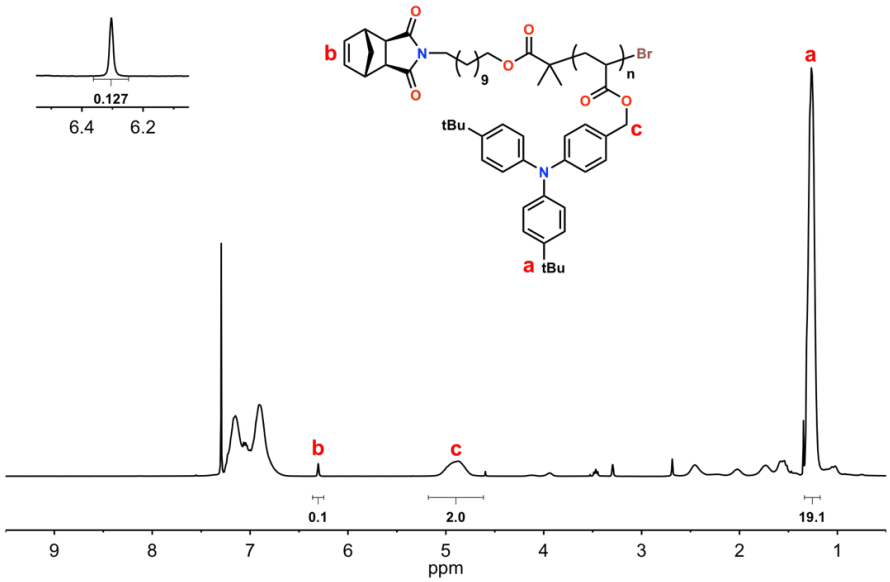

B.2 EML-MM

^{1}H NMR spectrum of **EML-MM** in $CDCl_3$. * = CH_2Cl_2.

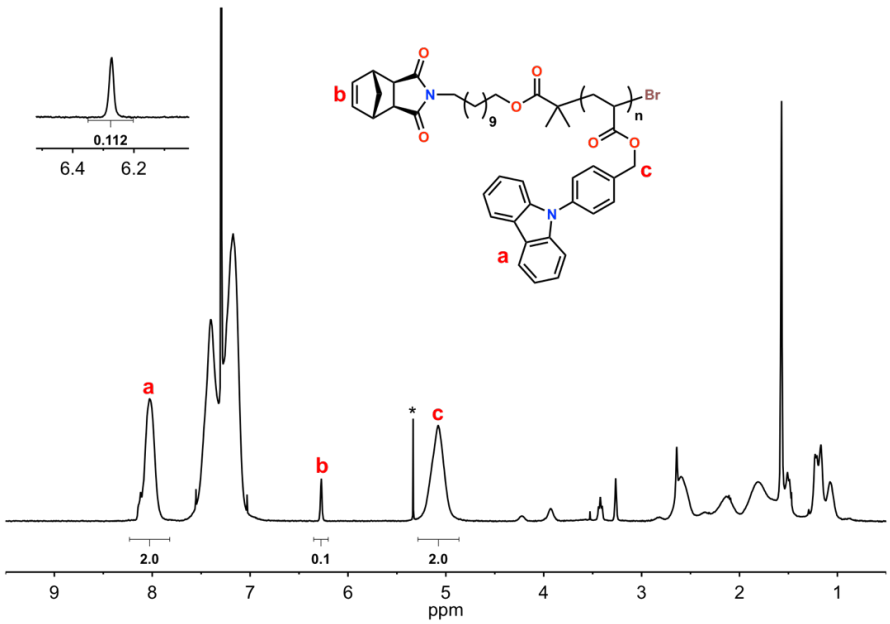

B.3 ETL-MM

^{1}H NMR spectrum of **ETL-MM** in $CDCl_3$. * = CH_2Cl_2.

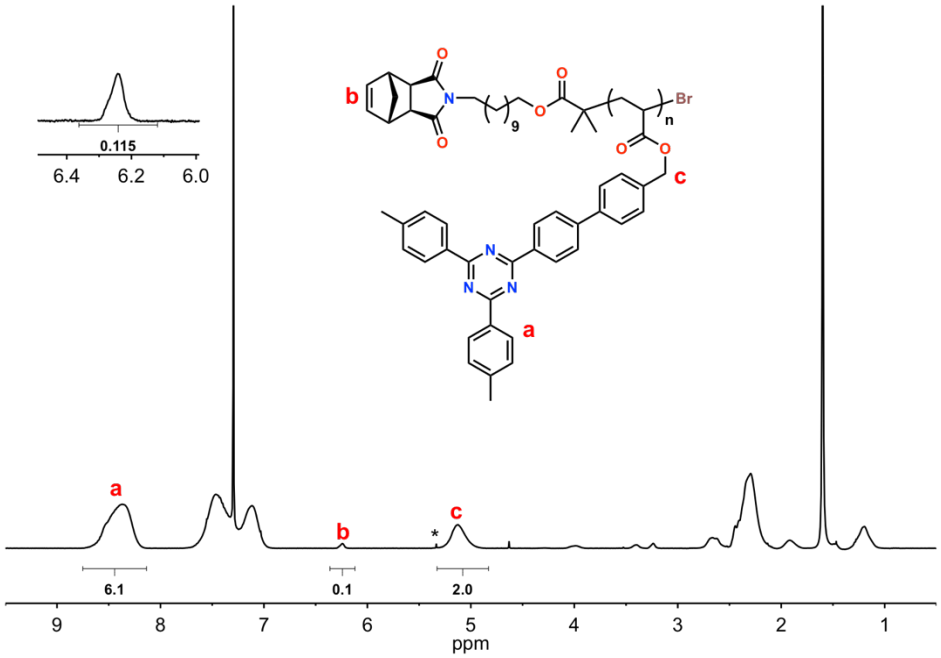

B.4 (EML-*co*-IR)-MM

^{1}H NMR spectrum of (**EML-*co*-IR)-MM** in $CDCl_3$.

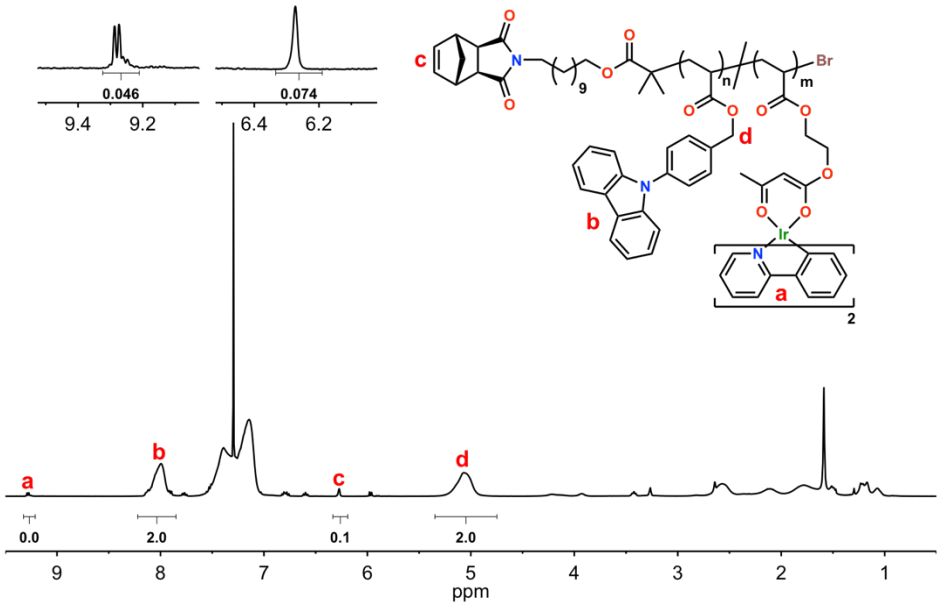

B.5 HTL_{100}-BB

^1H NMR spectrum of **HTL_{100}-BB** in $CDCl_3$.

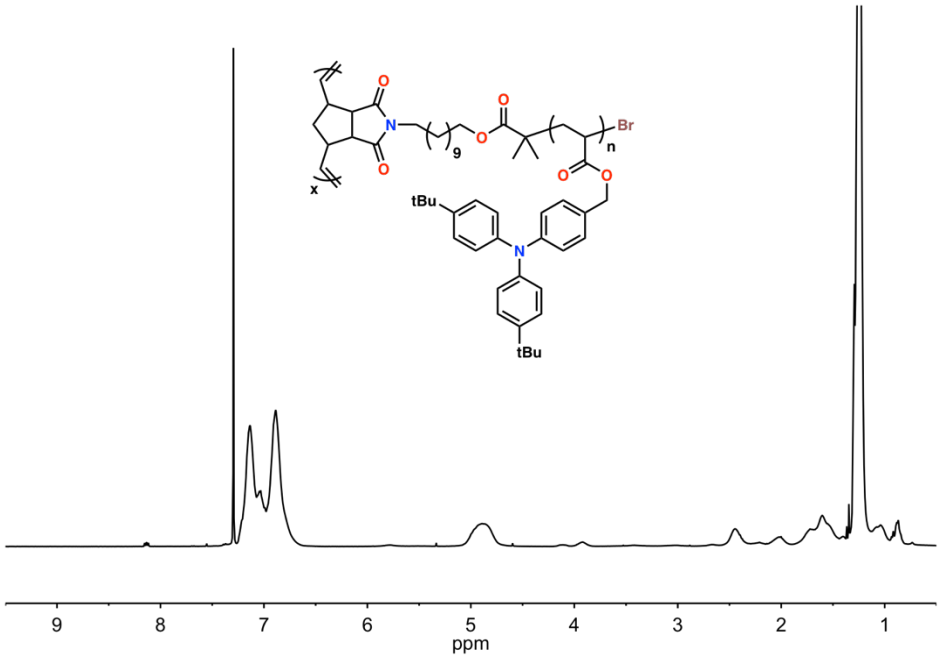

B.6 EML_{100}-BB

^1H NMR spectrum of **EML_{100}-BB** in $CDCl_3$. * = CH_2Cl_2.

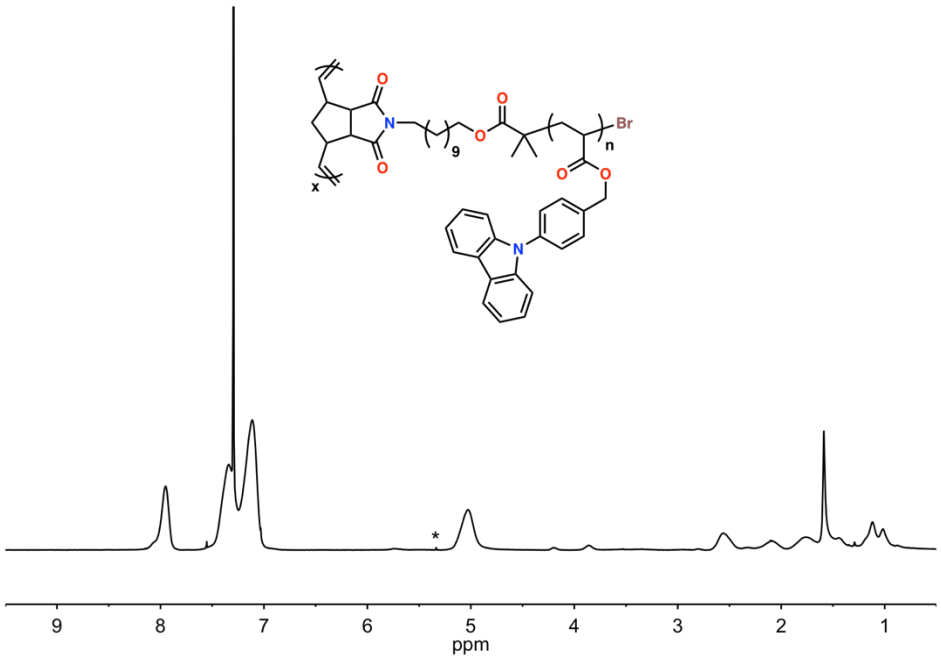

B.7 ETL_{100}-BB

^1H NMR spectrum of **ETL_{100}-BB** in $CDCl_3$. * = CH_2Cl_2.

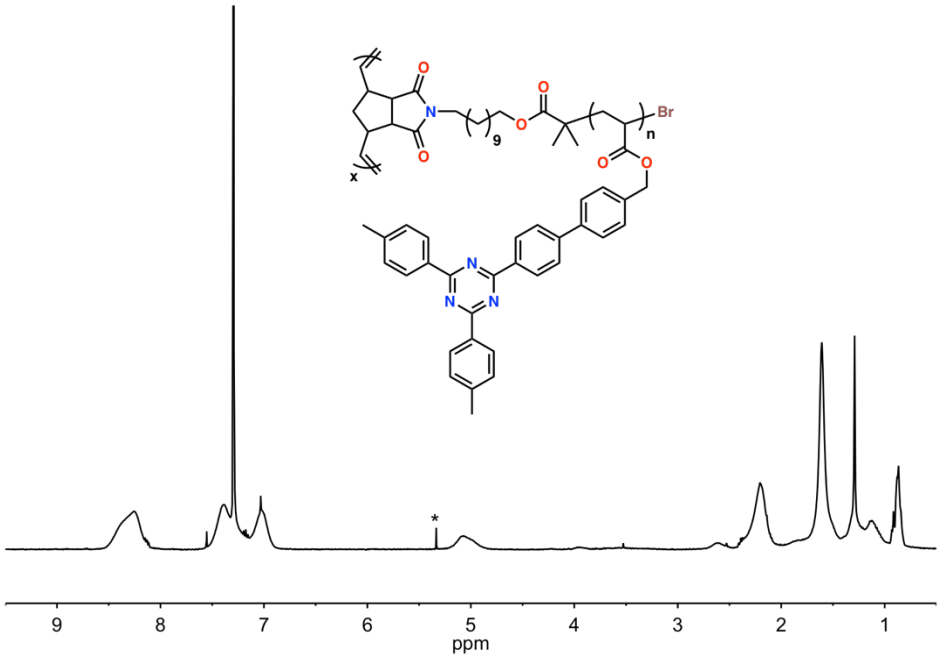

B.8 (HTL_{75}-*b*-ETL_{75})-BB

^1H NMR spectrum of **(HTL_{75}-*b*-ETL_{75})-BB** in $CDCl_3$. * = CH_2Cl_2.

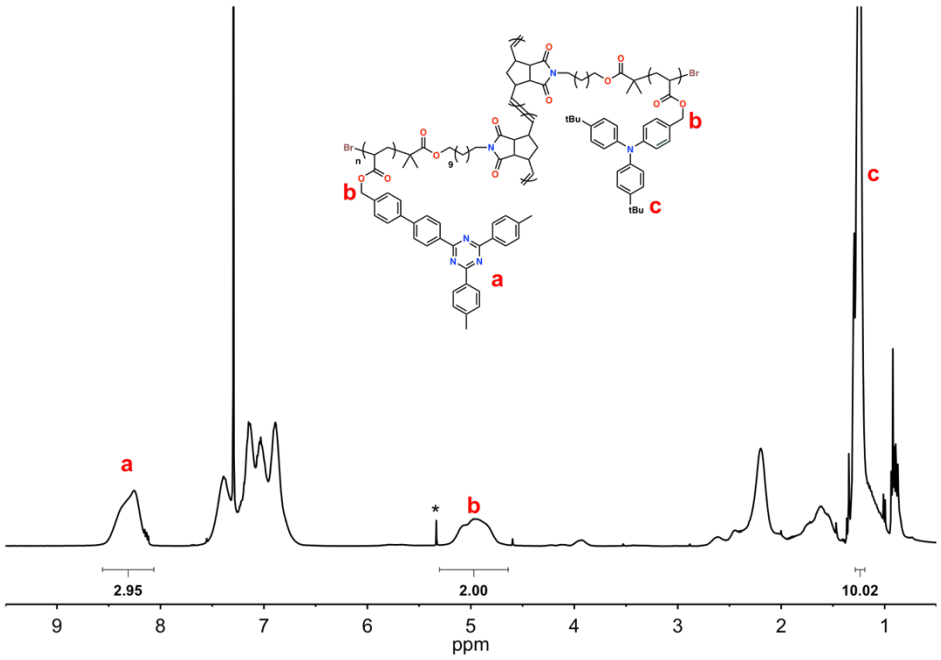

B.9 (EML$_{75}$-*b*-HTL$_{75}$)-BB

^{1}H NMR spectrum of **(EML$_{75}$-*b*-HTL$_{75}$)-BB** in $CDCl_3$. * = CH_2Cl_2.

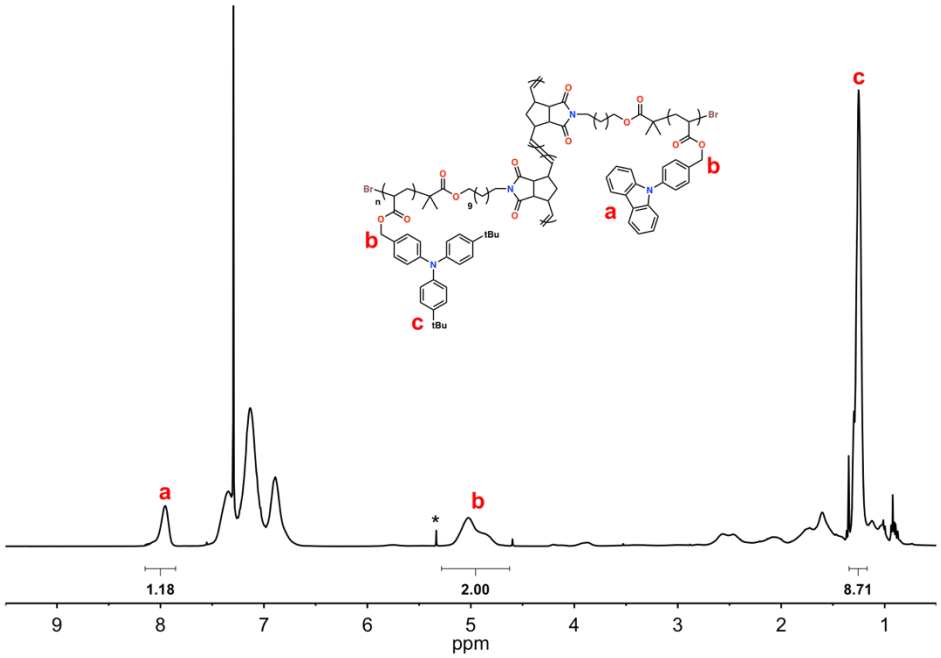

B.10 (EML$_{75}$-*b*-ETL$_{75}$)-BB

^{1}H NMR spectrum of **(EML$_{75}$-*b*-ETL$_{75}$)-BB** in $CDCl_3$. * = CH_2Cl_2.

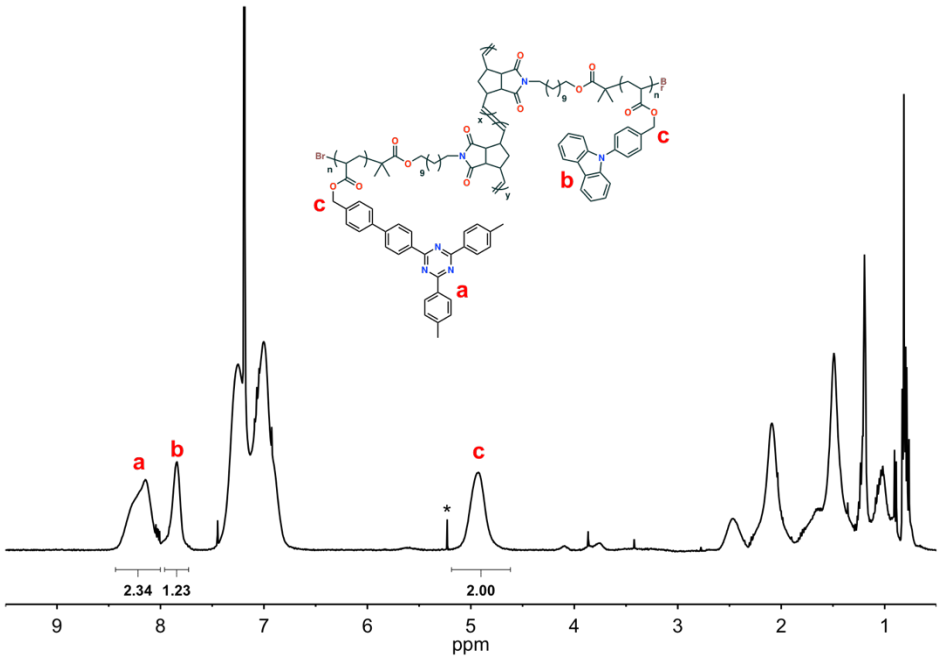

B.11 (HTL$_{50}$-*b*-(EML-*co*-Ir)$_{30}$-*b*-ETL$_{50}$)-BB

^{1}H NMR spectrum of **(HTL$_{50}$-*b*-(EML-*co*-Ir)$_{30}$-*b*-ETL$_{50}$)-BB** in $CDCl_3$. * = CH_2Cl_2.

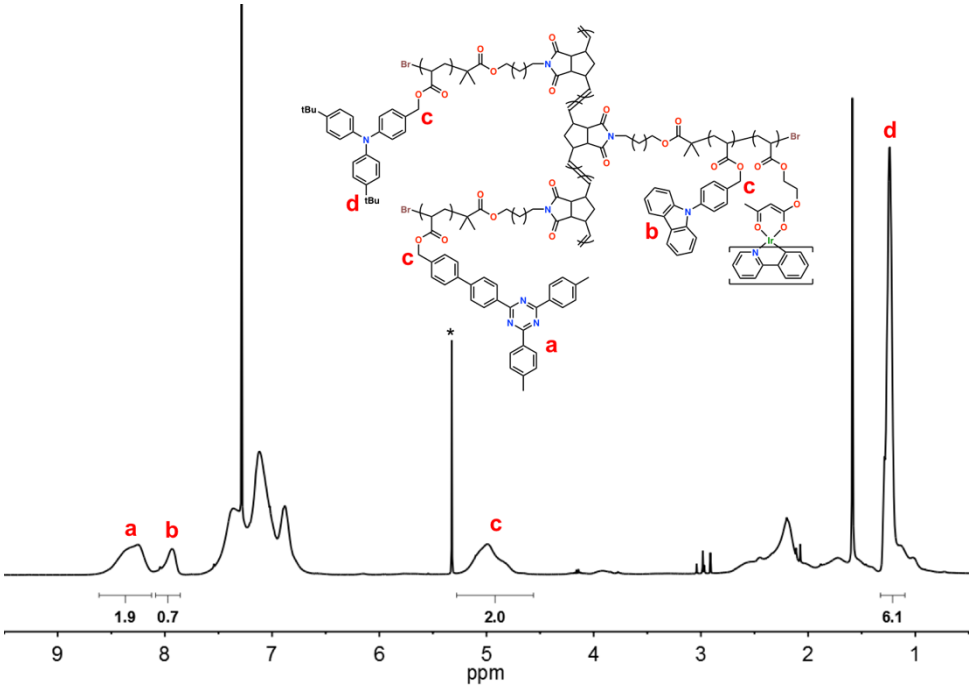

Appendix C : NMR spectra for Chapter 4

C.1 tBuODA-MM

^{1}H NMR spectrum of **tBuODA-MM** in $CDCl_3$.

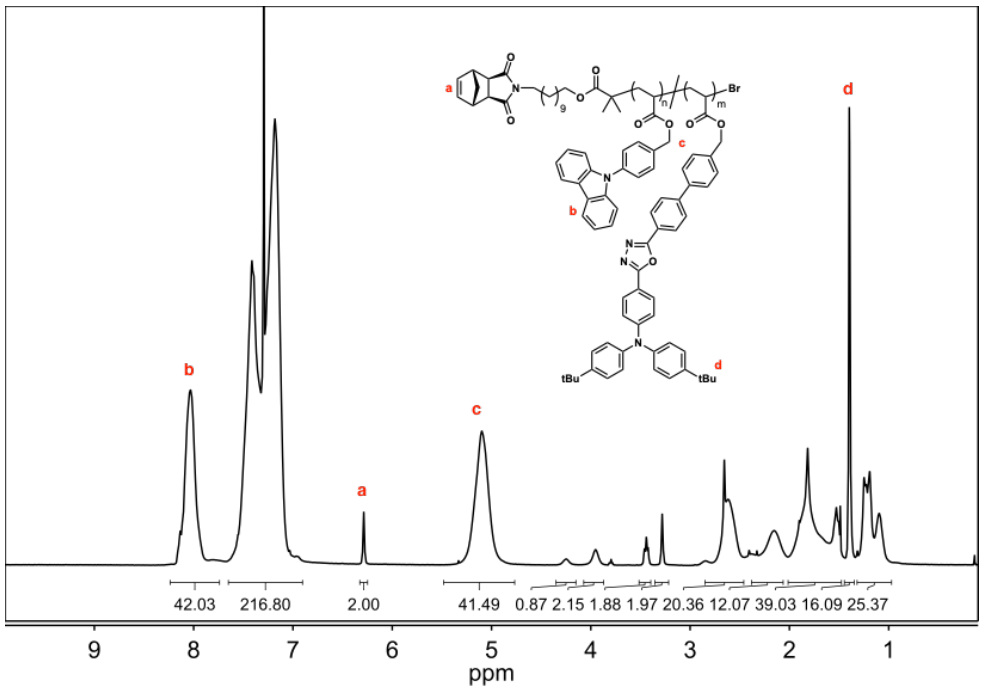

^{13}C{^{1}H} NMR spectrum of **tBuODA-MM** in $CDCl_3$.

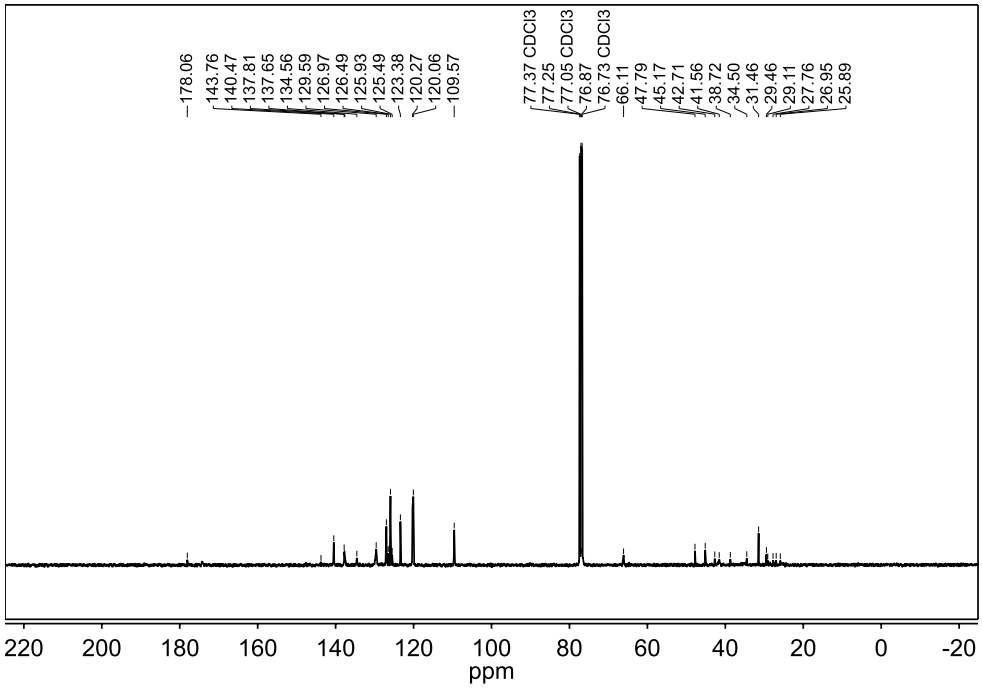

C.2 IrPIQ-MM

^{1}H NMR spectrum of **IrPIQ-MM** in $CDCl_3$.

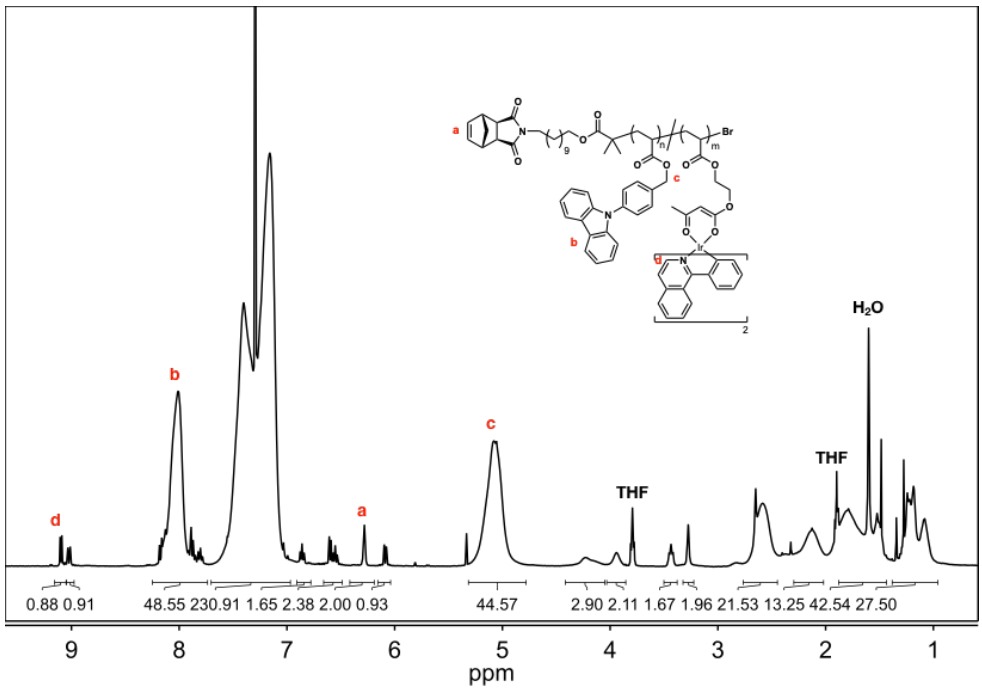

^{13}C{^{1}H} NMR spectrum of **IrPIQ-MM** in $CDCl_3$.

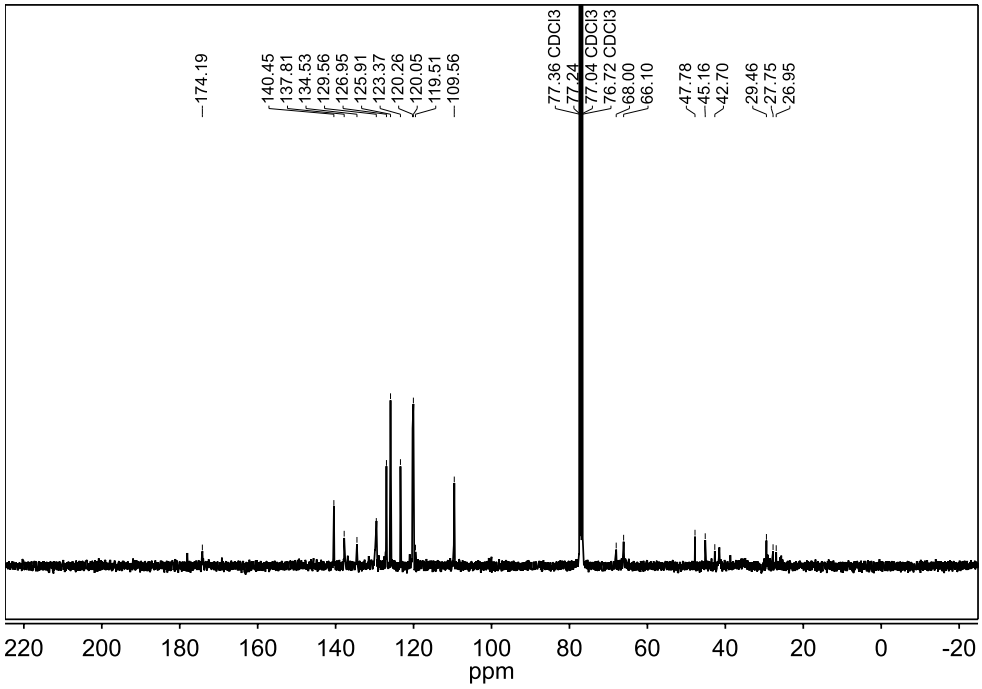

C.3 IrPPY-MM

^{1}H NMR spectrum of **IrPPY-MM** in $CDCl_3$.

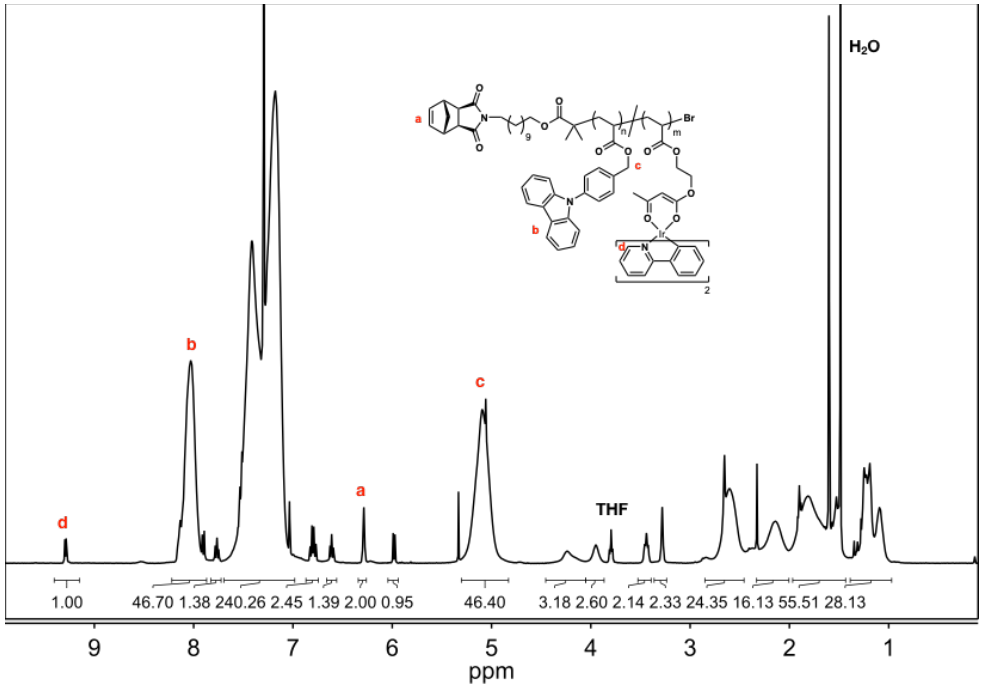

^{13}C{^{1}H} NMR spectrum of **IrPPY-MM** in $CDCl_3$.

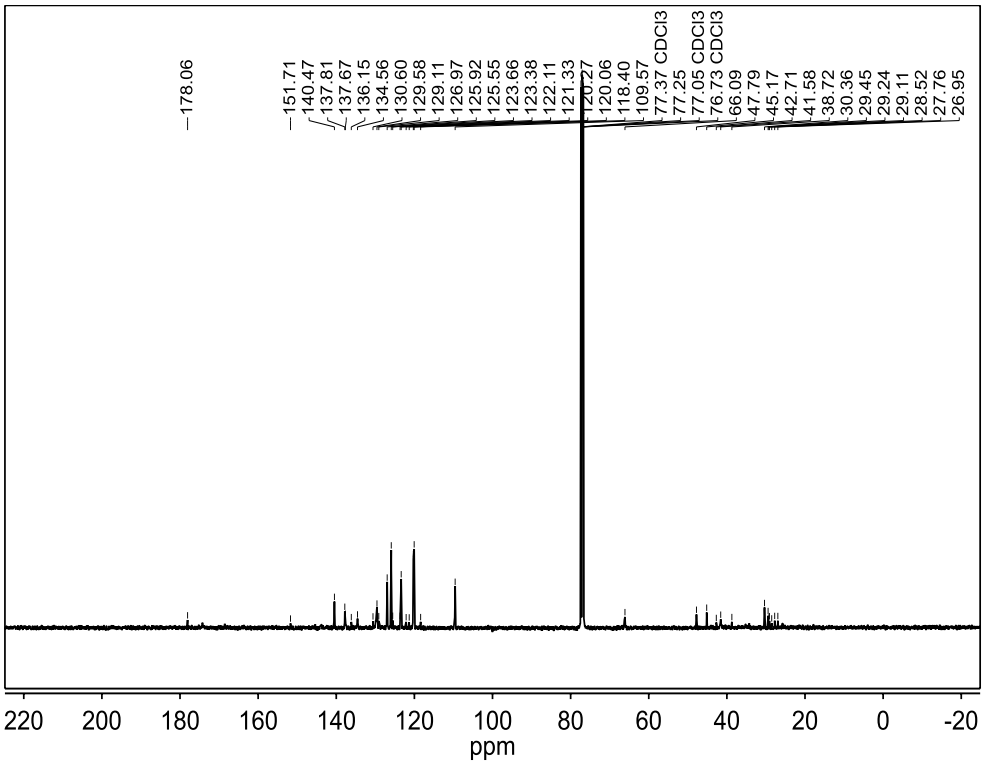

C.4 $tBuODA_{150}$-BB

^{1}H NMR spectrum of **$tBuODA_{150}$-BB** in $CDCl_3$.

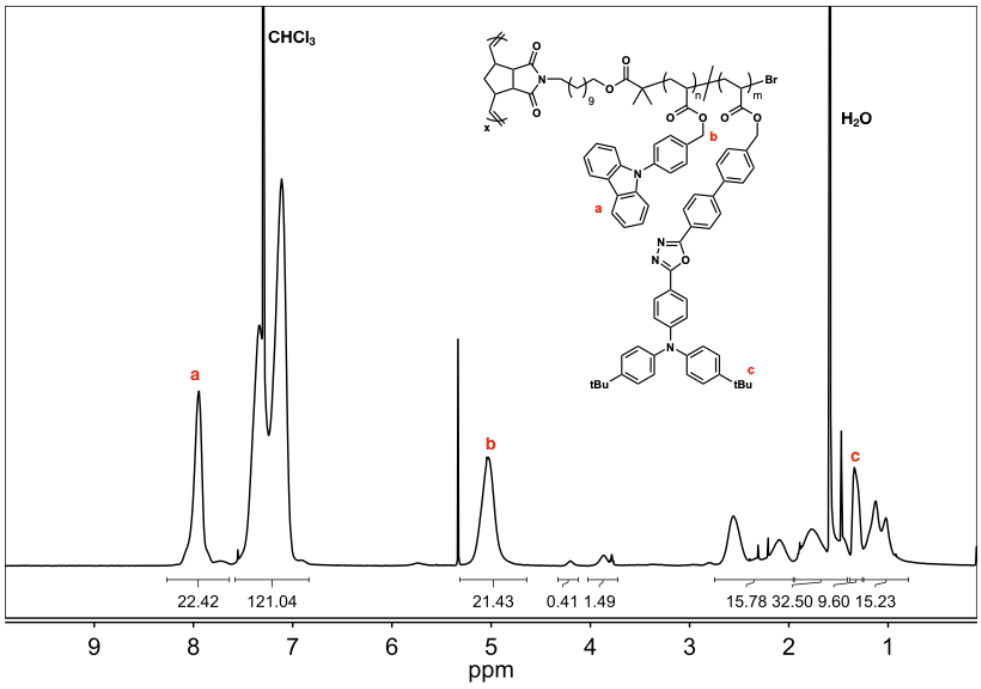

C.5 $IrPPY_{150}$-BB

^{1}H NMR spectrum of **$IrPPY_{150}$-BB** in $CDCl_3$.

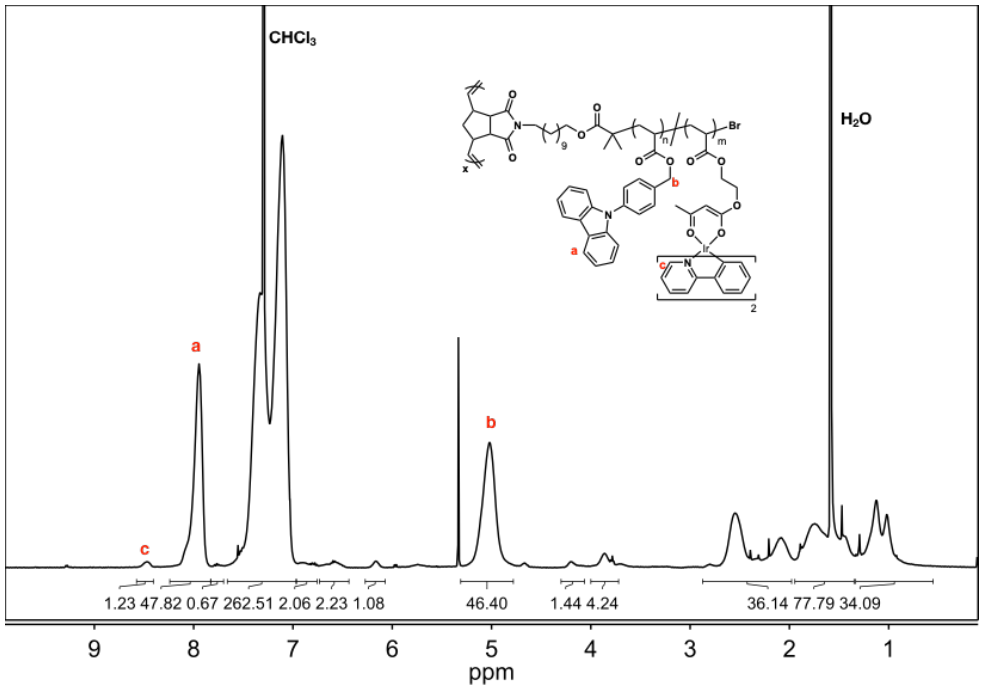

C.6 IrPIQ$_{150}$-BB

^{1}H NMR spectrum of **IrPIQ$_{150}$-BB** in $CDCl_3$.

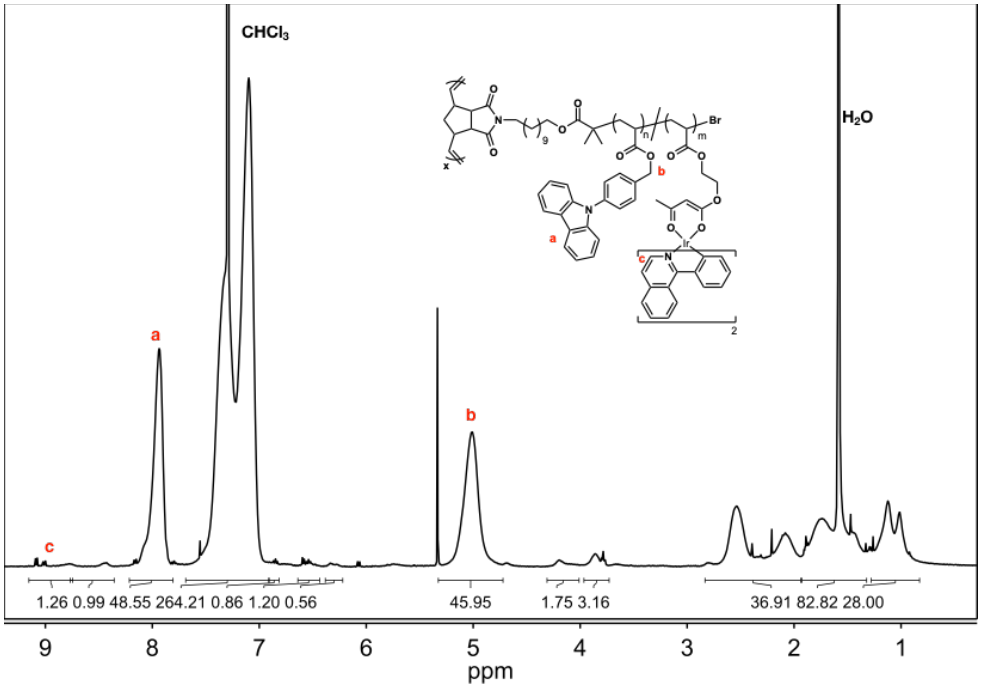

C.7 tBuODA$_{75}$-*b*-IrPPY$_{75}$-BB

^{1}H NMR spectrum of **tBuODA$_{75}$-*b*-IrPPY$_{75}$-BB** in $CDCl_3$.

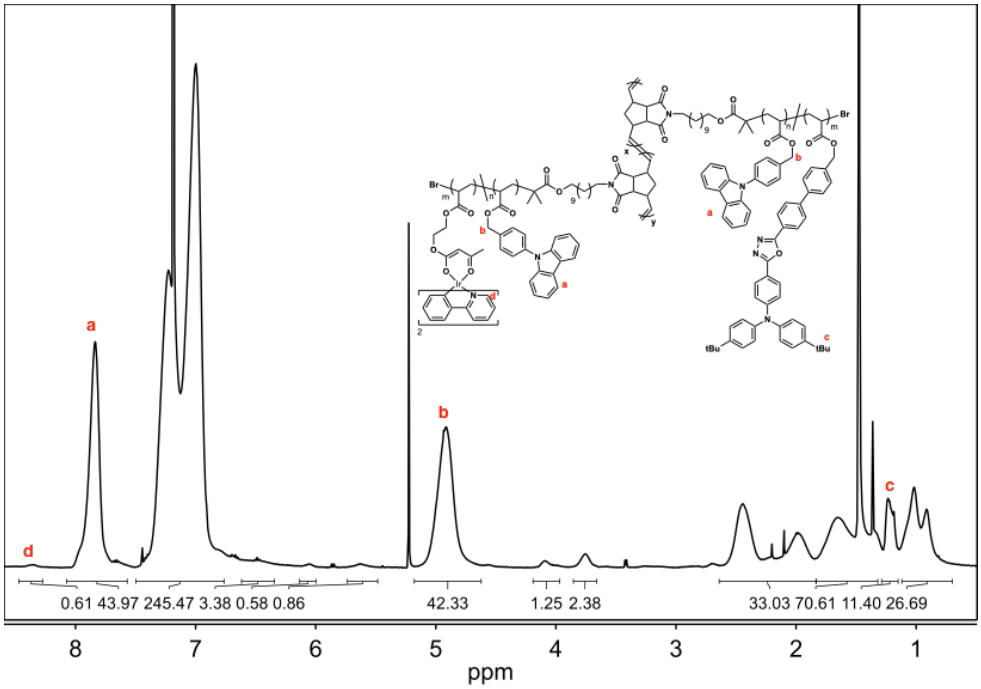

C.8 IrPPY$_{100}$-*b*-IrPIQ$_{50}$-BB

^{1}H NMR spectrum of **IrPPY$_{100}$-*b*-IrPIQ$_{50}$-BB** in $CDCl_3$.

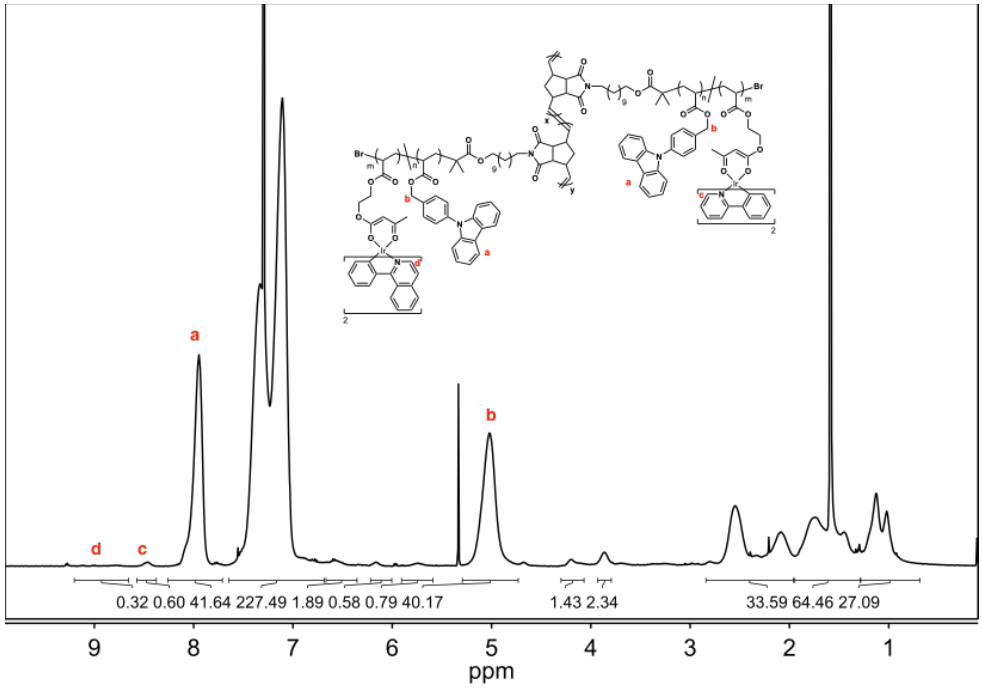

C.9 tBuODA$_{50}$-*b*-IrPPY$_{50}$-*b*-IrPIQ$_{50}$-BB

^{1}H NMR spectrum of **tBuODA$_{50}$-*b*-IrPPY$_{50}$-*b*-IrPIQ$_{50}$-BB** in $CDCl_3$.

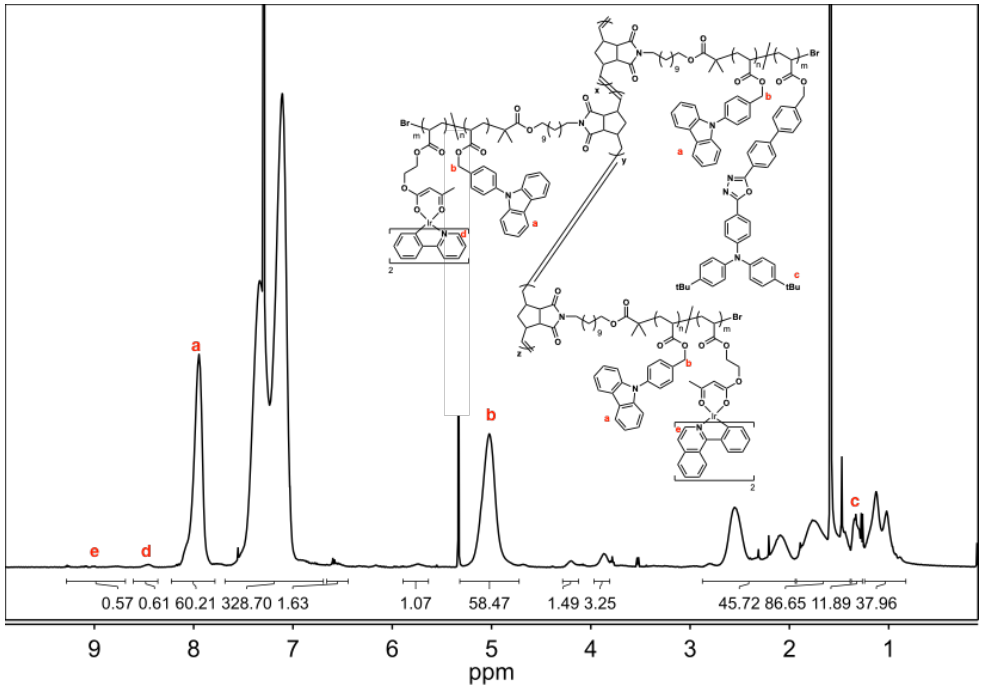

C.10 tBuODA$_{60}$-*b*-IrPIQ$_{90}$-BB

^{1}H NMR spectrum of **tBuODA$_{60}$-*b*-IrPIQ$_{90}$-BB** in $CDCl_3$.

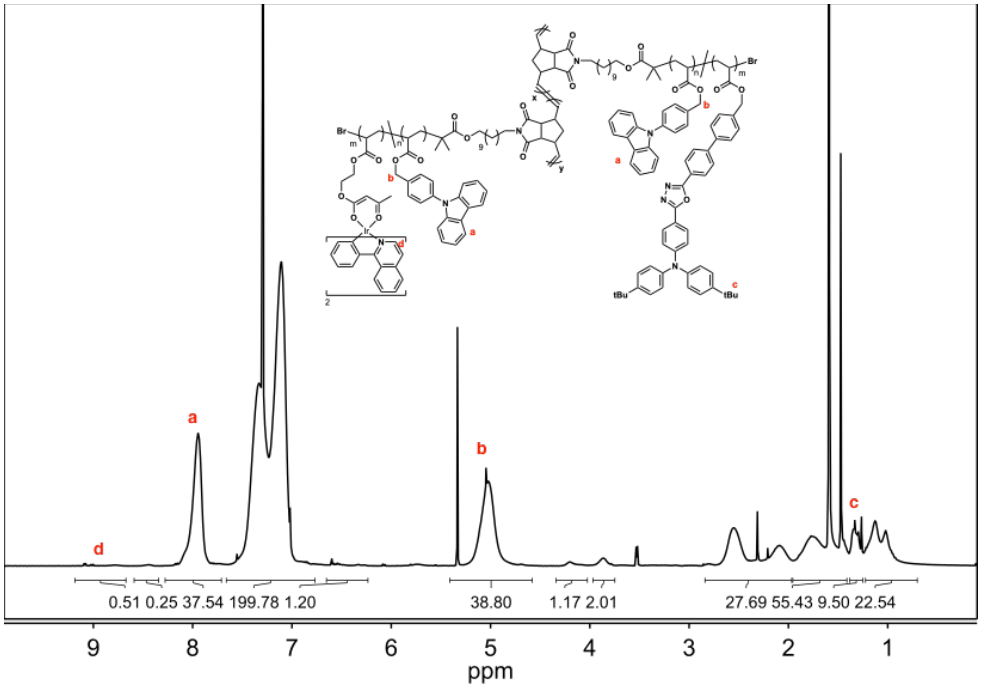

C.11 ETL-MM

^{1}H NMR spectrum of **ETL-MM** in $CDCl_3$.

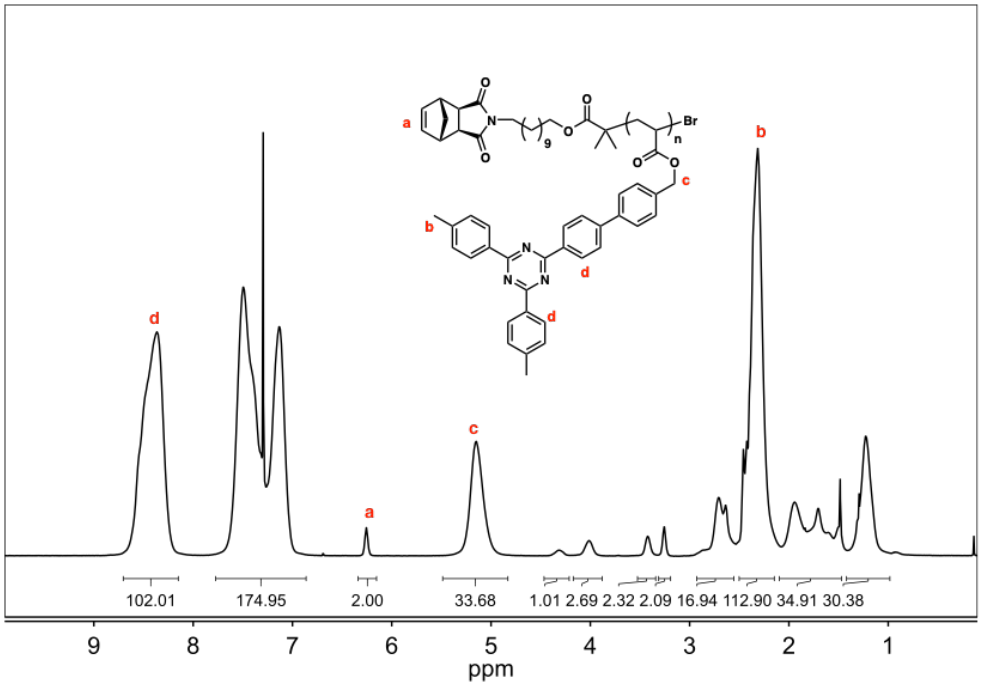

$^{13}C\{^{1}H\}$ NMR spectrum of **ETL-MM** in $CDCl_3$.

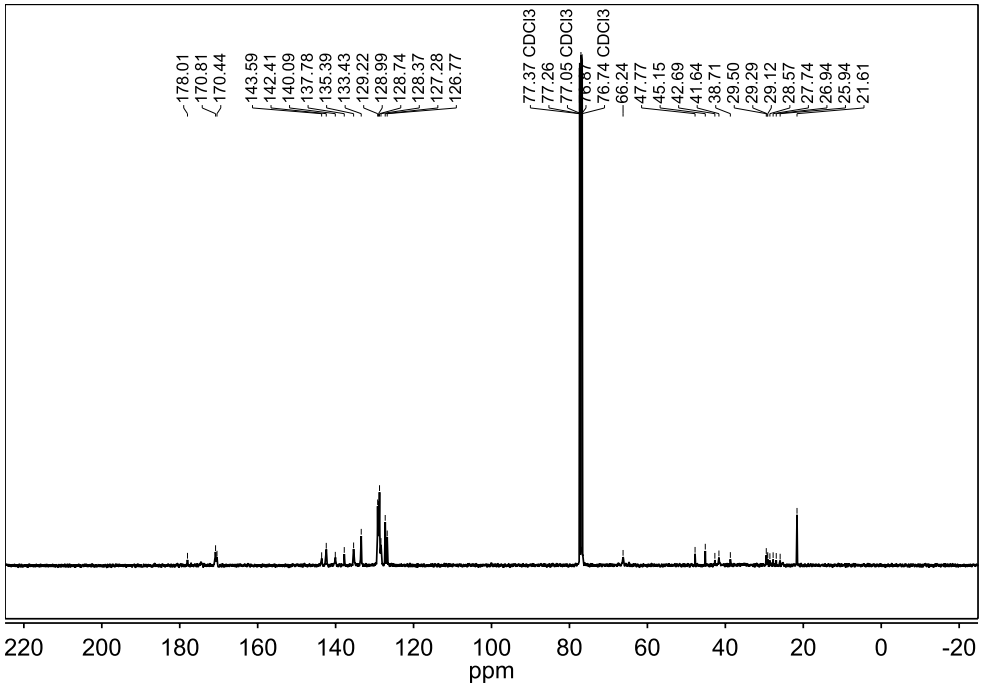

C.12 HTL-MM

^{1}H NMR spectrum of **HTL-MM** in $CDCl_3$.

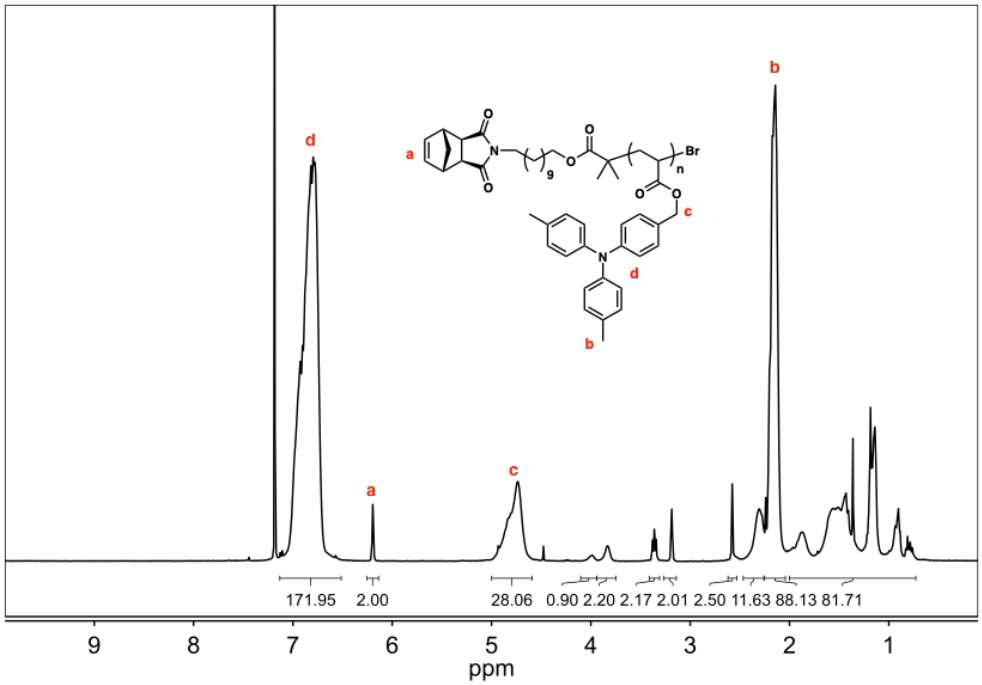

$^{13}C\{^{1}H\}$ NMR spectrum of **HTL-MM** in $CDCl_3$.

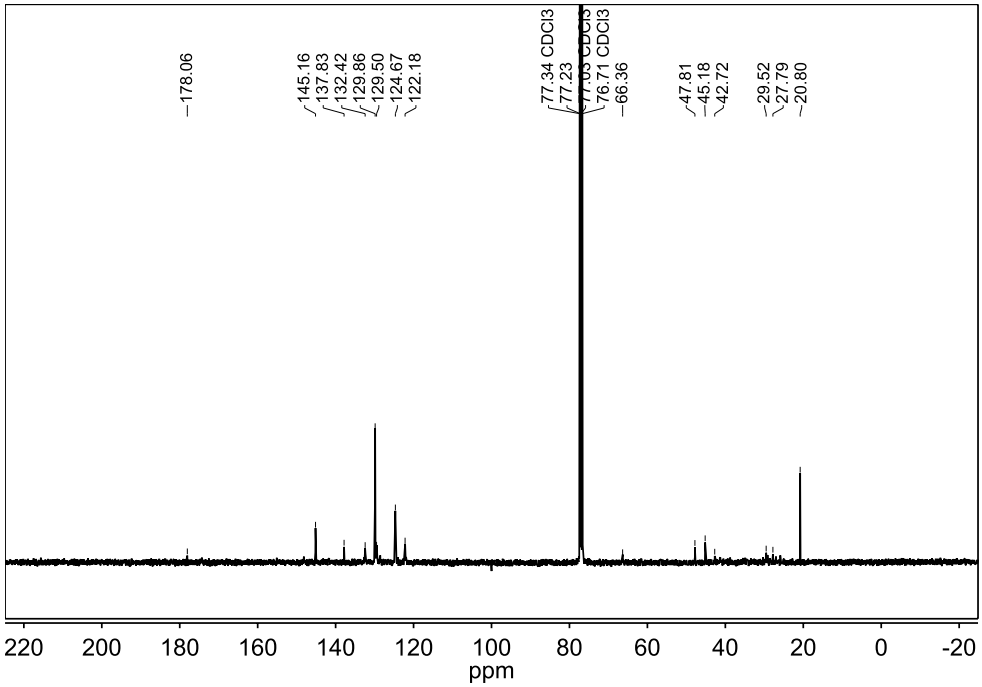

C.13 HTL$_{30}$-*b*-tBuODA$_{30}$-*b*-IrPPY$_{30}$-*b*-IrPIQ$_{30}$-*b*-ETL$_{30}$-BB

^{1}H NMR spectrum of **HTL$_{30}$-*b*-tBuODA$_{30}$-*b*-IrPPY$_{30}$-*b*-IrPIQ$_{30}$-*b*-ETL$_{30}$-BB** in $CDCl_3$.

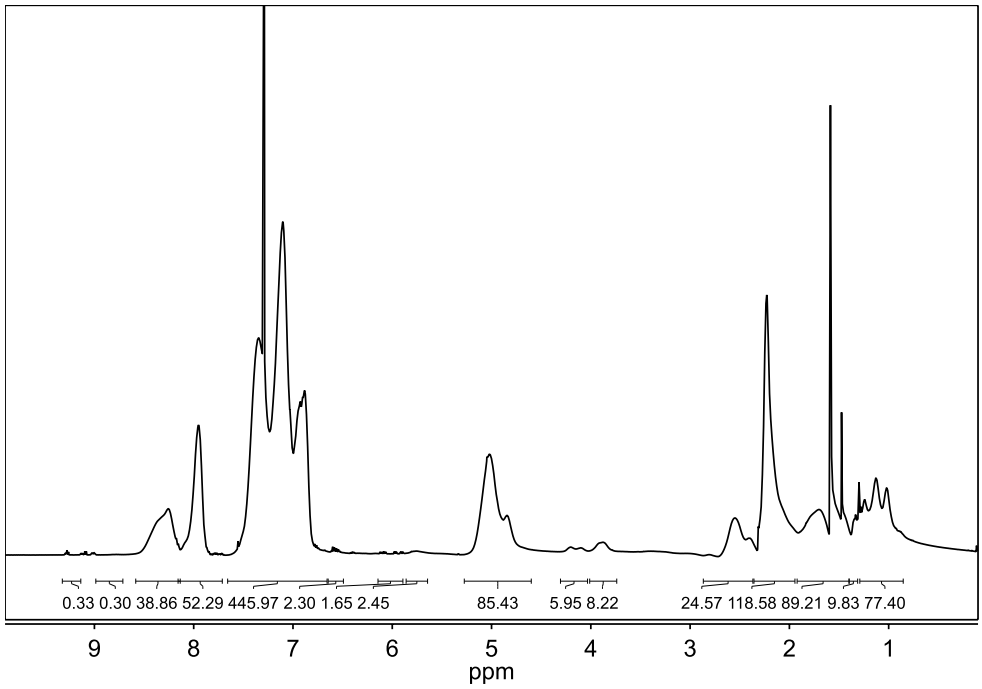

Appendix D : NMR spectra for Chapter 5

D.1 5.2

^{1}H NMR spectrum of **5.2** in **DMSO-*d*$_6$**.

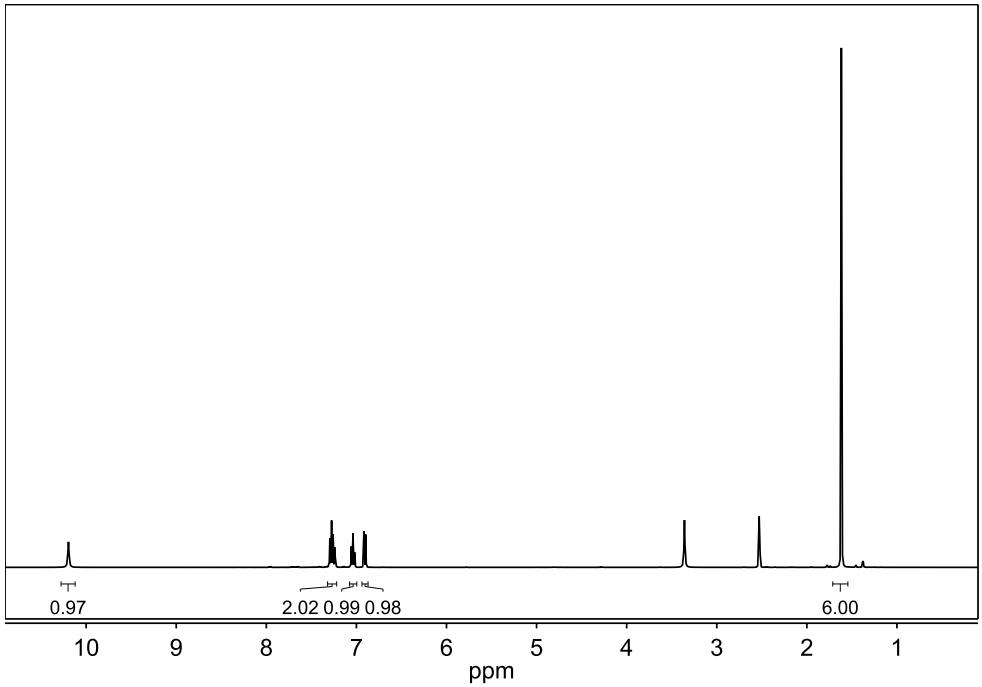

^{13}C {^{1}H} NMR spectrum of **5.2** in **DMSO-*d*$_6$**.

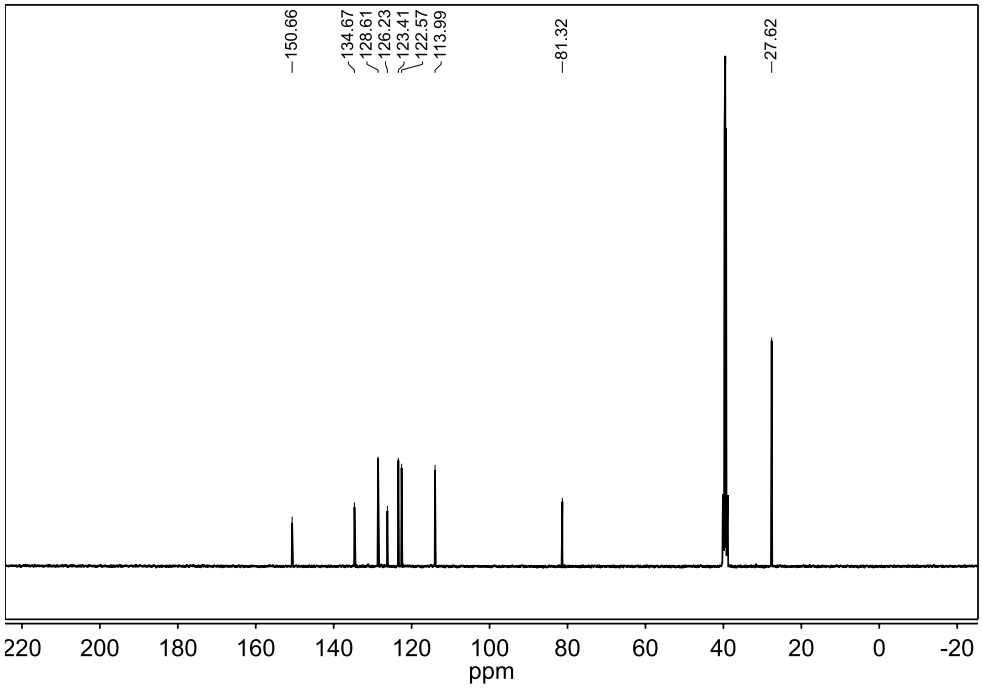

D.2 5.3

^{1}H NMR spectrum of **5.3** in **DMSO-*d*$_6$**.

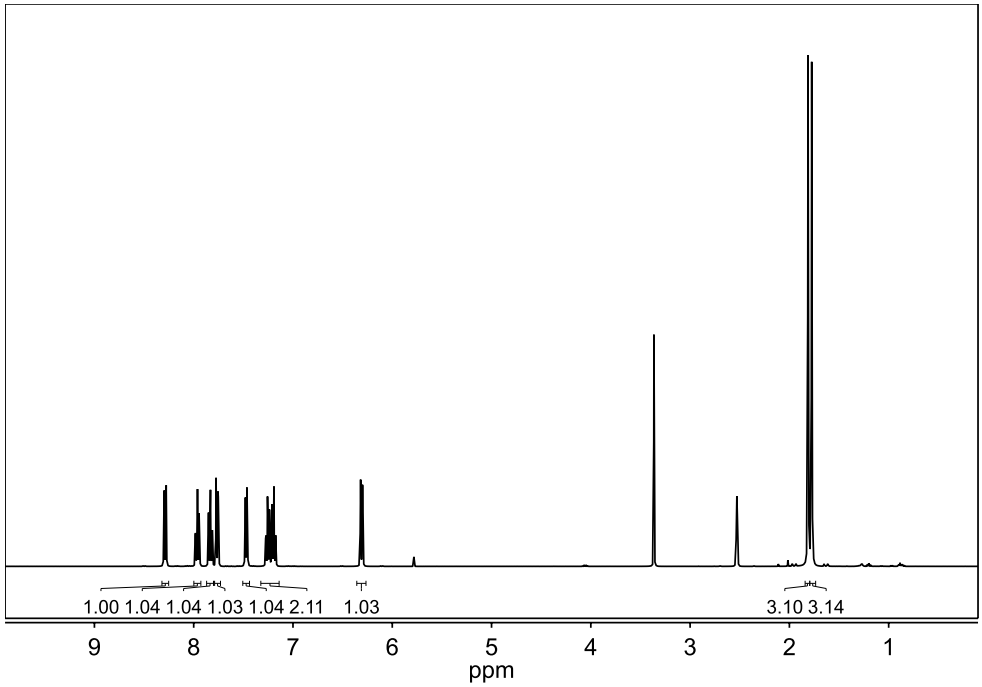

^{13}C {^{1}H} NMR spectrum of **5.3** in **DMSO-*d*$_6$**.

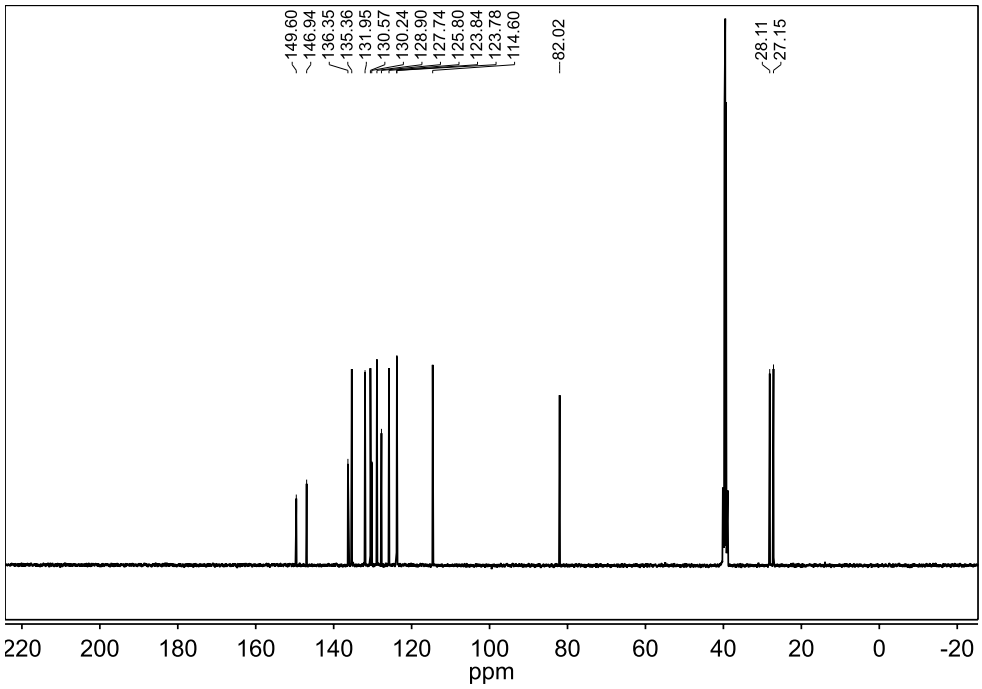

D.3 5.4

^{1}H NMR spectrum of **5.4** in **DMSO-*d*$_6$**.

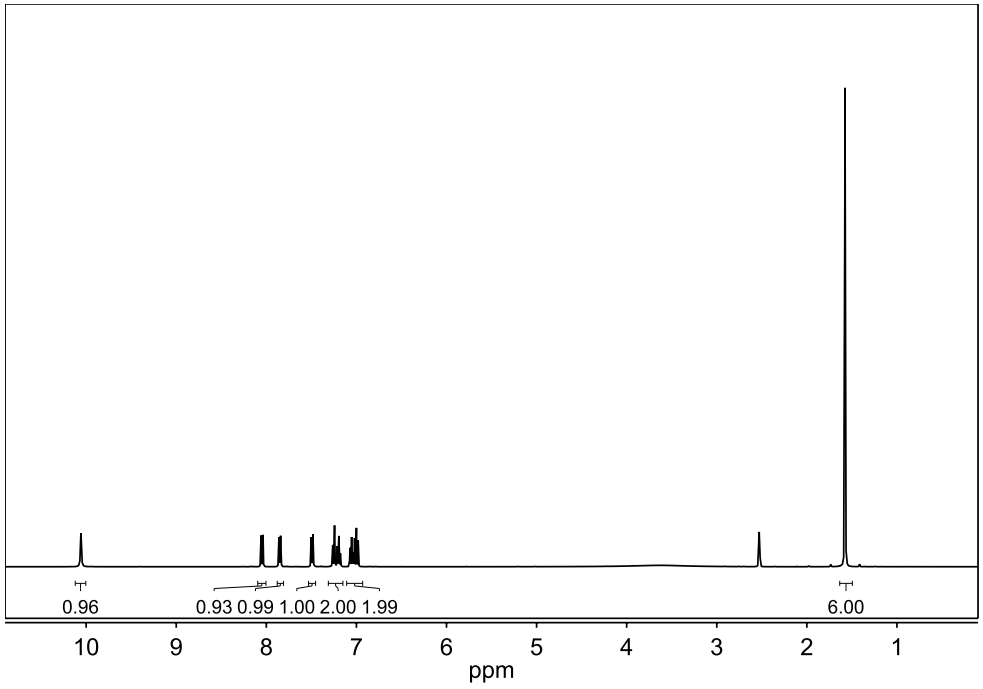

^{13}C {^{1}H} NMR spectrum of **5.4** in **DMSO-*d*$_6$**.

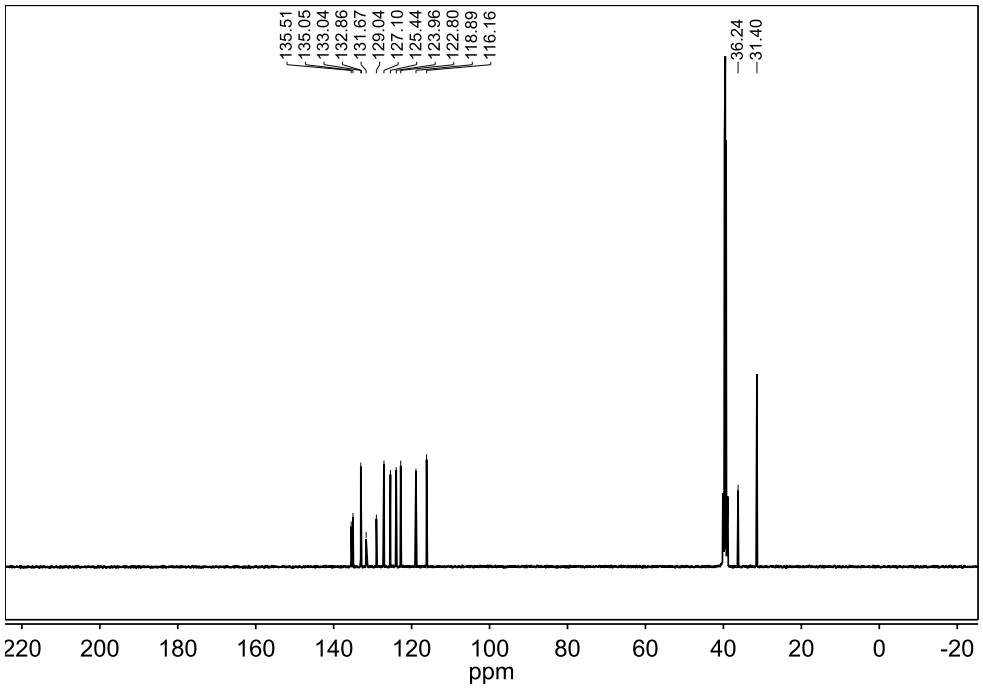

D.4 5.5

^{1}H NMR spectrum of **5.5** in **DMSO-*d*$_6$**.

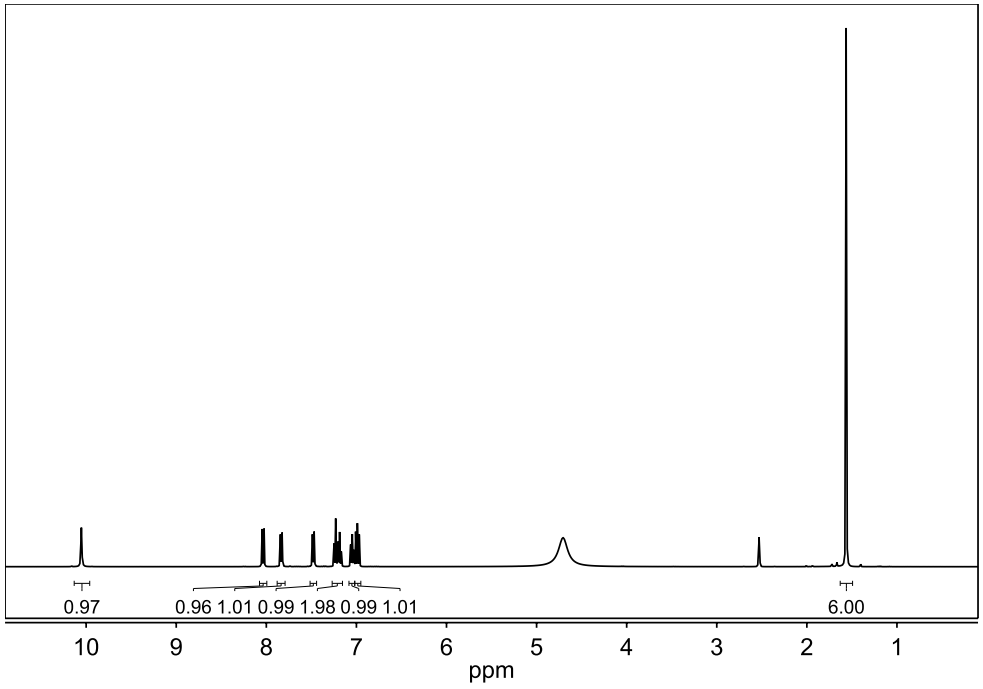

^{13}C {^{1}H} NMR spectrum of **5.5** in **DMSO-*d*$_6$**.

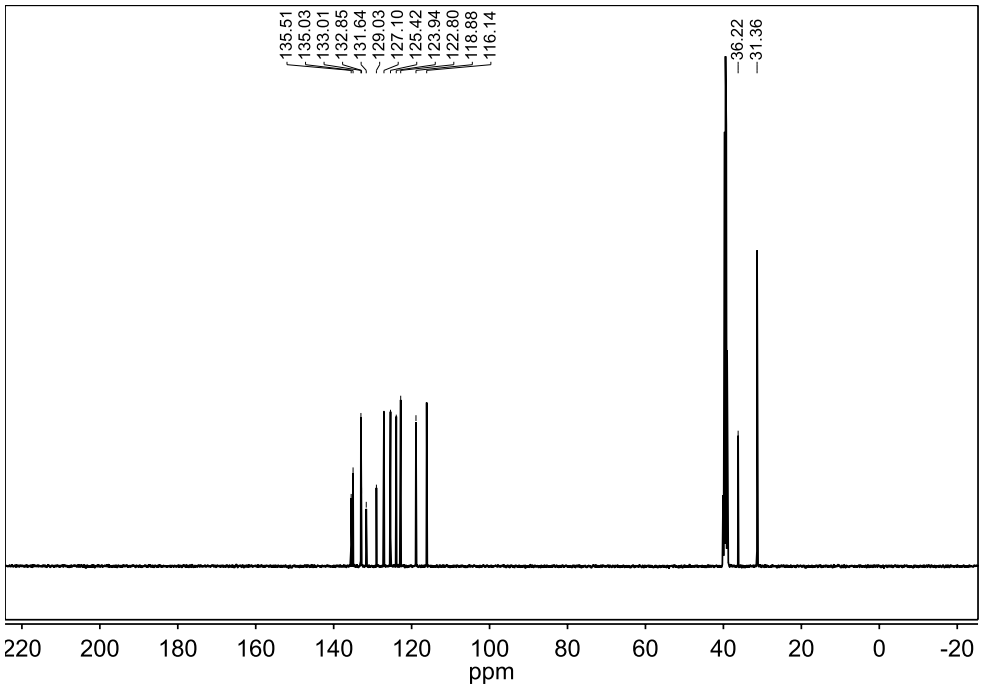

D.5 5.6

^{1}H NMR spectrum of **5.6** in **DMSO-*d*$_6$**.

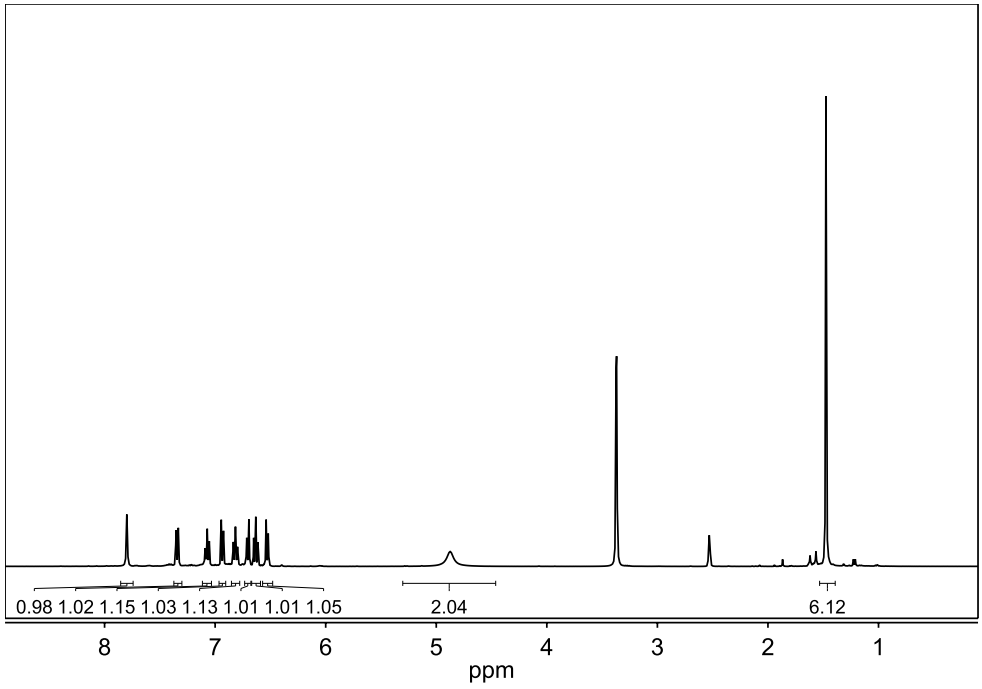

^{13}C {^{1}H} NMR spectrum of **5.6** in **DMSO-*d*$_6$**.

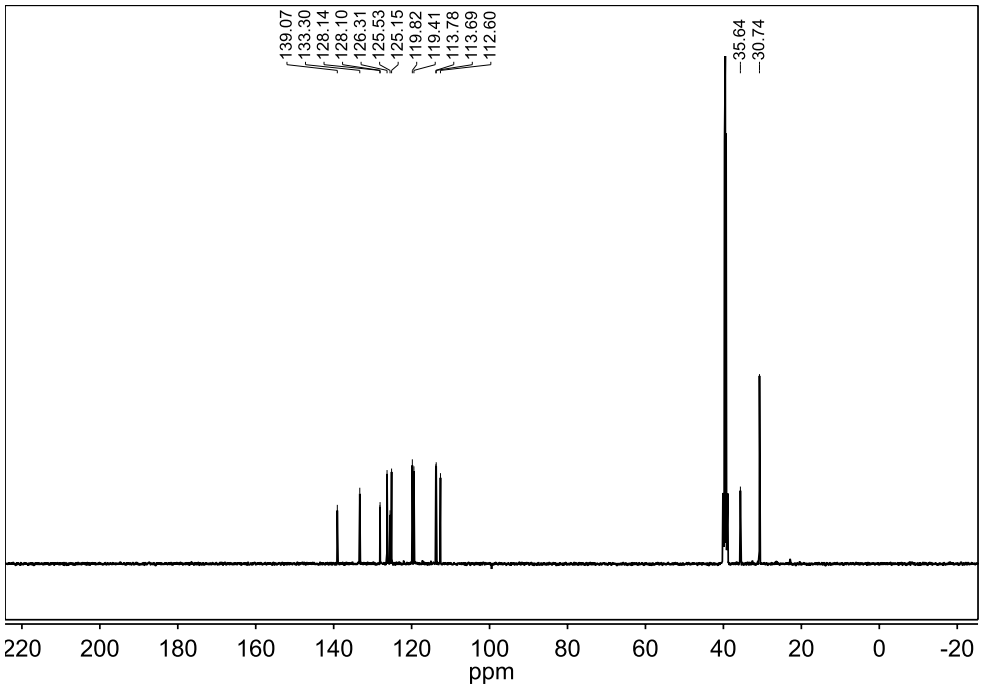

D.6 5.7

^{1}H NMR spectrum of **5.7** in **DMSO-*d*$_6$**.

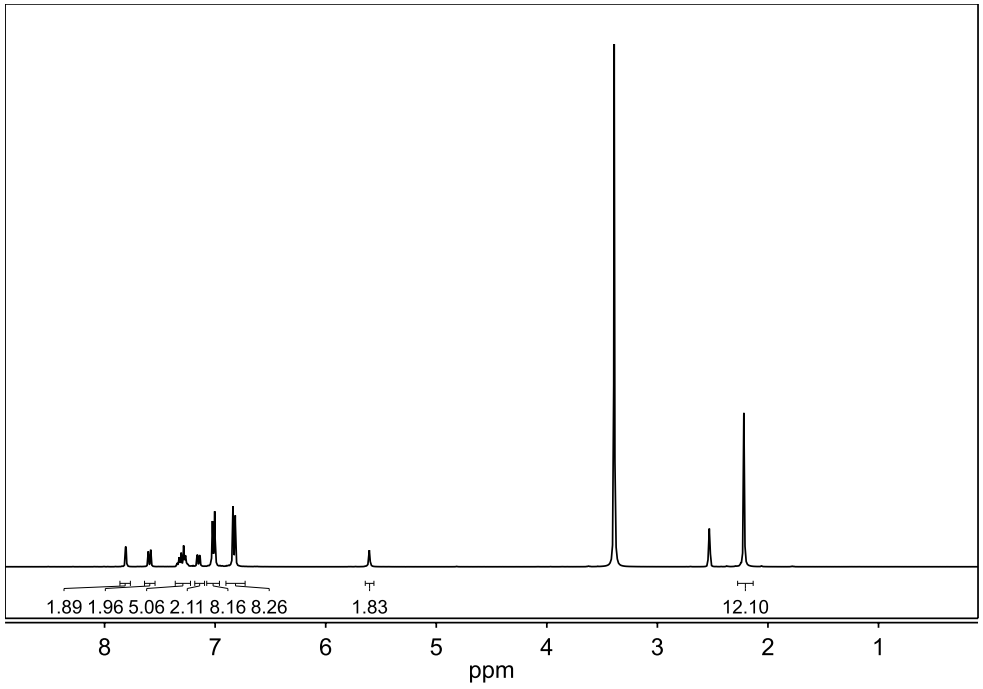

^{13}C{^{1}H} NMR spectrum of **5.7** in **DMSO-*d*$_6$**.

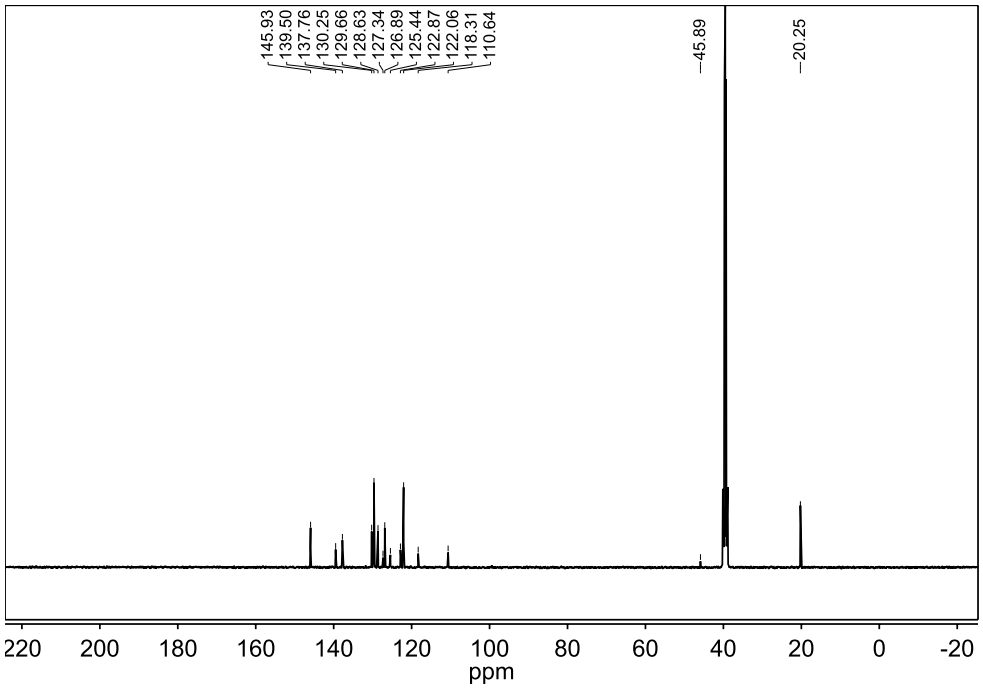

D.7 5.8

^{1}H NMR spectrum of **5.8** in **benzene-*d*$_6$**.

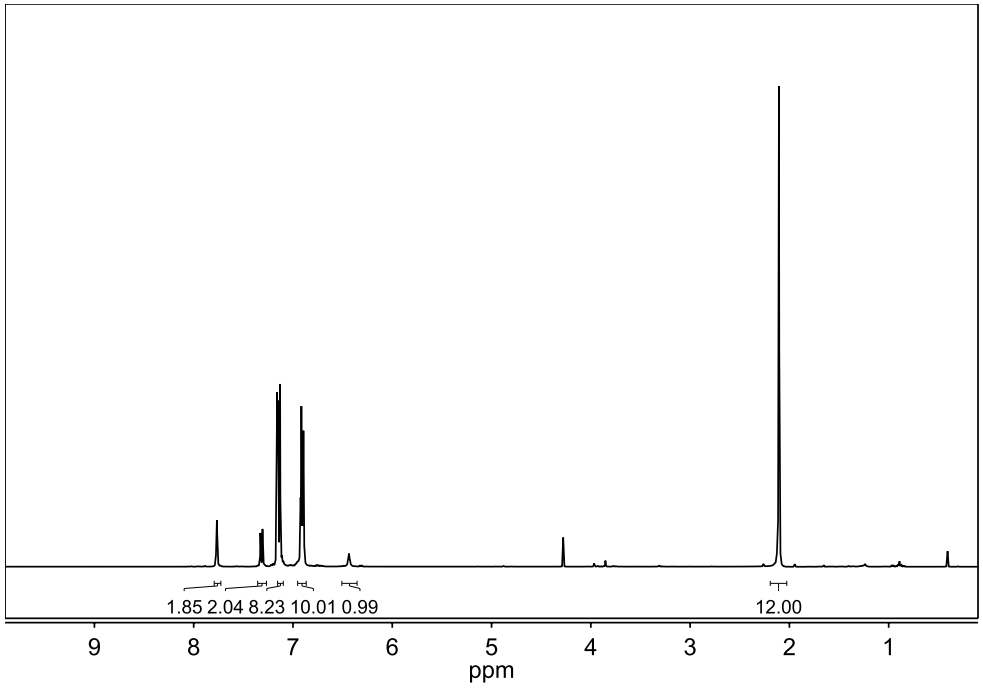

^{13}C {^{1}H} NMR spectrum of **5.8** in **benzene-*d*$_6$**.

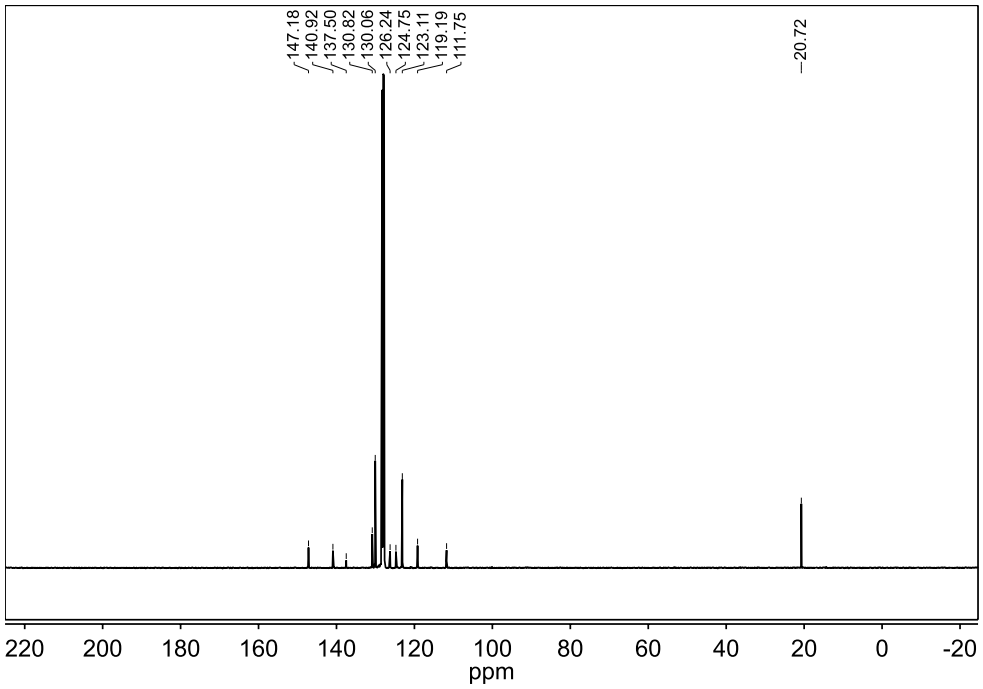

D.8 5.9

^{1}H NMR spectrum of **5.9** in **benzene-*d*$_6$**.

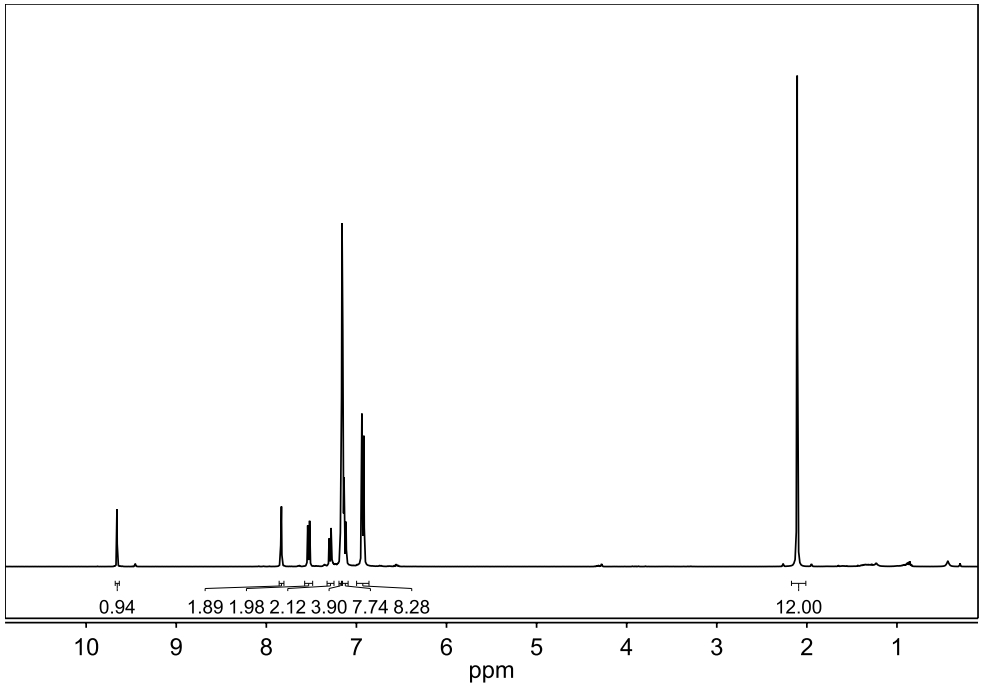

^{13}C {^{1}H} NMR spectrum of **5.9** in **benzene-*d*$_6$**.

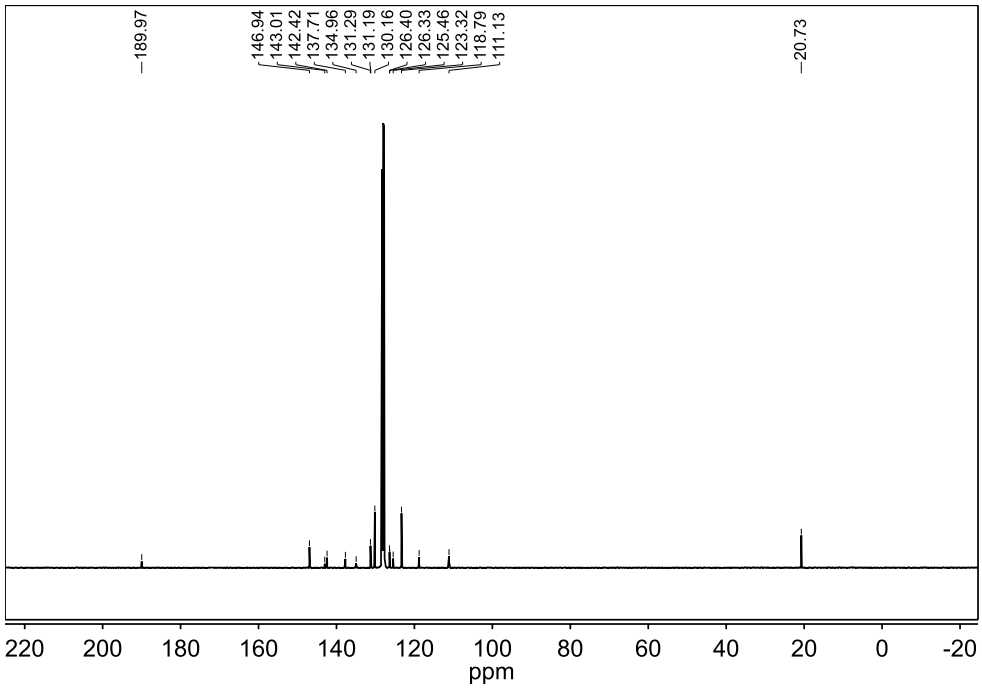

D.9 5.10

^{1}H NMR spectrum of **5.10** in **$CDCl_3$**.

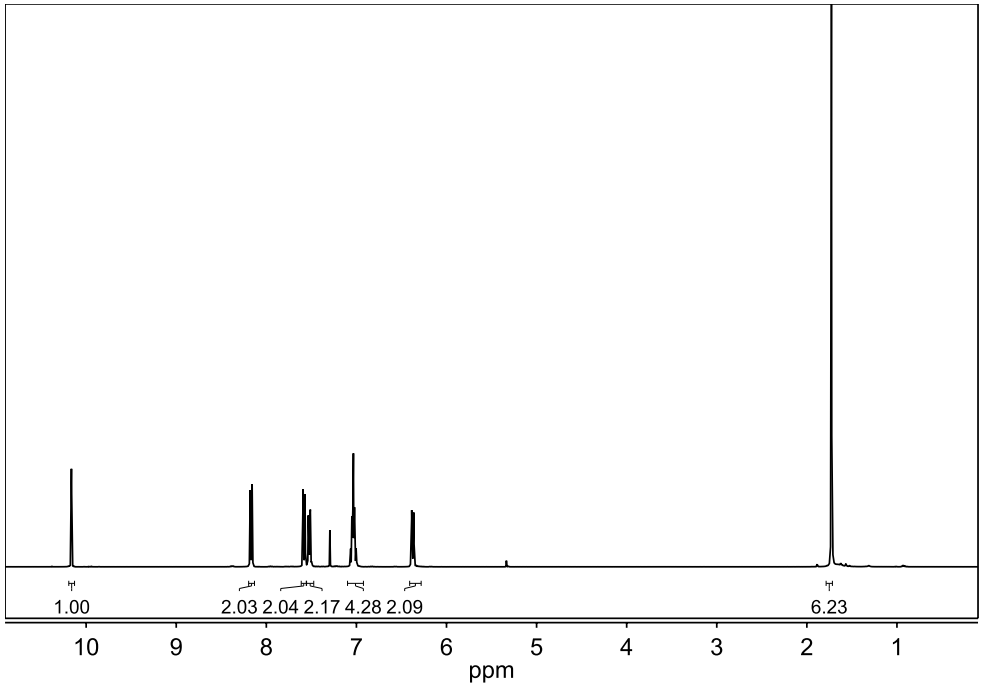

^{13}C {^{1}H} NMR spectrum of **5.10** in **$CDCl_3$**.

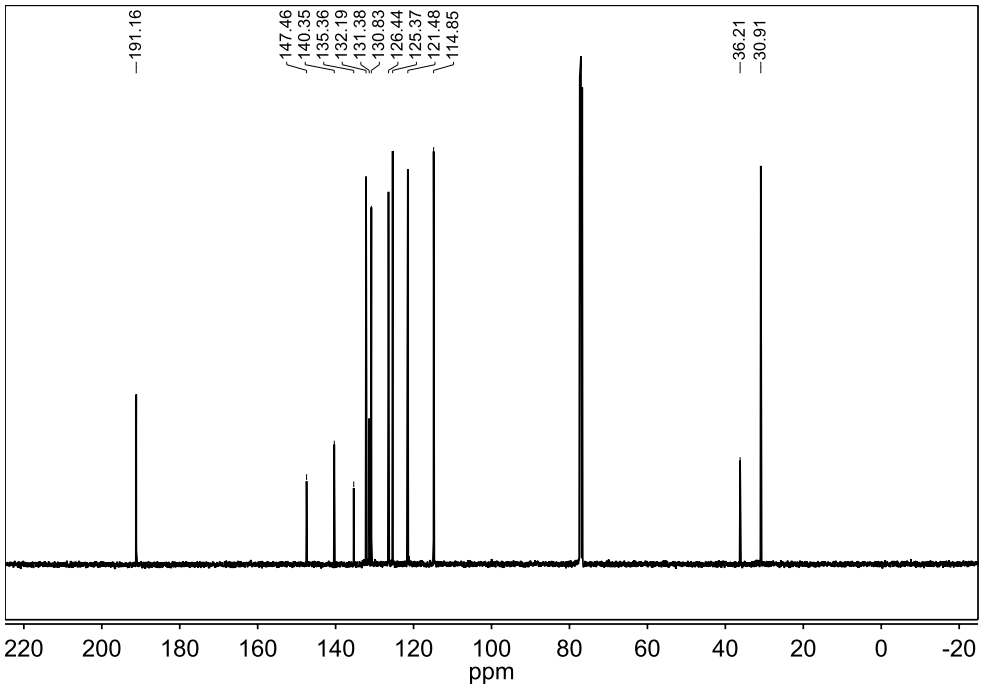

D.10 PXZ-IMAC

^{1}H NMR spectrum of **PXZ-IMAC** in **methylene chloride-*d*$_2$**.

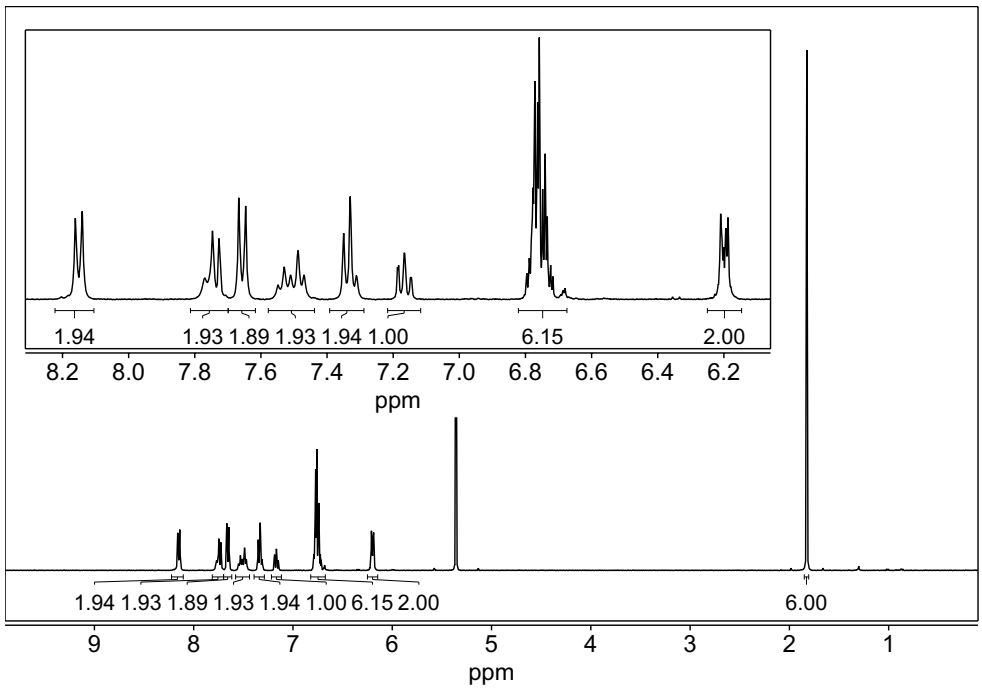

^{13}C {^{1}H} NMR spectrum of **PXZ-IMAC** in **methylene chloride-*d*$_2$**.

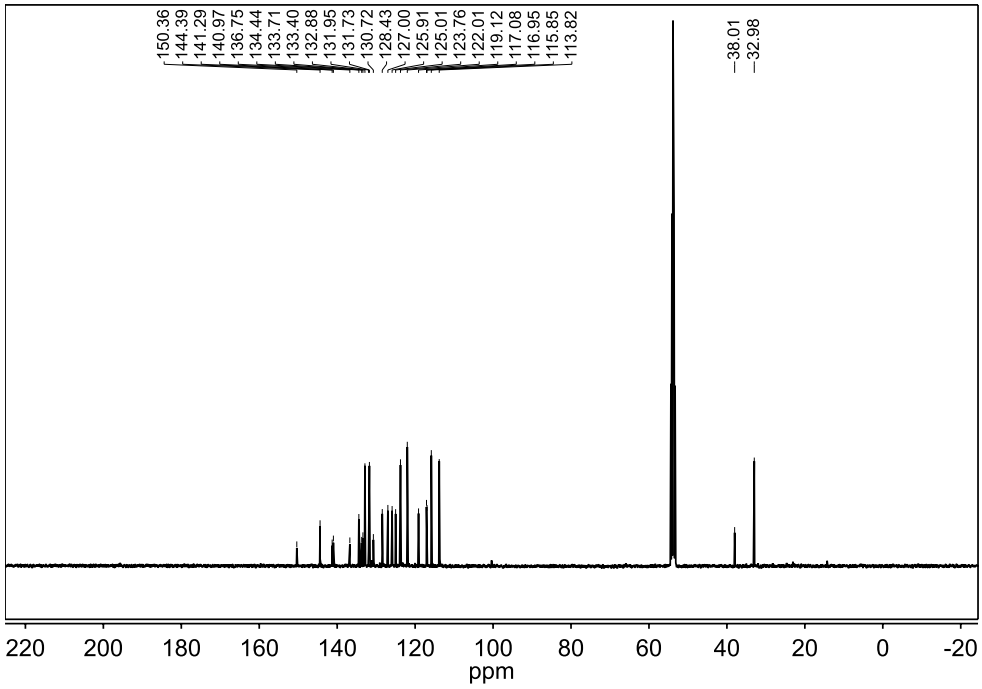

D.11 PTZ-IMAC

^{1}H NMR spectrum of **PTZ-IMAC** in **methylene chloride-*d*$_2$**.

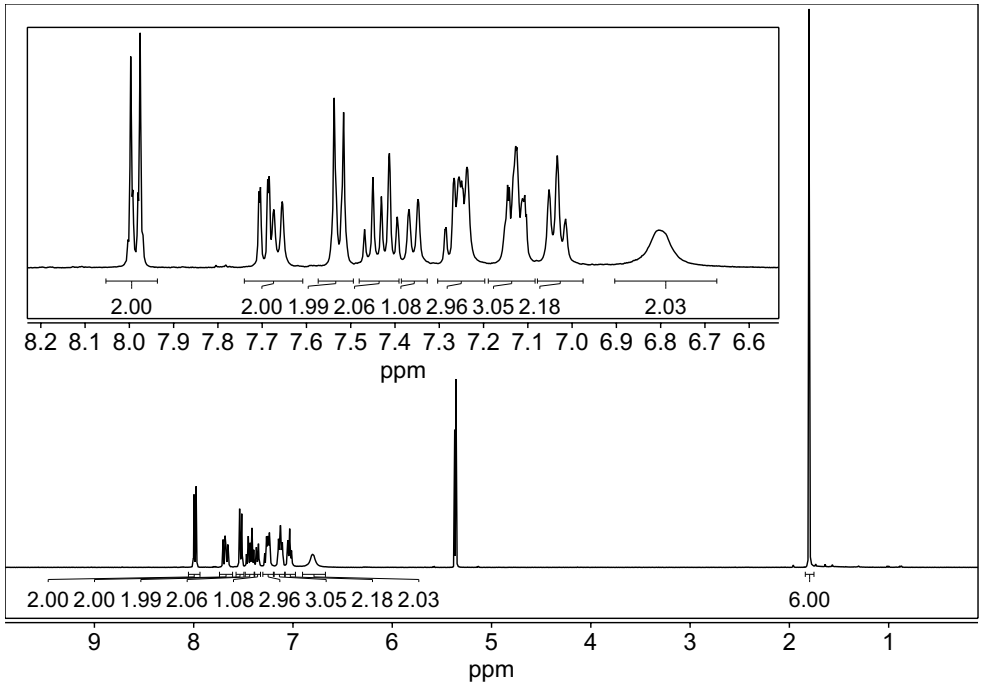

^{13}C {^{1}H} NMR spectrum of **PTZ-IMAC** in **methylene chloride-*d*$_2$**.

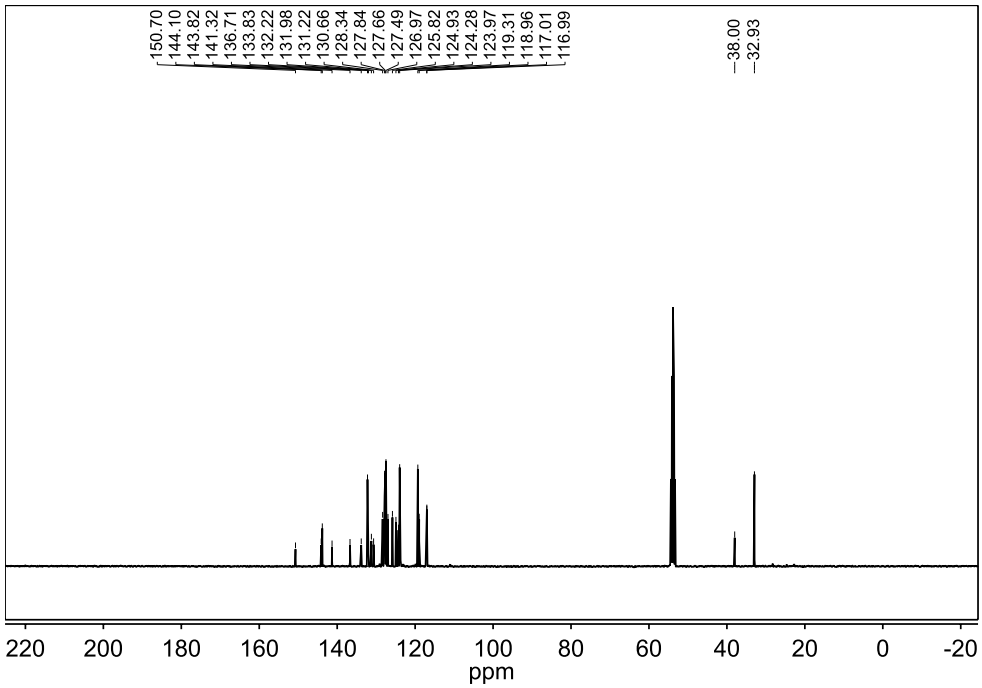

D.12 ACR-IMAC

^{1}H NMR spectrum of **ACR-IMAC** in **methylene chloride-*d*$_2$**.

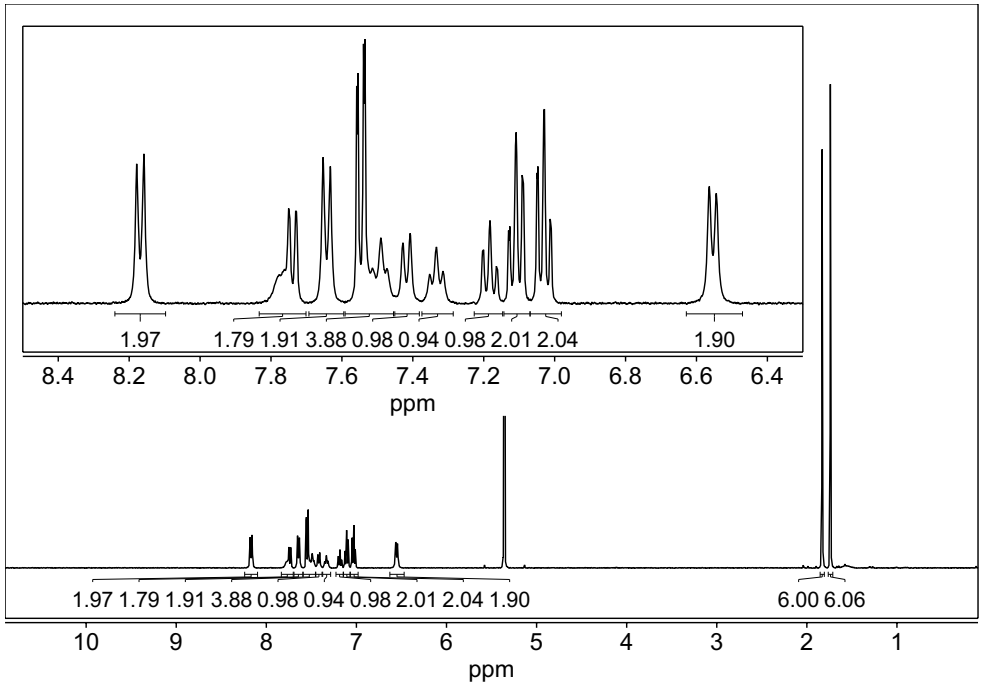

^{13}C {^{1}H} NMR spectrum of **ACR-IMAC** in **methylene chloride-*d*$_2$**.

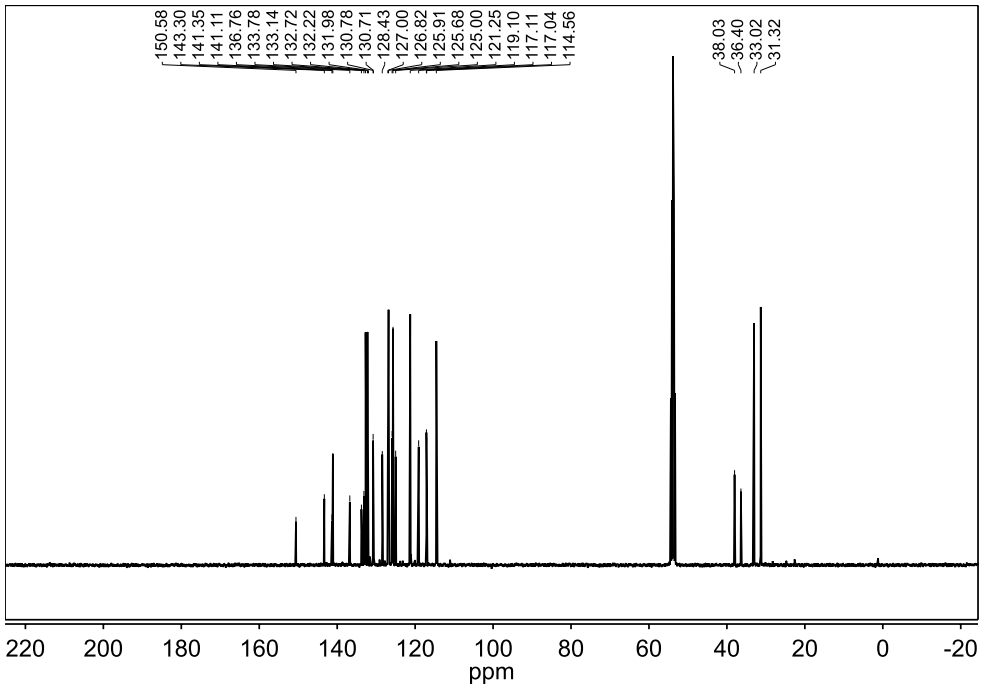

D.13 CZ-IMAC

^{1}H NMR spectrum of **CZ-IMAC** in **DMSO-*d*$_6$**.

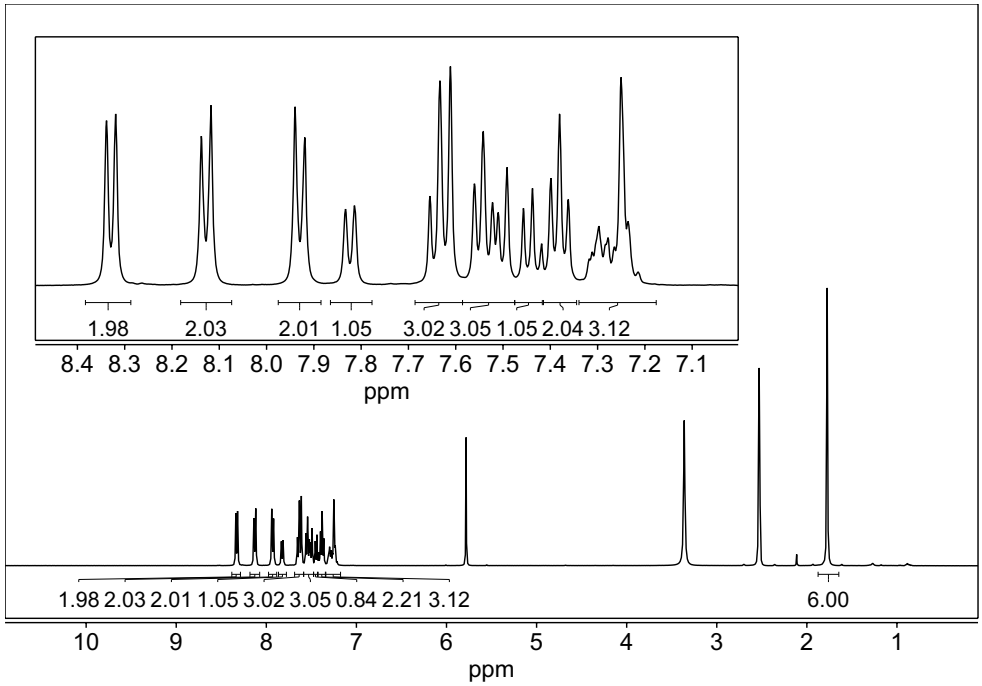

^{13}C {^{1}H} NMR spectrum of **CZ-IMAC** in **DMSO-*d*$_6$**.

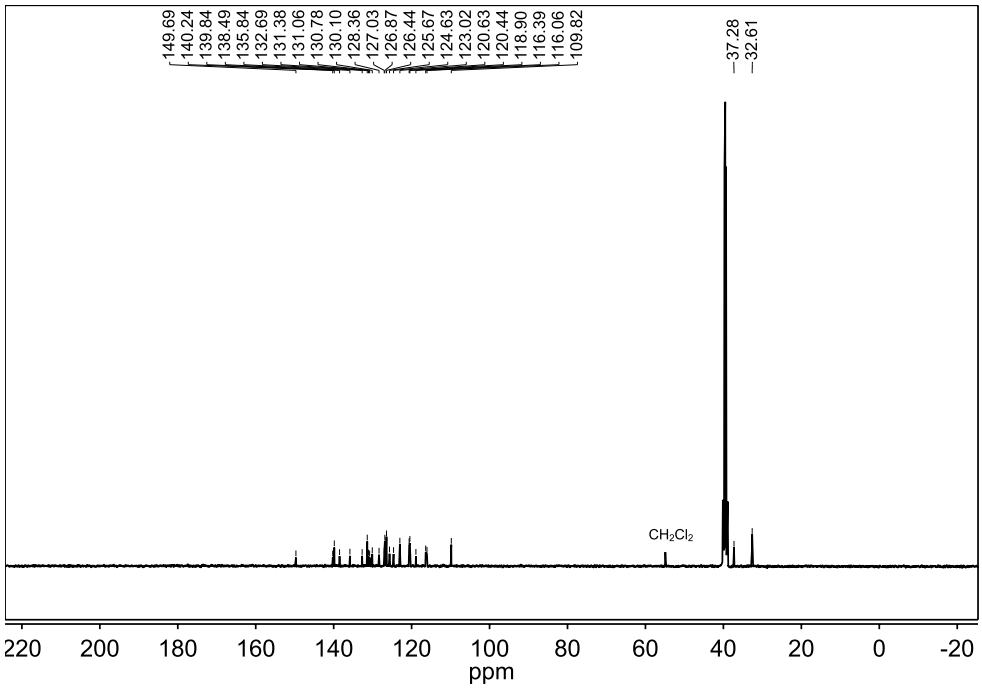

D.14 TerCZ-IMAC

^{1}H NMR spectrum of **TerCZ-IMAC** in **methylene chloride-*d*$_2$**.

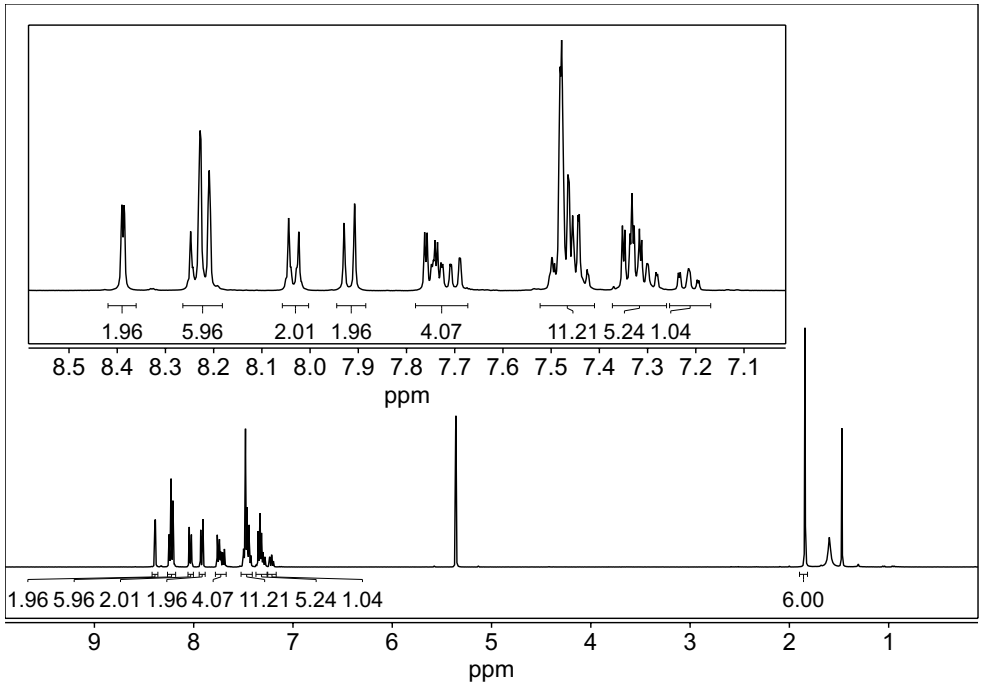

^{13}C {^{1}H} NMR spectrum of **TerCZ-IMAC** in **methylene chloride-*d*$_2$**.

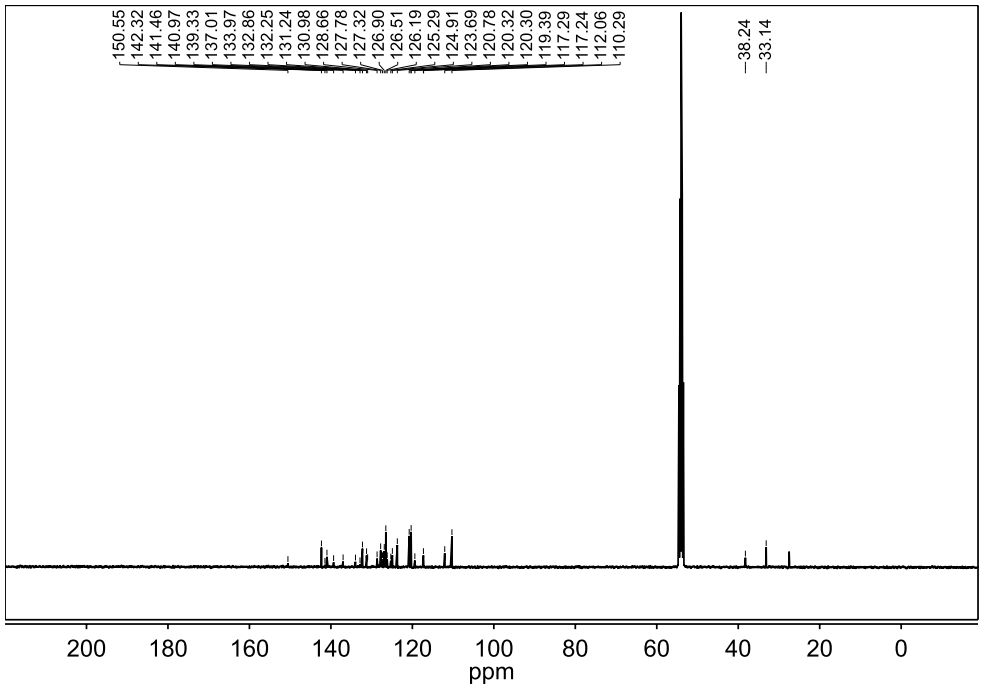

D.15 TolCZ-IMAC

^{1}H NMR spectrum of **TolCZ-IMAC** in **benzene-*d*$_6$**.

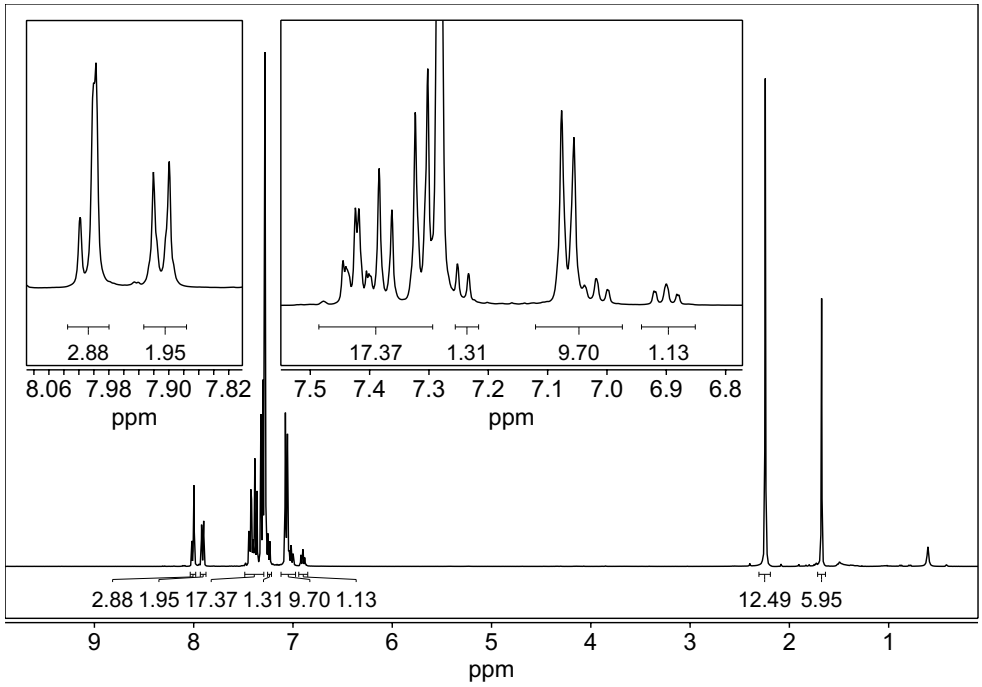

^{13}C {^{1}H} NMR spectrum of **TolCZ-IMAC** in **benzene-*d*$_6$**.

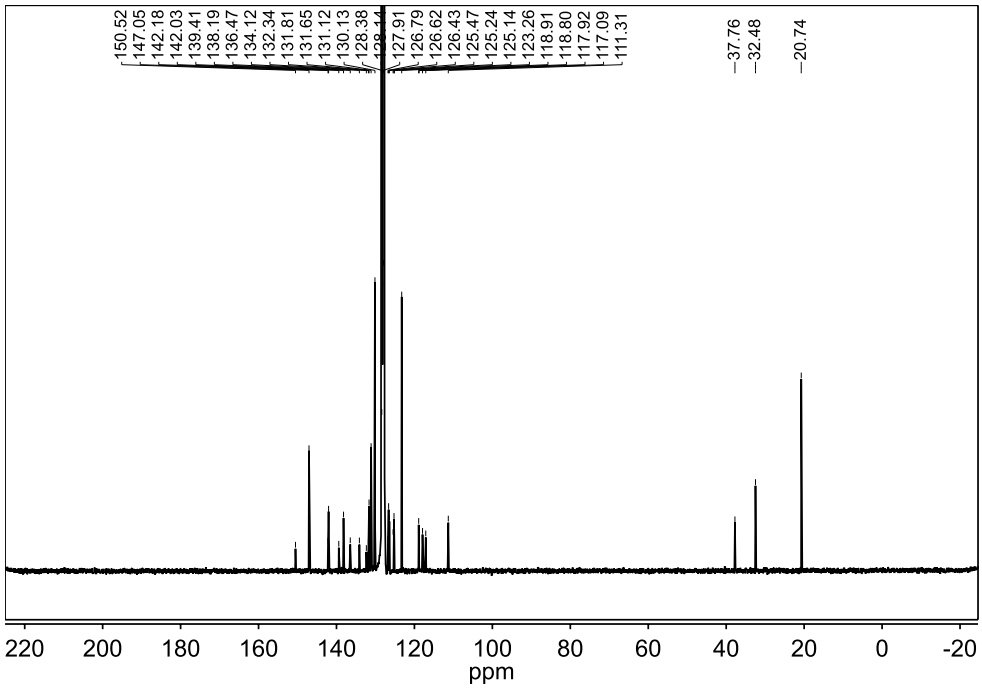

Appendix E : NMR spectra for Chapter 6

E.1 tBuTPI-PBI

^{1}H NMR spectrum of **tBuTPA-PBI** in **methylene chloride-*d*$_2$**.

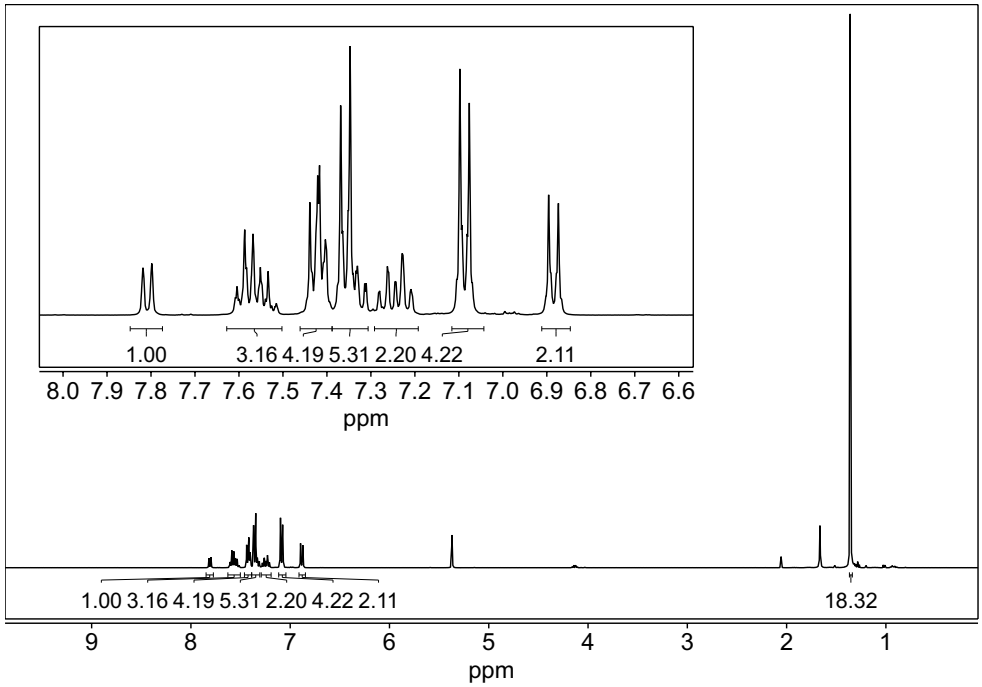

^{13}C{^{1}H} NMR spectrum of **tBuTPA-PBI** in **methylene chloride-*d*$_2$**.

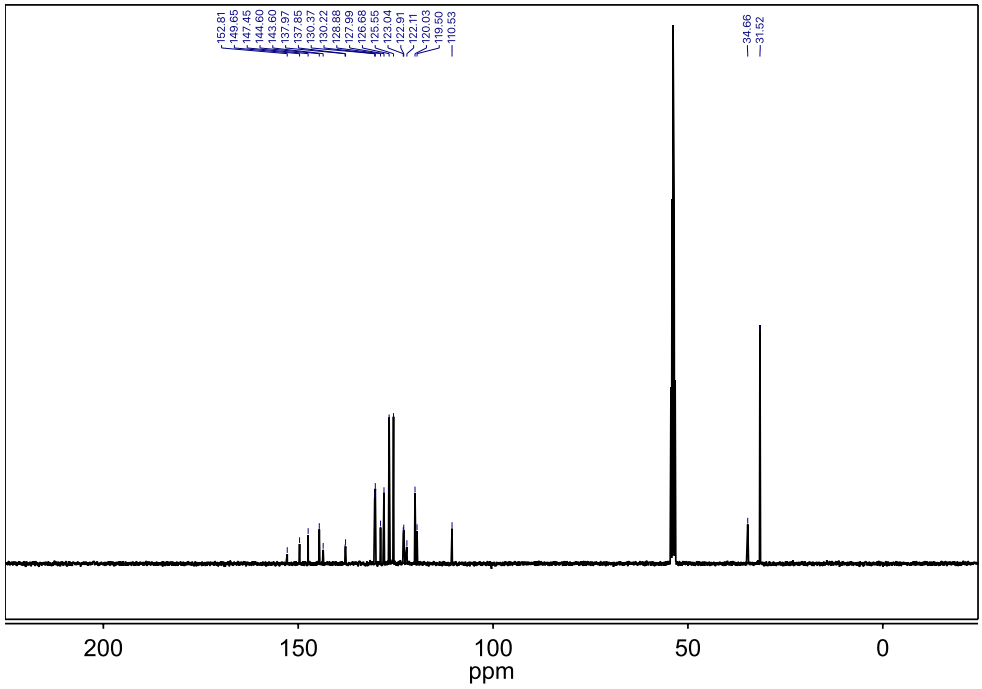

E.2 tBuTPI-IMAC

^{1}H NMR spectrum of **tBuTPA-IMAC** in **methylene chloride-*d*$_2$**.

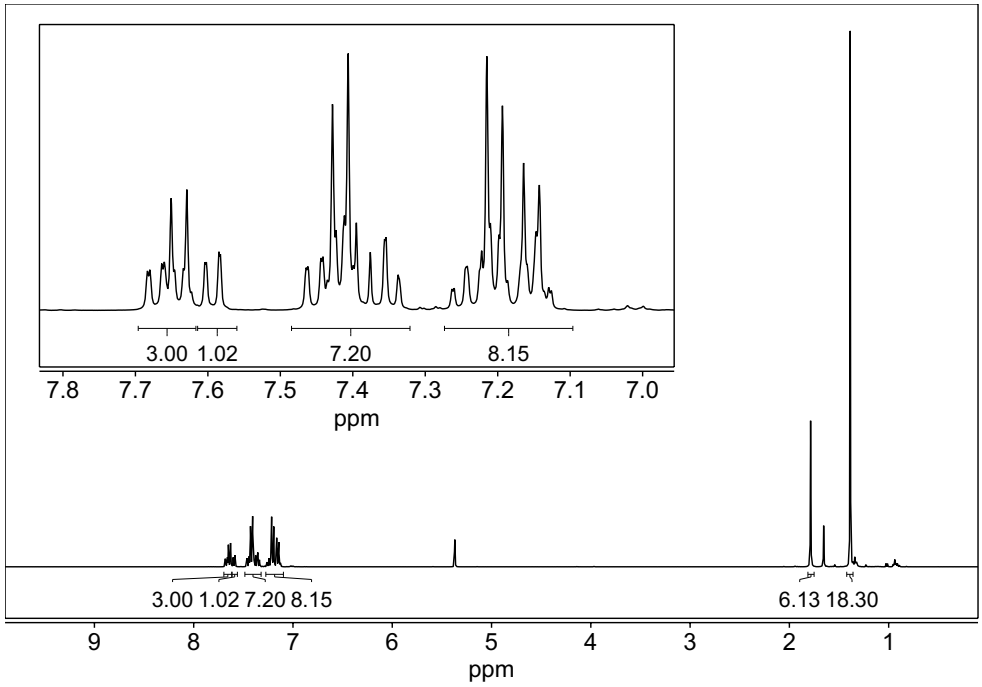

^{13}C{^{1}H} NMR spectrum of **tBuTPA-IMAC** in **methylene chloride-*d*$_2$**.

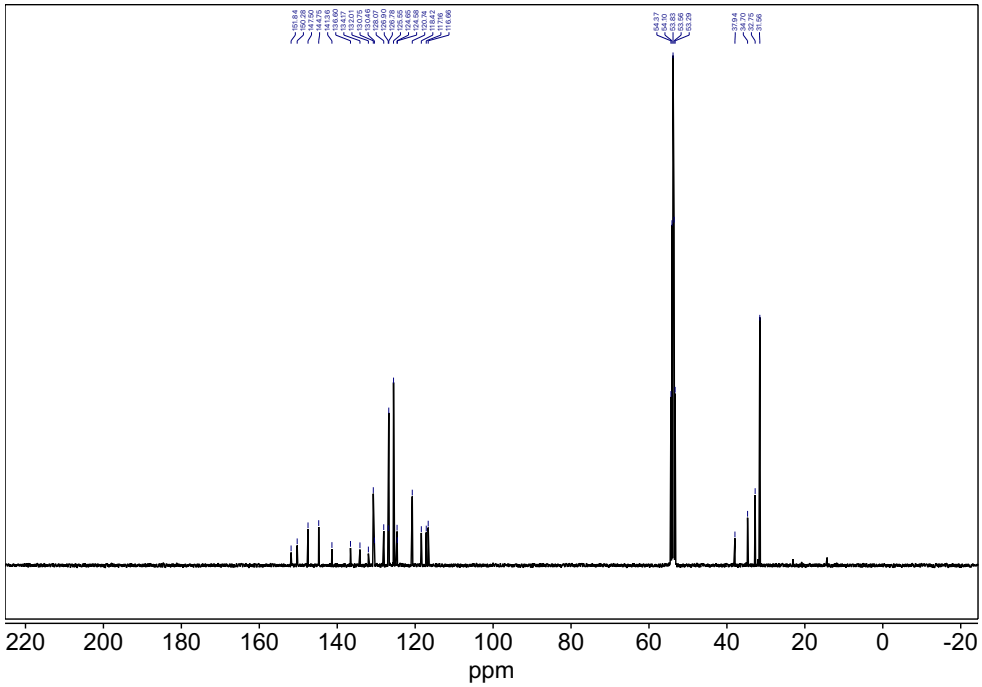

E.3 HMAT-IMAC

^{1}H NMR spectrum of **HMAT-IMAC** in **methylene chloride-*d*$_2$**.

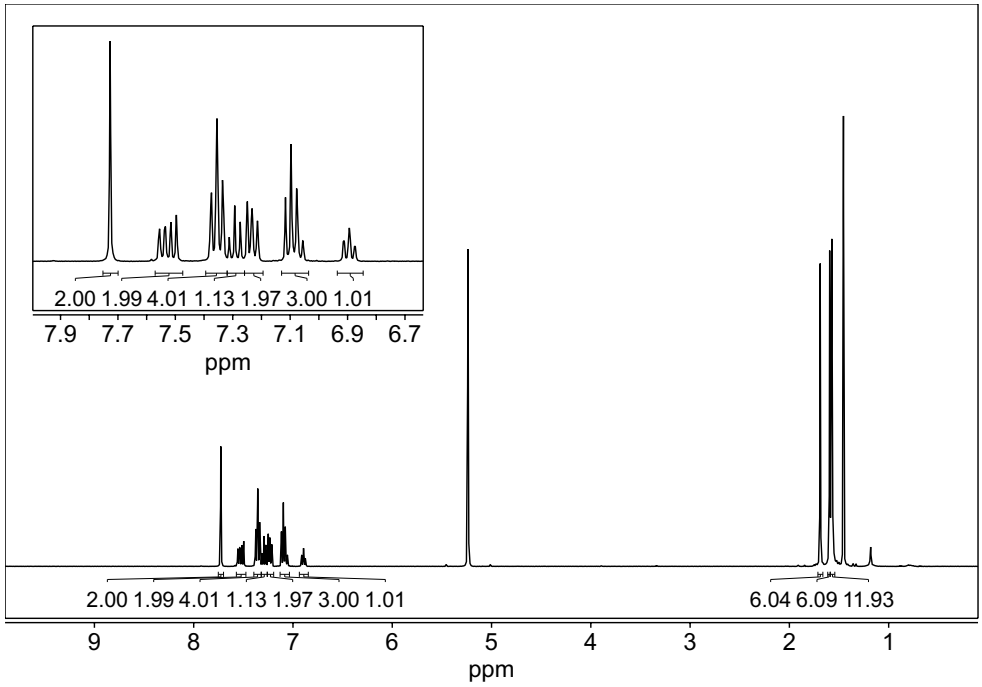

^{13}C{^{1}H} NMR spectrum of **HMAT-IMAC** in **methylene chloride-*d*$_2$**.